ION BEAM MIXING AND ELECTROCATALYTIC CHARACTERISTICS OF THIN FILM Ni/Pd SURFACE ALLOYS

BY

© USMAN GBADEBO AKANO

A Thesis

Submitted to the School of Graduate Studies
in partial Fulfilment of the Requirement for the Degree

Doctor of Philosophy

McMaster University

January 1987

ISBN 0-315-40252-0

ION BEAM MIXING CHARACTERISTICS OF THIN FILM Ni/Pd SURFACE ALLOYS

DOCTOR OF PHILOSOPHY (1987)
(Materials Science and Engineering)

McMASTER UNIVERSITY
Hamilton, Ontario

TITLE: Ion Beam Mixing and Electrocatalytic Characteristics of Thin Film Ni/Pd Surface Alloys

AUTHOR: Usman Gbadebo Akano, B.Sc. (EE) University of Ife, Nigeria

M.Eng. (McMaster University)

SUPERVISORS: Dr. D.A. Thompson
Dr. W.W. Smeltzer
Dr. J.A. Davies

NUMBER OF PAGES: xvi,273

ABSTRACT

Atomic mixing resulting from heavy-ion bombardment of thin-film Ni/Pd bilayers and thin Pd markers sandwiched between two Ni layers has been investigated. Experiments were carried out using 120 keV Ar^+ and 145 keV Kr^+ ions for doses $0 - 4 \times 10^{16}$ cm^{-2} over a wide temperature range (40 - 673K). The resulting interdiffusion was measured using 2 MeV $^4He^+$ ion backscattering in-situ. In some cases, additional depth analysis was undertaken using Auger Electron Spectroscopy (AES) with sputter depth profiling. The influence of film microstructure and bombardment-induced microstructural changes on tne mixing have been assessed with transmission electron microscopy (TEM). The electrocatalytic behavior of the ion-mixed bilayer samples was determined for the hydrogen evolution reaction in strong KOH solution, using potentiostatic polarization techniques.

The amount of ion beam mixing is found to vary with the square root of the ion dose for temperatures $\lesssim$ 573K. Also, at 40K, where it is assumed that no significant thermally activated process contributes to the mixing, it is found that the mixing is dependent on the damage energy, F_D, deposited at the interface region. Between 40 and $\sim$ 400K, the mixing parameter shows a weak temperature dependence with an apparent activation energy $E_a \sim 0.1$ eV. This suggests that some interstitial diffusion contributes to the inter-mixing in this temperature regime. Above $\sim$ 473K, the mixing (at each temperature) increases rapidly with ion dose for ir radiation doses $\lesssim 5 \times 10^{15}$ cm^{-2} with high initial mixing efficiencies of

6 - 35 atoms/ion between 573 - 673K. This initial rapid mixing level eventually slows to a less rapid ($\sim$ 1.2 atoms/ion at 673K) rate for doses $\geq 5\times10^{15}$ cm^{-2}. TEM observations of the irradiated and unirradiated films suggests that the change to a less rapid mixing rate is correlated with an increase in the average grain diameter (10 - 80 nm) in the film following ion bombardment, and therefore with a reduction in the contribution of grain boundary diffusion to the intermixing.

For samples annealed, without irradiation, below $\sim$ 473K, no measurable interdiffusion of the Ni/Pd layers was observed. For samples annealed above $\sim$ 473K, Whipple analyses of the interdiffusion show two distinct regions - lattice diffusion-dominated region near the original interface and grain boundary diffusion dominated region further away from the interface. The lattice diffusivities, D_ℓ', under thermal annealing conditions were evaluated and ranged from $\sim$ 0.22 to 52×16^{-16} cm^{-2}-sec^{-1} for Pd diffusing in Ni, and 0.33 to 56.6×10^{-16} cm^2-sec^{-1} for Ni diffusing in Pd between 523 - 673K. These lattice diffusivities are high because of enhancement of diffusion by defects present in the as-prepared films. The grain boundary diffusion coefficients (for Pd diffusion in Ni boundaries) D_B varied from $\sim 5.4\times10^{-14}$ cm^2-sec^{-1} at 523K to $\sim 3\times10^{-11}$ cm^2-sec^{-1} at 623K, with an apparent activation energy $E_B \sim 1.35$ eV and a prefactor $D_B^o \sim 0.75$ cm^2-sec^{-1}.

Under irradiation conditions, ion irradiation results in an enhancement of the mixing especially below $\sim$ 400K where almost an order of magnitude enhancement over thermal anneal only, was observed. At $\sim$ 673K, the contribution of equilibrium defects to interdiffusion overwhelms the irradiation effects. The diffusion coefficients under irradia-

tion, D_{rad}, were also evaluated and ranged from ~ 4 to 70×10^{-16} cm^2-sec^{-1} at 523 and 673K with apparent activation energy $E_a \sim 0.57$ eV.

For Pd films deposited on large-grain Ni substrates, thermal annealing and/or ion bombardment result in mixing levels that are almost two orders of magnitude lower than observed from small-grained Ni/Pd couples, though under irradiation conditions, radiation enhancement of the mixing was also observed.

As potential electrocatalysts for the H_2 evolution reaction in strong KOH solution, the ion-beam mixed surface alloys (in the over-potential range $\leq$ 0.4 V) show superior performance over smooth Ni, and Ni coated with evaporated Pd.

ACKNOWLEDGEMENTS

I wish to thank my supervisors, Dr. D.A. Thompson and Dr. W.W. Smeltzer for their support and guidance during the course of this research. Dr. J.A. Davies' continued support and criticisms have been invaluable and are hereby gratefully acknowledged.

I would like to thank the staff of the Tandem Accelerator Laboratory and the Radiation Effects group, in particular Mr. J. Stark, Mr. W. Williams, Mr. B. Diacon and Mr. B. McClelland for technical support.

It has been a pleasure to work with fine colleagues, past and present - Dr. N. Parikh, Ms. D. Stevanovic, Dr. A. Ibrahim, Mr. R. McCaulay-Newcombe and Mr. M. Fernandes. I also wish to thank Dr. S.A. Adediran and Mr. S. Aryee for being there when I needed emotional outlet.

My sincere thanks to Mrs. Helen Kennelly for her patience in typing the many editions of this thesis.

The financial support of McMaster University and University of Ife, Nigeria, is gratefully acknowledged.

Lastly, but certainly not the least, I am indebted to my wife, Ify, for her patience and continued support and encouragement throughout my stay at McMaster.

TABLE OF CONTENTS

LIST OF FIGURES

CHAPTER I

INTRODUCTION

Over the last ten years the phenomenon of ion beam induced atomic mixing has attracted considerable attention. First because it represents a major limitation on the depth resolution of all surface analytic techniques employing ion sputtering for depth profiling. Secondly because ion beam mixing provides a method for forming surface alloys by the intermixing of atoms between a thin overlayer film and substrate subjected to energetic ion irradiation. Such alloys can potentially find use in a variety of applications.

The application of ion implantation, for example, to improve the corrosion, oxidation and wear resistance of metals is well established (e.g. G. Dearnaley 1974), and the field of electrocatalysis would appear to be an exciting area of potential application of ion implantation and ion mixing of materials by modifying the surface of electrodes. One application of considerable current interest is hydrogen production via the electrolysis of water. At the moment most commercial electrolysers employ Ni in one form or another as electrode material basically because of its relatively low cost, good corrosion resistance and moderate overpotentials for the O_2/H_2 evolution reactions. However, for hydrogen production by water electrolysis to become competitive with alternate sources like fossil fuels, improved electrode performance is required. One way to achieve this is by alloying of suitable electrocatalysts with

a substrate metal. Pt and Pd have been shown (Miles 1975) to have the lowest overpotential of all elements for the hydrogen evolution reaction in strong caustic solutions. These materials are in general expensive and there is a need to minimize their consumption. Formation of surface alloys by ion beam mixing can possibly facilitate such a reduction in cost.

As a technique for surface alloy formation ion beam mixing has some potential advantages over direct ion implantation. These are:

1) higher concentration levels of the alloying element may be achieved than is possible by direct implantation where sputtering limits the maximum concentration levels attainable,

2) a given alloy composition may often be achieved at considerably lower ion dose than by direct implantation, whilst using more easily attainable ions such as Ar^+, Kr^+ etc.

3) novel alloy phases not normally present in the equilibrium phase diagram, as well as equilibrium phases may be induced by energetic ion bombardment.

However, at present the ion beam mixing process is not completely understood. It is generally recognized that there may be several mechanisms contributing to the mixing process. At sufficiently low temperatures where lattice defects are immobile collisional mixing resulting from repeated displacements of atoms within collision cascades dominates. At higher temperatures, where defects are mobile, additional mechanisms such as radiation enhanced diffusion (Wang 1984) may contribute to the overall mixing. Theoretical predictions (e.g. Sigmund et al, 1981)

based on these mechanisms are, however, often at variance with experimental results (Paine 1982, Paine et al 1985). For example in collisionally similar systems where one would expect a similar degree of mixing at low temperatures, experimentally observed mixing varies widely from system to system (Picraux 1982). Also in some systems (typically compound-forming systems) ion beam mixing results in alloys with equilibrium phase compositions similar to those obtained by thermal treatment, (e.g. Pt.-, Ni-silicides), while in others the resulting alloy phase may differ from the equilibrium phase e.g. Ni-Ag and Au-Co (Mayer 1981). As a result it is difficult to predict a-priori either the degree of mixing or even what alloy phases will result from ion bombardment.

This thesis reports in part on a systematic investigation of the ion beam mixing process in the Ni/Pd system. Ni/Pd was selected for these studies because of its feasability as cathode material for the production of hydrogen through the electrolysis of water in concentrated caustic solutions. Two kinds of target configurations were employed: the first consists of a thin ($\sim$ 1 nm) layer of Pd buried between two Ni layers. The mixing in this system approximates the diffusion-like spreading of a Pd marker in an Ni matrix, and the role of chemical driving forces is expected to be minimum. The second kind of configuration more appropriate to surface alloy formation is of interest for practical applications, and consists of an evaporated Pd layer on an Ni substrate, thus forming a semi-infinite bilayer couple. Supplies of Pd and Ni may be unlimited for typical ion doses used and the system is free to form binary

phases of any composition. Chemical driving forces may also play a role.

The influence of ion species (120 KeV Ar^+ and 145 keV Kr^+), ion dose ($0.3-4\times10^{16}$ cm^{-2}), dose rate ($0.43-5.5\times10^{12}$ ions $cm^{-2}sec^{-1}$) and temperature (40-673K) on the mixing have been studied. The mixing resulting from ion bombardment and/or temperature has been characterized principally by Rutherford backscattering (RBS) analysis using MeV He^+ ions. The influence of film microstructure and grain boundary diffusion on the mixing is also assessed.

The electrocatalytic activity of the ion beam mixed Ni/Pd couples for the hydrogen evolution reaction in $\sim$ 6N KOH solution has also been studied using electrochemical polarization techniques. The electrode activities were characterized in terms of the hydrogen overpotential of the electrode and its dependence on the surface concentration of Pd.

In chapter 2 a limited review of the applications of ion implanted and ion beam mixed material is given, including applications to oxidation, corrosion resistance and electrocatalysis. The properties of Ni, Pd and Ni/Pd alloys relevant to this work are also reviewed in this chapter. The principles of heavy-ion/solid interactions relevant to ion beam mixing including energy loss and slowing down processes and the nature of defects produced in ion irradiated metals are discussed in chapter 3. Also in chapter 3 the various ion beam mixing mechanisms and the proposed theoretical models are discussed along with results on marker spreading and bilayer mixing experiments.

In chapter 4 the analysis techniques are described. These include the theoretical aspects of light MeV ions backscattering (RBS) and the

principles of mass identification and impurity depth profiling using RBS. Electrochemical polarization techniques are also discussed. The experimental facilities for ion beam processing and ion beam analysis, and the electrochemical apparatus for the polarization measurements are the topics of chapter 5. Sample preparation methods and the types of experiments performed are also discussed in this chapter.

In chapter 6, the experimental results are given. They are divided into three sections. In section 6.1 results of the spreading of buried thin Pd markers in Ni are given; ion mixing of Ni/Pd bilayer couples are discussed in section 6.2; in section 6.3, the electrochemical polarization measurements on ion beam mixed electrodes used as cathodes in ∿ 6N KOH solution are given and discussed.

Finally in chapter 7, a summary of the observations and conclusions regarding the ion beam mixing in the Ni/Pd system and the electrocatalytic properties of the alloys are given.

CHAPTER 2

RECENT APPLICATIONS OF ION BEAM PROCESSING OF METALS

2.1 Introduction

In a variety of metallurgical applications it is often necessary to develop materials with improved oxidation, aqueous corrosion and wear resistance as well as improved electrocatalytic properties. The usual approach for forming such materials is by bulk-alloying of a base metal with elements which enhance the desired properties. It is known for example (Fontana et al 1978) that addition of Cr, Mo and Ni imparts greater corrosion resistance to steel, and that small additions of noble metals to Ti (Stern et al 1960) can improve its corrosion resistance in non-oxidizing strong acids. Small additions of Pd to Ti result in a galvanic couple having a passivating-potential which is more noble than the passivity potential for Ti. Similarly Damjanovic et al (1966) have shown that the activity of Rh cathodes for the hydrogen evolution reaction in KOH solution can be improved by alloying with Pt. Similar measurements by Bockris et al (1968) on Au-Pd and Au-Pt cathodes show that the quantity of evolved hydrogen on these alloys is $\sim 10^3$ higher than on pure Au.

The oxidation resistance of metals and alloys may also be improved by the addition of beneficial elements. The addition of Al to Fe-Cr alloys (Dearnaley 1981) for example imparts greater oxidation resistance by the formation of a coherent Al_2O_3 which strongly resists further ion transport and therefore the oxidation of Fe.

However since corrosion, oxidation and electrocatalysis are surface and near surface phenomena it may not be necessary to produce bulk alloys to improve these properties, and surface layer alloying may often serve to impart adequate oxidation, wear and corrosion resistance and catalytic activity to metals with intrinsically inferior properties.

The range of surface alloys that can be prepared by conventional means (thermal diffusion) is however limited by the equilibrium phase diagrams. Equilibrium phases and, in principle, metastable phases can be produced by ion beam processing irrespective of the compositional constraints of the equilibrium phase diagram, though the metastable phase may lead to the precipitation of equilibrium phases if the temperature is high enough. Mayer et al (1981), for example, using ion beam mixing techniques (chapter 3) were able to produce metastable single phase Ag-Cu and Au-Co alloys which were stable against precipitation to two phase alloys up to $\sim$ 200^{o}C and $\sim$ 350^{o}C, respectively. Also in many cases only minute quantities of beneficial atoms are required to effect changes in the corrosion, electrochemical wear and oxidation properties of materials. Ion implantation and ion beam mixing may therefore result in a more economical way of changing these properties in comparison with normal bulk-alloying procedures. In section 2.2 a limited review of the application of ion implantation and ion beam mixing to improved oxidation and corrosion resistance of metals is given. In section 2.3 electrocatalysis of the H-redox reaction on metallic surfaces and the application of ion implantation and ion beam mixing to it is reviewed.

2.2 Ion implantation of metals

Ion implantation technique has been used to improve a variety of properties of metals and alloys in recent years. Its application to improve the mechanical properties of metals such as friction, wear and hardness is well-established (Dearnaley 1970, 1982, Hartley 1975,1980). Its application to improve the oxidation resistance (Grant 1975), corrosion resistance (Ashworth et al 1977) and electrocatalytic activity (Wolf 1980) of metals and alloys has also been demonstrated.

2.2.1 Improved oxidation resistance

The oxidation resistance of metals and alloys can be improved in several ways. It is well-known for example that some oxides e.g. Al_2O_3 and Cr_2O_3, form coherent films which serve as barriers to further oxygen or base metal diffusion. Also structural defects such as grain boundaries and dislocations are known to provide easy diffusion paths for the transport of oxygen or cations. In Ti for example Smeltzer et al (1961) concluded that the oxidation proceeded by the transport of oxygen along $\sim$ 1 nm diameter dislocation pipes. If these easy diffusion paths can be blocked effectively, the oxidation rate can be substantially reduced. Typical blocking impurities are large oversized, or insoluble atoms.

Benjamin and Dearnaley (1976) have shown that ion implantation of barium, caesium, ytterbium and europium into Ti lead to improved oxidation resistance of Ti. Apparently these elements form oxide precipitates at the short-circuit diffusion paths in Ti thereby protecting the base metal against further oxidation. Fig. 2.1 shows the oxidation kinetic of Ba-implanted and unimplanted Ti and indicates that at 600^{o}C the oxidation of

the sample implanted with 2×10^{16} Ba^+ cm^{-2} is $\sim$ a factor of 5 less than the unimplanted Ti. Similar observations have been made by Goode (1976) on the oxidation of cerium-implanted Ni, and by Bennett et al (1980) on the oxidation of Ce^+-implanted stainless steel.

Al and Cr are often used as alloy additions to provide protective oxide films. Bernabai et al (1980) using this idea studied the oxidation kinetics of Al^+-implanted Fe-Cr-Al-Y alloy containing 1.45% Al. Their results, which are shown in Fig. 2.2 for alloys oxidized in air at 1100°C, show that the oxidation rate constant has been reduced by a factor of $\sim$ 140 for the sample implanted with 10^{17} Al^+ ions cm^{-2}. Subsequent analysis showed that the oxide scale on the implanted samples was primarily Al_2O_3 in contrast to the unimplanted samples whose scales consisted of $\sim$ 40% mixed oxides of Fe and Cr. Similar improvement in the oxidation resistance of Cu following Al implantation has been observed by Rickards et al (1980).

Dearnaley et al. (1973) have also investigated the thermal oxidation of ion implanted stainless steel and found that implantation of Bi, In and Al ions all result in a lower oxidation rate of stainless steel. In a related study Naguib et al (1976) examined the influence of B, C, N and Ne implantation on the thermal oxidation of Cu. Their results show that a B dose of $\sim 10^{17}$ ($\sim$ 15 at. % peak concentration) is quite effective in reducing the oxidation rate while both Ne and N were not so effective. C on the other hand increased the oxidation rate. The role of ion implantation on the high temperature oxidation of metals has been discussed recently by Galerie (1982) and Dearnaley (1983).

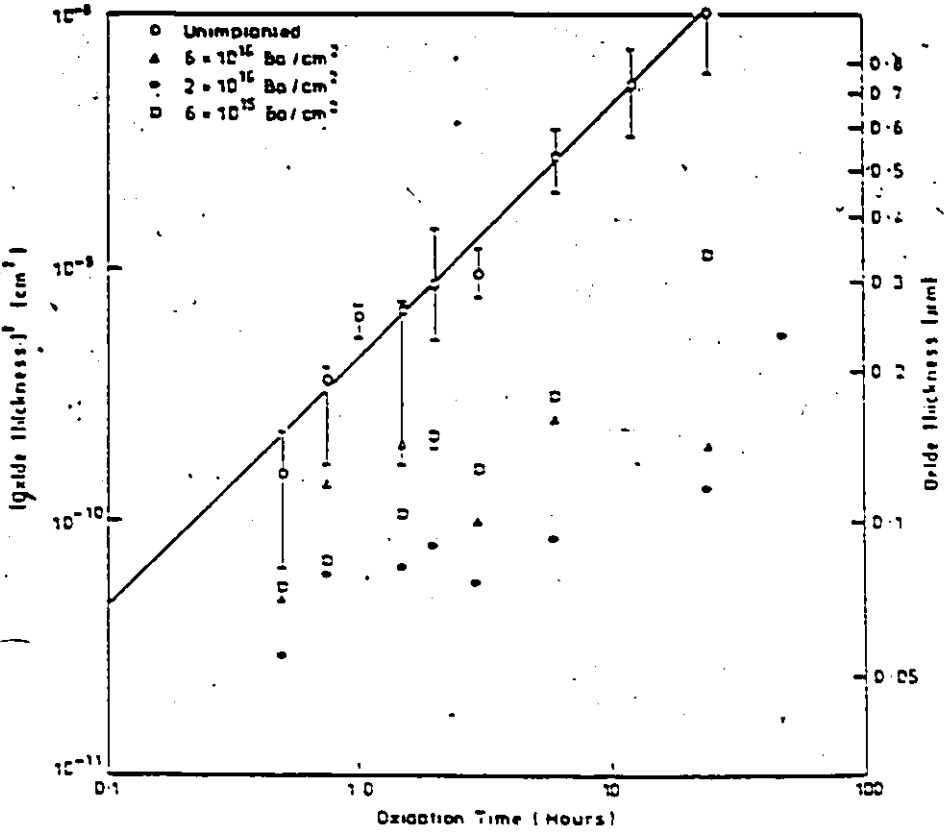

Fig. 2.1: The oxidation kinetics of titanium at 600°C after implantation with barium to different doses

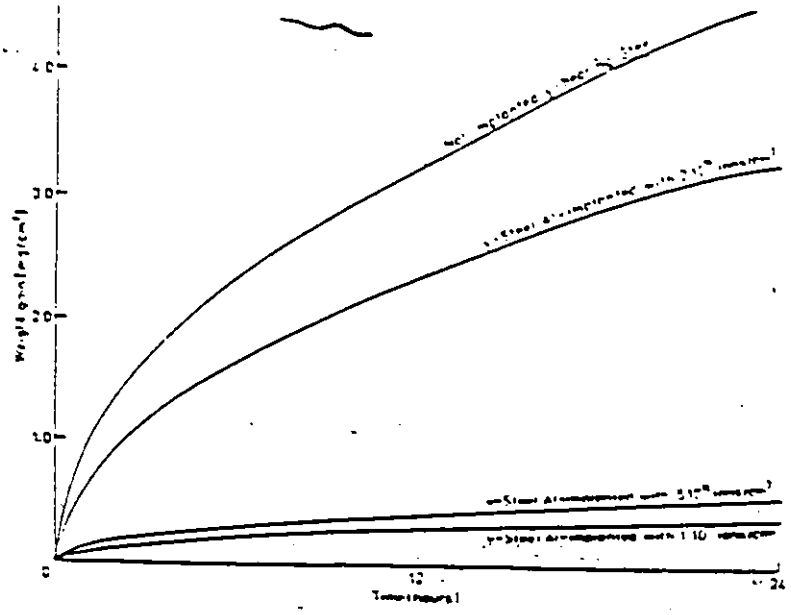

Fig. 2.2: The oxidation kinetics of Fe-Cr-Al-Y alloy at 1100°C for different doses of implanted Al.

2.2.2 Corrosion resistance

Aqueous corrosion of metallic surfaces takes place by an electrochemical mechanism involving two simultaneous and complementary reactions, namely metal dissolution (oxidation) at the anode and deposition reaction at the cathode. Anodic dissolution will be high only if it is supported by an efficient cathodic process. If the cathodic process is slow, this will control the anodic dissolution rate. However even in the absence of cathodic control a marked reduction in the corrosion rate is possible if the metal is self-passivating. This passivation has been attributed (Fontana et al.1978) to the formation of a surface film which acts as an efficient barrier to the corroding medium.

The most common method employed in the study of metallic corrosion kinetics is the polarization technique (chapter 4). In this technique a potential is applied between the test electrode (anode) and an auxillary electrode (typically Pt). The current passing through the cell is then a measure of the corrosion rate for an electrode of a given surface area at a particular value of the applied potential. Fig. 2.3 shows a typical polarization curve for Fe. Polarizing the electrode to more positive potentials first leads to higher corrosion rate. At potentials > E_{pp}, the passivating potential, there is a reduction in corrosion rate from i_{crit} to i_{pass} due to the formation of a passive film. This passivity is maintained until at much larger potentials >> E_{pp} the passive film breaks down, passivity is lost and higher corrosion rates again are obtained.

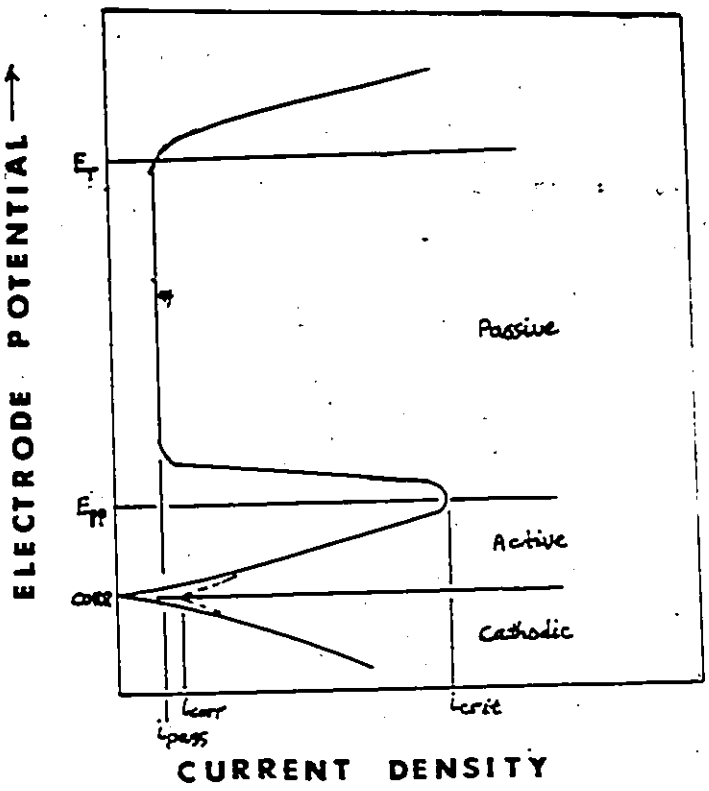

Fig. 2.3: Schematic of typical polarization curve for Fe.

In the design of corrosion-resistant alloys one usual approach is to promote passivity by bulk alloying with elements which tend to lower the passivation potential, E_{pp}, and the critical current density i_{crit}. It is known, for example, (Fontana et al. 1978) that addition of Cr, Mo and Ni to steel to form stainless steel imparts greater corrosion resistance in this manner. Small alloy addition of Pd to Ti is also known (Stern et al. 1960) to reduce the corrosion rate of Ti in non-oxidizing strong acids. In this case the mixed potential of the alloy is more noble than the passivating potential of pure Ti and the alloy is self-passivating. Tomashov et al. (1980) have shown that only small additions of Pd or Pt (0.1 to 0.5%) to Ti are needed to ensure its corrosion protection. The use of ion im-

plantation technique to introduce such expensive alloying additions helps to minimize materials costs.

Munn and Wolf (1985) have used this method to improve the corrosion behavior of Ti. They found (Fig. 2.4) that for Ti samples implanted with 400 KeV Pd^{2+} ions to a dose of $2x10^{16}$ cm^{-2} the onset of anodic dissolution in 20% H_2SO_4 is delayed for $\sim$ 100 days while anodic dissolution of the unimplanted Ti begins after only 6 - 10 hours immersion in the solution. Similar observation has been made by Lichter et al (1982) on the corrosion behavior of Pt implanted Ti in 1N H_2SO_4. Their results show that even for low Pt doses ($\sim 4.6x10^{14}$ cm^{-2}) the surface alloy does not become anodic until after times > 700 minutes. The corrosion behavior of Pd-implanted Ti has also been studied by Hubler et al (1980) and shows that the implantation of $1x10^{16}$ Pd^{+} ions cm^{-2} ($\sim$ 4% peak concentration) reduces the corrosion rate of Ti in 1N H_2SO_4 by a factor of 10^3 compared to Ti.

Ion implantation has been used to improve the corrosion resistance of other systems as well. Covino et al (1978), for example have shown that the implantation of 25 KeV Ni or Cr ions ($.85-3.4x10^{16}$ Ni^{+}/cm^2) into Fe results in a surface alloy which exhibits, in boric acid solution, pitting- and general-corrosion characteristics which are comparable to nominally equivalent bulk alloys. Al-Saffar et al (1980) have also shown that the implantation of Mo into Al and high strength Al alloys improves the resistance of the metal and the alloy to pitting corrosion in sulphate solutions containing chlorine. The influence of Au, Pb, Hg (Wolf et al 1982) and Cu (Ferber et al 1980) implantation on the corrosion behavior of Fe has also been studied. Au and Cu implantation lead to higher corrosion

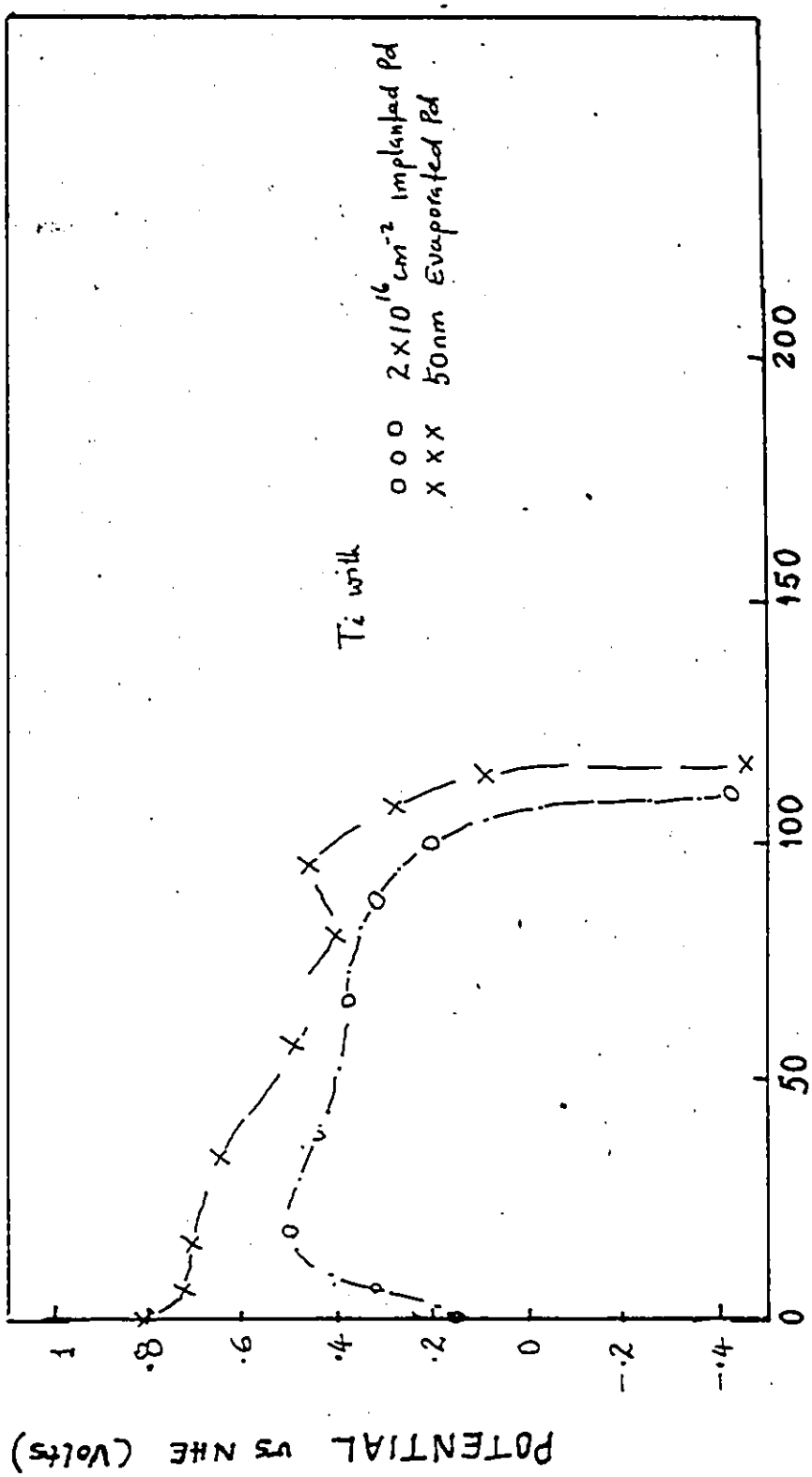

Fig. 2.4: Corrosion potential-time curve for titanium with implanted and evaporated Pd layers in 20% H_2SO_4 at room temperature.

rates while Hg and Pb implantations impeded the corrosion.

Ion impact can itself affect corrosion behaviour of metals either through lattice damage resulting from ion bombardment or through increased surface area of the electrode resulting from sputtering. It is therefore useful to assess those effects that are due to the radiation damage vis-a-vis the chemical effects of the implanted species. This can be done by implanting chemically inert species into the test electrodes. This type of study has been done by Ashworth et al. (1978) who implanted Ar into Fe and by Ferber et al. (1980) who implanted Ne and Ar into Fe. In both studies inert gas implantation leads to a slightly higher corrosion rate of Fe which the authors attribute to the surface roughening effect of sputtering.

Recent reviews by Ashworth et al.(1980), Clayton (1981) and Dearnaley (1983,1985) detail examples of the beneficial effects of ion implantation on the oxidation and corrosion resistance of metals.

2.2.3 Ion beam mixing and corrosion resistance

The maximum concentration of an alloying component that can be achieved by ion implantation is limited by sputtering. Higher concentrations however can be obtained by the technique of ion beam mixing (discussed in detail in chapter 3). Though the ion beam mixing technique confers greater flexibility in the range of surface alloys that may be produced by ion beam processing, very little work has been published on its application to improve the oxidation and corrosion resistance of metals.

Bhattacharya et al. (1985) have studied the corrosion properties of Ni-Mo and Ni-Ti amorphous alloys produced by ion beam mixing. Their results show that the critical current density, i_{crit}, needed to achieve

passivation of the Ni-Mo alloy is ∿ 30 times less for the ion beam mixed alloy than for equivalent alloy produced by co-deposition of Ni and Mo. Their result for ion beam mixed Ni-Ti alloy is shown in Table 2.1 and shows that i_{crit} for the ion beam-mixed alloy can be a factor of 40 less than for the co-deposited Ni-Ti alloy and $\sim 10^2$ times less than for pure Ni.

Table 2.1: Critical current density measured on various Ni-Ti alloys

Ion Dose Au^+/cm^2	Alloy	i_{cri} ($\mu A/cm^2$)
$1x10^{15}$	Ni_{50}-Ti_{50}	$\sim 5x10^3$
$3x10^{15}$	Ni_{50}-Ti_{50}	$\sim 4x10^3$
$10x10^{15}$	Ni_{50}-Ti_{50}	$\sim 1x10^3$
Co-deposited	Ni_{50}-Ti_{50}	$\sim 4x10^4$
0	Ni	$\sim 1x10^5$

In a related study Munn and Wolf (1985) studied the corrosion behavior (in 20% H_2SO_4) of Pd-implanted Ti, ion-beam-mixed (Ar and Kr ions) Pd-Ti alloys and Ti with evaporated Pd layers. Their results (Fig. 2.5) show that the ion beam mixed alloy is more corrosion resistant than either the Pd-implanted Ti or the Pd on Ti and remains passive after 300 days in solution. The ion mixed alloy has better corrosion resistance apparently because it ensures both better adhesion between the Pd and Ti (vs. evaporated film), and higher surface concentration of Pd (vs. implanted Pd). Similar observations have been made by Fedrizzi et al. (1985) on the corrosion resistance of ion-beam-mixed Ni-Sn alloys and by Matteson (1985) on the corrosion and oxidation of Al/C alloys produced by ion irradiation.

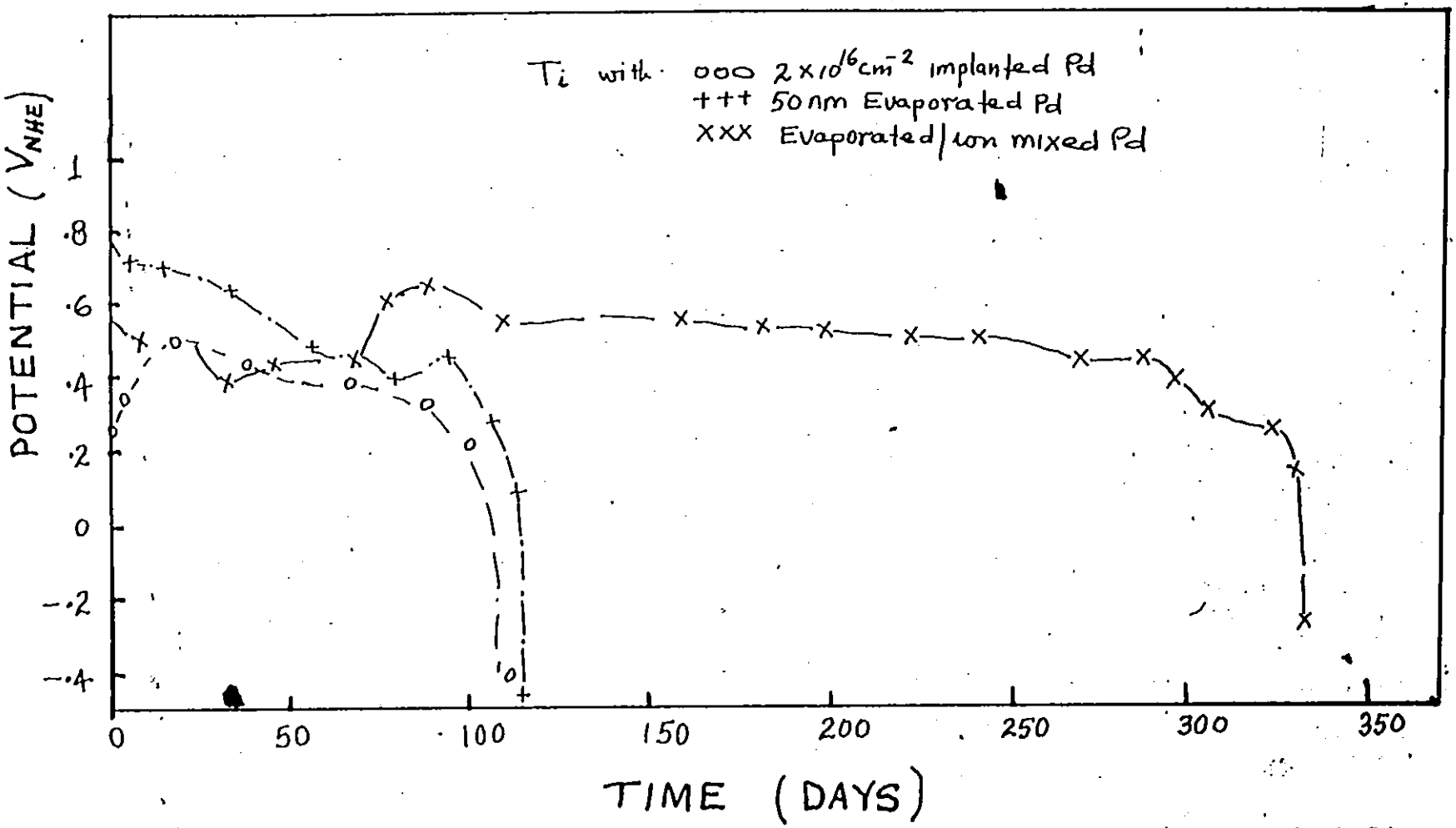

Fig. 2.5: [3]Corrosion potential-time curve for titanium with implanted, evaporated and ion-beam-mixed Pd layers in 20% H_2SO_4.

2.3 Electrocatalysis and water electrolysis

Following the energy crunch of the 1970's, interest in alternative energy sources to fossil fuels increased dramatically. One such attractive non-fossil source is the generation of power by fuel cells. Fuel cells are particularly attractive because they require little or no moving parts, little skilled labor to maintain and the by-product (water) is non-polluting. The feed materials (hydrogen and oxygen) can be economically produced from a cheap renewable resource; water. In addition increased demands for hydrogen for use by the fertilizer, chemical and other industries in the face of dwindling fossil sources means that bulk generation of hydrogen via the electrolysis of water will continue to be important. Although the electrolysis of water is potentially a reversible process, the efficiency is limited by the departure of the electrodes from reversible behavior.

The parameter of importance in evaluating water electrolysis cells is the magnitude of the cell voltage which is composed of the various contributions (Leroy et al 1978) shown by

$$E = E_{rev} + \eta_A + \eta_C + \eta_{ohm}$$

where E_{rev} is the thermodynamic decomposition voltage, η_A is the departure of the anode electrode potential from the reversible value (anodic overpotential), η_C is the cathode overpotential and η_{ohm} is the ohmic drop in the electrolyte between the anode and cathode. Table 2.2 shows typical values of the components of water electrolysis cell voltage.

Table 2.2 Typical components of water electrolysis cell voltage current density 150 mA/cm^2, T = 75°C. Source: (Bockris et al 1981)

E_{rev}	= 1.19V
η_A	= 0.40V
η_C	= 0.30
η_{ohm}	= 0.25 V
Cell voltage	= 2.14 V

The electrode overpotentials lead to additional losses in the cell in addition to those incurred by the resistance of the cell. For any fixed current through the cell however, the overpotential varies with the chosen electrode material according to its properties as an electrocatalyst and can be greatly reduced by using certain metals.

The kinetics of electrode processes will be discussed in chapter 4; here we simply note that there are two contributions to the electrochemical polarization of an electrode: activation and concentration polarizations. In the absence of concentration polarization, the electrode overpotential is determined solely by activation polarization. Activation polarization refers to electrochemical reactions which are controlled by a slow step in the reaction sequence. During H_2-evolution this slow step may be electron transfer or the formation of hydrogen molecules. The activation overpotential, η_a, is given by the Tafel equation (Bockris 1969)

$$\eta_a = \frac{\pm 2.303\ RT}{\alpha n F} \log \frac{i}{i_0} \qquad (2.1)$$

where R is gas constant, T is temperature, α is a transfer coefficient, n is number of electrons involved in the reaction, F is the Faraday constant,

i is the current density and i_0 is the exchange current density and describes the rate of oxidation and reduction reactions at an equilibrium electrode. The + is for anodic overpotential and - for cathodic overpotential.

Eq. (2.1) can be written as

$$\eta = a + b \log i \qquad (2.2)$$

where $$a = \frac{2.303RT}{\alpha nF} \log i_0$$

$$b = \frac{2.303RT}{\alpha nF}$$ is a constant called the Tafel slope.

Fig. 2.6 shows the plot of η vs log i for a hydrogen electrode. At the reversible potential, the overpotential $\eta = 0$ and the oxidation/reduction reactions proceed at an equal rate given by i_0. i_0 is a property of the electrode material and varies widely, for any particular reaction, from one material to another. For example for the H/H^+ reaction i_0 varies from 10^{-3} A/cm^2 for Pt to 10^{-12} A/cm^2 for Hg (Fontana et al 1978). Materials like Pt with high exchange current densities are then the better electrocatalysts for such reactions.

2.3.1 Overpotential of the oxygen evolution reaction

The oxygen evolution reaction on metals and alloys has been studied by several groups e.g. Damjanovic et al (1966) (Rh, Ir and Pt-Rh alloy), Appleby et al. (1978) (Pt, Ir and Ni) and Miles (1975) (several metals). These studies show that Ni and the noble metals Rh, Pd, Ir and Pt have minimum overpotentials for the oxygen evolution reaction especially in concentrated alkali solutions. It is therefore not surprising that most commercial electrolyzers now employ Ni or anodized Ni as electrode material.

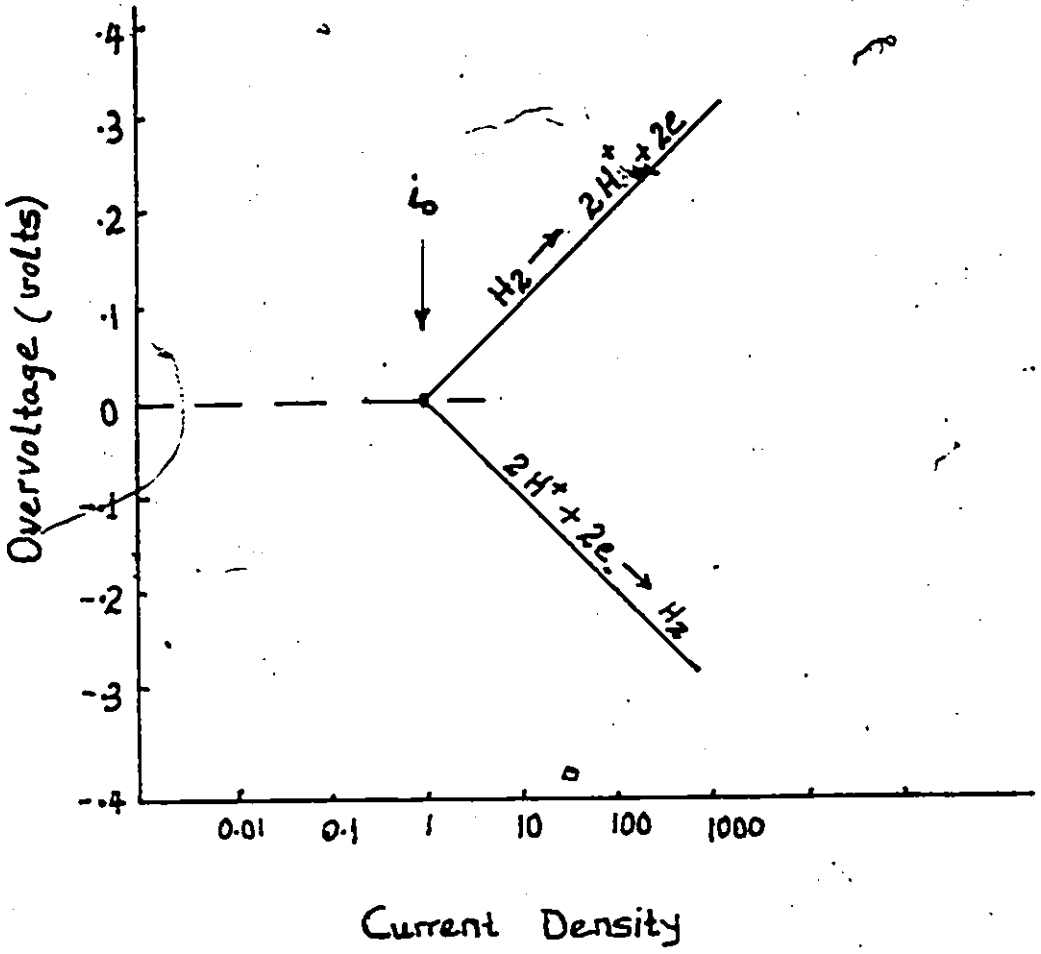

Fig. 2.6 Typical activation polarization curve for a hydrogen electrode.

Akano et al (1980) and Thompson et al (1982) have attempted to reduce the oxygen overvoltage on Ni electrodes by implanting various noble metals into Ni. Their results indicate that except for Ag no appreciable reduction of overpotential results from noble metal alloying of nickel. Even more important is their observation that in every case loss of the noble metal into solution occured over the two day test period, the loss ranging from 90% for Ru to 12% for implanted Pt. The alloying additions remaining within the electrode were observed to be buried deep beneath a nickel oxide layer and therefore not available to catalyse the oxygen evolution reaction. These results (Miles (1975), Appleby (1978), Akano (1981) and Thompson (1982)) indicate that noble metal catalysis for oxygen evolution in strongly alkaline solutions at elevated temperatures is unnecessary, and that nickel or anodized nickel electrodes probably represent the most effective surface for this reaction. Recent results by Balej (1985) on the electrocatalysis of oxygen evolution on various mixed oxide electrodes confirms that nickel anodes have by far the lowest overvoltage.

2.3.2 Overpotential of the hydrogen evolution reaction

The cathode activation potential (η_c) contribution to the overall cell voltage is given, in general, by the Tafel equation (Eq. (2.1) (Bockris and Reddy (1970))

$$\eta_c = \frac{2.303RT}{\alpha F} \log \frac{i}{i_0} \quad .$$

Because the overpotential associated with the hydrogen evolution reaction is less than that associated with the oxygen evolution reaction, the inducement to develop better cathode electrocatalysts has been lacking.

Reduction in the overpotential at high current densities is possible by working at high pressures since this reduces the gas bubble diameter and consequently the overall ohmic drop between the electrodes. This reduction in cell potential however amounts to $\sim$ 100 mV at 100 atmospheres for 25% KOH (Bockris et al. 1983). Further performance gains can be obtained by increasing the operating temperature. Miles et al. (1976) have studied the influence of temperature on the kinetic parameters for the hydrogen and oxygen evolution reactions on Ni electrodes in 50 w/o KOH solution. The Tafel lines indicate an improvement in exchange current density, i_0, with increasing temperature, especially for the oxygen evolution reaction and less so for the hydrogen evolution. An additional problem associated with working at higher temperatures is the stability of the seperator material in use with current commercial electrolysers. In order to obtain the evolved gases in a reasonably pure and safe condition, a semi-permeable diaphragm is usually placed between the electrodes to prevent the gases mixing. The diaphragm material used should have low ohmic resistance in the electrolyte, be resistant to chemical attack in the electrolyte and its cost must be reasonable. Woven asbestos fibre cloth is almost always used as diaphragm because it meets all these requirements. However above 80^{o}C, it is not very stable (Srinivasan et al. 1977) and operating the cell at higher temperatures will mean, therefore, finding a replacement for asbestos in its present form as a separator material. For cells operating at low temperatures ($\sim$ 80^{o}C), major reduction in

electrode overpotentials, especially of the hydrogen electrode, will require an improved electrocatalyst in conjunction perhaps with higher area electrodes.

2.3.3 Electrocatalysis of the hydrogen evolution reaction

As pointed out in section 2.2.1, the exchange current density i_0 describes the rate at which a particular reaction proceeds on an electrode at equilibrium potential. The rate at any given potential is given by the current density i through the cell at that potential. The electrocatalytic activity of an electrode for a particular reaction is then the rate (i cm^{-2}) at which that reaction proceeds, at a given potential on the electrode. The relative catalytic activity of the two electrodes is then given by the relative current densities measured on the electrodes at the same potential.

Schuldiner et al. (1957) have studied the hydrogen evolution reaction on Au, Pd and a series of Au/Pd alloys in 2N H_2SO_4 solution. The alloys range in composition from 19% to 100% Au. They observed that for Pd concentration < 50%, the overpotential on the alloy is the same as on pure gold, while for Pd concentration $\geq$ 50% the overpotential decreases rapidly towards that of pure Pd. Similar hydrogen overvoltage measurements in acid solutions on Ni, Pd and a series of Ni/Pd alloys have been made by Hoare et al. (1958). On the pure elements (Fig. 2.7) the measured Tafel slopes were 40 mV/decade and 120 mV/decade for Pd and Ni respectively. It is interesting that all the alloys including those with low Pd content show the same Tafel slope as pure Pd, namely 40 mV/decade. Fig. 2.7 shows that the largest reduction in overpotential was exhibited by alloys with

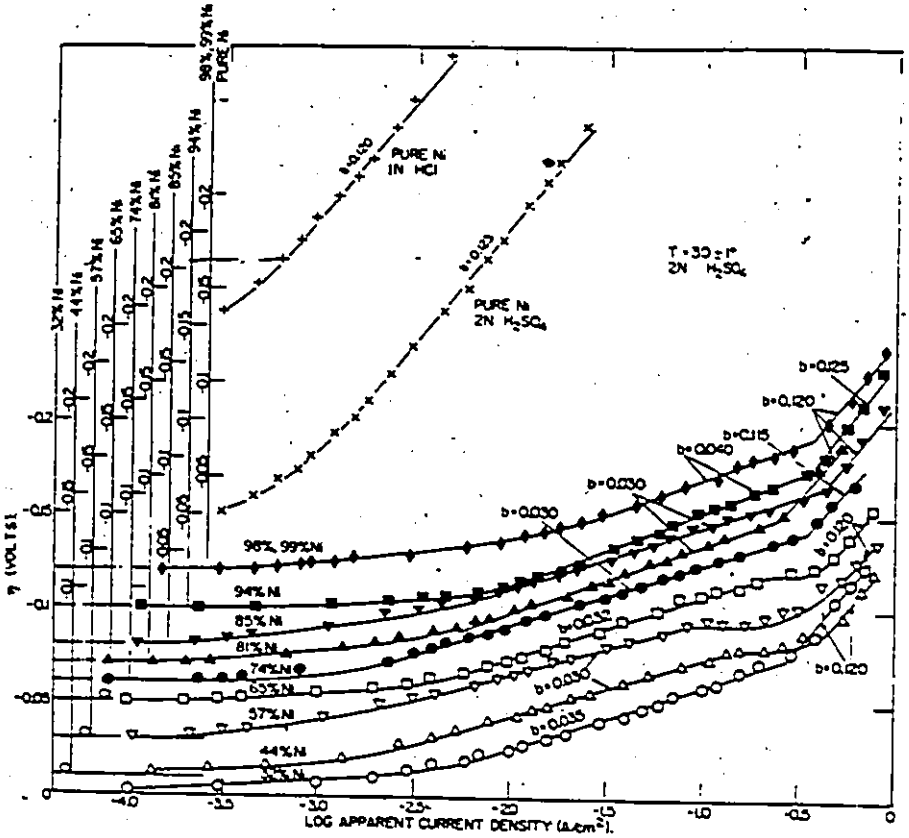

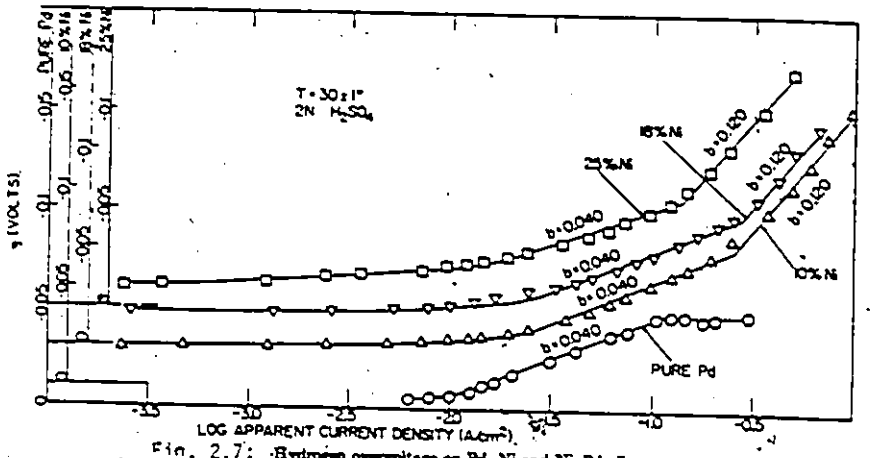

Fig. 2.7: Hydrogen overvoltage on Pd, Ni and Ni-Pd alloys.

Pd content $\geq$ 75%, the reduction increasing linearly with Pd content. For Pd content < 75%, the catalytic activity is relatively low but much higher than for nickel and is weakly dependent on Pd concentration. Measurements by Hoare et al. (1960) of the hydrogen evolution reaction in 2N H_2SO_4 on Rh, Pd and Rh-Pd alloys show the hydrogen potential of Rh cathodes can be reduced by systematic additions of Pd. Damjanovic et al. (1966) have also shown that a Rh-60% Pt cathode behaves essentially as a Pt electrode for hydrogen evolution in KOH solution.

Bockris et al. (1968) have also measured the overpotential of the hydrogen evolution reaction on Ni-Pd, Ni-Pt, Au-Pd, Au-Pt and Pt-Pd alloys in 1N H_2SO_4 and 0.1 N NaOH solutions. For the Au alloys the exchange current density varied from < 10^{-5} A/cm^2 for pure Au to $\sim 10^{-3}$ A/cm^2 for pure Pt or Pd in both acid and alkaline solutions. Similar results were obtained for Pt-Ni and Pd-Ni, the exchange current density varying linearly with composition from $\sim 10^{-6}$ A/cm^2 for pure Ni to $\sim 10^{-3}$ A/cm^2 for pure Pd (or Pt) Fig. 2.8). Most of the early work on the catalysis of the hydrogen evolution was carried out in acid solution or dilute alkali solution. The bulk of this work has been reviewed by Brooman and Kuhn (1975). Miles (1975) has evaluated the electrocatalytic activity of a whole range of elements in strong alkali solutions (30% KOH) and 80^{o}C. The most striking feature is the periodic variation of the hydrogen overpotential with atomic number of the elements, Fig. 2.9. As expected Pd and Pt are the best catalysts for the hydrogen evolution reaction while Hf and Hg are the worst. Similar observations have been made by Kita (1966).

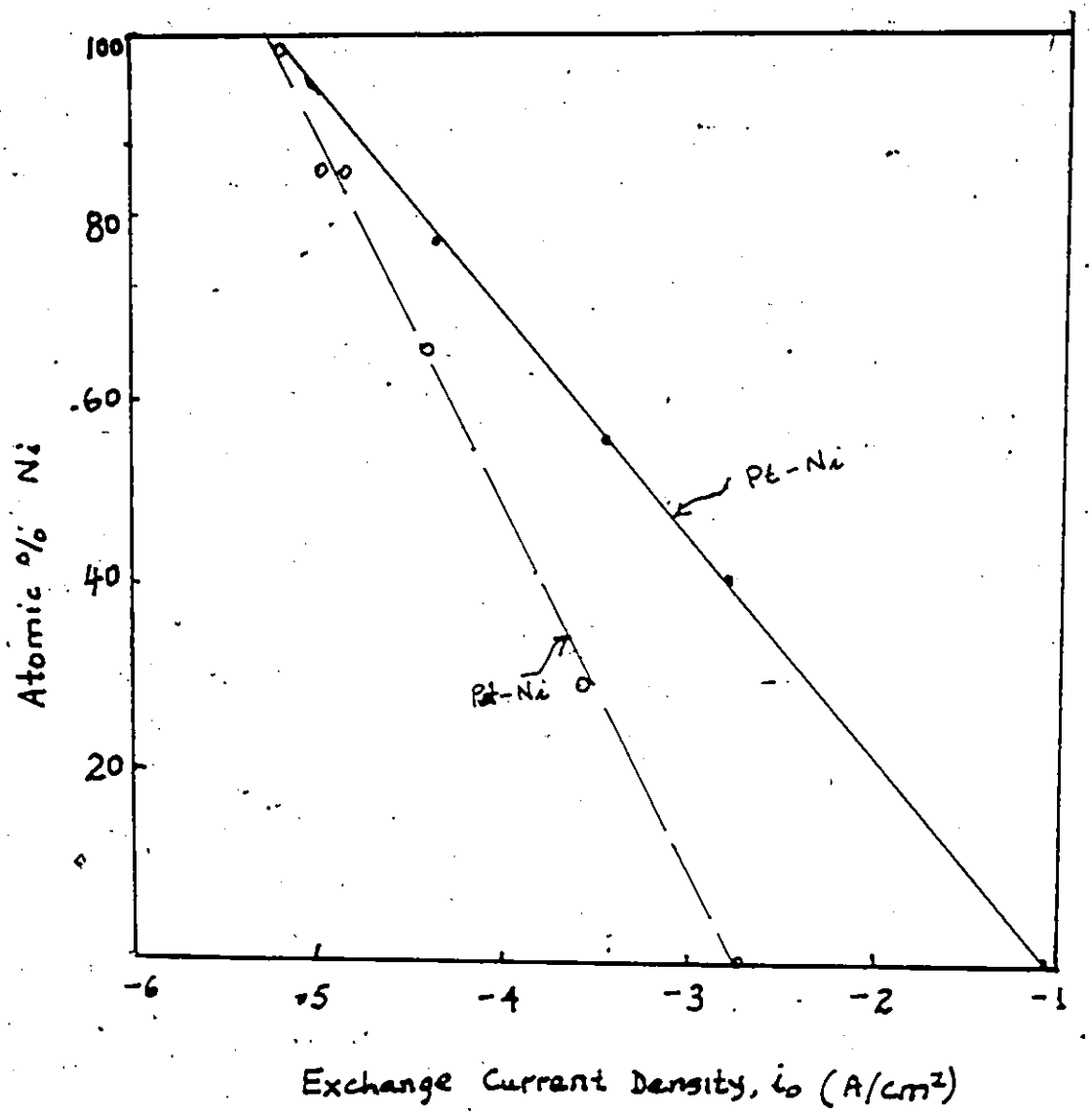

Fig. 2.8: Variation of the exchange current density for the hydrogen evolution reaction on Ni with Pd or Pt content.

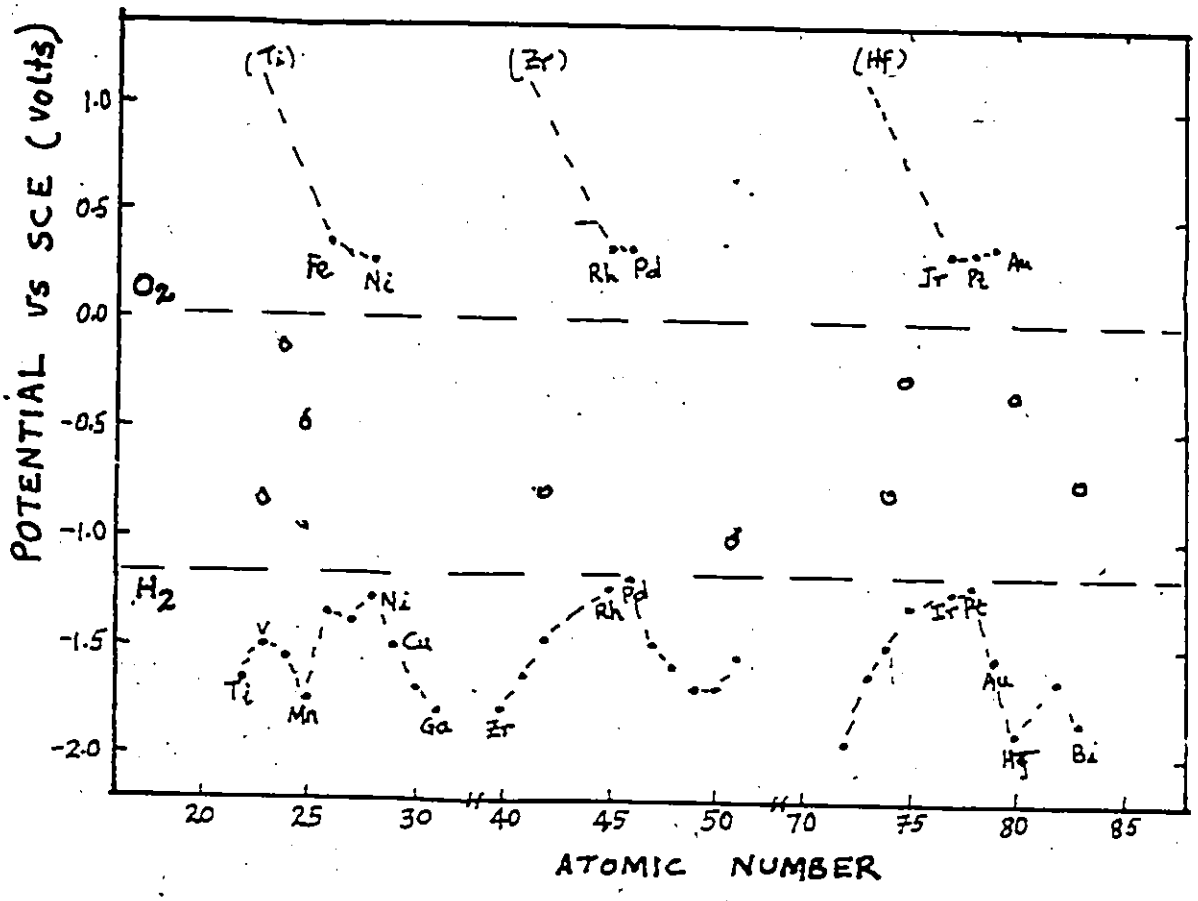

Fig. 2.9: The periodic dependence of overpotential, at a current density of 2 mA cm^{-2}, for O_2 or H_2 evolution in-30% KOH at 80°C, on atomic number.

Despite the overwhelming evidence that noble metals like Pt or Pd can catalyze the hydrogen evolution reaction the search for novel cathode materials has for all intents and purposes ignored the noble metals. This is mainly because the relative cost of these metals makes bulk alloys a rather expensive proposition. Instead hydrogen electrocatalysts tested to date include the mixed transition metal oxides, cobalt molybdate ($CoMoO_4$), prepared by a thermal treatment (Appleby 1978), plated metals and alloys, e.g. Fe, Ni, W and Ni-30% Co alloy electrodeposits on mild steel (Gonzalez 1980). Others include metal sulfides (e.g. nickel sulfides) prepared electrochemically on smooth nickel plates (Prigent 1978) and metal borides, typically nickel borides, (Ni_2B) with and without noble metal catalyst loading (Jurray 1980).

2.3.4 Ion beam processing of electrocatalysts

The principles and techniques of ion implantation and ion beam mixing will be discussed in chapter 3. Here we simply state the salient potential advantages of ion implantation and ion beam mixing. Since electrocatalysis is essentially a surface effect, bulk alloying of noble metal to produce better catalysts is not necessary and only the near surface region need be so modified. The power of the ion implantation technique lies in the fact that it allows any solid target to be injected with any impurity or alloying element to the level of a few atomic percent. The surface alloy composition achievable by ion implantation is limited to a few percent of implant due to sputtering. Higher concentrations are pos-

sible through the process of ion beam mixing. In this process, a thin evaporated layer (10-50 nm) of an alloying element is evaporated on the surface of the substrate. A beam of energetic ions, usually inert gas ions (Ar^+, Kr^+, etc.), is used to bombard the composite target. By momentum transfer an intermixing of the elements proceeds resulting in an alloyed surface layer which may be equilibrium, metastable solid solutions or amorphous phases.

a) Ion implanted electrocatalysts

Although electrocatalysis would appear to be a very exciting potential application of ion implantation, very little work has been published in this area. Voinov et al. (1974) observed a considerable increase in the hydrogen oxidation rate on platinum-implanted carbon electrodes, the activity being dependent on the amount of platinum at the surface. Grenness et al. (1974) implanted tungsten and tungsten oxide electrodes with 200 KeV Rt^+ ions to doses ranging from $0.2 - 2x10^{16}$ ions cm^{-2} and studied the catalytic activity of the electrodes for the hydrogen evolution reaction in 1M H_2SO_4. They found that even for doses as low as $2x10^{15}$ Pt^+ cm^{-2}, the catalytic activity of the electrodes increased by orders of magnitude and approached that of platinum itself. The activity of the Pt-implanted anodized tungsten was however considerably higher than that of Pt-implanted unanodized tungsten. In a similar study Ferber et al. (1980) have measured the overpotentials for the hydrogen evolution reaction on ion-implanted Fe electrodes in H_2SO_4. The Fe electrodes were implanted with Ne, Ar, Cu, Pb and Au ions to doses ranging from $0.05 - 1x10^{17}$ ions cm^{-2}. They found that Pb^+ implantation led to a reduction of the electrode activity while Ne^+ and

Cu^+ had little effect. Au^+ implantation on the other hand enhanced the activity of the Fe electrode for H_2-evolution by a factor of up to 10.

In a related study, Kasten et al. (1980) studied the electrocatalytic activity of Pt-implanted Fe and compared the results with pure Fe and iron with a monolayer coverage of platinum. The current densities measured for the hydrogen evolution from acid solutions with these electrodes as cathodes are shown in Fig. 2.10. It can be seen that the implantation of 10^{16} Pt-ions cm^{-2} leads to an increase of the catalytic activity of iron for the hydrogen evolution by several orders of magnitude. The activity approaches easily the one for smooth platinum. Though the Pt content in the surface layer is only $\sim$ 10 at.%, the high dose implants have higher activity than smooth Pt. For the electrodes with monolayer coverages of Pt, their activities are also higher than for pure Fe, but well below either the Pt-implanted iron or smooth platinum.

O'Grady et al. (1981) have also studied the electrocatalytic activity of Pt-implanted RuO_2 electrodes, and Rabette et al (1979) that of Pt-implanted Al_2O_3 electrodes. A brief summary of the electrocatalysis at ion implanted electrodes has been discussed by Wolf (1979).

A review of the subject has been recently given by Wolf (1981) Table 2.3 gives a summary of some of the work on ion implantation in electrocatalysis. This review shows that a majority of the published works on the electrocatalysis of implanted electrodes have been concerned with Pt as the implanted catalyst, and deservedly so because of its well known high catalytic activity for the H-redox reaction. Almost all of these works were also in acids and few in concentrated alkali solutions. The results in general show that order of magnitude increases in activity can

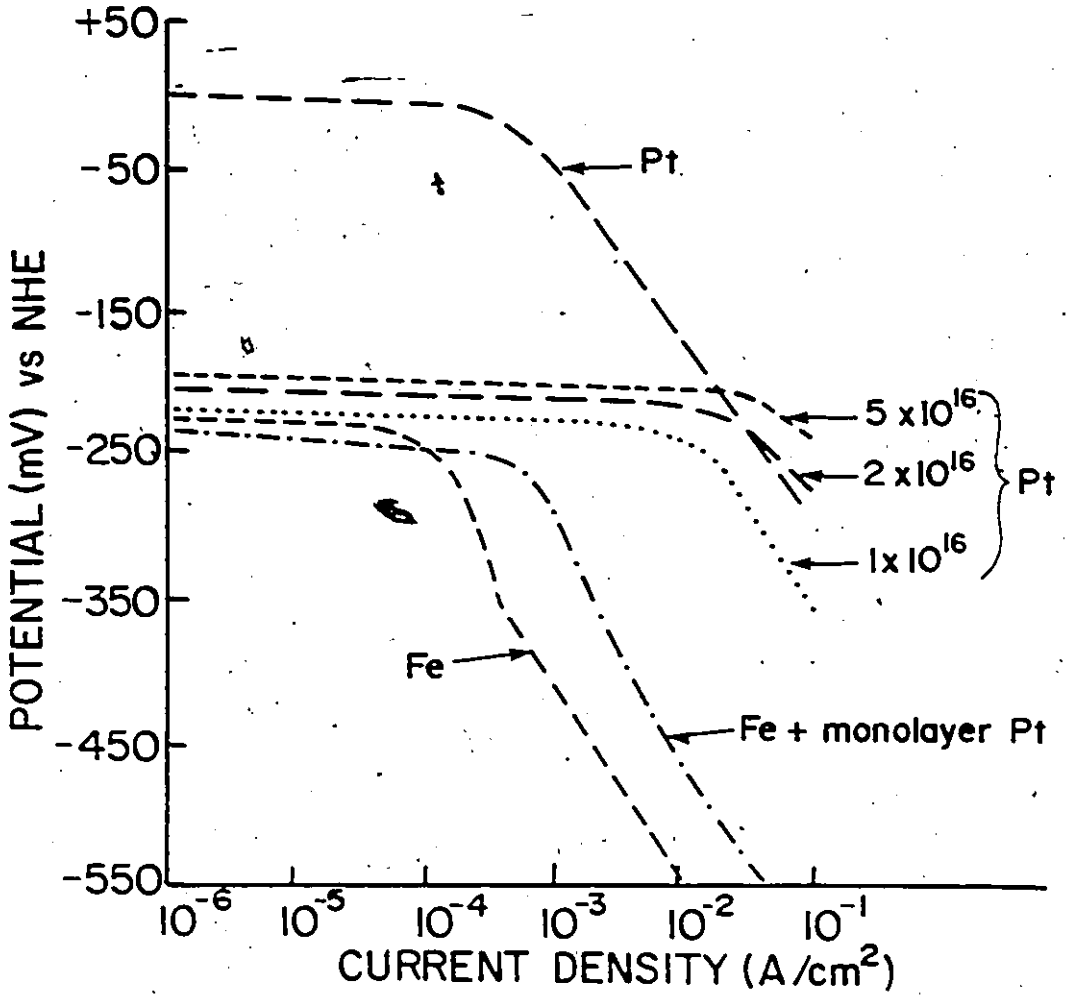

Fig. 2.10: Current-potential curve for pure iron and iron with evaporated and implanted Pt, showing the activity of Pt-implanted iron approaches that of pure Pt.

Table 2.3: Summary of some of the work on ion implantation in electrocatalysis

Reaction	Basic Material	Implanted/ ion mixed element	Dose ion/cm^2	Activity at η = 50 mV	Activity Ratio Implanted/smooth Metal	Ref.
Hydrogen Redox Reaction	Smooth Au	-	-	0.01	1	Ferber et al. (1980)
	Smooth Pt	-	-	1	1	Kasten et al. (1980)
	W	Pt	2×10^{16}	10	10	Grenness et al. (1974)
		Pt	10^{16}	Positive Effect	-	Voinov (1974)
	C	Au	5×10^{16}	.22 (300 mV)	0.1	
	Fe	Pb	5×10^{16}	0.02	-	Ferber (1980)
		Au	5×10^{16}	20	2×10^3	Kasten (1980)
		Pt	5×10^{16}	1.3×10^2	1.3×10^2	
Oxygen Redox Reaction	Ni (KOH)	Ag	5×10^{16}	40% decrease of overpotential		Akano (1981)
H_2 Evolution	C	Pt	Implanted	-	0.1	Wolf (1982)
			ion mixed	-	10	
Reaction	Ti	Pd	Implanted	-	2	Munn (1985)
			ion mixed		10	

be obtained by the implantation of beneficial materials. However limitations to maximum achievable concentration by direct implantation plus the fact that the implanted species may not be immediately available at the electrode surface to catalyze the reaction represent a limitation of the technique. Grenness et al. (1974) in their work on Pt-implanted W found that the electrodes had to be subjected to several conditioning polarization sweeps before the electrodes would exhibit their full catalytic power. It is quite possible that the W gradually dissolved during the reconditioning process, thereby eventually making the implanted Pt available at the electrode surface. The failure to recondition the electrodes is possibly why no increased activity was obtained for Pt-implanted Cu and Au for H_2-evolution (Wolf, 1979).

b) Ion mixing and electrocatalysis

One way to overcome the concentration limitations is to form the sample alloys by ion-beam mixing. For such electrodes the surface concentration can be high, and the electrocatalyst is immediately available at the surface to provide sites for the reaction. Such electrodes have been studied by Wolf et al. (1982). They studied the polarization behaviour of Pt-implanted carbon and Ar(Kr) ion-mixed carbon-platinum electrodes for the hydrogen redox reaction. It was shown that the activity of ion-beam-mixed carbon/Pt for the hydrogen redox-reaction was considerably higher than for Pt-implanted carbon (Fig. 2.11). In a similar study Munn et al. (1985) studied the polarization behaviour of Ti, titanium covered with thin film Pd, Pd-implanted Ti and Ti/Pd surface alloy produced by ion beam mixing with Ar and Kr ions. The test reaction was H_2-evolution in 20% H_2SO_4. The cathodic current density ($\sim$ 1800 A m^{-2}) obtained on the

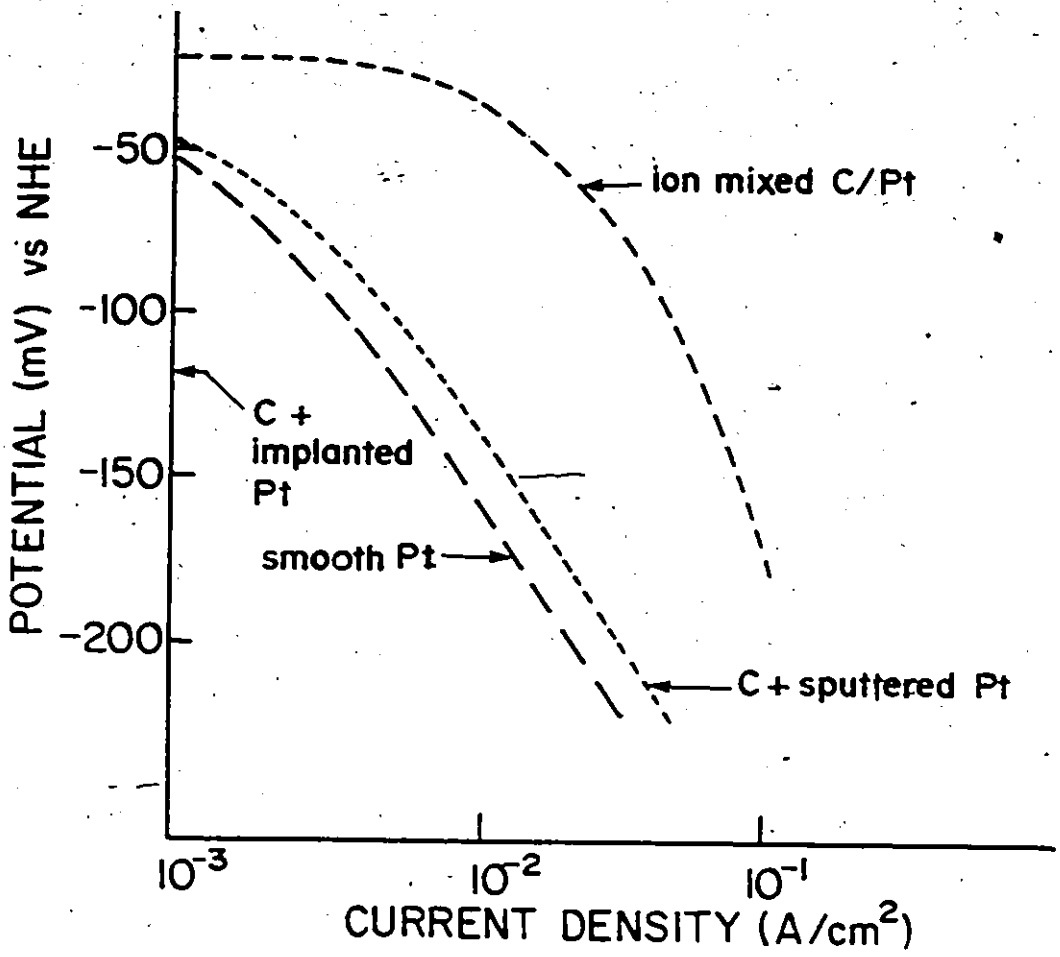

Fig. 2.11: Current-potential curve for differently treated carbon electrodes.

ion-beam mixed Ti/Pd electrode is a factor of 4 higher than that on the Pd-implanted electrode, and almost an order of magnitude higher than that of evaporated Pd. These studies suggest that electrocatalysts fabricated by ion-beam mixing are probably superior to those fabricated by direct implantation of the catalyst.

2.4 Some relevant properties of Ni and Pd

The electrode chosen for this work is Ni. This choice is due to the good corrosion and catalytic properties of Ni and also because of its relatively low cost compared to the other excellent electrocatalysts (e.g. Pt). As pointed out in the previous pages, Ni is now the accepted electrode material in commercial electrolysers using strong KOH solutions, and in fuel cells. Ni has 2 outermost electrons and its d-shell is electron deficient. This causes certain pecularities in the formation of Ni -- compounds and metallic alloys. Its only known crystal structure is f.c.c. with lattice parameter $a \sim 3.52$ Å. It has very low chemical activity and forms a thin protective oxide (NiO) at room temperature. As a catalyst, it is the most active (Kornilov 1963) in the 4th period in reactions with H and O. Five natural isotopes of Ni are known with ^{58}Ni being the most abundant ($\approx$ 68%).

Palladium (Pd) with atomic number Z = 46, mass number M = 106 is a member of the Pt group of metals and is akin to Pt in general appearance. It has a silvery lustre and is extremely malleable and ductile. Its only known crystal structure is fcc with lattice constant a = 3.89 Å (at 20°C), number density 6.8×10^{22} at-cm^{-3} and melting point of 1552°C. Pd is

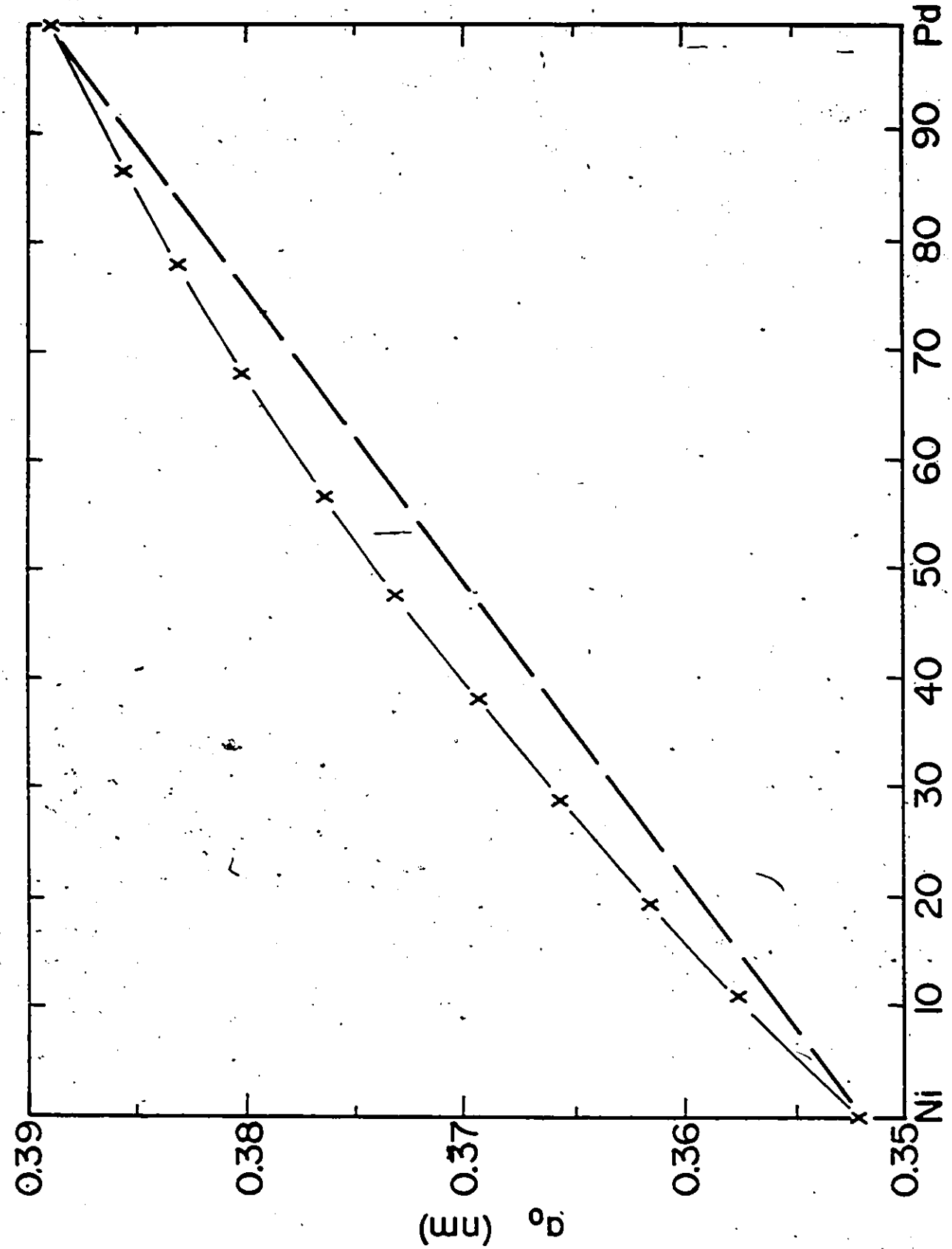

Fig. 2.12: Variation of the lattice parameter of Ni-Pd alloys with Pd content.

Table 2.4: Some physical properties of Ni and Pd

Parameter	Ni	Pd
Atomic number	28	46
Mass number	58	106
Number density/cm^3 ($\times 10^{22}$)	9.14	6.8
Lattice constant, nm	0.35	0.39
Melting point, ^oC	1453	1552
Crystal structure	fcc	fcc
Vacancy formation energy, eV	1.33-1.6	
Vac. migration energy, eV	1.38-1.5[a]	
Interstitial formation energy, eV	4[b]	
Interstitial migration energy, eV	0.15[c]	

a. Seeger et al. (1970)

b. Bakker H. (1968)

c. Lampert et al. (1972)

generally resistant to attack by a considerable number of industrial chemicals. It is the lightest and least expensive of the Pt group metals. Pd is widely used for electrical contacts because it is usually free of tarnish. As a catalyst, it is the most effective, especially in finely dispersed form, in hydrogenating liquid and gaseous phase reactions, for example the production of ethylene from acetylene (Simons, 1967). It is widely used in the recombination of hydrogen and oxygen and in the production of pure H_2 by diffusion of hydrogen through Pd membranes. Pd adsorbs considerable amounts of hydrogen which it readily takes up to the extent of 800 - 900 times its own volume at room temperature. In this regard Pd and its alloys are potential candidates for hydrogen storage from which the hydrogen can later be extracted for use as fuel by change of pressure or temperature (H.C. Angus 1981). Table 2.4 lists some of the relevant physical properties of Ni and Pd.

2.4.1 Ni-Pd alloys

A continuous series of solid solutions crystallize from Ni-Pd melts (Fig. 2.12). In X-ray studies of Ni-Pd alloys containing from 0 - 100% Pd, Hultgren et al (1939) observed that all the alloys were fcc under all annealing conditions. No compounds, superlattices or miscibility gaps were detected in annealing periods as long as 2 weeks at 600°C and 3 weeks at 400°C, as well as slow cooling from 600°C for a period of 15 days. The lattice constants vary smoothly from pure Ni (3.52 Å) to pure Pd (3.89 Å) with a positive deviation from Vegard's law of additivity of atomic radii (Fig. 2.12). Similar measurements by Bidwell (1964) over a temperature range from 25°C to 900°C confirm the conclusions of Hultgren et al.

CHAPTER 3

ION BEAM MIXING

In this chapter the concepts of and the processes leading to the intermixing of layered solids by ion irradiation are discussed. The basic concepts of ion beam mixing are discussed in section 3.1. Since ion mixing is a special case of the kinetic processes occurring during ion bombardment, the theory of atomic collision in solids relevant to the ion beam mixing process will be given in section 3.2. Then in section 3.3 the various mechanisms thought to contribute to ion beam mixing are reviewed. Finally in section 3.4 the available experimental data on ion mixing are reviewed and compared with the theoretical models.

3.1 Concept of Ion Beam Mixing

When energetic ions impact upon a solid they deposit energy in the material via collisions with the atoms and electrons of the solid. One consequence of the energy transfer to target atoms is the creation of a cascade of moving atoms. If the ion energy is high enough so that the ion penetrates beyond the interface between two materials, A and B, the recoiling atoms created near the interface may have sufficient energy to cross the interface. The result is the intermixing of A and B atoms in the interface region. The sample configurations commonly employed in the study of ion beam mixing are shown in Fig. 3.1. In Fig. 3.1(a) a thin marker of element A is sandwiched between 2 layers of B material. Typical thicknesses of layer A are $\sim$ 1 nm so that the system then approximates the spreading of impurity A (following ion irradiation) in a matrix

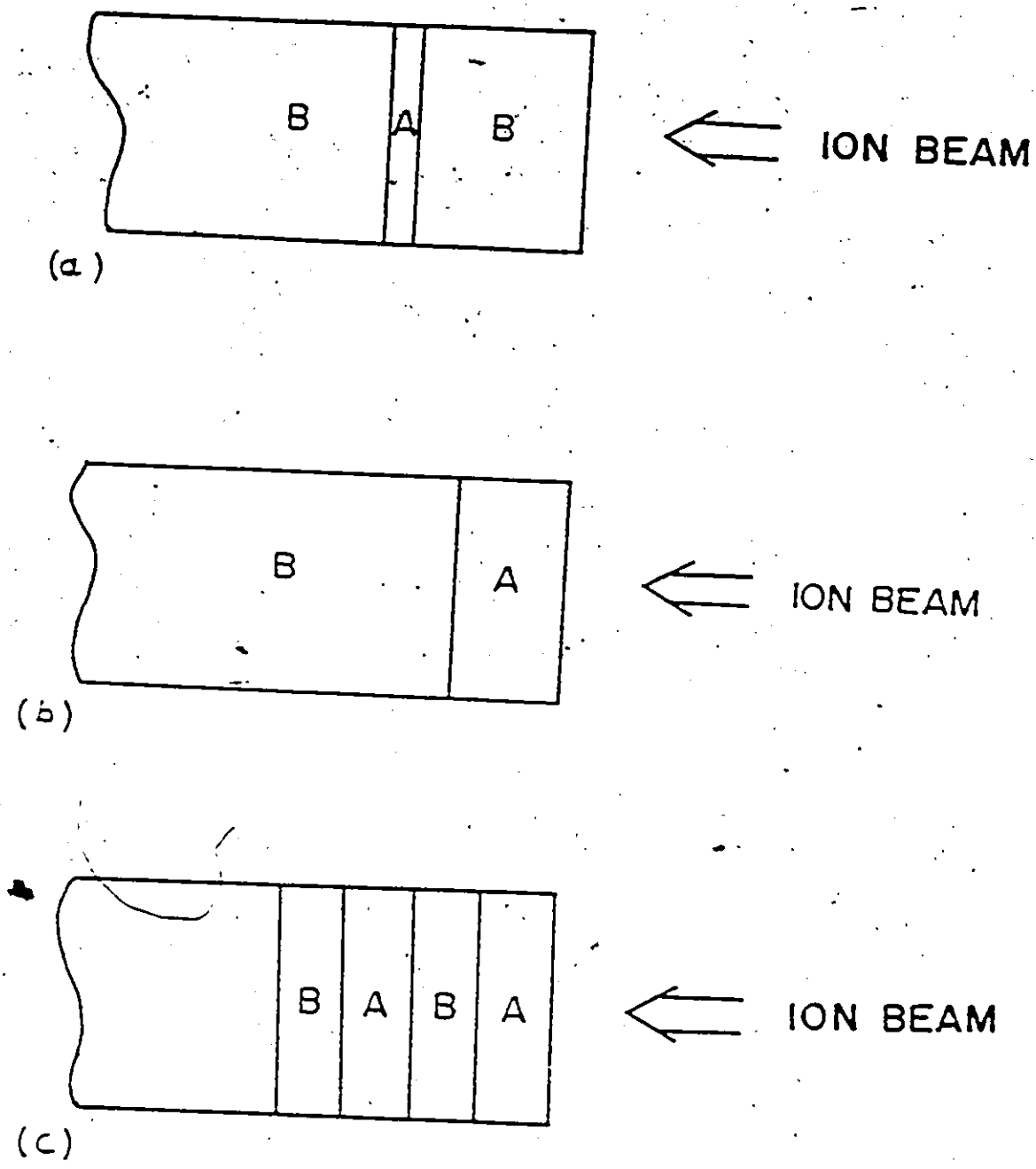

Fig. 3.1: Sample configurations commonly employed in ion beam mixing studies. a) markers b) bilayer c) multilayers.

made up largely of B atoms.

The second type of geometry is shown in Fig. 3.1(b). A thin film of element A is evaporated onto substrate B; the thickness of A should be less than the range of the bombarding ion. A and B then form a semi-infinite diffusion couple and are free to form continuous solid solutions, intermediate phases or compounds upon ion bombardment. The third sample configuration normally employed is shown in Fig. 3.1(c) and consists of alternate thin evaporated layers of A and B and the overall thickness is less than the ion range. Because A (or B) atoms now have to be displaced only over a few interatomic distances to be mixed into the other layer, this geometry represents the most efficient mixing configuration. Novel, non-equilibrium alloys of any composition can be prepared simply by varying the ratio of the thicknesses of A to B layers. Tsaur et al (1980) have used this method to produce Ni-Ag alloys varying in composition from 0 - 100% Ag in an otherwise immiscible Ni-Ag system.

Before proceeding to describe the ion beam mixing process and the mechanisms thought to contribute to it, it is useful to consider the process underpinning ion beam mixing phenomena namely interaction of energetic heavy ions with solids which is now discussed in the next section.

3.2 Atomic Collisions in Solids

In this section the processes describing ion-solid interactions for heavy keV ions are discussed. This discussion will include energy loss processes and the resulting lattice damage produced by the ions as they slow down in the target. The amount and nature of such damage and their annealing characteristics will also be discussed.

3.2.1 Theory of Atomic Collisions

Certain assumptions are basic to the theory of atomic collisions in solids:

a) The collision is binary, i.e. a moving atom interacting with one stationary atom at a time. This assumption will be valid provided the mean-free-path between collisions >> the mean interatomic spacing, d.

b) The collision can be described classically and is non-relativistic. This is valid if the wavelength, λ, >> b, the distance of closest approach in a head-on collision.

c) The elastic and inelastic energy loss processes can be considered independent and separable. Elastic interactions result in both momentum exchange and change of direction (scattering) while electronic losses are due to a continuous and gentle slowing-down of the ion through its interactions with electrons of the target atoms. Momentum transfer to electrons is small because of the small mass of the electron; consequently, electronic losses do not lead to a deflection of the ion trajectory.

3.2.2 Elastic Collision Process

In Fig. 3.2 which shows the collision orbit in the Laboratory (Lab) and centre of mass (C.M.) systems, an ion of mass M_1, charge Z_1e and velocity v_1 (energy E) approaches an atom of mass M_2, charge Z_2e which is initially at rest in the Lab frame of reference. During the collision the ion transfers kinetic energy T to the struck atom and emerges with energy $E' = E-T$ at an angle ϕ_1 relative to its initial direction. The struck atom M_2 recoils with kinetic energy T at an angle ϕ_2 with respect to the initial ion trajectory. Often, one needs to know the recoil energy T, the energy E'

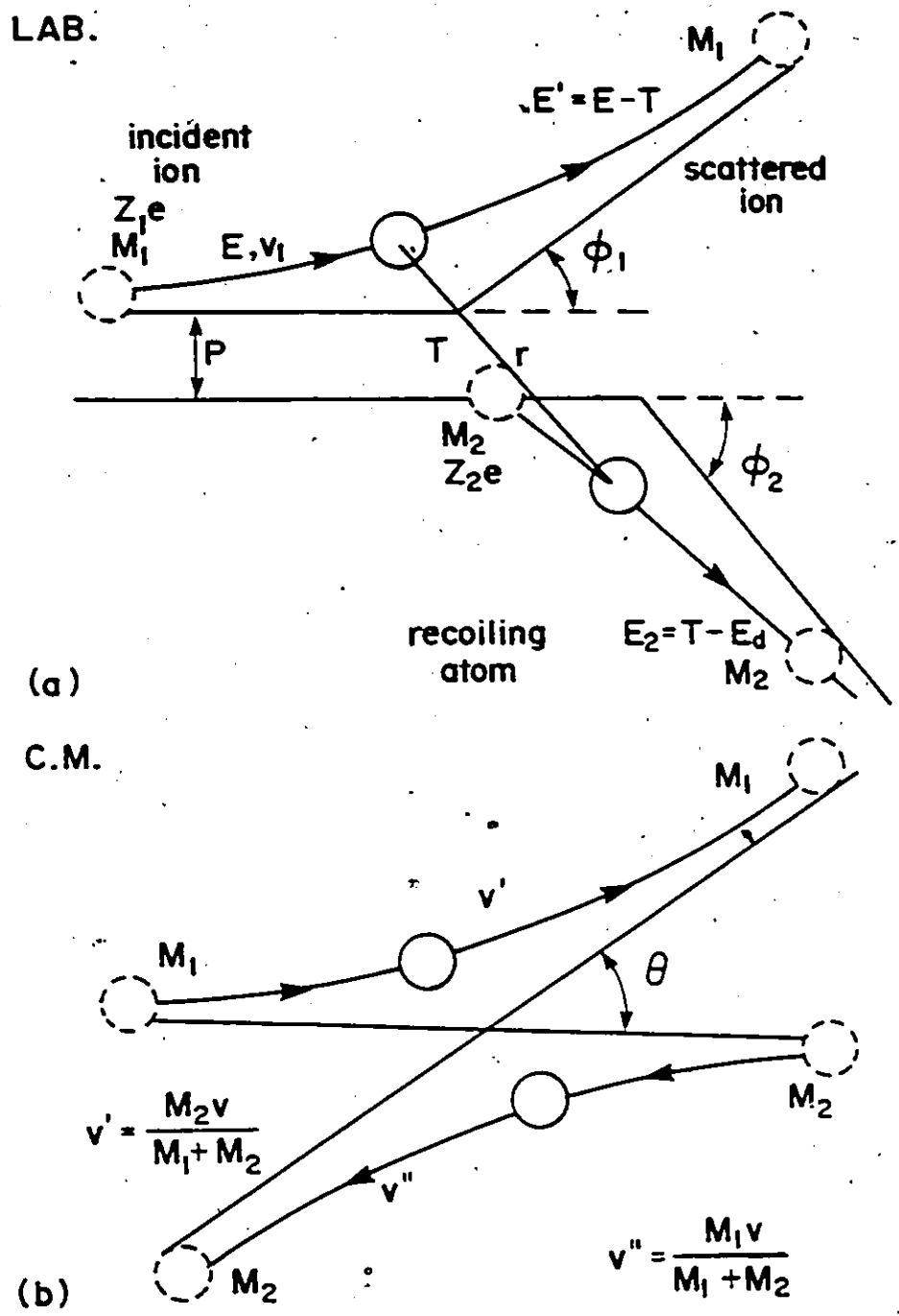

Fig. 3.2: a) A binary collision in the laboratory coordinate system.
b) A binary collision in the centre of mass coordinate system.

of the particle after scattering and the scattering angle θ in the c.m. system.

Using the laws of conservation of energy and momentum in the C.M. system we find that

$$T = \frac{4M_1M_2}{(M_1+M_2)^2} E_1 \sin^2 \frac{\theta}{2} \tag{3.1}$$

$$= T_m \sin^2 \frac{\theta}{2} \quad , \tag{3.2}$$

where

$$T_m = E_1\gamma \quad \text{and} \quad \gamma = \frac{4M_1M_2}{(M_1+M_2)^2} \quad . \tag{3.3}$$

T_m is the maximum possible energy transfer to M_2. The scattering angle θ in the C.M. system is

$$\theta = \pi - 2p \int_0^{u_0} \frac{du}{\left[1 - \frac{V(u)}{E'} - p^2u^2\right]^{\frac{1}{2}}} \tag{3.4}$$

where: p = impact parameter

$$E' = \frac{M_2E}{M_1+M_2}$$

$$u = \frac{1}{r} \quad , \quad u_0 = \frac{1}{r_0}$$

and r_0 is the point of closest approach

$V(r)$ is the interaction potential between the two particles. The scattering angle ϕ_2 in the Lab is related to that in the C.M. by

$$\tan\phi_2 = \frac{\sin\theta}{(1-\cos\theta)} \quad . \tag{3.5}$$

In general we need a detailed knowledge of all aspects of atomic collisions. For example one wishes to know the number of recoils produced in the energy interval between T and T+dT and their spatial distributions. To obtain this type of information the scattering angle θ must be known which is possible only if a detailed knowledge of the interaction potential V(r) is known (Eq. (3.4)).

The problem now is a judicious choice of the interaction potential V(r), valid over all impact parameters, since a wide range of impact parameters are possible depending on ion-target combinations and ion energies.

3.2.3 Interaction Potentials

The collisions of interest between energetic moving ions and target atoms are those with impact parameter $p \ll d$, i.e. collisions for which the interaction potentials V(r) are repulsive. Since the interaction potential between two atoms depends on their separation r, we can define two reference points on the scale of separation: 1) the Bohr radius a_0 (= 0.053 nm) of the hydrogen atom. This gives a rough idea of the position of the atomic electron shells. 2) the interatomic spacing d ($\approx$ 0.3 nm).

i) when $r \ll a_0$, the potential is due to the interaction between the bare nuclear charges Z_1e and Z_2e and the potential is essentially coulombic

$$V(r) = \frac{Z_1 Z_2 e^2}{r} \qquad (3.6)$$

ii) when $a_0 < r < d$ the inner electron shells overlap. The interaction leads to a less repulsive potential (compared to coulombic potential) because of the electrostatic screening of the nuclear charges by the innermost electrons. The potential found ap-

propriate in this range of separation is the Thomas-Fermi (1948) screened coulomb potential of the form

$$V(r) = \frac{Z_1 Z_2 e^2}{r} \chi(\frac{r}{a}) \qquad (3.7)$$

where $\chi(\frac{r}{a})$ is the screening function and

$$\chi(r \to 0) = 1 \quad , \quad \chi(r \to \infty) = 0 \quad ;$$

a is the Thomas-Fermi screening radius and is given (Lindhard et al 1968) as

$$a = 0.8853 a_0 / (Z_1^{2/3} + Z_2^{2/3})^{\frac{1}{2}} \qquad (3.8)$$

iii) At intermediate separations $r \approx d$, corresponding to low energy ions, the Born-Meyer (1932) potential of the form

$$V(r) = Ae^{-Br}$$

is often used. A and B are constants.

3.2.4 Differential Cross-Sections

A particularly useful concept is that of differential cross-section. The differential cross-section for particle scattering is defined as

$$d\sigma_n(\theta) = 2\pi p dp \qquad (3.9)$$

such that all particles falling on an area $2\pi p dp$ at an impact parameter p, will be scattered through an angle between θ and $\theta + d\theta$, the relation between dp and $d\theta$ coming from Eq. (3.4) by differentiation. Knowing V(r) enables p to be expressed in terms of θ. Then using $T = T_m \sin^2(\frac{\theta}{2})$, p may be expressed in terms of T and consequently $d\sigma_n$, the differential cross-section for collision with recoils in dT at T follows.

Lindhard et al (1968) have solved Eq. (3.4) for θ by assuming a power-law approximation to the Thomas-Fermi potential of the form,

$$V(r) \propto \frac{1}{r^m}$$

and obtained a differential scattering cross-section for energy transfer T given by

$$d\sigma_n(T) = CE^{-m}T^{-1-m}dT \tag{3.10}$$

where

$$C = \frac{\pi}{2}\lambda_m a^2 \left(\frac{M_1}{M_2}\right)^m \left(\frac{2Z_1Z_2}{a}\right)^{2m} \tag{3.11}$$

and

$$\lambda_m = 2m\left(\frac{K_m\Gamma_m}{2}\right)^{2m}$$

This cross-section is considered universally acceptable for $\frac{1}{4} \leq m \leq 1$, the value of m depending on ε where ε is Lindhard's reduced energy parameter, given by

$$\varepsilon = \frac{a}{b} = \frac{aM_2E_1}{Z_1Z_2e^2(M_1+M_2)} \tag{3.12}$$

3.2.5 Energy Loss Processes

While slowing down in the target an ion loses energy at a rate $-\left(\frac{dE}{dR}\right)_n$ to elastic (or nuclear) and $-\left(\frac{dE}{dR}\right)_e$ to inelastic (or electronic) collision processes. Though these two types of process are correlated, Lindhard and Scharff (1961) have suggested that they can be treated separately. Thus the total energy loss per unit length $\left(-\frac{dE}{dR}\right)$ is the sum of the nuclear and electronic losses

$$\frac{dE}{dR} = \left(\frac{dE}{dR}\right)_n + \left(\frac{dE}{dR}\right)_e$$

The ion energy is thus shared between nuclear and electronic interactions

$$E = \nu(E) + \eta(E)$$

where $\nu(E)$ and $\eta(E)$ are the energies deposited into nuclear and electronic interactions respectively.

i) Nuclear Stopping

The energy loss resulting from the interaction between the incident ion and the screened nuclear charge of the target atom is known as the elastic or nuclear energy loss, $(\frac{dE}{dR})_n$. This energy loss is obtainable from the scattering cross-section discussed in the previous section:

$$(\frac{dE}{dR})_n = N \int_0^{T_m} T d\sigma_n = N S_n(E) \qquad (3.13)$$

where N is the atomic number density and $S_n(E)$ is, by definition, the stopping cross-section. A comprehensive unified theory of nuclear stopping has been described by Lindhard et al (1968) in terms of the reduced energy parameter, ε and a dimensionless range, $\rho = RN\pi a^2\gamma$. The result (Fig. 3.3) is a universal nuclear stopping curve for $S_n(\varepsilon)$ for all ion-target combinations and all energies.

ii) Electronic Stopping

The energy loss resulting from the interaction of the incident ion and target electrons is called the electronic (or inelastic) energy loss. Three regions of inelastic stopping can be identified: the maximum interaction between the ion and atom electrons occurs and the stopping is maximum

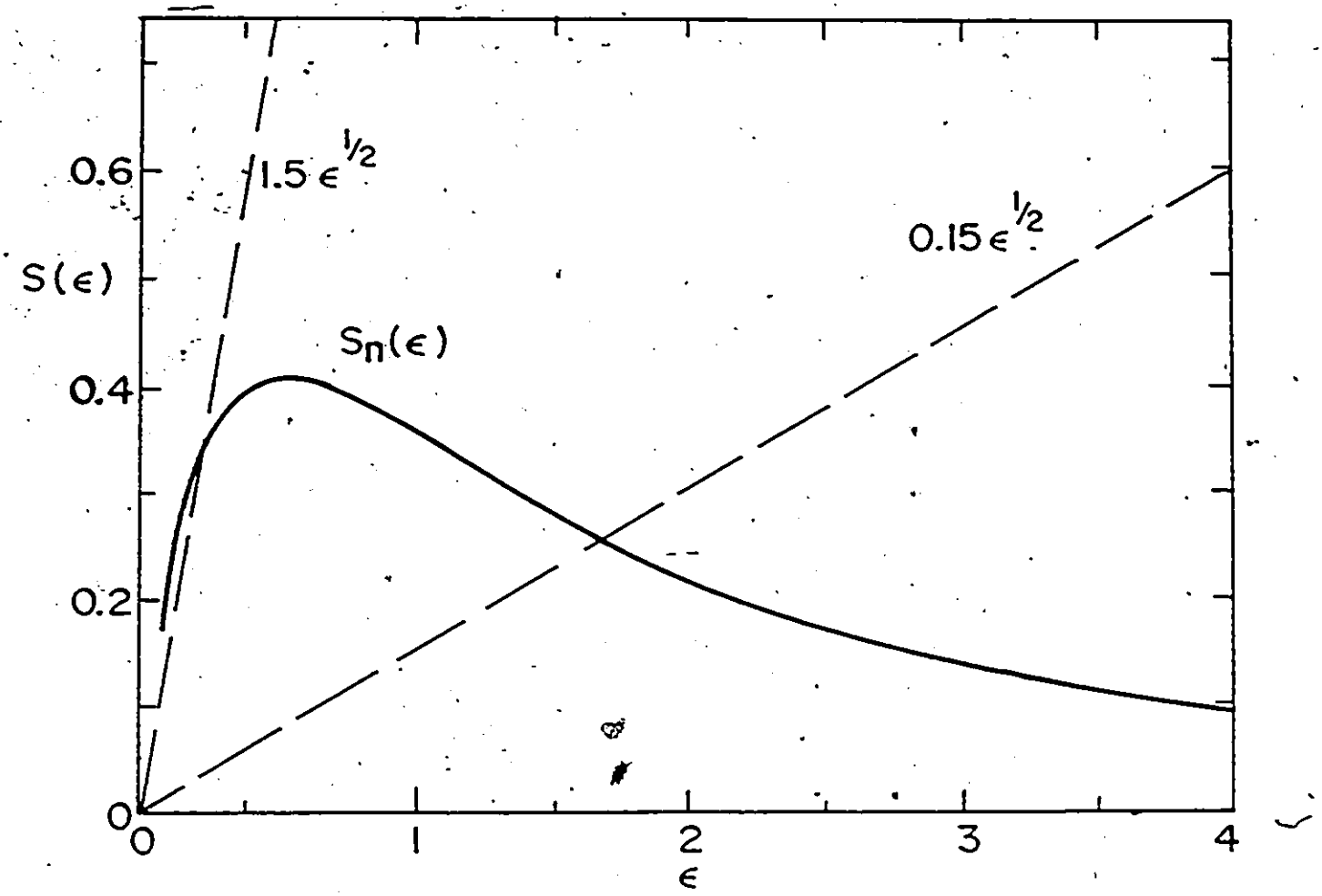

Fig. 3.3: Nuclear and electronic stopping powers in terms of the dimensionless energy parameter ε. Electronic stopping is given for K = 0.15 and 1.5.

when the ion velocity $v_1 \sim v_B Z_1^{2/3}$ (where v_B is the orbital velocity of the hydrogen atom electron) i.e. ion velocity $\sim$ K-shell electron velocity. When $v_1 >> v_B Z^{2/3}$, the coupling between the ion and target electrons is weaker, the stopping decreases with increasing particle velocity and is given by the Bethe-Bloch formula. At velocities appropriate to ion implantation ($v_1 < v_B Z_1^{2/3}$), the stopping is proportional to ion velocity and Lindhard et al (1961) show that the stopping power can be expressed as

$$\left(\frac{d\varepsilon}{d\rho}\right)_e = S_e(\varepsilon) = - K\varepsilon^{\frac{1}{2}} \quad . \tag{3.14}$$

Typical value of K for ion implantation work is $\sim 0.1 - 0.2$, ie. provided $Z_1/Z_2 \gtrsim 0.5$. However because K depends on ion-target combinations, no universal electronic stopping curve exists. Fig. 3.3 also shows $S_e(\varepsilon)$ for two values of K. At high energies ($\varepsilon \gtrsim 10$) typical of MeV light ions electronic stopping dominate while for $0.1 \lesssim \varepsilon \lesssim 2$ typical of keV heavy ions both electronic and nuclear losses contribute to stopping.

3.2.6 Range and Damage Energy Distributions

The collisions leading to the energy losses described in the last section are statistical in nature since different ions will have a different number and sequence of collision events before they come to rest. Consequently there will be a Gaussian-like distribution of ion ranges and deposited elastic energy which gives rise to lattice damage and one can talk about a mean ion range and mean damage range, and straggling quantities which describe these distributions about their mean. The most useful quantities are the projections of the mean range in the initial direction of the ion (projected range) $\bar{R}_p$ and its straggling, ΔR_p, whilst for damage the distribution is described by the mean projected damage range, $\bar{R}_D$, and

it straggling, ΔR_D.

A comprehensive treatment of the spatial distribution of ion ranges based on a linear transport equation statistical description has been developed by Lindhard et al. (1963), and that of deposited energy distribution by Winterbon et.al. (1970). These descriptions lead to integral equations from which the spatial moments of the range or deposited energy distributions can be obtained. The particular distributions can then be constructed from their spatial moments. For ions and energies typical of ion implantation work, both the range and deposited energy distribution are often close to Gaussian in shape. Consequently the Edgeworth expansion, a weighted Gaussian distribution, is commonly used because of its simplicity. For ions incident normal to target the normalized range distributions are given by

$$F(x,E) = \frac{\xi}{(2\pi\sigma^2)^{\frac{1}{2}}} \exp \frac{-(x-\langle x\rangle)^2}{2\sigma^2} \quad f(\eta_e) \qquad (3.15)$$

where $\xi = 1$ for ion range and $E\nu(E)$ for damage

$\sigma^2 = \langle \Delta x^2 \rangle$ is the variance in depth and

$\langle X \rangle$ is the mean depth corresponding respectively to range or damage,

$f(\eta_e)$ is the Edgeworth expansion weighting factor, where

$$\eta_e = \frac{x-\langle x\rangle}{\sigma}$$

Fig. 3.4 shows an example of the damage energy distribution for 120 keV Ar^+ ions in Ni.

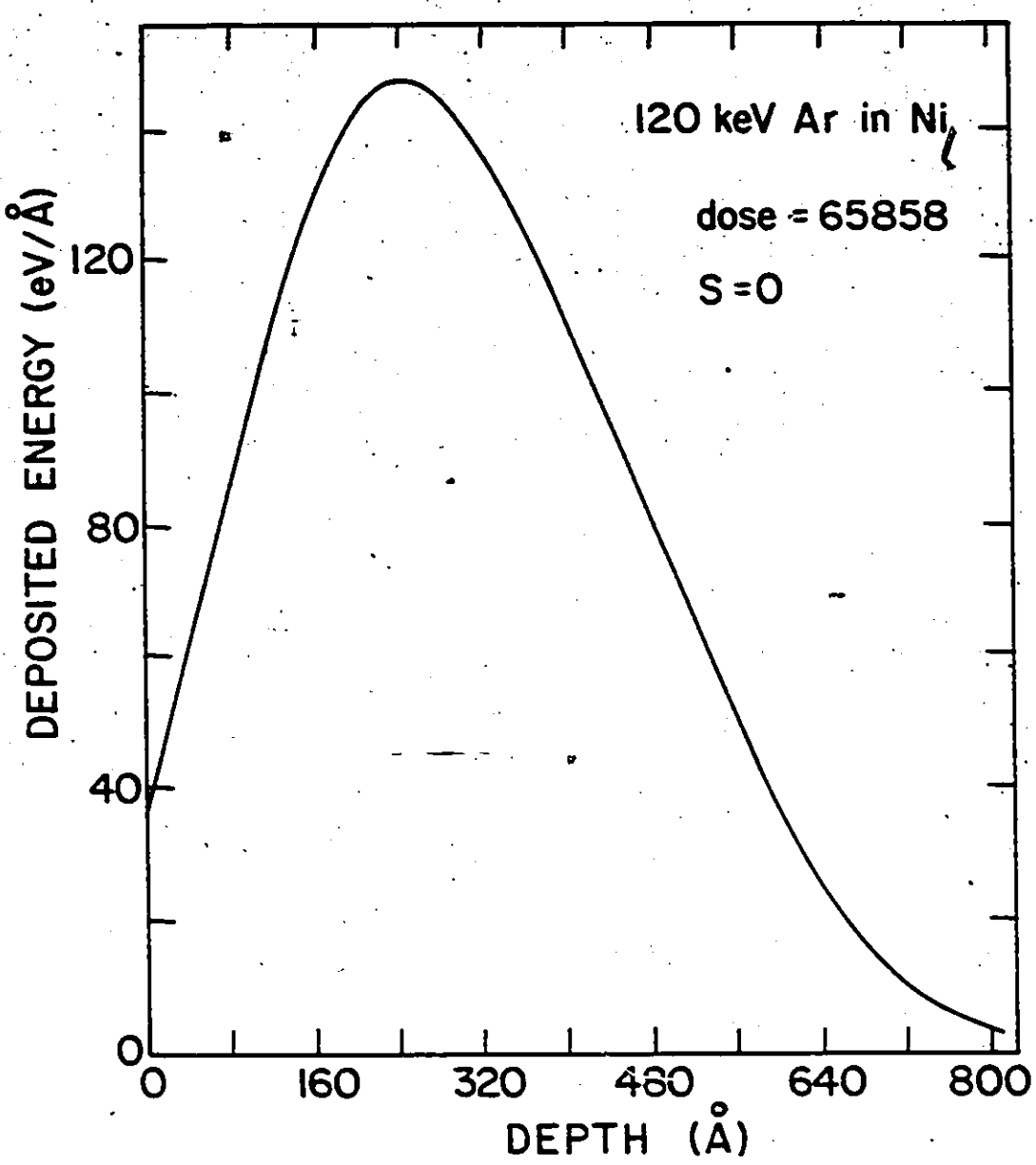

Fig. 3.4: Damage energy distribution for 120 KeV Ar ions in Ni.

3.2.7 Number of Displaced Atoms

One consequence of energy deposition into elastic collision events is the displacement of atoms from their lattice sites. Such displacements have far reaching ramifications on the properties of materials as they may lead directly to lattice damage and atomic mixing and indirectly to radiation-enhanced diffusion. It is therefore of considerable interest in the ion beam mixing to know both the number and type of displaced atoms, and their spatial distribution produced in irradiated solids. However, except in the simplest cases where light particle (electron) irradiation is used, it is difficult to predict the type and distribution of defects produced. Also, defects may be mobile at the irradiation temperature, leading to interstitial-vacancy recombination or migration to the external surface and internal surfaces like grain boundaries and dislocations. Alternatively, defects may agglomerate to form complex defect clusters. The net result is that the calculated defect concentrations and spatial distributions may be vastly different from measured values, especially for heavy ion irradiation.

Although no theory is available to predict the types and distributions of defects produced, Sigmund (1969) has developed a linear transport equation description which enables the number of defects produced to be evaluated. In this description, the average number of recoiling atoms, $F(E,E_0)$, set in motion with initial energy E_0 by a primary of energy $E >> E_0$ is

$$F(E,E_0) = \frac{m}{\psi(1)-\psi(1-m)} \cdot \frac{E}{E_0^2} \qquad (3.16)$$

where m is the exponent appearing in the power approximation to the scattering cross-section and $\psi(x) = \frac{d}{dx} \ell n \Gamma(x)$ is the digamma function. The average number of Frenkel pairs produced can be obtained by integration in energy. The Kinchin-Pease (1955) model specifies that a well defined threshold energy E_d must be transferred to a struck atom to permanently displace it from its lattice site. Sigmund (1969) has modified the Kinchin-Pease model by in-

cluding the effect of replacement collisions and has determined that the number, N_d, of displaced atoms per incident ion is

$$N_d = \frac{0.84\nu(E)\cdot E}{2E_d} \qquad (3.17)$$

where $\nu(E)$ is the fraction of incident ion energy E, deposited into elastic collisions.

3.2.8 The Nature of Radiation Damage in Metals:

Collision theory estimates of the number of displaced atoms given in the last section are average quantities and do not represent the effect of a single ion. Neither does it predict the final state of lattice disorder. Unless the temperature is sufficiently low (typically $\sim$ 4K) annealing of damage by defect migration may occur. A characteristic feature of displacements in metals is the large recombination volume of an isolated point defect, of the order of 125 atomic volumes. Thus, E_d is determined by the energy lost to the environment by an atom trying to escape the recombination volume. In high density cascades typical of heavy ions in heavy metals, defect densities may become much higher than the stability limit determined by the recombination volume. In such cases point defect annihilation by mutual recombination of vacancies and interstitials may result, or the defect volume may collapse to vacancy and interstitial clusters (P. Sigmund (1968)). Recent molecular dynamics calculations for low energy displacement events ($\leq$ 500 eV) in Cu by King and Benedek (1983) and in Mo (Guinan and Kinney (1981)) indicate that $\sim$ 40 atoms change lattice sites for every Frenkel pair produced. This ratio is likely to be significantly

higher for more energetic cascade events and in pre-damaged crystals so that the measured number of free defects may be orders of magnitude smaller than the collision theory estimates. Values as low as 10^{-2} have been reported (Macht et al. 1985) for the fraction of freely migrating defects in Ni irradiated with Ni^+ ions.

3.2.9 Radiation Damage in Ni and Pd

The nature and annealing characteristics of radiation-induced damage in Ni and Pd have been studied by several authors - Nakagawa et al (1977) using thermal and fast neutron irradiation, Horak and Blewitt (1975) with thermal and fast neutron irradiation), Khanna and Sonnenberg (1981) using electron irradiation). Also Westmoreland et al (1975), Sprague et al. (1974) and Chen et al (1972,1973) have studied damage in Ni induced by Ni^+ ion irradiation.

i) Electron Irradiation

Khanna and Sonnenberg (1981) studied the isochronal annealing behavior of Ni wires irradiated at 4.5K with 3 MeV electrons. Irradiation with electrons are of special interest because they are expected to produce only isolated simple defects. The maximum energy which can be transferred to a nucleus by a relativistic electron of kinetic energy E is

$$T_m = \frac{2E(E+2m_eC^2)}{MC^2} \qquad (3.18)$$

where C is velocity of light, m_e is the rest mass of the electron and M is the rest mass of the nucleus, m_eC^2 = 0.511 MeV and C^2 = 931.5 MeV/a.m.u., so that the maximum energy transferrable to the nucleus by 3 MeV electrons

is ∿ 400 eV. As discussed in previous sections, low energy recoils are favored so that most of the displacements occur much below Tm and substantially well separated Frenkel pairs should result. The results of Khanna et al show that the electrical resistivity increased linearly with electron dose. Their annealing curves show a stage I recovery peak near 55K, a complex stage II recovery with a major peak at ∿ 216K and a stage III peak near 400K. Stage I has been attributed to vacancy-interstitial recombination while stage II is thought to be due to interstitial annihilation at sinks. Stage III recovery has been attributed to vacancy migration to sinks e.g. interstitial clusters. The activation energy for stage III recovery was measured by Khanna to be 1.04±0.04 eV and is independent of radiation dose and sample purity and remains constant through the stage III temperature range in contrast with values obtained from quenching experiments (H. Mehrer 1965) where the activation energy ranged from 0.9 to 1.27 eV.

ii) Neutron Irradiation

Damage induced by thermal and fast neutron irradiation of Ni and Pd have also been studied by Horak and Blewitt (1974) and Nakagawa et al (1977). The samples were irradiated to different fluences at 4.6K and the recovery of irradiation induced resistivity was studied up to 700K. In addition Horak et al estimated the number of Frenkel pairs produced per neutron and found that the ratio of the measured to the calculated defects produced is 0.39 and 0.33 for Ni and Pd respectively following thermal neutron irradiation. For fast neutron irradiation, the numbers are even lower at ∿ 0.2 and ∿ 0.17 for Pd and Ni respectively. The values

for fast neutron irradiation are consistent with the effect of defect cascade size on the properties of materials mentioned in section 3.2.8. Indeed the work of Nagakawa et al shows that the radiation induced resistivity in both Ni and Pd is nonlinear and tends to a saturation level at high fast neutron doses ($\sim 1 \times 10^{19}$ n/cm^2). At high doses defect cascade overlap becomes more probable and consequently leads to increased vacancy-interstitial recombination within the defect volume.

Fig. 3.5 shows the isochronal resistivity recovery curves of thermal-neutron irradiated Ni and Pd. For thermal neutron irradiated Ni, the main stage I is found at $\sim$ 55K similar to that observed by Horak et al. for electron irradiation, and accounts for $\sim$ 41% of the total recovery. Stage II consists of several sub-peaks from 60 to 246K with a major peak around 216K. Stage II contributes an additional 47% recovery. Stage III begins at $\sim$ 250K and extends to $\sim$ 400K, the major annealing process in stage III being due to long range vacancy migration to annihilation sinks outside the cascade. Stage III recovery in fast neutron irradiated Ni is characterized by vacancy-interstitial recombination as many of the vacancies are tied up in clusters and consequently not available for long range diffusion. The annealing behaviour of irradiated Pd is similar and is shown also in Fig. 3.5.

iii) Heavy Ion Irradiation

Heavy ion irradiation damage in Ni has also been studied by several authors. Al-Tamimi et al (1985) for example have studied the stability of defects produced in single crystal Ni irradiated with 60 keV Sb^+ and 120 keV Sb_2^+ ions at 40K and 300K. The objective was to study the influence of high energy density cascades on the stability of defects produced.

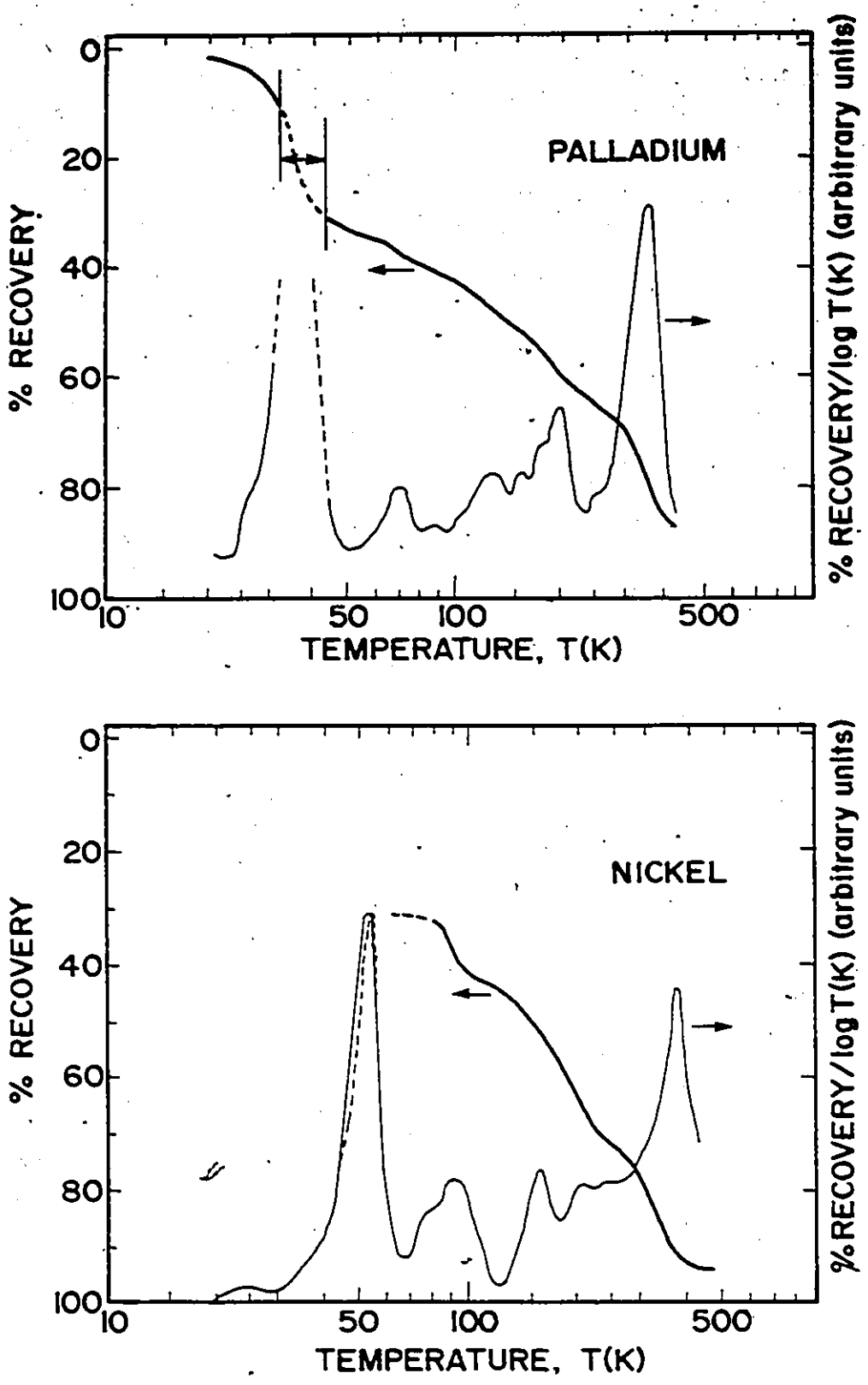

Fig. 3.5: Isochronal recovery of resistivity following thermal-neutron irradiation of Pd and Ni.

Sb_2^+ implantation is expected to almost double the local energy density, $\bar{\theta}$, within the cascade surrounding each implanted ion (compared to Sb^+ irradiation) without significantly increasing the cascade dimensions. The resulting damage was analysed by RBS/channeling technique with a 2 MeV $^4He^+$ beam Their results show that for both 40K and 300K irradiations the retained damage is substantially higher for Sb_2^+ irradiation than for Sb^+ irradiation, especially at room temperature. This must mean that a greater fraction of defects produced by Sb_2^+ irradiation are stable against thermal anneal than is the case for Sb^+ implantation. It is conceivable that the defects produced by Sb_2^+ implants are retained in the form of vacancy and interstitial clusters since the interstitials created are likely to be transported to greater distances than are the vacancies. Electron microscopy observations by Norris (1969a,1969b) on Ni foils irradiated with 80-150 keV heavy ions (Au^+,Hg^+) show that vacancy clusters were formed for low dose irradiations ($\sim 10^{15}$ m^{-2}) while both vacancy and interstitial clusters were observed for high dose irradiations ($\sim 10^{19}$ m^{-2}). Similar observations have been made by Chen et al. (1972) and Chen (1973) who irradiated Ni foils with 100 keV doubly-charged nickel ions.

3.3 Ion Beam Mixing Processes

It is now generally recognized that there are several basic mechanisms which may contribute to the ion beam mixing phenomenon. First, ballistic or collisional mixing may be induced by recoil implantation and collision cascades. In the process of slowing down, the ion transfers some of its kinetic energy to target atoms via atomic collisions and causes many displacements in the process. Displacements are terminated when the

recoils do not receive sufficient energy to be displaced. This collisional phase lasts for times of $\sim 10^{-13}$ sec. After the displacement phase, there is a relaxation phase ($\sim 10^{-11}$ sec) during which the recoils lose their excess energy to the surrounding lattice via lattice vibrations. Atomic motion during this phase is random, short-range and confined essentially within the vicinity of the original cascade, and leads to a thermal rearrangement of unstable defect configurations via close-pair recombination. Provided the collision cascade is not so dense as to reduce the effective displacement energy (Thompson 1981), collisionally induced mixing should scale with F_D, the ion energy deposited per unit length into elastic collisions, and is expected to be independent of temperature.

Beyond the collisional and relaxation phases, mobile defects generated by the irradiation may contribute to mixing by a diffusional process. This radiation-enhanced diffusion is thermally activated and therefore depends on the substrate temperature.

In the following, a brief exposition of the theoretical treatment of these mixing mechanisms, and the observed mixing rates in different systems is given. The subject has been reviewed recently by Paine et al (1985), Mayer (1981), Wang (1984) and Nicolet et al (1984).

3.3.1 Primary Recoil Mixing

During collision with the target atoms, large energies ($\sim$ keV) may be transferred by the ion to some target atoms so that such atoms are directly relocated a significant distance and may be implanted beyond the interface. The range of such high energy recoils compared to later generation of recoils is large and their contribution to mixing is usually observed as a deep

penetrating tail. However, as shown earlier (Eq. (3.16)) the recoil distribution has a $1/E^2$-dependence on energy. Therefore, the majority of the displacements will be due to lower energy higher order displacements, and the contribution of recoil implantation to ion beam mixing is not expected to be large. Theoretical treatments of recoil mixing have been given by Kelly et al (1980) and Littmark et al (1980). These treatments predict that under standard ion beam mixing conditions (overlayer thickness of several tens of nanometers) recoil implantation contributes little to observed mixing.

3.3.2 Cascade Mixing

Collision cascade mixing is the layer intermixing resulting from a series of consecutive displacements of the atoms near the interface. It is due primarily to low-energy later-generation recoils and it is isotropic and athermal.

Though the mixing process is not diffusional in the classical sense, most of the theoretical treatments of cascade mixing are based on diffusional analogy. Haff et al (1977) for example, proposed a theoretical model based on diffusion in a gas. To approximate the model to solids, they assumed that only a fraction of the atoms along an ion damage track is actually undergoing translational motion. Their effective 'diffusion coefficient' is

$$D = \frac{1}{6}\frac{\dot{\phi}\ell d}{E_d \cdot N} \cdot F_D \qquad (3.19)$$

where $\dot{\phi}$ is the ion flux, ℓ is the mean distance between collisions, d is the cascade diameter, N is the matrix atomic density and F_D is the energy deposited by

the ion per unit length at the interface. The problem with this model is that the three parameters ℓ, d and E_d can only be estimated. E_d, for example, is not known for most metals and is even less known in the mixed layers. Also, one can only make crude estimates of ℓ and d, hence the model contains large uncertainties. An estimate of D for the spreading of a Pd marker in Ni induced by Ar-irradiation can be made with reasonable values of ℓ, d and E_d. A reasonable value for ℓ is several interatomic distances, say $\sim$ 1 nm. For 120 keV Ar ions in Ni, $F_D \sim 1400$ eV/nm and d $\sim$ 20 nm (calculated from Winterbon (1970)). Andersen (1977) has tabulated the E_d values for several elements and gives the effective displacement energy for Ni $\sim$ 30 eV. Thus Eq. (3.19) gives $\frac{\Delta\sigma^2}{\phi} \approx 2.1\times10^{-28}$ cm^4/ion which is about a factor of twenty greater than measured (see Chapter 6.1). Similar disagreement between this model and experiments has been observed by Matteson et al (1979). A qualitatively similar model has been proposed by Andersen (1979).

A collisional mixing model based on the transport theory of the stopping of energetic particles in matter has been proposed by Sigmund et al. (1980). The model predicts that the mixing is dominated by contributions from low energy (eV) and high energy (keV) cascades of matrix recoils, the low energy contribution being dominant for doses of the order of 10^{16} cm^{-2}. It also predicts a net mean shift of the impurity profile, to the surface for heavy impurities or to deeper depths for lighter impurities, as a result of the relocation of the matrix atoms past the marker. Paine (1982) and Wang (1984) have compared the experimental spreading of Pt markers in Si with the predictions of this model and found that the low energy cascade model can underestimate the mixing by an order of mag-

nitude. Also the predicted mean impurity shifts are rarely observed, and when they are observed, the shifts are generally in the opposite direction to that predicted (e.g. Wang 1984).

Matteson (1981) proposed a cascade mixing model which includes both low and high energy recoil contributions. In this random-walk model the mixing is due to the displacements of impurity atoms (species 3) caused by the matrix atom recoils (species 2) initiated by the ion of species 1. The recoil spectrum of species 3 within the concepts of power law scattering can be evaluated by the methods described previously, and combined with a knowledge of the mean square range of species 3 recoils in the matrix species 2, leads to an analytical expression for the mixing parameter

$$Dt = N\langle \bar{r}^2 \rangle = \frac{m/(4m-1)}{\psi(1)-\psi(1-m)} \cdot \frac{g_{32}}{(N_2 C_{32}^m)^2} \frac{C_{23}^m \gamma_{23}^{1-m}}{N_2 C_{22}^m} F_D \phi \int_{E_{min}}^{E_{max}} E_3^{4m-2} dE_3 \qquad (3.20)$$

where the mean square range given by Sanders (1968) of

$$\bar{r}^2 = \frac{g_{32}}{(N_2 C_{32}^m)^2} \cdot E_3^{4m} \qquad (3.21)$$

has been used. E_{min} can be taken to be the displacement energy E_d, and $E_{max} = \gamma_{12}\gamma_{23}E$. The C_{ij}'s are the coefficients in the power law approximation to the scattering cross-section

$$C_{ij}^m = \frac{\pi}{2} \, m a_{ij}^2 \left(\frac{M_i}{M_j}\right)^m \left(\frac{2Z_i Z_j e^2}{a_{ij}}\right)^{2m} \qquad (3.22)$$

Matteson has suggested a piece-wise integration of Eq. (3.20) commensurate

with appropriate values of m: m=0 at eV energies m = 1/3 at intermediate energies and m = 1/2 at higher energies. This model seems to give a better estimate, within a factor of two, of the observed mixing of Pd markers in Ni (see Chap. 6.1), and the mixing of various impurities in Si (Matteson 1981).

Before reviewing the data on cascade mixing and the relevance of the various models presented above we will first examine another process that may contribute to ion mixing, namely, radiation enhanced diffusion.

3.3.3 Radiation Enhanced Diffusion (RED)

Results on most mixing experiments indicate two temperature regimes - a low temperature regime where the mixing is independent of temperature and a higher temperature regime where the mixing shows a temperature dependence. The temperature dependence is generally thought to be due to enhanced diffusion due to radiation-produced defects. Radiation enhances diffusion basically in two ways: (1) increased concentration of mobile point defects over and above the thermal equilibrium values and (2) accelerated motion of the defects possibly as a result of the increased jump frequencies of the defects.

Enhanced self-diffusion in crystalline solids has been described by Dienes and Damask (1958), Myers et al. (1976), Myers (1980) and others. In the formalism of Dienes et al. (1958), diffusion occurs as a result of motion of vacancies and interstitials and the enhanced diffusivity is given as

$$D_{rad} = D_v C_v + D_i C_i \qquad (3.23)$$

where D_v, C_v are the diffusion coefficients and concentrations respectively

of vacancies and D_i, C_i are for interstitials. The problem then reduces to estimating the values of C_v and C_i under irradiation. The chemical rate theory description of these concentrations gives

$$\frac{\partial C_v}{\partial t} = D_v \nabla^2 C_v + \alpha K_0 - K_{iv} C_i C_v - K_{sv} C_{sv} (C_v - C_v^o) \tag{3.24}$$

$$\frac{\partial C_i}{\partial t} = D_i \nabla^2 C_i + \alpha K_0 - K_{iv} C_i C_v - K_{si} C_{si} (C_i) \tag{3.25}$$

where C_v^o is the vacancy concentration without irradiation, K_{iv} is the rate constant for mutual recombination of interstitial-vacancy pairs, K_{si} (K_{sv}) are the rate constants for annihilation at fixed sinks with concentrations C_{si} and C_{sv}. K_0 is the defect production rate (atomic fraction/sec) and can be estimated from the modified Kinchin-Pease model. αK_0 then is the concentration of freely migrating defects and is usually $\ll K_0$ as discussed previously. The annihilation rate constants depend on the recombination volume and the density of sinks such as dislocations etc. Thus (F.S. Ham 1958) gave

$$K_{iv} = \frac{4\pi R_{iv}}{\Omega} (D_i + D_v) \sim \frac{4\pi R_{iv} D_i}{\Omega} \tag{3.26}$$

$$= 4\pi R_{iv} N D_i$$

where R_{iv} is the radius of the recombination volume and Ω is the atomic volume and N the atomic density of material. Similarly

$$C_{sv} \cdot K_{sv} = C_{sv} \frac{4\pi R_v D_v}{\Omega} = \frac{D_v}{\ell} \tag{3.27}$$

$$C_{si} \cdot K_{si} = C_{si} \frac{4\pi R_{si} D_i}{\Omega} = \frac{D_i}{\ell} \tag{3.28}$$

where ℓ is the characteristic diffusion length to an annealing sink.

A numerical solution to equations (3.24) and (3.25) has been given by Myers (1976) but they can be solved easily at steady-state and when spatial variations in C_v and C_i are small. In this case the solution is simplified further:

i) At high temperature where C_v^o is high and vacancies are mobile

$$D_{rad} = D_v C_v^o \tag{3.29}$$

i.e. normal thermal diffusion dominates.

ii) At intermediate temperatures when defects annihilate mostly at fixed sinks then

$$D_{rad} = 2\alpha K_0 \ell^2 \tag{3.30}$$

so that D_{rad} is independent of temperature and is directly proportional to the defect production rate K_0.

iii) At still lower temperatures where defects annihilate by mutual recombination

$$D_{rad} = \left(\frac{\alpha K_0 D_v}{\pi R_{iv} N}\right)^{\frac{1}{2}} \quad \text{if only vacancies are mobile} \tag{3.31}$$

or

$$D_{rad} = \left(\frac{\alpha K_0 D_i}{\pi R_{iv} N}\right)^{\frac{1}{2}} \quad \text{if only interstitials are mobile .} \tag{3.32}$$

In this case $D_{rad} \propto K_0^{\frac{1}{2}}$ and is temperature-dependent with activation energy $E_a = E_v^m/2$ (or $E_i^m/2$). Fig. 3.6 shows the temperature dependence of D_{rad} measured on electron irradiated Ni.

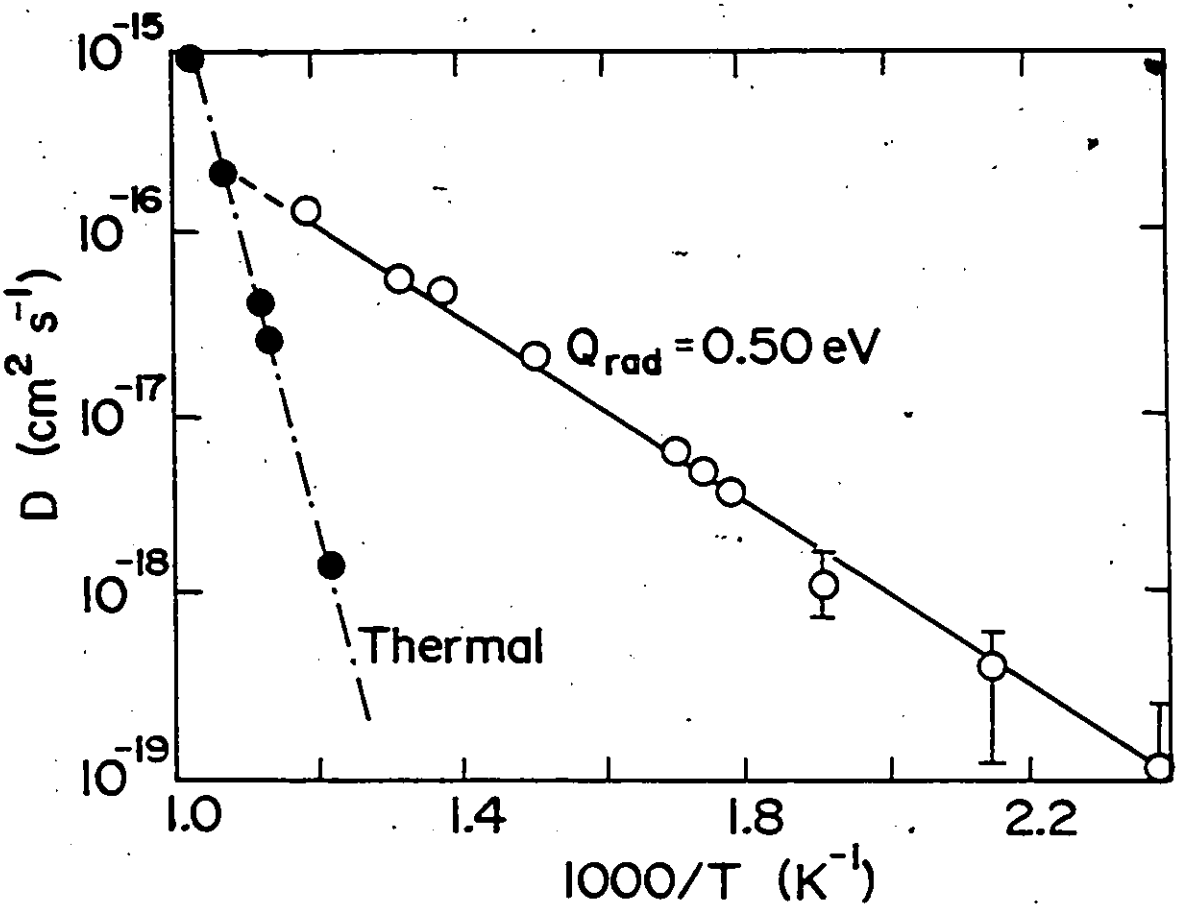

Fig. 3.6:. Temperature-dependence of the diffusion coefficient under irradiation for electron irradiated Ni (Harkness et al. 1975).

3.3.4 Review of Ion Mixing Data

Most forms of the theory of collisional mixing predict a linear dependence of the mixing parameter on fluence ϕ and nuclear energy deposited per ion per unit length, F_D, in the target. Matteson's (1981) model predicts an additional linear dependence on the maximum energy transferable in matrix-impurity collisions ($\gamma_{12}\gamma_{23}E_1$).

In the analysis of mixing experiments, the amount of mixing is usually characterized by either the number of impurity atoms/ion which has crossed the original interface, of a bilayer couple or by the increased broadening of this interface. In the marker experiments, where a thin impurity source is sandwiched between two layers of matrix (Fig. 3.1a), the impurity profile both before and after irradiation is often Gaussian in shape and the mixing is characterized by the increased variance ($\Delta\sigma^2$) of the distribution following ion bombardment.

i) Fluence, ϕ, Dependence

The linear-dependence on fluence predicted by many of the collisional mixing models is generally observed in both the marker and bilayer systems. Fig. 3.7 which shows the ϕ-dependence of the spreading of thin Pt markers in Si (Paine 1982) is typical. Similar observations have been made on the mixing of Cu/Al couples (Besenbacher et al 1982), thin Au markers in Ni and Au/Ni bilayers (Bottiger 1985) and the mixing of thin Pt, Au, W, Fe and Ti in Al and Al_2O_3 matrix (Barz 1984). There are exceptions however; for example the work of Clark et al. (1983) for Si in Ge which shows a less than linear dependence on ϕ, and that of Poker et al. (1984) on Au/Si bilayers which shows a ϕ^2-dependence. Besenbacher et al also

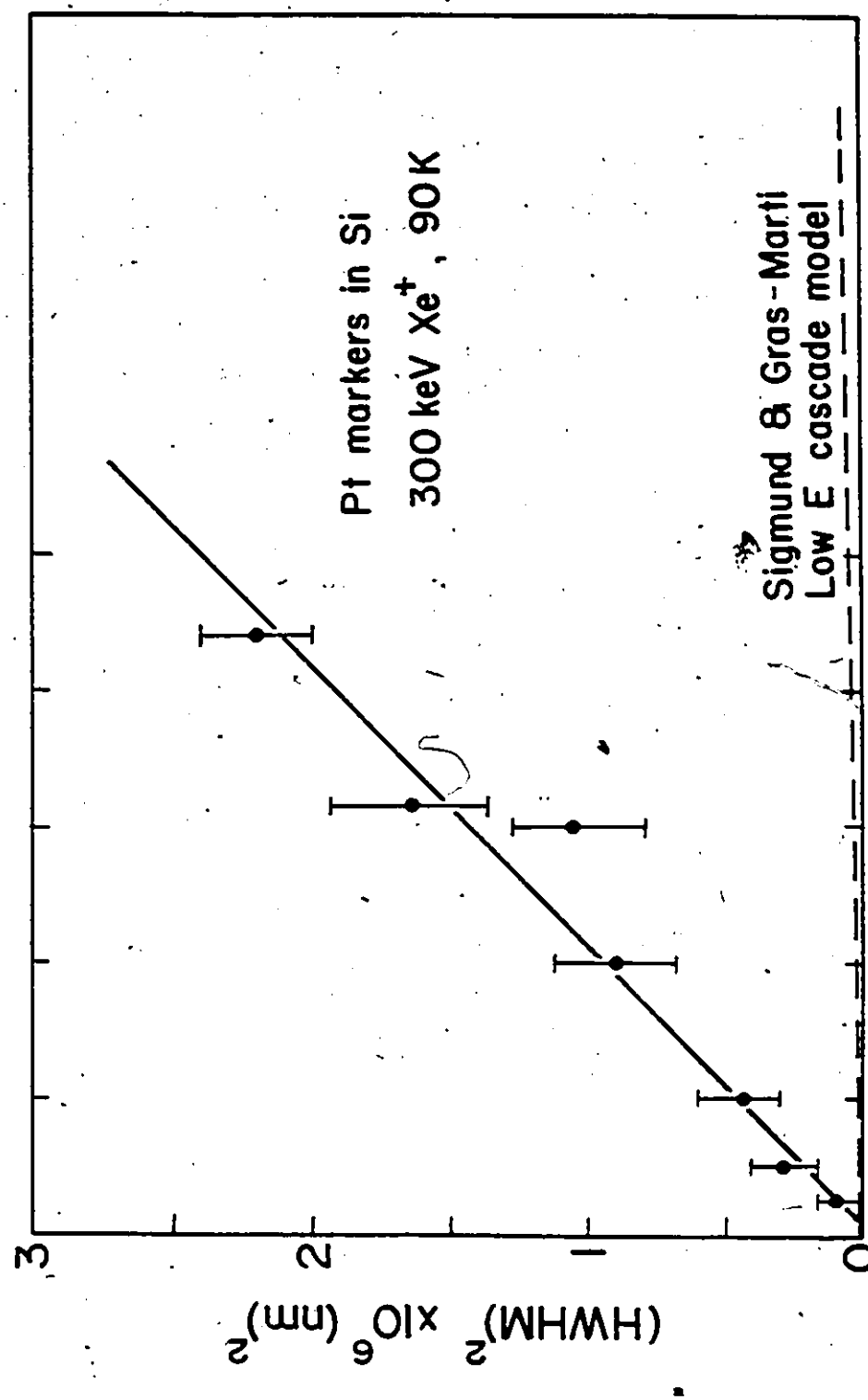

Fig. 3.7: Fluence dependence of the spreading variance for Pt markers in Si.

estimated the contribution of direct recoil implantation to the mixing of Cu/Al couples bombarded with 500 keV Xe^+ ions. They found an efficiency (mixed atoms/ion) of $\sim$ 0.25 atoms/ion for recoil mixing and $\sim$ 12 atoms/ion for cascade mixing thus confirming Littmark's (1980) prediction that the direct recoil implantation contribution to observed mixing is small.

ii) F_D-dependence

Fig. 3.8 shows the F_D-dependence for the mixing of Au marker in Ni and for the mixing of Pt/Si bilayers. For the marker systems a linear dependence on F_D is observed for Au markers in Ni (Bottiger et al 1984). Similar linear dependence on F_D was observed (Nicolet et al 1984) for various markers in Al, Al_2O_3, Si, SiO_2 irradiated with He, Ar, Kr and Xe ions. For bilayers many systems with large F_D (> 3000 eV/nm) have been investigated and a significant nonlinear dependence on F_D has been observed. Kr and Xe irradiation, for example, produce about a factor of 4 more effective mixing in Pt.Si bilayer than He and Ne irradiation (Averback et al. 1984).

The mixing efficiencies also vary from system to system, even for collisionally similar systems, and are generally higher than the value predicted by many of the cascade mixing models (Fig. 3.7). Westendorp et al (1982) for example studied the mixing of collisionally similar Cu/Au and Cu/W couples irradiated with 300 keV Kr ions at 300K. From the point of view of collision cascade mixing Cu/Au and Cu/W are similar systems because of the similar masses of Au and W. Their results show (Fig. 3.9) that after a dose of 5×10^{15} cm^{-2} an homogeneously mixed layer $\sim$ 40 nm thick has occured in the Cu/Au couple while only a small broadening ($\sim$ 3 nm) of the Cu/W interface was found after irradiation.

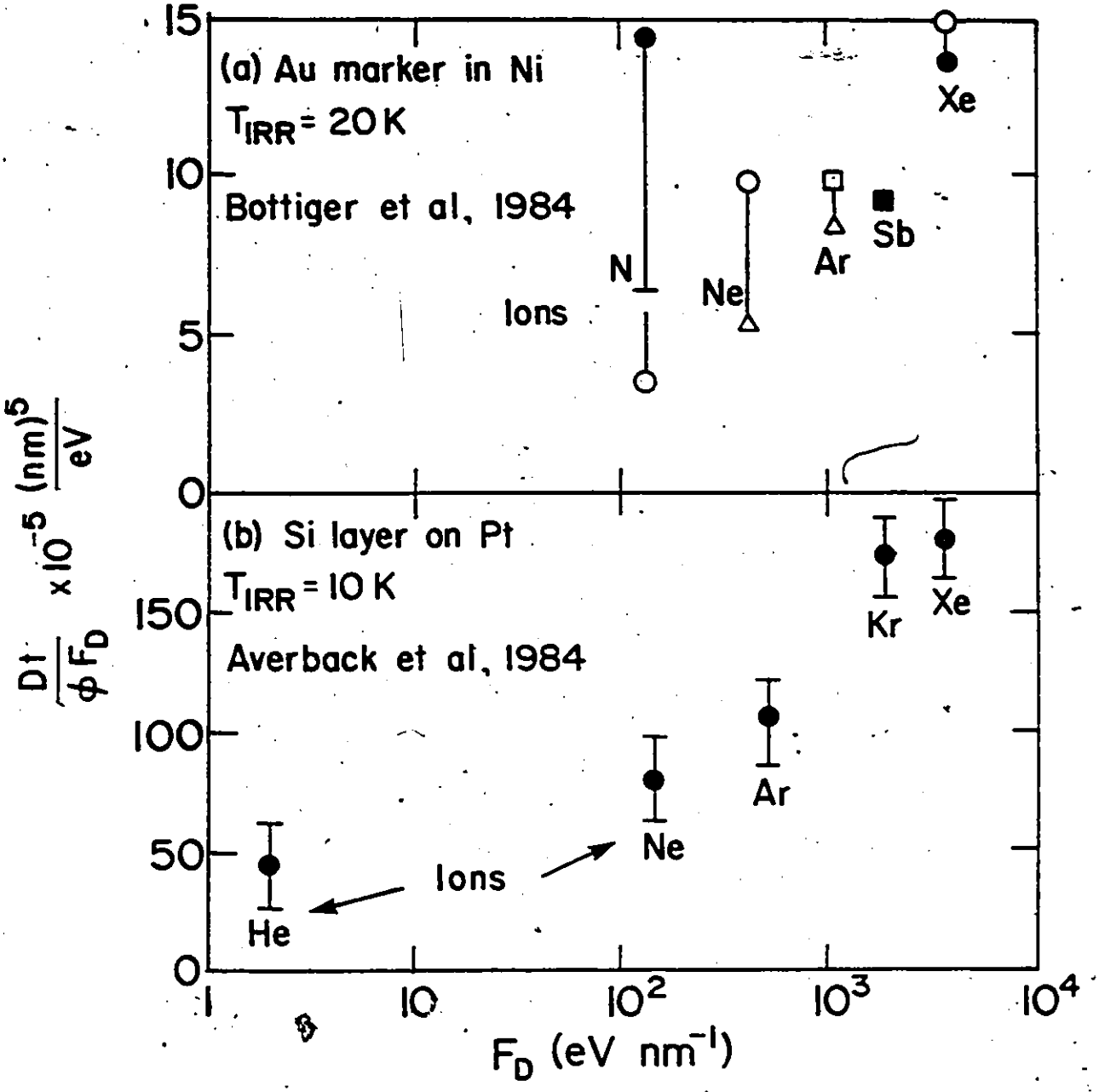

Fig. 3.8: F_D-dependence of the mixing of Au markers in Ni and Pt/Si bilayer couples.

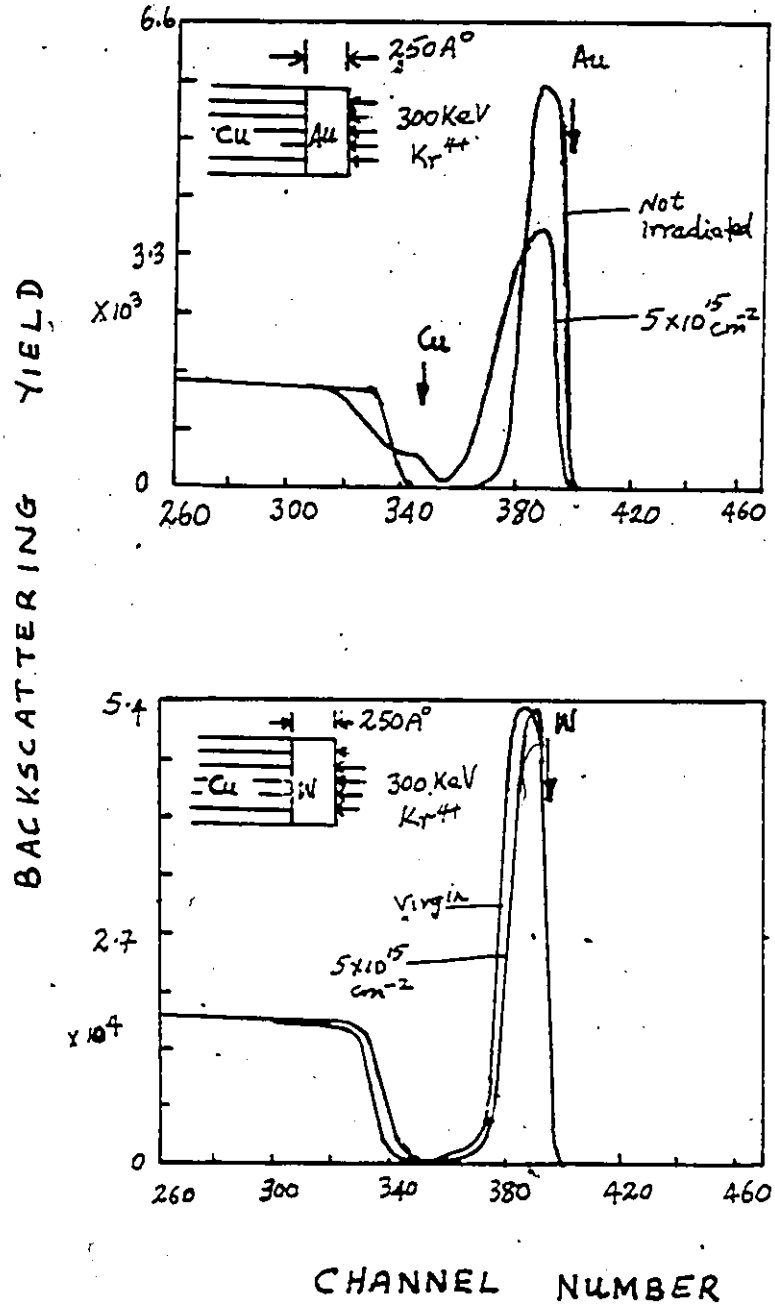

Fig. 3.9: Mixing induced by 300 KeV Kr irradiation of collisionally similar Cu/Au and Cu/W bilayer couples.

Similar observations have been made by Picraux et al. (1982) concerning the mixing of collisionally similar Al/Sb and Al/Ag couples following 400 keV Xe irradiation at 300K. They found mixing rates of $\sim$ 0.56 Sb/ion for Al/Sb and 2.6 Ag/ion for Al/Ag couples. The larger mixing observed for Cu/Au and Al/Ag suggests that chemical driving forces may play some role in ion mixing since Cu/Au and Al/Ag are soluble systems whereas Cu/W and Al/Sb have negligible solubilities.

iii) Temperature-dependence

Most of the data on the temperature dependence of mixing show two temperature regimes. Below a critical temperature T_c, which depends on the system, observed mixing is generally independent of temperature. Above T_c, the mixing increases strongly with temperature. This temperature-dependent behaviour has been observed both in the marker and bilayer experiments. Fig. 3.10, which shows the temperature dependence of the mixing of Ni films on Si (Averback 1982) irradiated with 250 keV Ar ions is typical. It is independent of temperature between 10 and $\sim$ 200K. Above 200K it becomes temperature dependent. Bottiger et al. (1985) have made similar observations in the mixing of Au markers in Ni and of Ni/Au bilayers irradiated with 500 keV Xe^+ or 150 keV Ar^+ ions where the mixing is independent of temperature up to $\sim$ 400K.

The temperature-independent mixing is usually ascribed to collisionally induced mixing but as pointed out in the last section, chemical driving forces may be playing a role. The temperature dependent region is believed to be due to contributions from purely thermal effects and radiation-enhanced diffusion. However the K_0-dependence predicted by

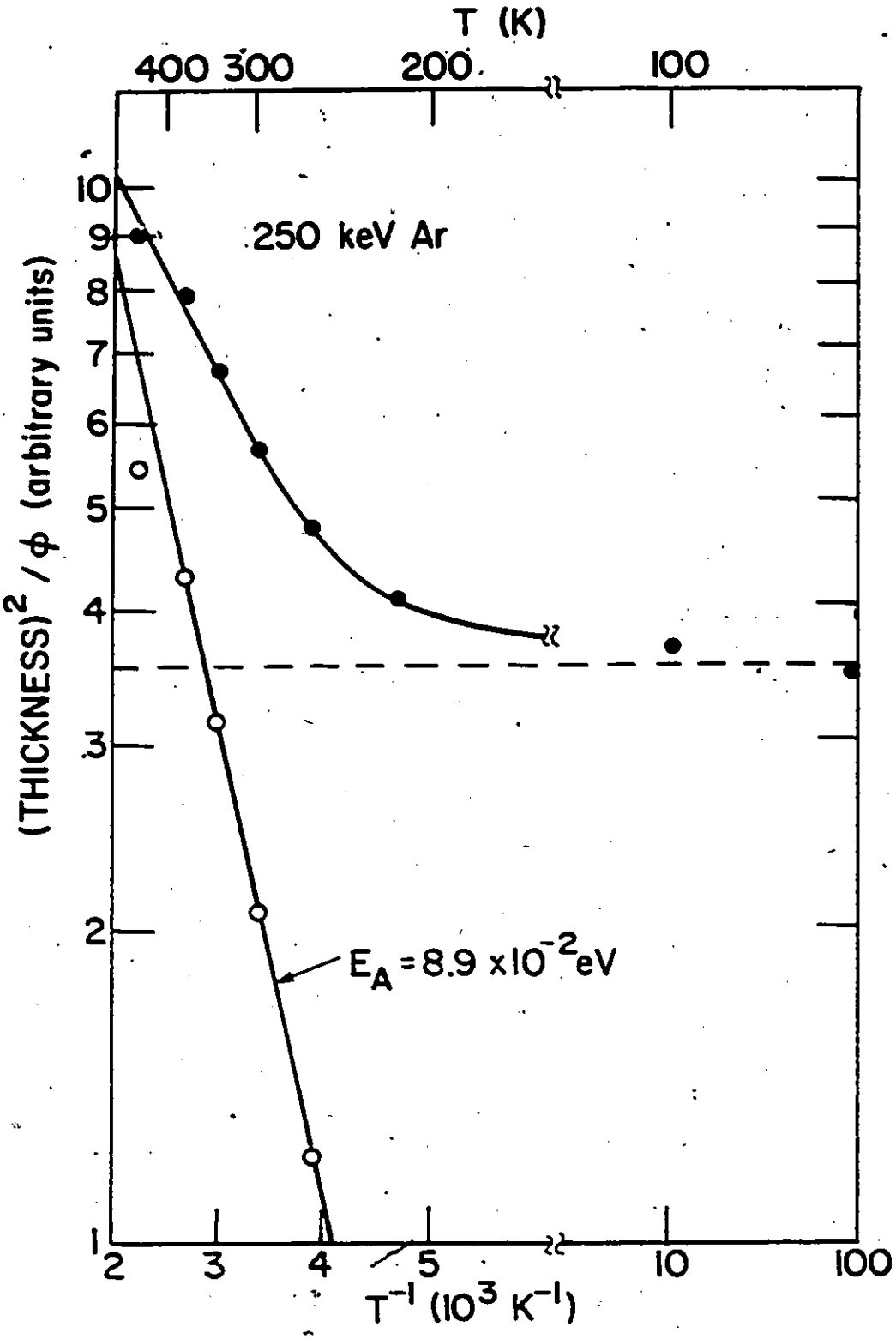

Fig. 3.10: Temperature-dependence of the mixing of Ni films on Si.

Eq. (3.29) have largely not been observed (Averback et al (1982).

The available experimental data on ion beam mixing have been reviewed by Mayer et al (1981), Matteson et al. (1983), Wang (1984) and more recently by Paine et al (1985) and Averback (1986).

CHAPTER 4

ANALYSIS TECHNIQUES.

4.1 Introduction

The main analysis technique used in this work for the characterization of the interdiffused layer is the backscattering of light MeV ions (RBS). Although many other analytical techniques, notably Auger electron spectroscopy, SIMS and neutron activation (combined with sputter profiling) can give basically the same information and are frequently employed, the RBS technique is superior in certain respects. Though not as sensitive as SIMS or neutron activation it is capable of providing quantitative information without recourse to standards. It is fast and, because information on the depth distribution of any component can be obtained without sectioning or ion sputtering, it is essentially non-destructive. It is particularly useful for ion-beam mixing studies because, in our case, in-situ analysis can be carried out immediately following heavy ion bombardment. Combined with the channeling technique it can furnish information about the epitaxy of the evaporated layers on single crystal substrates and the lattice location of implanted or ion-beam mixed atoms.

In section 4.2 the theoretical aspects of RBS will be given. Its application to the depth profiling of diffused species will be given in section 4.3. In section 4.4 the principles of electrode overpotential measurements including the concepts of reference potentials will be given.

4.2 Rutherford backscattering spectroscopy (RBS)

Four basic concepts enter into the description of RBS and each confers special capabilities. The concept of kinematic factor and mass identification is discussed in 4.2.1 while the Rutherford scattering cross-section confers the capability for quantitative analysis and is discussed in section 4.2.2. The ability to obtain depth information is accomplished via the energy loss process and the concept of stopping cross-sections. This is discussed in 4.2.3. The ion energy straggling, which is discussed in 4.2.4, places a finite limit on the precision with which energy losses and hence depths as well as mass identification can be resolved by RBS,

4.2.1 Kinematic factor

When a beam of energetic light particles (e.g. MeV $^4He^+$ ions) strikes the surface of a target some of these will undergo wide angle elastic collisions with target atoms. The energy of the backscattered particles depends on the mass and energy of the particle, the mass of its collision partner as well as on the scattering angle. Since both energy and momentum are conserved in the collision process the energy E_1 of the particle after scattering, can be obtained:

$$E_1 = KE_0 \qquad (4.1)$$

where E_0 is the incident energy of the particle and K is the kinematic factor and is given, in LAB system, by

$$K = \left[\frac{(M_2^2 - M_1^2 \sin^2\theta)^{\frac{1}{2}} + M_1 \cos\theta}{M_1 + M_2}\right]^2 \qquad (4.2)$$

where M_1 and M_2 are the masses of the particle and the target atoms respectively. K depends only on M_1, M_2 and θ, so that by monitoring the energy of the backscattered particles at a specific angle θ, the mass/masses and hence the identities of the atoms in the target can be determined. When $\theta = 180^o$, K is minimum. Most RBS facility set-ups are such that the backscattered particles are detected near $\theta = 180^o$ (e.g. 160^o) since this arrangement produces the largest difference in K values (and hence the energy separation) between two types of atoms whose masses differ by a small amount. For a fixed θ and same projectile, this separation and hence the mass resolution can be improved by increasing the projectile energy E_0 consistent with the Rutherford scattering law. For $^4He^+$ particles and scattering angle $\theta = 160^o$, the kinematic factor $K_{Ni} = 0.7675$ for Ni and $K_{Pd} = 0.8642$ for Pd.

Fig. 4.1 shows a schematic of the beam, target and detector in a typical backscattering experiment. The incident beam of MeV protons or helium ions is collimated with a set of apertures before striking the target. A small fraction of these particles will backscatter from the target through wide angle collisions and be collected by a suitably placed particle detector (typically a silicon surface barrier detector) situated at an angle 180-θ from the initial beam direction and subtending a solid angle $d\Omega$ at the target.

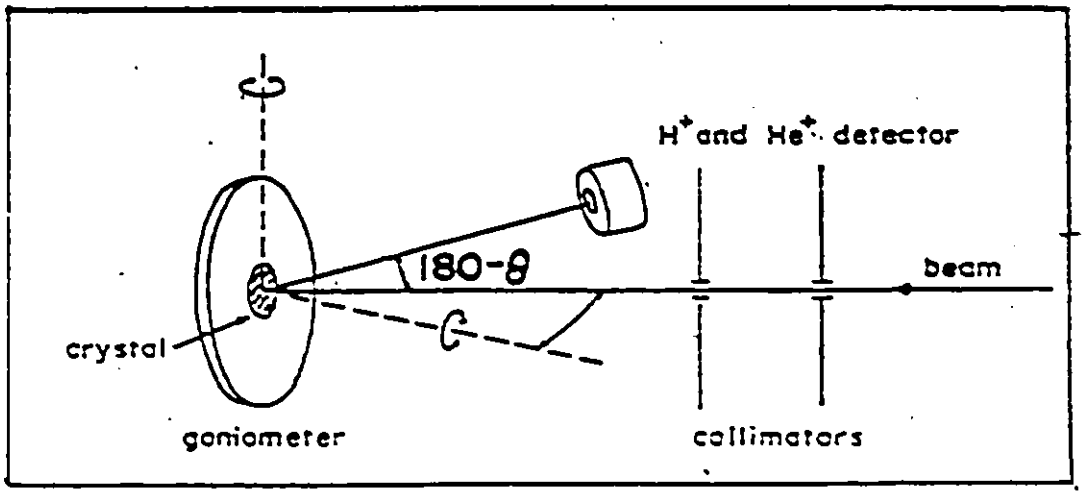

Fig. 4.1 Schematic diagram of the experimental set-up for a channeling-backscattering experiment

4.2.2 Rutherford scattering cross-section

For ion-target combinations having $\varepsilon = a/b \gg 1$ ($\varepsilon \gtrsim 100$) where ε is Lindhard's reduced energy parameter (Eq.(3.12)), the appropriate differential scattering cross-section is that given by the Rutherford formula. In the LAB system it is given by

$$\frac{d\sigma}{d\Omega} = 1.296\times10^{-27} \left(\frac{Z_1 Z_2}{E}\right)^2 \left[\sin^{-4}\left(\frac{\theta}{2}\right) - 2\left(\frac{M_1}{M_2}\right)^2 + \cdots\right] \qquad (4.3)$$

where E is the particle energy in MeV, Z_1, Z_2 are the atomic numbers of projectile and target respectively. This cross-section is appropriate for light energetic particles (e.g. 1 - 2 MeV protons or 0.5 - 3 MeV $^4He^+$) interacting with solids, since then the interaction between the two nuclei

is well described by a fully unscreened collision. However, L'Ecuyer and Davies (1980) have shown that for high Z_2 atoms there is a small correction (up to 4%) to the Rutherford formula, due to the screening effect of the outer and inner electrons. The scattering cross-section then is

$$\frac{d\sigma}{d\Omega} = 1.296\times10^{-27} \left(\frac{Z_1 Z_2}{E}\right)^2 \left[\sin^{-4}\frac{\theta}{2} - 2\left(\frac{M_1}{M_2}\right)^2 + \cdots\right]F \qquad (4.4)$$

where $F = 1 - 0.049\, Z_1 Z_2^{4/3}/1000\, E$.

For 2 MeV $^4He^+$ on Ni or Pd, this factor is almost unity ($\sim .995$)

The differential scattering cross-section is simply the probability that a collision event will occur in which the incident particle is scattered through an angle θ into a solid angle $d\Omega$. The total number of detected scattered particles, H, depends on the number of scattering centres per unit area ($N\Delta x$), the number of incident particles, Q, the collision cross-section and the solid angle subtended by the detector ($\Delta\Omega$):

$$H = (N\Delta x) \cdot Q \cdot \frac{d\sigma}{d\Omega} \cdot \Delta\Omega \,. \qquad (4.5)$$

Thus, if $\frac{d\sigma}{d\Omega} \cdot \Delta\Omega$ and Q are known, we can determine the areal density ($N\Delta x$) of the target atoms simply by measuring the number of detected particles. Equation (4.4) shows that $\frac{d\sigma}{d\Omega}$ has a Z_2^2-dependence so that the backscattering yield is high for high-Z elements, i.e. RBS is more sensitive to heavy elements than to lighter ones.

4.2.3 Energy loss and stopping cross-sections

Fig. 4.2 shows the RBS spectrum of a polished polycrystalline Ni sample obtained using 2 MeV He^+ ions. The characteristics of this spectrum can be evaluated by considering the schematic shown in Fig. 4.3 When a particle of energy E_0 strikes the surface of the target it may undergo wide angle collision with surface atoms, and backscatter to the detector with energy E, given by Eq. 4.1. Those particles which penetrate beyond the surface lose energy to ionization and excitation of target atoms. If some of these backscatter from atoms located at depth x the energy of the particles before scattering at x is $E_2 = E_0 - \Delta E_{in}$ where ΔE_{in} is the energy lost in penetrating the target. These particles then backscatter with energy $K(E_0-\Delta E_{in})$ and are detected at energy $K(E_0-\Delta E_{in})-\Delta E_{out}$, where ΔE_{out} is the energy lost on the outward path. A continuous spectrum of backscattered particles will therefore result for all energies $< E_1$.

If S(E) is the electronic stopping power, we can calculate the detected energy E(x) of those particles backscattering at depth x. For normal incidence

$$E_1(x) = K[E_0 - \int_0^x S(E)dx] - \int_{\frac{x}{\cos\theta}}^0 S(E)dx \quad . \qquad (4.6)$$

In the surface approximation, which is valid for not too large depths, the stopping power for the inward path can be approximated by $S(E_0)$ and that for the outgoing path can be evaluated at $E_1 = KE_0$ i.e. $S(KE_0)$. Then

$$E_1(x) = K[E_0 - xS(E_0)] - \frac{x}{\cos\theta} S(KE_0) \quad . \qquad (4.7)$$

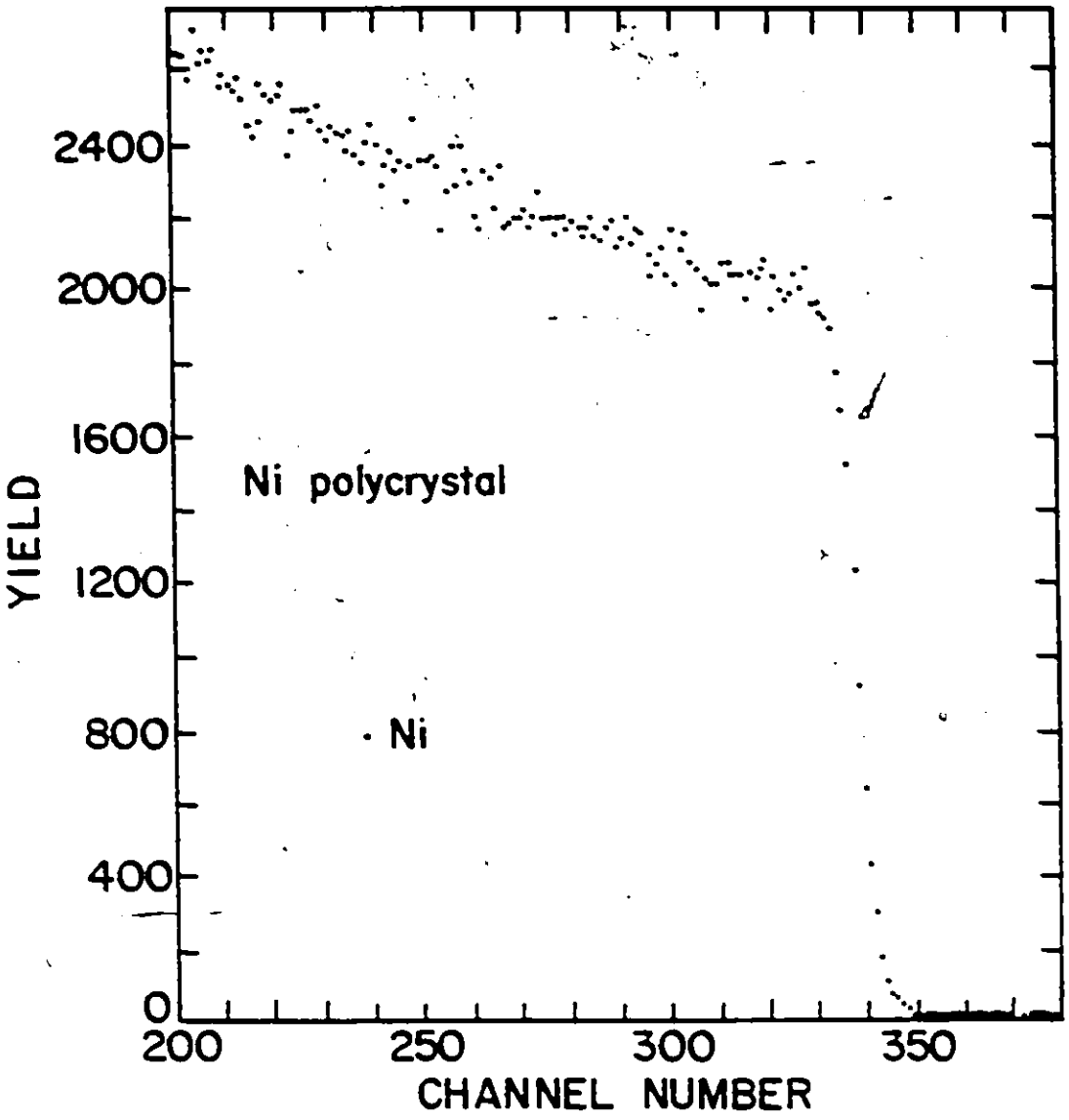

Fig. 4.2: RBS spectrum of a polished polycrystalline Ni sample.

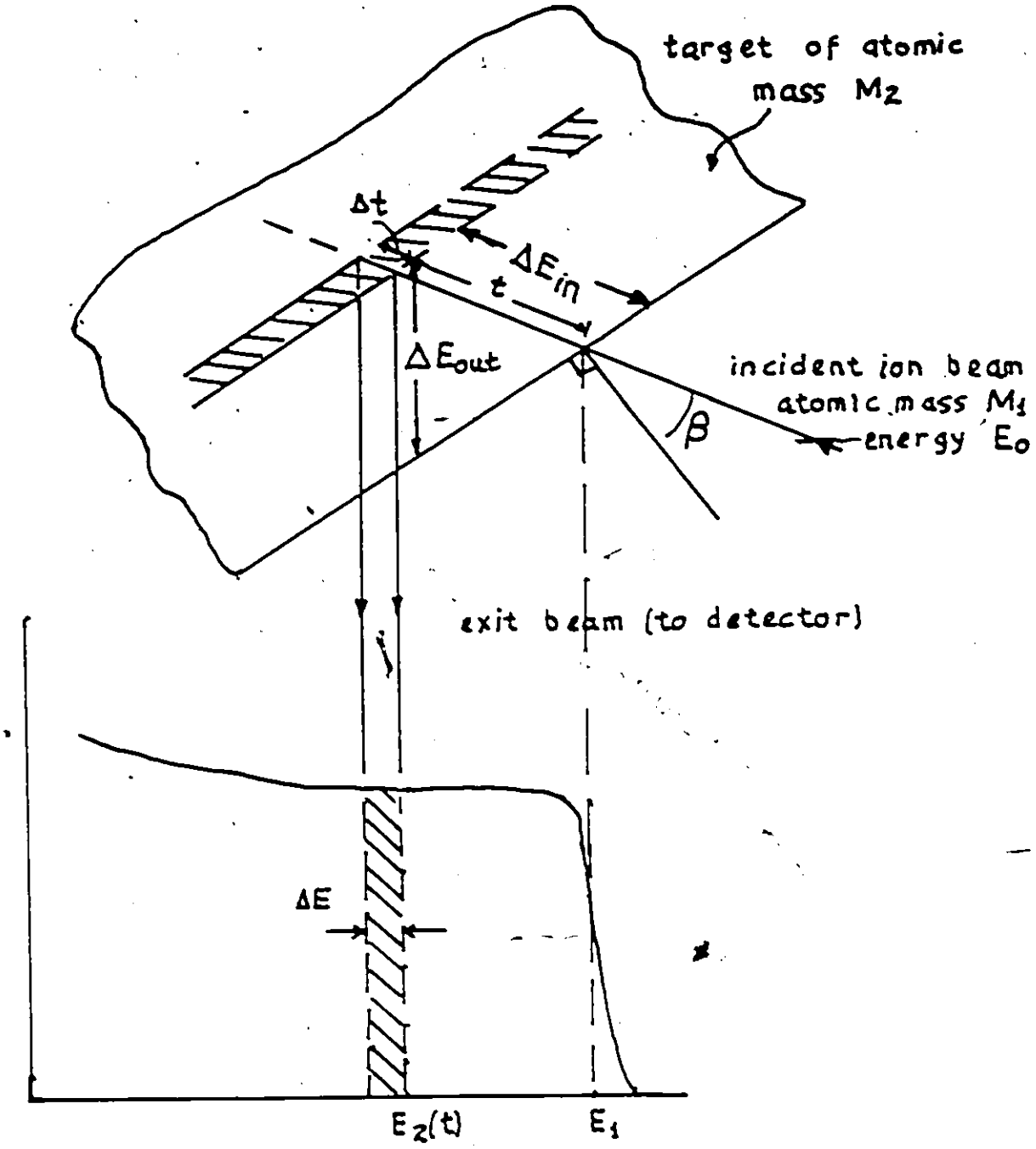

Fig. 4.3: Typical backscattering spectrum of an amorphous target.

The difference in the detected energy of particles backscattering from the surface, and from depth x is then

$$KE_0 - E_1(x) = \Delta E = \left(KS(E_0) + \frac{1}{\cos\theta} S(KE_0)\right) x \quad . \tag{4.8}$$

If δE is the energy per channel, the energy scale of Fig. 4.2 then becomes an incremental depth scale δx

$$\delta x = \frac{\delta E}{\left(KS(E_0) + \frac{1}{\cos\theta} S(KE_0)\right)} \quad . \tag{4.9}$$

The total energy loss factor [S] is defined as

$$[S] \equiv \left[KS(E_{in}) + \frac{1}{\cos\theta} S(E_{out})\right] \tag{4.10}$$

so that

$$\Delta E = [S]\Delta x \quad .$$

We can define a stopping cross-section factor ε such that

$$\Delta E = [\varepsilon]N\Delta x \tag{4.11}$$

where

$$[\varepsilon] = \left[K\varepsilon(E_{in}) + \frac{1}{\cos\theta} \varepsilon(E_{out})\right] \quad . \tag{4.12}$$

The advantage of using $[\varepsilon]$ is that we do not need a knowledge of the target density and we can therefore treat a gas or solid equivalently. It also enables interpolation from one element to another to be more reliably done when direct information is not available. The stopping cross-section therefore makes direct conversion of energy scale to a depth scale possible and gives RBS its depth profiling capability.

The kinematic factor for H and He scattering, the differential scattering cross-section for H and He at various scattering angles and the stopping cross-sections for He of various energies are tabulated by Chu et al. (1978). Table 4.1 gives these parameters for Ni and Pd for a 2 MeV He^+ beam incident normal to the surface and a scattering angle $\theta = 160^o$.

Table 4.1 Scattering Parameter for Ni and Pd

Paramater	Ni	Pd
K	0.7675	0.8642
$\frac{d\sigma}{d\Omega} \times 10^{-24}(\frac{cm^2}{str})$	1.07	2.91
$[\varepsilon_0] \times 10^{-15}(\frac{eV\ cm^2}{atom})$	131.2	181.88
Atomic Density, N ($x10^{22}$ at/cm^3)	9.14	6.8

4.2.4 Energy straggling and depth resolution

There are two main contributions to the energy (and depth) resolution of the RBS technique. The first is due to the response function of the detection system and is revealed as the finite slope of the surface edge near channel 340 in Fig. 4.2. For surface barrier detector this energy resolution, $\Delta E_r \approx 15$ KeV (FWHM) which then translates to the equivalent depth resolution Δt_r through Eq. (4.11). For Ni or Pd target and 2 MeV He^+ ions and $\theta = 160^o$ Δt_r = 12.2 nm for Ni and 12.1 nm for Pd at the surface.

The second contribution is due to the statistical fluctuation in the energy loss of the particles as they penetrate the target, this fluctuation being referred to as energy straggling. The energy straggling of light energetic particles is given approximately by Bohr (1915) as

$$\Omega_B^2 \equiv 4\pi(Z_1 e^2)^2 \cdot NZ_2 t \qquad (4.13)$$

where t is the thickness of the target, and the straggling increases with layer thickness t or the electron density in the target. Experimentally, straggling shows up as a decreased slope of the low energy edge of a thin film spectrum. The slope of the lower energy edge near channel 370 in the Pd spectrum of Fig. 4.4 is due to both the system resolution, ΔE_r, and straggling, ΔE_s. In the Gaussian approximation, both contributions add in quadrature, so that energy resolution is given by

$$(\delta E_1)^2 = (\Delta E_r)^2 + (\Delta E_s)^2 \quad . \qquad (4.14)$$

In general the contribution of energy straggling to depth resolution is small amounting to $\sim$ 3.6 KeV ($\sim$2.9 nm) at a depth of 40 nm in Pd for 2 MeV He^+ ions.

4.3 Depth profiling with RBS

For a sample like that shown in Fig. 4.4 which consists of two elements, the particles backscattering from the A atoms and B atom at the surface will be detected at energies $K_A E_0$ and $K_B E_0$ respectively while those particles backscattering from deeper layers will have energies given by Eq. (4.7). In the case of Fig. 4.4 which shows the RBS spectrum of a Ni

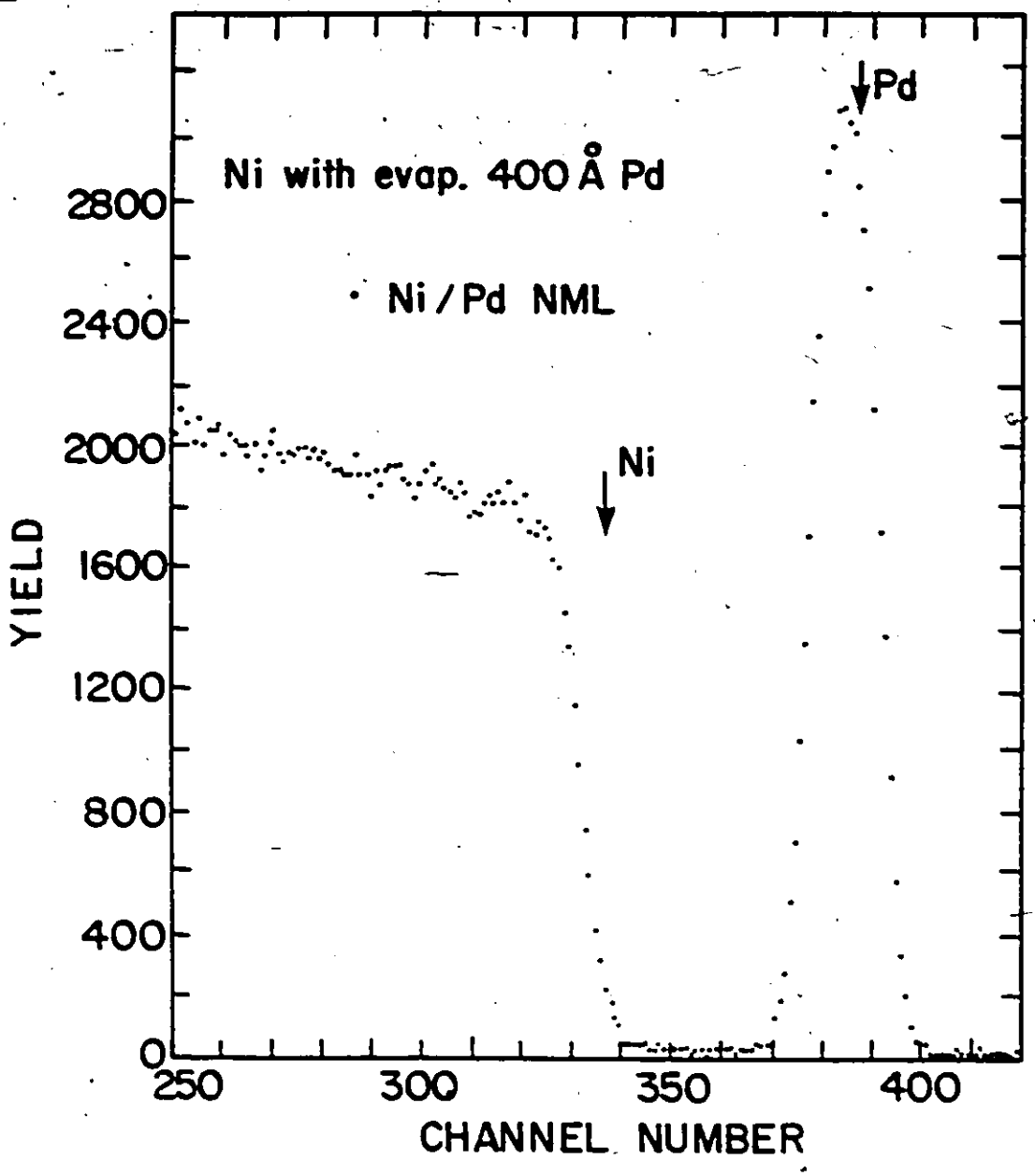

Fig. 4.4: RBS spectrum of a Ni substrate with an overlayer film of Pd.

sample with an overlayer of ∿ 40 nm Pd, the peak at channel 385 is the Pd signal while the Ni edge at channel ∿ 330 is shifted by ∿ 13 channels below where a Ni signal would appear if Ni atoms were on the surface.

The height of the backscattering spectrum for scattering near the surface of a pure target made up of A atoms is given by

$$H_A^A(E_0) = Q \frac{d\sigma_A}{d\Omega}(E_0) \cdot d\Omega \cdot \frac{\delta E}{[\varepsilon(E_0)]_A^A} \qquad (4.15)$$

where δE is the energy per channel of the detection system, Q is total number of incident particles and $[\varepsilon]_A^A$ the stopping cross-section of pure A. For particles scattering from below the surface, $d\sigma_A/d\Omega$ and $[\varepsilon]_A^A$ evaluated at energies just before scattering must be used:

$$H_A^A(E_1) = \frac{d\sigma_A}{d\Omega}(E_A) \cdot d\Omega \cdot Q \cdot \frac{\delta E'}{[\varepsilon(E_A)]_A^A} \qquad (4.16)$$

where E_A is the particle energy just before scattering from A atoms, E_1 is detected energy and $\delta E'$ is energy/channel at depth x. According to Eq. (4.3)

$$\frac{d\sigma}{d\Omega}(E_A) = \frac{d\sigma}{d\Omega}(E_0)/\frac{E_0^2}{E_A^2} . \qquad (4.17)$$

There is an additional correction to δE arising from the fact that particles with slightly different energies after scattering at x undergo slightly different energy losses on their outward path. Chu et al. (1978) have shown that the energy width of one channel at the surface, δE, is related to the energy width/channel, $\delta E'$, at depth x by

$$\frac{\delta E'}{\delta E} = \varepsilon(KE_A)/\varepsilon(E_1) \quad .$$

Thus

$$H_A^A(E_1) = \frac{d\sigma_A}{d\Omega}(E_A)\cdot d\Omega\cdot Q\cdot\frac{\varepsilon_A'(K_AE_A)}{\varepsilon_A(E_1)}\cdot\frac{\delta E}{[\varepsilon(E_1)]_A^A} \quad . \qquad (4.18)$$

For a sample which consists of a mixture of A and B atoms, the spectrum height due to backscattering from A atoms in the mixture is given by

$$H_A^{AB}(E_1) = \frac{d\sigma_A}{d\Omega}(E_A)\cdot d\Omega\cdot Q\cdot\frac{N_A^{AB}}{N^{AB}}\cdot\frac{\delta E}{[\varepsilon(E_A)]_A^{AB}}\cdot\frac{\varepsilon^{AB}(K_AE_A)}{\varepsilon^{AB}(E_1)} \quad . \qquad (4.19)$$

Similarly for backscattering from B atoms

$$H_B^{AB}(E_1) = \frac{d\sigma_B}{d\Omega}(E_B)d\Omega\cdot Q\cdot\frac{N_B^{AB}}{N^{AB}}\cdot\frac{\delta E}{[\varepsilon(E_B)]_B^{AB}}\quad\frac{\varepsilon^{AB}(K_BE_B)}{\varepsilon^{AB}(E_1)} \qquad (4.20)$$

where N_A^{AB}, N_B^{AB} are number of atoms of A and B respectively in the mixture, $\varepsilon^{AB}(E)$ is the stopping cross-section for the mixture and evaluated at energy E. $[\varepsilon(E)]_A^{AB}$ and $[\varepsilon(E)]_B^{AB}$ are the total scattering cross-section for scattering off A and B atoms respectively. ε^{AB} is assumed to obey the Bragg's rule of additivity of stopping cross-sections

$$\varepsilon^{AB} = \frac{N_A^{AB}}{N^{AB}}\cdot\varepsilon_A + \frac{N_B^{AB}}{N^{AB}}\cdot\varepsilon_B \quad . \qquad (4.21)$$

In Eqs. (4.18-4.20) the term containing the ratio of the stopping cross-section is of order unity (for Ni/Pd alloys it varies from 1.07 for 100% Pd to 1.08 for 0% Pd) and can be neglected. Then the relative atomic concentration of element A in a mixture of A/B can be determined by three different methods:

i) from the ratio of the yield H_A^{AB} of element A to that of element B, H_B^{AB} in the same RBS spectrum (Eqs. (4.19) and (4.20))

$$\frac{H_A^{AB}}{H_B^{AB}} = \frac{\frac{d\sigma_A}{d\Omega}(E_A)}{\frac{d\sigma_B}{d\Omega}(E_B)} \cdot \frac{N_A^{AB}}{N_B^{AB}} \cdot \frac{[\varepsilon(E_B)]_B^{AB}}{[\varepsilon(E_A)]_B^{AB}}$$

$$= \frac{\frac{d\sigma_A}{d\Omega}(E_A)}{\frac{d\sigma_B}{d\Omega}(E_B)} \cdot \frac{C_A}{1-C_A} \cdot \frac{[\varepsilon(E_B)]_B^{AB}}{[\varepsilon(E_A)]_A^{AB}} \qquad (4.22)$$

ii) from the ratio of the spectra heights due to backscattering from A atoms in the A/B mixture to that due to A atoms in a pure A sample

$$\frac{H_A^{AB}}{H_A^{A}} = C_A \cdot \frac{[\varepsilon(E)]_A^{A}}{[\varepsilon(E)]_A^{AB}} \qquad (4.23)$$

iii) from the ratio of the spectra heights of B in the mixture to that for pure element B

$$\frac{H_B^{AB}}{H_B^{B}} = (1-C_A) \frac{[\varepsilon(E)]_B^{B}}{[\varepsilon(E)]_B^{AB}} \qquad (4.24)$$

In Eqs. (4.23) and (4.24) two different spectra are involved - for pure A (or B) and for the mixture. These different spectra must be taken under identical conditions e.g. analysing beam current and detector dead time, otherwise the spectra heights will carry different experimental errors into the calculated concentrations. In Eq. (4.22), because only one spectrum is involved, identical errors will exist in the yields of A or of

B. In the three methods for calculating concentration, the only unknown in the expressions is the concentration C_A. Because the stopping cross-sections also depend on C_A (Eq. (4.21)), the only way to obtain C_A is by an iterative procedure, usually by a computer algorithm which is discussed in Chapter 5. Fig. 4.5 shows an RBS spectrum of a diffused Ni/Pd couple and the concentration profiles obtained using Eq. (4.22) above.

4.3.2 Depth scales

According to Eq. (4.11) the difference in the detected energy of particles backscattering from the surface and those backscattering from the depth x is

$$\Delta E = [\varepsilon_0] \cdot Nx \quad .$$

Thus the depth scale for A atom distribution is

$$x_A = \delta E_A / [\varepsilon]_A^{AB} \cdot N^{AB} \tag{4.25}$$

and for B atoms

$$x_B = \delta E_B / [\varepsilon]_B^{AB} \cdot N^{AB} \tag{4.26}$$

where δE_A and δE_B are energy/channel associated with A and B respectively.

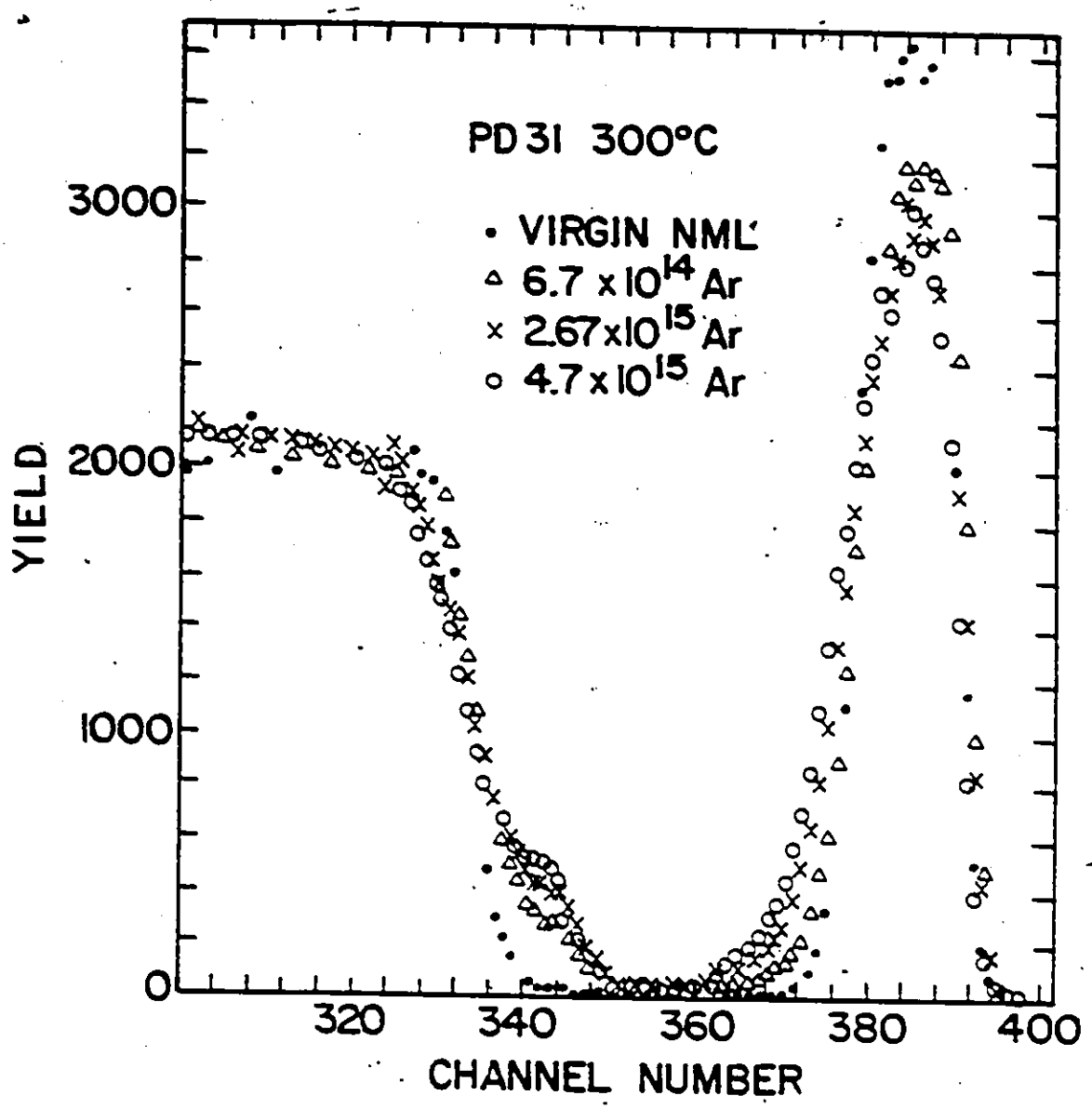

Fig. 4.5a: RBS spectra before and after 120 KeV Ar^+ irradiation at 673k

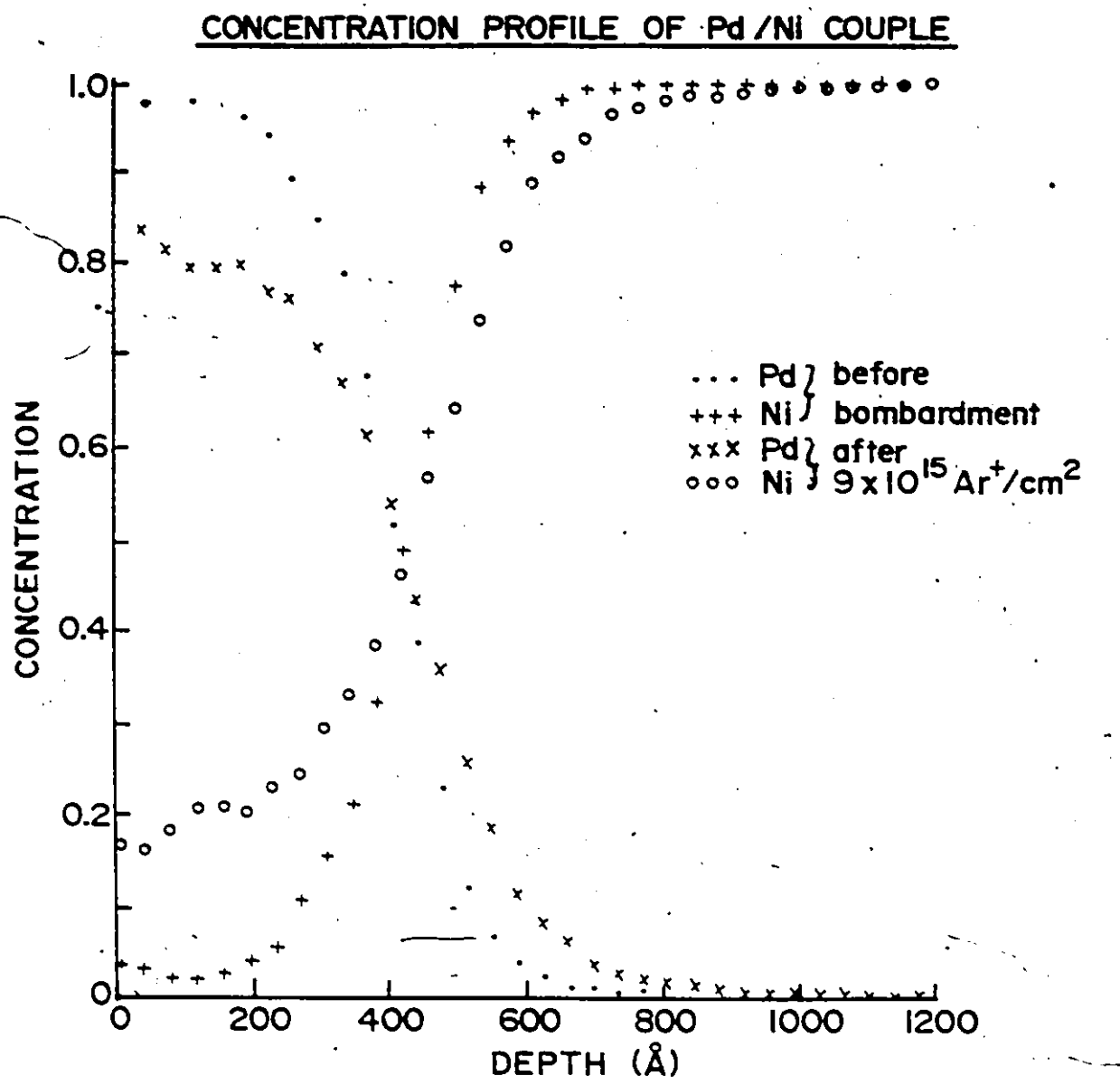

Fig. 4.5: Concentration profile of a Ni/Pd couple obtained with Eq. (4.22).

4.4 Electrochemical Polarization Technique

When a metallic material is introduced into an aqueous media, it will assume a certain potential called its rest potential. At the rest potential the rates of the anodic and cathodic processes are equal, and the electrode is said to be at equilibrium. If this equilibrium is disturbed, for example by the application of an external potential or current, the electrode is said to be polarized. If the impressed source is negative, the anodic sites on the electrode gradually become neutralized and the cathodic process finally dominates and the electrode is said to be cathodically polarized. On the other hand if the impressed source is positive, the anodic process will prevail and the electrode becomes anodically polarized.

Many different polarization techniques exist for the study of electrode kinetics, including steady state and non-steady state methods. In this work, the steady state potentiostatic technique was employed. A potentiostat is an electronic device which is capable of maintaining an electrode potential at a preset constant value simply by adjusting the current between the test and the counter electrodes to a value necessary to maintain the preset electrode potential. To obtain a current-voltage curve, the potential of the electrode is varied linearly with time at a slow rate ($\sim$ 2 mV/sec) over the desired potential range and the current at desired potential is measured.

In water electrolysis (from caustic solutions), hydrogen evolution occurs at the cathode by an overall reaction of the form

$$2H_2O + 2e^- \rightarrow H_2 + 2OH^-$$

The rate at which this evolution, or any electrochemical reaction, proceeds is determined by the current density. The measured current density is composed of both the anodic and cathodic currents since a cathodic reaction cannot occur in isolation and requires an anodic reaction to sustain it. Anodic current is considered positive while cathodic current is considered negative.

4:4.1 Exchange current density, i_0, and overpotential, η .

The exchange current density is the rate of the oxidation or reduction reactions when the electrode is at equilibrium potential. Under these conditions, no net current exists, and i_0 expresses the rate at which a particular process proceeds under equilibrium conditions. The electrode potential when the net current is zero is called the equilibrium potential, E_{rev}, of the electrode for the reaction.

When an external current or potential is impressed, a net current flows through the cell and the electrode potential differs from the equilibrium value. This difference is called the overpotential, η,

$$\eta = E - E_{rev} \qquad (4.27)$$

and may be regarded as the extra potential necessary to reduce the energy barrier of a process to a value such that the process proceeds at a desired rate. Cathodic processes are associated with negative overpotentials and anodic processes with positive overpotentials. The relationship between the activation overpotential and the total current is given by the Butler-Volmer equation:

$$i = i_0\{\exp \frac{\alpha nF}{RT} - \exp -(1-\alpha) \frac{nF}{RT}\} \qquad (4.28)$$

where i_0 is exchange current density (Amps/cm^2) for the reaction, η is the overpotential (volts), α is a transfer coefficient, R is gas constant T is the temperature (K) and F is the Faraday constant ($\sim$ 96500 Coulombs). The first term in Eq. (4.28) represents the contribution of the anodic process to the total current while the second term represents the cathodic contribution.

When the electrode is cathodically polarized and the overpotential is high, i.e. highly negative overpotentials, then the current is mainly cathodic

$$i = i_0 \exp - \frac{(1-\alpha)nF}{RT} \qquad (4.29)$$

or

$$\eta = \frac{RT}{(1-\alpha)F} \ln i_0 - \frac{RT}{(1-\alpha)F} \ln i$$

or

$$\eta = \frac{2.303RT}{(1-\alpha)F} \log i_0 - \frac{2.303RT}{(1-\alpha)F} \log i \qquad (4.30)$$

This equation can be written as a Tafel type equation

$$\eta = a + b \log i \qquad (4.31)$$

The Tafel parameters

$$a = \frac{2.303RT}{(1-\alpha)F} \log i_0$$

$$b = \frac{2.303RT}{(1-\alpha)F}$$

are characteristic of an electrode reaction. The Tafel slope b is obtained by differentiating Eq. (4.31), i.e.

$$b = \frac{\partial \eta}{\partial \log i} .$$

Consequently the unit of b is mV/decade. A large value of b corresponds, in the case of hydrogen evolution, to vigorous gas evolution. Fig. 4.6 shows a η vs log i plot for a Ni electrode. Experimentally, b is obtained from the slope of the linear portion of the η vs logi plot. The exchange current density i_0 is a very useful parameter for comparing the electrocatalytic activities of different electrode materials for a given reaction and is obtained experimentally by extrapolation of the linear portion of the η vs log i plot to the reversible potential where $\eta = 0$.

4.4.2 Types of overpotential

The rate equation (Eq.4.28) above is valid only for activation-controlled processes. Consequently Eq. (4.30) gives only the activation overpotential. Another source of overpotential in electrode reaction is the finite rate of transport of reactants to, or of products from, the electrode-solution interface. When the rate of material transport to the interface is less than the rate of electrochemical reaction, the concentration at the electrode surface will be less than in the bulk. The resulting diffusion overpotential η_d is given by (Bockris et al.1969)

$$\eta_d = E - E_r = \frac{RT}{nF} \ln\left(1 - \frac{i}{i_L}\right) \qquad (4.32)$$

where i_L is the limiting current density determined by the maximum rate of diffusion of reactants to the electrode, n is the number of electrons involved

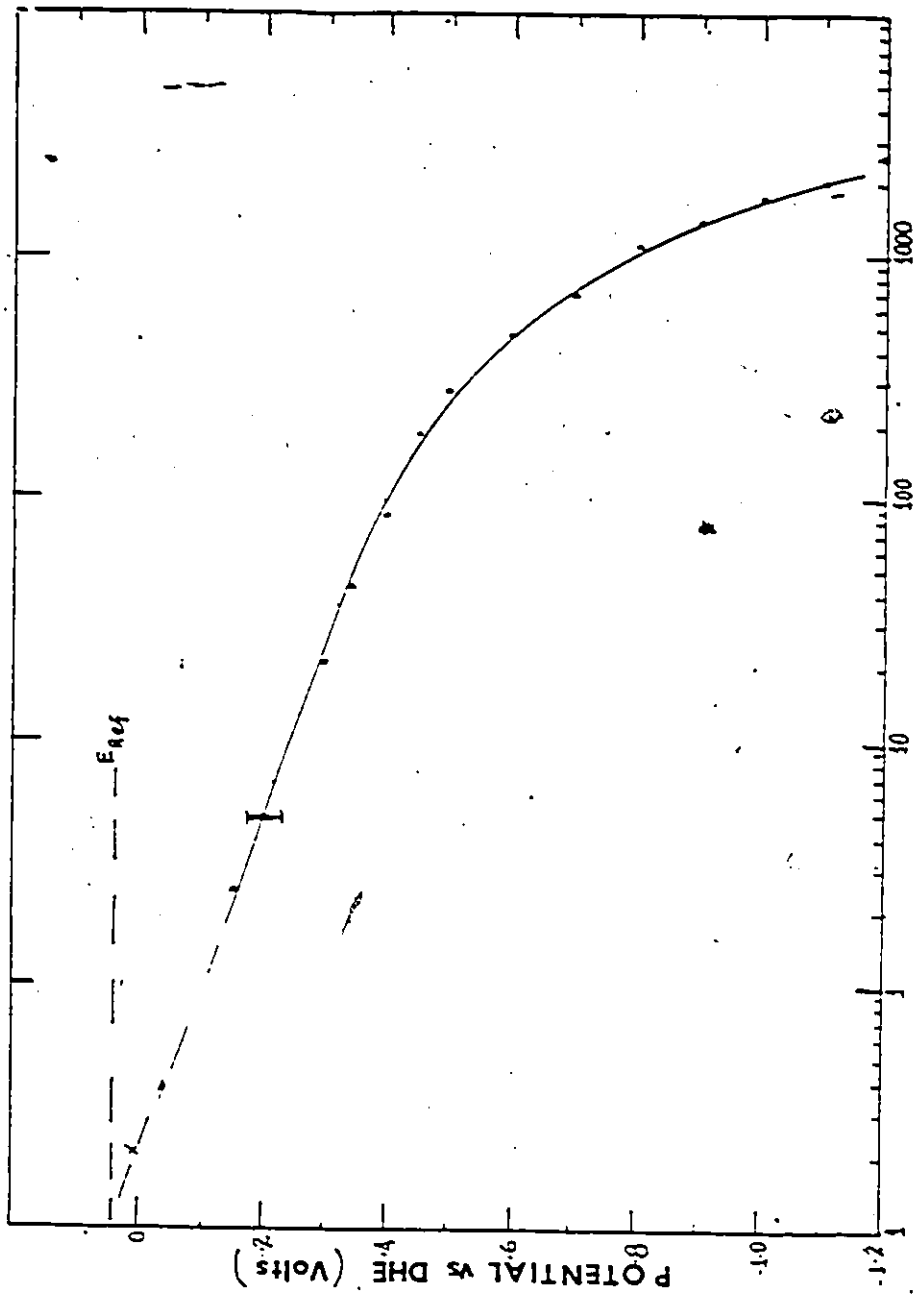

Fig. 4:6 : Overpotential of Ni electrodes for hydrogen evolution in

in the reaction.

An additional contribution to overpotential arises from the solution resistance between the working electrode and the reference electrode. This ohmic overpotential, η_R, is proportional to the current density in a solution and depends on cell configuration. The measured overpotential is then given by

$$\eta = \eta_a + \eta_d + \eta_R \quad --$$

η_d and η_R can be reduced by using solutions of high concentration of reactants, and η_R by minimizing the separation between the working and reference electrodes.

4.4.3 Measurement of overpotential

The measurement of an electrode potential (or overpotential) is made with respect to a reference. By convention, the potential of the hydrogen-hydrogen ion ($2H^+ + 2e^- \Rightarrow H_2$) reaction at standard conditions is arbitrarily set equal to zero and used as reference, since it is relatively easy to establish a reversible hydrogen electrode. Chemically inert elements like Pt (or Pd) serve as excellent electrodes for the reversible hydrogen-hydrogen ion reaction. At different points on the metal, hydrogen ions are reduced to hydrogen gas and hydrogen gas is oxidized to hydrogen ions, the function of the metal being mainly to facilitate electron transfer. The establishment of the reversible potential requires saturation of the solution with hydrogen by bubbling hydrogen gas through it.

The problem of bubbling H_2 through the solution can be avoided if a dynamic hydrogen electrode (DHE) first described by Giner (1964) is used

as reference. The DHE potential is established by passing a small (1 mA/cm^2) constant cathodic current through a 1 cm^2 platinized Pt electrode from a Pt counter electrode. The evolved hydrogen creates a hydrogen electrode whose potential differs only slightly ($\sim$ -40 mV) from the potential of a reversible hydrogen electrode (RHE).

These electrodes are particularly useful as reference electrodes for the hydrogen evolution reaction because identical reactions occur at the working electrode as at the reference electrode:

$$2H_2O + 2e^- \rightarrow H_2 + 2OH^-$$

with electrode potentials given by the Nernst equation

$$E = E^0 - \frac{RT}{2F} \ln \frac{a_{H_2} \cdot a_{OH}^2}{a_{H_2O}} \qquad (4.33)$$

The working electrode potential measured vs DHE therefore does not include the Nernstian effect and gives the reaction overpotential directly.

$$\eta = E \text{ vs DHE}$$

The exchange current density i_0 for the hydrogen evolution reaction on each electrode can be determined if the reversible electrode potential vs DHE reference is known. For the hydrogen evolution reaction the reversible potential E_{RHE} is given by

$$E_{RHE} = |\eta|_{DHE}$$

where η_{DHE} is the overvoltage of the DHE reference electrode at 1 mA/cm^2 as measured vs the RHE.

4.5 General techniques

4.5.1 Auger electron spectroscopy (AES)

A PHI 600 Auger electron spectrometer was used primarily to monitor how clean the interface between evaporated Pd and Ni substrate is since an oxide layer at the interface is known to greatly retard ion beam mixing. The lateral uniformity of some of the mixed samples was also analysed by Auger mapping. In some cases, especially after high temperatures ($\sim 700^{o}C$) mixing where the RBS signals from interdiffused Ni and Pd overlap, the alloy concentration profiles were determined by Auger analysis.

4.5.2 Transmission electron microscopy

A transmission electron microscope (Philips model EM300G) was used principally to determine (1) the microstructure and grain size of the as-evaporated films, (2) the resulting microstructure and grain size following ion mixing and/or thermal annealing and (3) the emergence of fibre texture after ion irradiation and/or annealing. These observations are used to correlate the observed diffusion effects with film grain size.

CHAPTER 5
EXPERIMENTAL TECHNIQUES

In this chapter, the experimental facilities and methods employed in the work reported in this thesis are presented. In section 5.1 the methods of sample preparation for ion beam mixing, transmission electron microscopy (TEM) and electrocatalysis studies are discussed. The ion implantation and RBS facilities and experiments are presented in section 5.2. In section 5.3 the apparatus and the experiments for evaluating the electrocatalytic activities of the ion beam mixed electrodes are given, while in 5.4 the TEM experiments are discussed.

5.1 Samples preparations

The substrates used in this work were polycrystalline and single crystal Ni, sodium chloride crystals and sapphire. The single crystal Ni samples are of (100) orientation and were kindly supplied by Prof. G. Carter (Salford University). The polycrystalline Ni were 99.99% purity Falconbridge Ni rod. The Ni rod $\sim$ 1 cm diameter was cut into discs $\sim$2 mm thick.

The polycrystalline nickel discs were polished with various grades of silicon carbide paper, using water as lubricant. This was followed by polishing on a rotating wheel impregnated with 6 micron diamond abrasive using kerosene as lubricant, and finally with 1 micron diamond paste. The specimen was then washed and cleaned in acetone. The single crystal nickel specimens were supplied polished. Surface damage was removed by polishing

on a vibratory polisher with 1 micron diamond paste, followed by polishing on a selvyt cloth impregnated with 0.3 micron alumina. The specimen was then electropolished in a solution of 60% H_2SO_4 (maintained at 0^oC) at a current density of 0.6 A/cm^2. In some cases the polycrystalline Ni samples were also electropolished prior to evaporation. After electropolishing the samples were washed in distilled water and transferred to a vacuum evaporation chamber. The sodium chloride substrates were cleaved in air and transferred immediately to the evaporation chamber.

The following types of samples were prepared:

i) For the buried Pd marker studies, either polycrystalline nickel or sapphire substrates were used. Samples for these experiments were prepared by sequential vacuum evaporation (without breaking vacuum) of 2.5 nm Pd followed by $\sim$ 100 nm Ni, then $\sim$ 1 n.m. Pd layer and finally an $\sim$ 30 nm Ni overlayer on Ni or sapphire substrates by electron beam heating. The rationale for this sample configuration is discussed in section 6.1.

ii) Samples for the ion beam mixing of Ni/Pd bilayers were prepared either on Ni single crystals with (100) orientation normal to the surface or on polycrystalline Ni substrates. The polycrystalline Ni samples were discs $\sim$ 1 cm diameter and $\sim$ 2 mm thick. On to these substrates were evaporated $\sim$ 100 nm Ni and finally 40 nm Pd overlayer by electron beam heating without breaking vacuum.

iii) Samples for TEM studies were prepared on air-cleaved NaCl crystals as described for the Ni/Pd bilayers. The Ni and Pd evaporated layers were 30 nm and 30 nm respectively.

iv) For the catalysis studies, samples were used either as prepared for the Ni/Pd bilayer case or after they had been subjected to ion irradiation.

The base pressure in the evaporation chamber was $\sim 10^{-7}$ torr and rose to $\sim 3\times10^{-7}$ torr during evaporation. Typical evaporation rates were $\sim$ 10 nm/min and evaporated thicknesses were determined by a quartz crystal thickness monitor. Absolute evaporated thicknesses (for films evaporated on sapphire) were determined by the RBS technique.

5.2 Ion beam mixing and RBS experiments

5.2.1 Ion implantation and RBS apparatus

The accelerator facility at McMaster for ion implantation and in-situ RBS analysis study is shown schematically in Fig. 5.1. It consists of a 150 kV ion implanter coupled to a 3.5 MV Van de Graaff accelerator. Ion beams from either accelerator can be directed to the target through the use of a common analysing magnet.

The ion implanter is a Texas Nuclear Corporation Model 9509 Cockroft-Walton neutron generator which was modified to accomodate a Danfysik 911A 'Universal' ion source suitable for producing ions from gaseous and solid sources. The analyzed ion mixing beam is collimated by a pair of apertures $\sim$ 1.3 m apart - a 2 mm wide aperture near the magnet and a 7 mm wide aperture near the target. To obtain a uniform implant the ion beam was rastered across the 7 mm aperture by two pairs of x-y electrostatic plates.

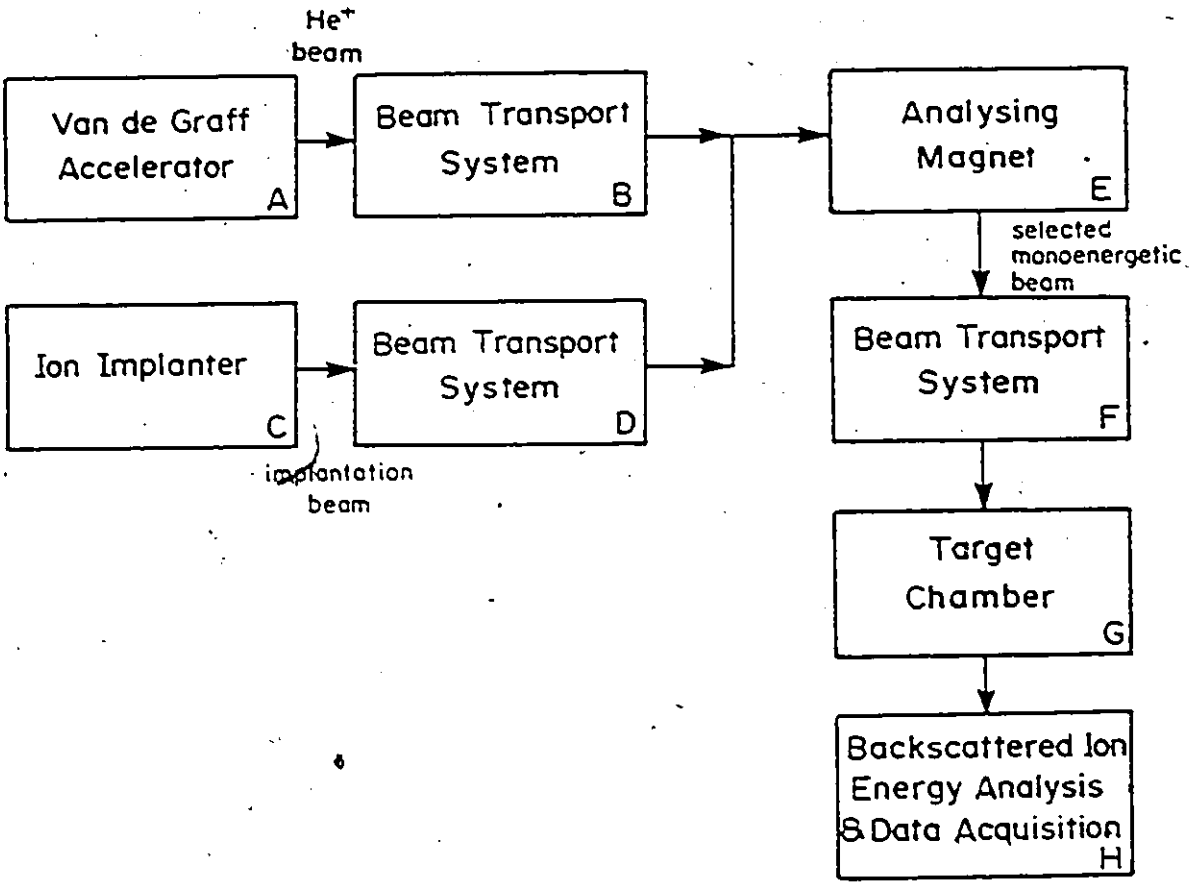

Fig. 5.1: Block diagram showing the ion implantation/ion beam analysis facility.

The ion beam mixed samples were analysed by RBS using 2 - 2.5 MeV He^+ ions from the Van der Graaff accelerator. The analysing beam was collimated using a pair of 0.75 mm diameter apertures. Typical analysing beam current densities were 2 - 5 nA/mm^2 to ensure that the detector dead time was maintained $\leq$ 5%.

5.2.2 Target chamber and data acquisition

The target chamber and data acquisition facilities have been described in detail by Walker (1977) and Parikh (1985). A schematic of the interior of the chamber is shown in Fig. 5.2. The target holder is mounted on a two-axis goniometer which enables the target to be tilted with respect to the beam. The target holder itself is in the form of a wedge whose normal is at 30^o from the beam normal when the goniometer tilt angle is 0^o. For normal beam incidence analysis, the goniometer is then tilted 30^o away from the beam normal to make the beam and sample normals coincident. This target holder arrangement enables improvement in depth resolution to be achieved simply by tilting the target with respect to the beam normal. Tilt angles of 45^o and 60^o were used in this work. For studies at elevated temperatures a heating element which is electrically isolated from the target through an isolation transformer is screwed to the target holder head. Power is supplied to the heater by a variac through the transformer. Target temperatures were measured with a chromel-alumel thermocouple thermally connected to (but electrically isolated from) the target holder head. Target tempera-

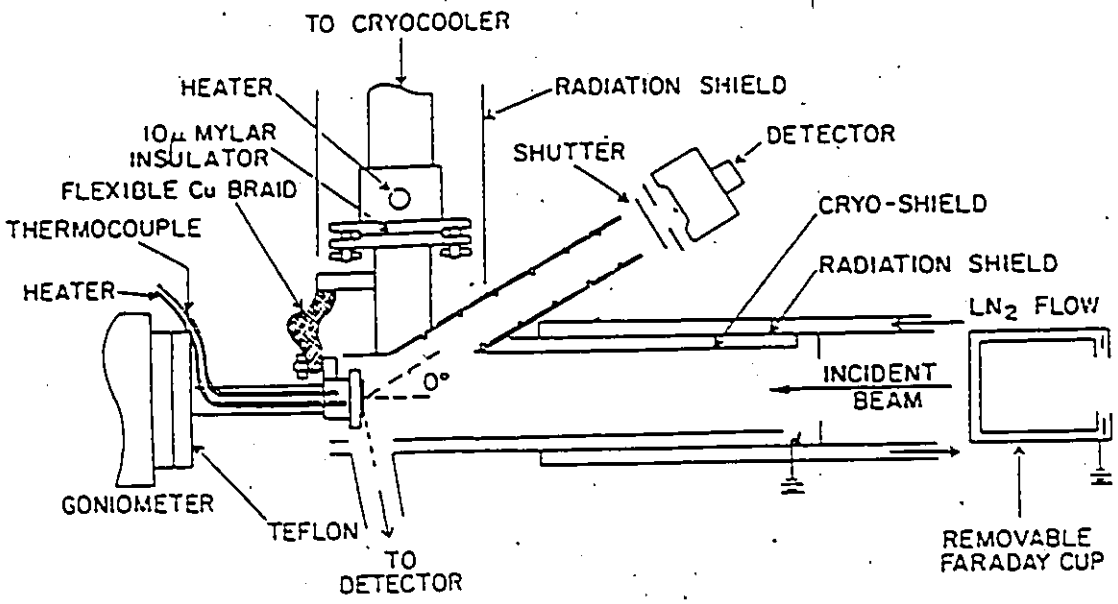

Fig. 5.2: Schematic of the target chamber.

tures were controllable to $\pm 2^{o}C$.

For low temperature studies the target was connected to a cryocooler by a flexible copper braid surrounded by a copper inner shield which is also connected to the cryocooler. For studies other than low temperatures only the inner shield surrounding the target was connected to the cryocooler. Both the inner shield and target were electrically isolated from the cryocooler by a 10 μm Mylar film. A second shield cooled by liquid nitrogen enclosed the inner shield. The inner cold shield operates at $\sim$ 20K and acts as a cryopump to reduce the effective pressure near the target to $< 10^{-10}$ Torr since the partial pressure of all gases except H_2, He and Ne is less than 10^{-10} Torr at this temperature. Loss of secondary electrons was suppressed by applying a -220 V voltage to a metal ring located at the beam entrance to the inner shield and 200 V between the target and the inner shield with target as positive terminal. Integrated total target currents were measured by summing the currents on the inner shield and target.

In the RBS analysis of the inter-diffused profiles the backscattered He^{+} particles were detected with a surface barrier detector (FWHM = 15 keV) situated at a scattering angle of 160^{o}. The detector was protected from radiation damage during heavy ion irradiation of targets by an externally controlled shutter. Figure 5.3 shows a block diagram of the data acquisition system. A current integrator (Ortec model 435) was used to measure the beam current on target (or on the Faraday cup during set-up). A timer/scaler (Ortec model 771) was used as a control unit for the data acquisition.

The backscattered He particles which reach the detector produce signals (pulses) which are proportional to the particle energies. Each

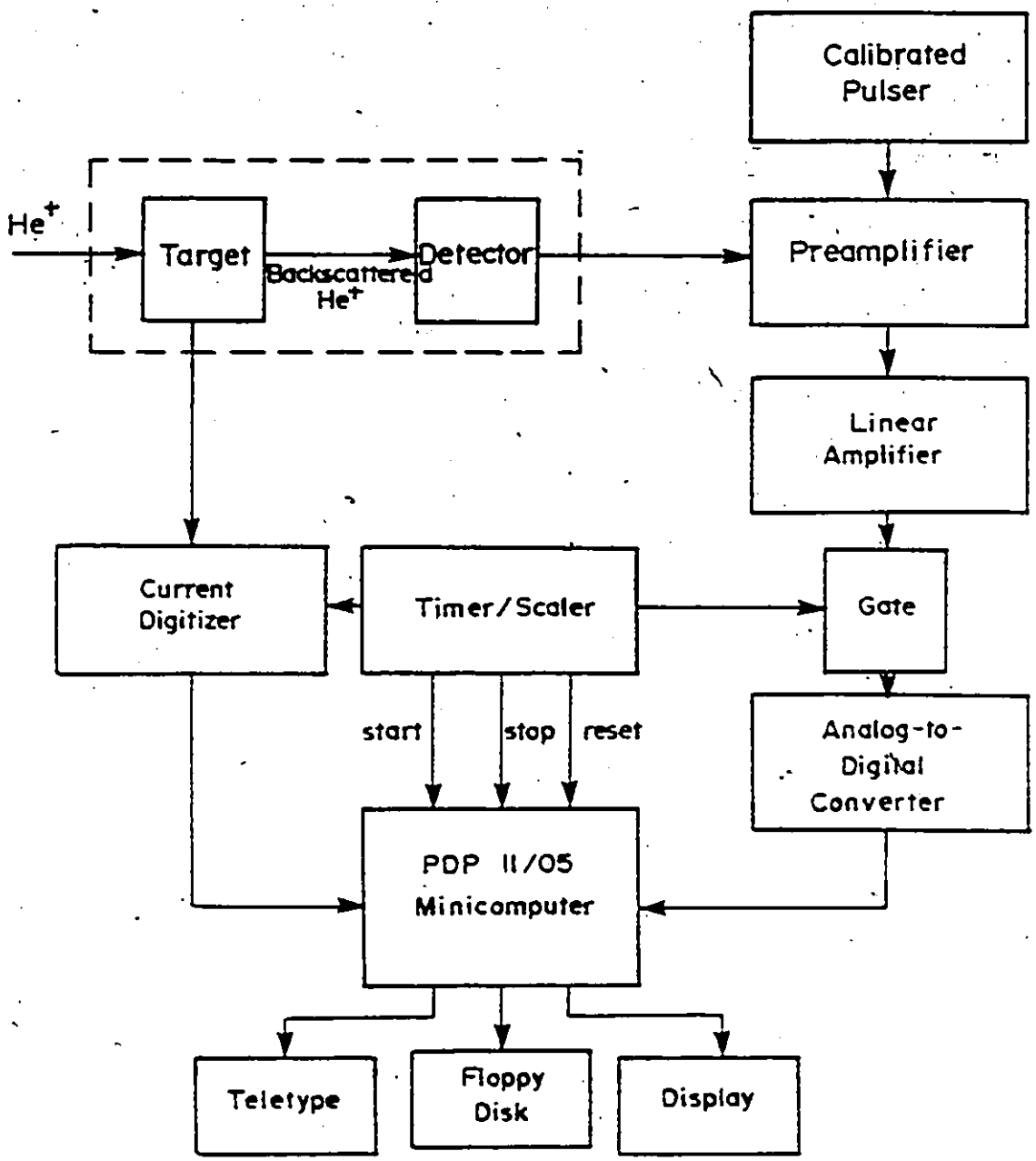

Fig. 5.3: A block diagram of the data acquisition system.

pulse then passes through a pre-amplifier (Canberra model 1408) and a linear amplifier (Ortec model 572) and is digitized using a Northern Scientific (model 8192) ADC which is connected to a PDP 11/05 computer programmed for pulse height analysis.

5.2.4 RBS Parameters

i) Detector solid angle, $\Delta\Omega$

The total number of counts in the RBS signal of a thin film of heavy impurity is given by

$$H = N\Delta x \frac{d\sigma}{d\Omega} \cdot \Delta\Omega \cdot Q \qquad (5.1)$$

where $N\Delta x$ is the areal density of target, $\Delta\Omega$ is the solid angle subtended at the centre of the target by the detector, Q is the total number of He ions hitting the target and $\frac{d\sigma}{d\Omega}$ is the differential cross-section for backscattering. $\Delta\Omega$ was determined geometrically. Additionally, determination of $\Delta\Omega$ was obtained by RBS analysis of a CRNL calibrated standard sample of silicon implanted with 5×10^{15} $(N\Delta X)$ Bi-cm^2. Then use of Eq. (5.1) gives $\Delta\Omega$ since H is determined from the RBS spectrum. Q, the total number of incident He^+ particles is measured and $\frac{d\sigma}{d\Omega}$, the differential scattering cross-section for He on Bi was taken from the tabulation of Chu et al. (1978). The solid angle for the 160^o detector was so determined to be 2.61×10^{-3} Str.

ii) Implantation dose

This can be determined from a knowledge of the total integrated charge on the target over the time of implant and the implanted area. For the set of apertures used, the implanted area was calibrated by implanting

a dose of Bi into a silicon target, analysing with RBS and deducing the dose per unit area from Eq. (5.1) with the aid of the calibrated detector geometry. The implant also changes the surface color of Si so that the implanted area can be measured geometrically to confirm the calculated implanted area. For Ar^+ irradiations, the ion doses were determined from the total integrated charge. In the case of Kr^+ implants the doses were determined also from the Kr peak in the backscattering spectrum to confirm the total integrated beam current and implant area.

iii) Analysing beam energy calibration

The energy of the incident beam was calculated from a knowledge of the gain (keV/channel) of the electronics and the detected energy (corrected for detector dead layer loss ≈ 30 KeV) of the particles backscattering from surface atoms. The gain of the ADC was determined by acquiring an energy spectrum from a precalibrated pulser (Ortec model 812) at various known energies and noting the channel position of each energy. The pulser was itself calibrated with respect to the detection system by acquiring a spectrum of alpha particles of known energies - 5.486, 5.443 and 5.389 MeV - emitted by an ^{241}Am source and normalizing the pulser output to match these energies.

iv) Stopping cross-section for helium

The semi-empirical values for the stopping cross-section ε ($eV/10^{15}$ atoms-cm^2) tabulated by Chu et al. (1978) were used in this work. Linear additivity of ε (Bragg's rule) was assumed in computing ε for the Ni/Pd alloys.

5.2.4 Ion Beam Mixing Experiments

i) Pd Marker Spreading

Samples for these experiments were prepared by sequential evaporation (without breaking vacuum) of 5 nm Pd followed by 100 nm Ni layer, then 1 nm Pd and finally 30 nm Ni overlayer, on polycrystalline Ni or sapphire substrates by electron beam heating. The base pressure in the evaporation chamber was $\sim 10^{-7}$ torr and rose to $\sim 3\times10^{-7}$ torr during evaporation. A schematic of the sample configuration is shown in Fig. 5.4. The deeper Pd marker is basically a reference marker and serves two main functions:

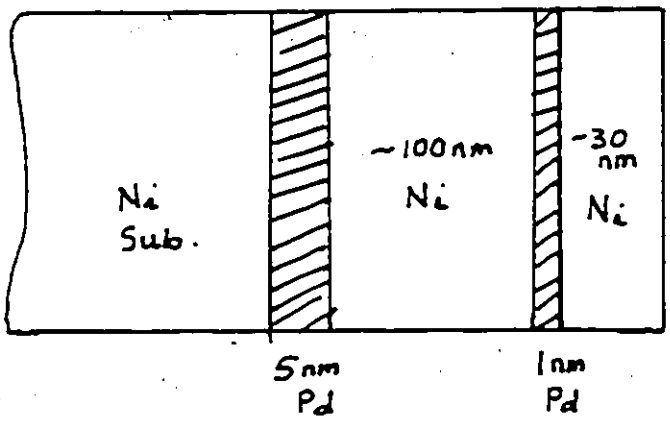

Fig. 5.4: Schematic of the sample confirugration used in the marker spreading experiments.

a) by measuring the separation between the peaks of both markers, the net shift, due to ion bombardment of the shallow marker, is separated from spurious effects such as beam energy shifts during the experiment, sputtering, etc.

b) by monitoring the peak width of the deep marker, the impurity spreading attributable to purely thermal effects is obtained since this marker is located well beyond the range of the bombarding ions.

The mixing of thin Pd markers in Ni was induced by 120 KeV Ar^+ and 145 KeV Kr^+ irradiations. Ion doses ranged from 0.2-4x10^{16} ions cm^{-2} with a dose rate of $\sim$ 3x10^{12} ions cm^{-2} sec^{-1}. Implantation temperatures ranged from 40 to 573K.

ii) Mixing of Ni/Pd Bilayer Samples

The mixing was induced by 120 KeV irradiation with doses ranging from 0.5 - 4x10^{16} ions cm^{-2} and dose rates of $\sim$ 0.6 and 5.0x10^{12} ions cm^{-2} sec^{-1}. Irradiation temperatures ranged from 298K to 673K. Intermixing resulting from pure thermal effects in this temperature range were also measured.

5.3 Polarization Apparatus and Measurements

5.3.1 Electrolysis Cell

The 3-compartment electrolysis cell used in this work is shown in Fig. 5.5. The main cell is a one-litre teflon beaker and contains the hot (30 wt % KOH) electrolyte and the test electrode (cathode). The test electrode is embedded in teflon so that the active areas of the electrode

are well defined. The beaker is equipped with a teflon cover to minimize evaporation losses and contamination from the environment. Appropriate ports are provided on the cover for gas escape and electrical leads.

The second compartment contains a Pt gauze counter electrode (anode). This compartment (completely sealed at the bottom) is equipped with a 1-cm diameter capillary connection to the main cell. This capillary opening is several cm above the level of the test electrode. This arrangement minimizes the mixing of electrolysis products and contamination of the test electrode. The third compartment, which is equipped with a 2 mm capillary connection to the main cell, contains the DHE reference. The reference electrode used in this work is the dynamic hydrogen electrode (DHE) which has been described by Giner (1964). A current of 1 mA/cm^2 is passed between the Pt gauze counter electrode and the DHE reference(C_{Ref}). The potential between C_{Ref} and a reversible H_2 electrode (1 cm^2 platinized Pt), R, is measured. This dynamic cathode potential is always small, $\sim$ 0.040 eV.

The solution was made from 180 gm of analar grade Baker potassium hydroxide pellets and 420 mls doubly-distilled water to make 30 wt % solution. The 30 wt % solution was used because the electrolyte conductivity is maximum at 30 wt % and consequently ohmic losses in solution are expected to be minimum.

The cell is brought to the operating temperature (80^oC) in an oil bath equipped with an oil immersion heater. The oil is circulated in the bath by an electric stirrer and stirring of the electrolyte occurs by convection. The bath temperature is controllable to $\pm 2^oC$.

5.3.2 Polarization Apparatus

The electrodes were polarized using a Princeton Applied Research Corporation (Model 173) potentiostat with a universal programmer (Model 175) in potential control mode. The resulting cell currents were recorded on an x-y chart recorder (PARC model RE0089). For the polarization of the DHE, a stabilized current source (Hewlett-Packard hp model 6186B) was used. The reference potential was measured with an hp (model 3465B) digital voltmeter with 20 MΩ input impedance. This potential is measured to ±2 mV.

5.3.3 Solution, cell and electrode preparation

1) Solution: 800 ml of the 30 wt % solution were placed in a teflon beaker and cleaned by pre-electrolysis. A Pt wire ∿ 6 cm long was used as cathode and a large area Pt gauze (in a second compartment as anode. The cathode was set to 1 A/cm^2 outside the cell before introduction into the solution. Each day the cathode was removed from solution, cleaned in aqua regia, doubly distilled water and hot flame. Doubly distilled water is added to the cell to compensate for evaporation losses. After ∿ 5 days of pre-electrolysis, no further black deposit on the Pt wire cathode was visible, but pre-electrolysis was continued for an additional 10 days.

2) Cell and counter electrode

The main cell as well as the counter and reference electrode compartments and the test electrode holder were scrubbed with aqua regia, washed thoroughly in doubly distilled water and rinsed in pre-

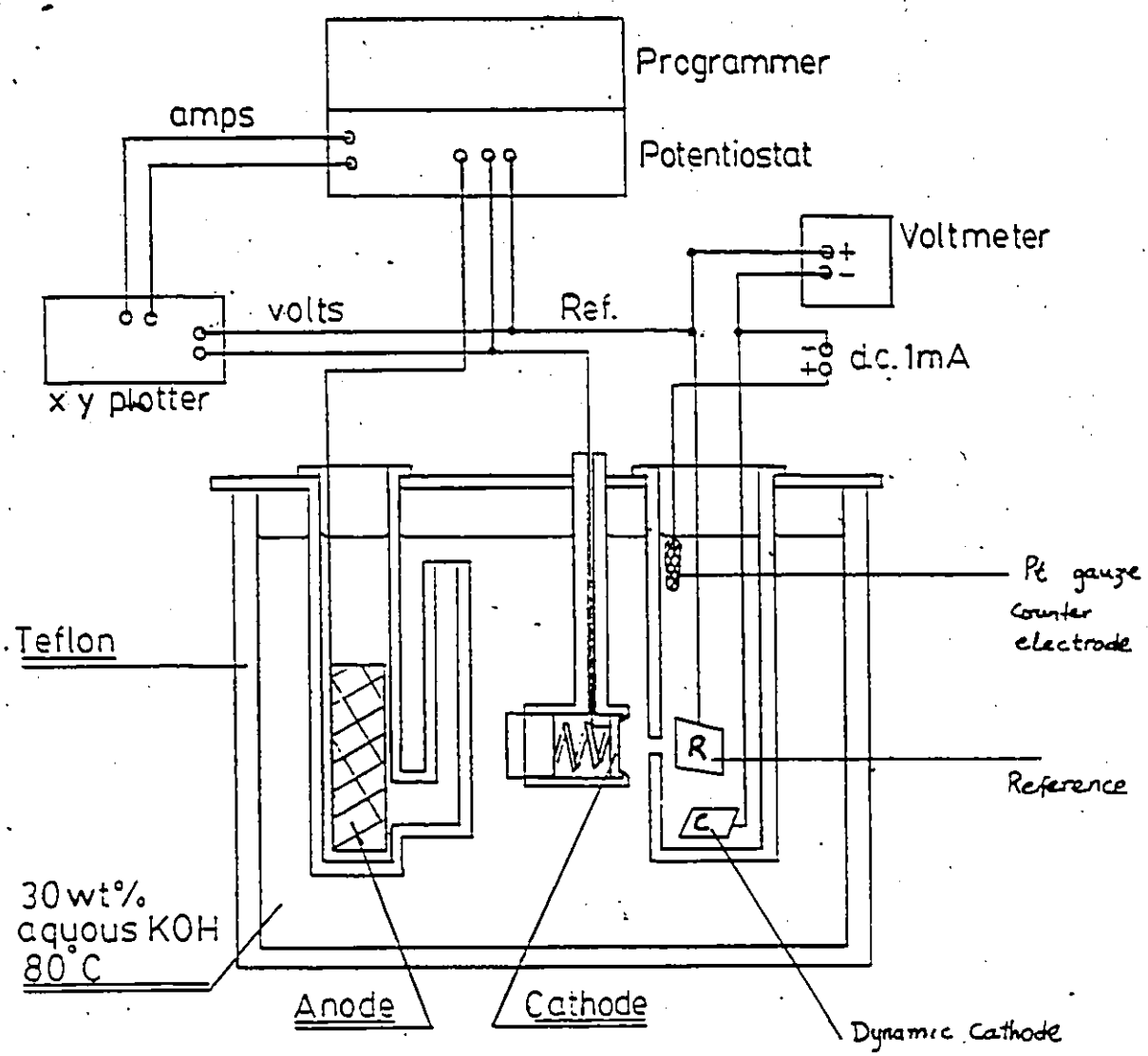

Fig. 5.5: Schematic of the electrolysis cell employed for the electrochemical polarization studies.

electrolysed KOH solution. The Pt gauze counter electrode was also treated.

2) Reference electrodes

The reference electrodes were always maintained moist in a solution of pre-electrolysed KOH. Electrical contacts with all the electrodes were made by spot welding Pt wire leads to the electrodes.

5.3.4 Current-Potential Measurements

The test cathode was biased to -1.3 V (with a Heathkit regulated power supply) outside the cell and then introduced into the solution. The potentiostat was then connected to the cell and the Heathkit disconnected. The potential was held at -1.3 V until the current became steady (after ~ 10 minutes). The current-potential curve for the first positive-going sweep (-1.3 V → 0) was then measured. The potential sweep rate used was 2 mV/sec. At the desired potential, the potential is held constant and the steady-state current measured. The negative-going sweeps were measured in the same manner. The reference potential was monitored throughout the measurements and its value was approximately constant at 40±5 mV.

Before each day's measurements it was necessary to recondition the reference electrodes. This is done by passing a much larger current (~ 10 mA/cm^2) than the normal 1 mA/cm^2 for a few minutes. This is necessary to establish a reversible hydrogen electrode at the electrode marked R in Fig. 5.5.

All the currents and potentials reported in this work are as measured. No corrections for iR drops were applied. The potentials are known to better than ±20 mV and the measured currents to ±2 mA at higher current densities and ±0.1 mA at low current densities.

CHAPTER 6

RESULTS AND DISCUSSIONS

This chapter is divided into four main sections. In section 6.1, the results of the spreading of thin buried Pd markers in Ni are given including the effects of ion species, ion dose and temperature. In section 6.2 results of the intermixing that occur following the annealing and ion bombardment of Ni/Pd bilayer couples are described. This description includes the role of grain boundary diffusion effects and their contribution to the observed mixing. Section 6.3 summarizes the TEM observations on the ion mixed Ni/Pd films, while in section 6.4 the electrocatalytic properties of the ion-beam mixed Ni/Pd couples for the H_2-evolution reaction in $\sim$ 6N KOH are given.

6.1 SPREADING OF Pd MARKERS IN Ni

As pointed out in section 3, the experimentally observed mixing may be due to various contributions. The transport of atoms set into motion via the collision cascade is one mechanism which must play a role, and is probably dominant at the temperatures where point defects are immobile. At higher temperatures, where the mixing increases with temperature, a radiation-enhanced diffusion mechanism is usually invoked. In addition chemical driving forces may be important especially in the compound-forming systems.

In order to examine both the nature of ion-beam mixing in the Ni/Pd system and the relevance of the various mixing mechanisms, the ion-beam induced spreading of thin Pd markers in Ni has been studied both as a function of ion dose ($1\text{-}30\times10^{15}$ cm^{-2}) and temperature (40-573K) with

120 KeV Ar^+ and 145 KeV Kr^+ ions. The dose rate during implantation was maintained constant at $\sim 3 \times 10^{12}$ ions cm^{-2} sec^{-1}.

Backscattering analyses were conducted with MeV He^+ ions. For the Ar^+-bombarded samples 2.0 MeV He^+ ions were used while 2.5 MeV He^+ ions were employed in the case of the Kr^+ ion bombarded samples. The higher energy He^+ ion is necessary to resolve the Kr peak signal from the shallow Pd marker signal. Implanted doses of Kr atoms were determined from the area of the Kr peak in the backscattering spectrum and checked against the total integrated beam currents and implant area. The results of the two techniques differed randomly by up to 10%. Since the signal from the Ar atoms could not be resolved from the Ni signal, the Ar doses were determined from the total integrated currents only.

To obtain good counting statistics in the marker signal, a He^+ dose of 8 μC was used. Shafer (1977) has shown that He^+ doses of 50-60 μC had no measurable damage effect on single crystal Fe, thus 8 μC doses of He^+ are not expected to contribute much to Pd marker spreading in Ni. Typical analyzing He^+ beam currents were 2-4 nA to ensure that the detector dead time was maintained at $\leq$ 5%.

6.1.1 Results

The Pd marker profiles measured by means of MeV He^+ backscattering were, in all cases, Gaussian before heavy ion irradiation and, with a few exceptions at very high doses, they were also Gaussian after irradiation. Fig. 6.1 shows a typical RBS spectrum for an unirradiated sample with polycrystalline Ni as substrate. The peak at channel 480 is the signal from the shallow Pd marker. The small dip in the RBS signal

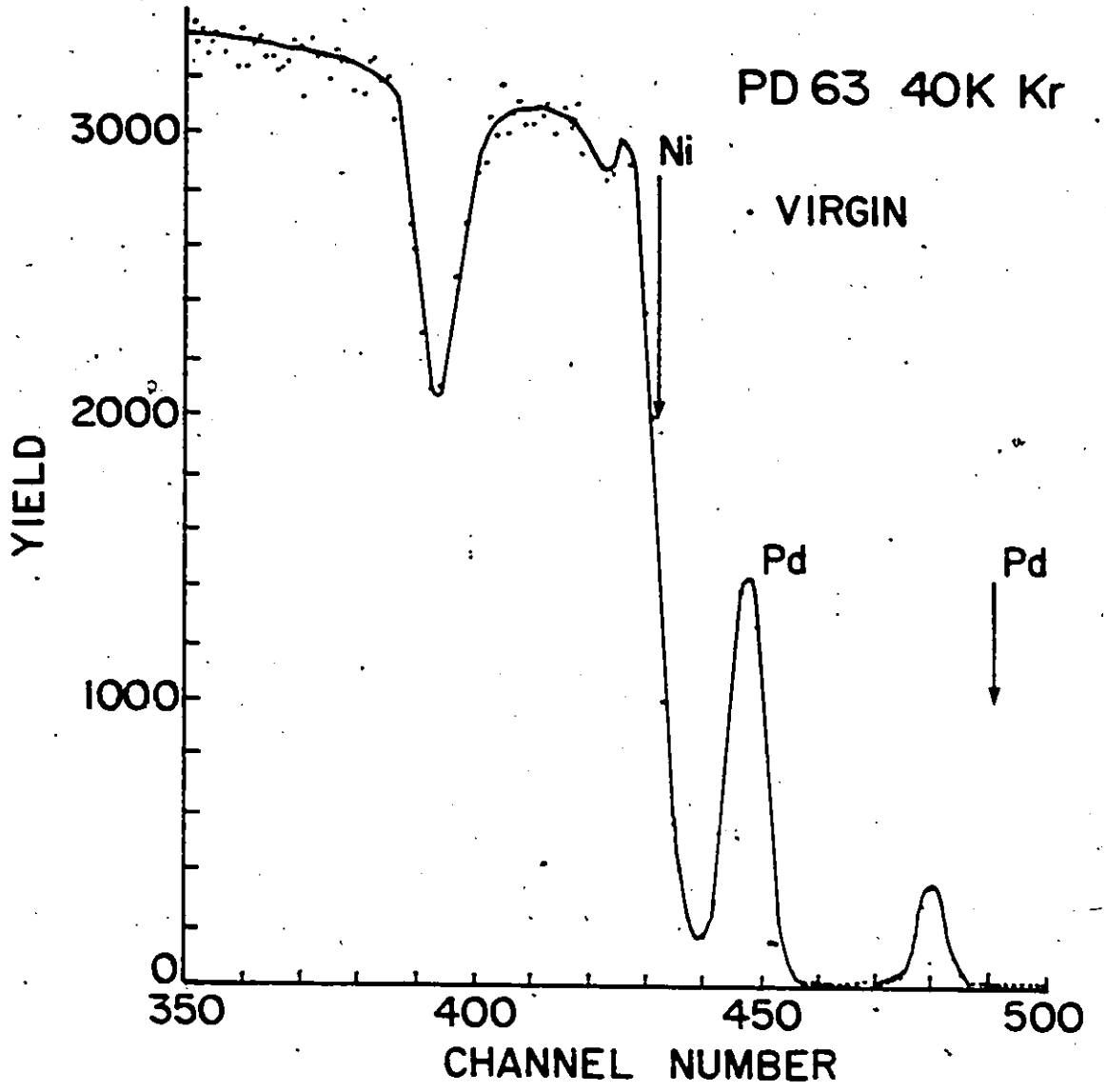

Fig. 6.1: Typical RBS spectrum of an unirradiated sample with polycrystalline Ni as substrate.

around channel 423 indicates the depth at which the shallow marker was located in Ni, and the major dip around channel 393 indicates the depth at which the deeper marker was located. The arrows indicate the channels where the signals from surface Pd and Ni atoms would appear. In this particular case the gain of the electronic system was 4.4 KeV/chan ($\sim$ 3.6 nm/channel). Thus the thickness of the shallow Pd marker (assuming bulk density $\sim 9.14 \times 10^{22}$ atom cm^{-3}) is $\sim$ 0.9 nm and is buried $\sim$ 30 nm in Ni. The deeper marker is $\sim$ 5 nm thick and is buried $\sim$ 140 nm beneath the surface.

Since the Pd marker signals are almost invariably Gaussian, the peak widths were determined by fitting Gaussian shaped curves to the data using least squares methods through a computer algorithm. Fig. 6.2 shows the results of such procedure for the unirradiated sample of Fig. 6.1 and the same sample after bombardment with 6.8×10^{15} Kr^+ ions cm^{-2} at 40K. The continuous curves are the Gaussian fits to the data.

The original width of the marker distribution together with the broadening due to the response function of the detector and the electronics system, and the He^+ ion straggling was found from the measured width of the unirradiated profile. The increase in the variance of the marker profile that may be due to ion mixing was calculated by subtracting in quadrature the variance before mixing from the variance after mixing:

$$\Delta^2 = \Omega^2_{post} - \Omega^2_{pre}$$

where Ω_{post} is the variance after ion bombardment, and Ω^2_{pre} is the variance of the unirradiated profile. The net increase in variances

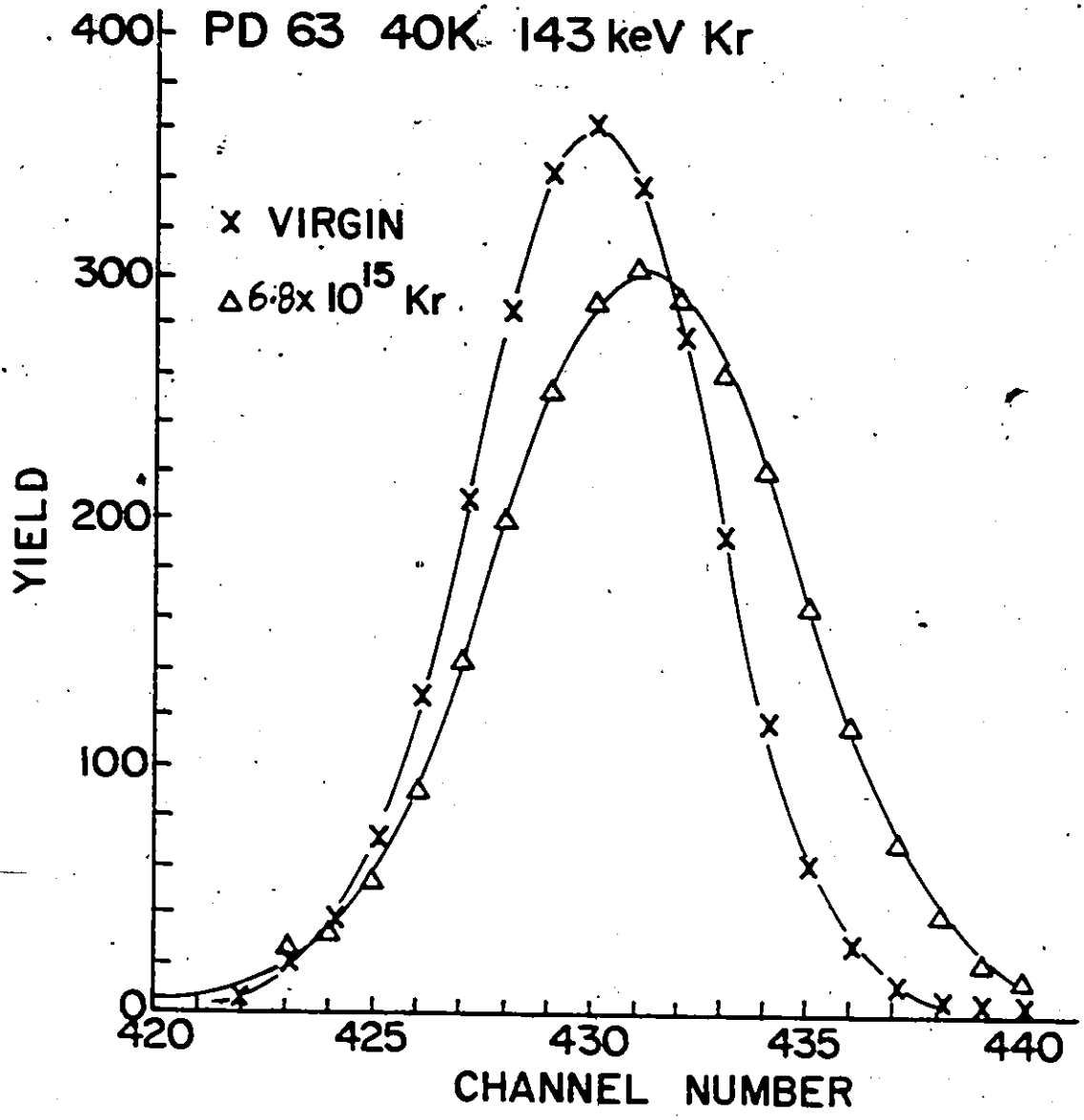

Fig. 6.2: RBS spectra of buried Pd marker before (birgin) and after irradiation at 40K with 6.8×10^{15} cm^{-2} of 145 KeV Kr^{+} ions.

Δ^2 (channel^2) for the broadening of the marker were converted to energy variances, and then to depth $\Delta\sigma^2$ via

$$\Delta\sigma^2 = \frac{\Delta^2(\Delta E)^2}{(N[\varepsilon_0]^{Ni}_{Pd})^2} \qquad (6.3)$$

where N is the atomic number density for Ni (9.14×10^{22} cm^{-3}), ΔE is the energy/channel of the detection system and $[\varepsilon_0]^{Ni}_{Pd}$ is the stopping cross-section factor for He^+ ion in Ni-Pd alloy. $\Delta\sigma^2$ then is a measure of the intermixing of the Pd marker in Ni resulting from ion bombardment and/or temperature. The uncertainty in this parameter is due to the statistical nature of the data points of the pre- and post-irradiation-profiles.

Figures 6.3(a)-(c) show the Pd profiles for doses ranging from 0-3×10^{16} cm^{-2} typical of samples irradiated with 120 KeV Ar^+ ions at 298K, while Figures 6.4(a)-(c) show typical profiles, at $\sim$ constant Ar^+ ion dose of $\sim 2\times10^{16}$ cm^{-2}, for samples irradiated respectively at 40, 298 and 473K. In these figures, the finite width ($\Delta\sigma_0^2$) of the unirradiated distribution is due to the energy straggling of the analyzing He^+ ions and the finite resolution of the detection system. The small shifts (in the position of the peak heights) between the irradiated and unirradiated spectra are all due to small fluctuations ($\sim$ 4 KeV) in the energy of the incident He^+ beam and also (at high doses) to ion sputtering of the Ni overlayer films. The apparent loss of Pd in some of the spectra (e.g. Fig. 6.3(a)) is due to small fluctuations in counting statistics resulting from slightly different integrated beam currents. In some cases (at high temperatures and high doses), the Pd loss is real

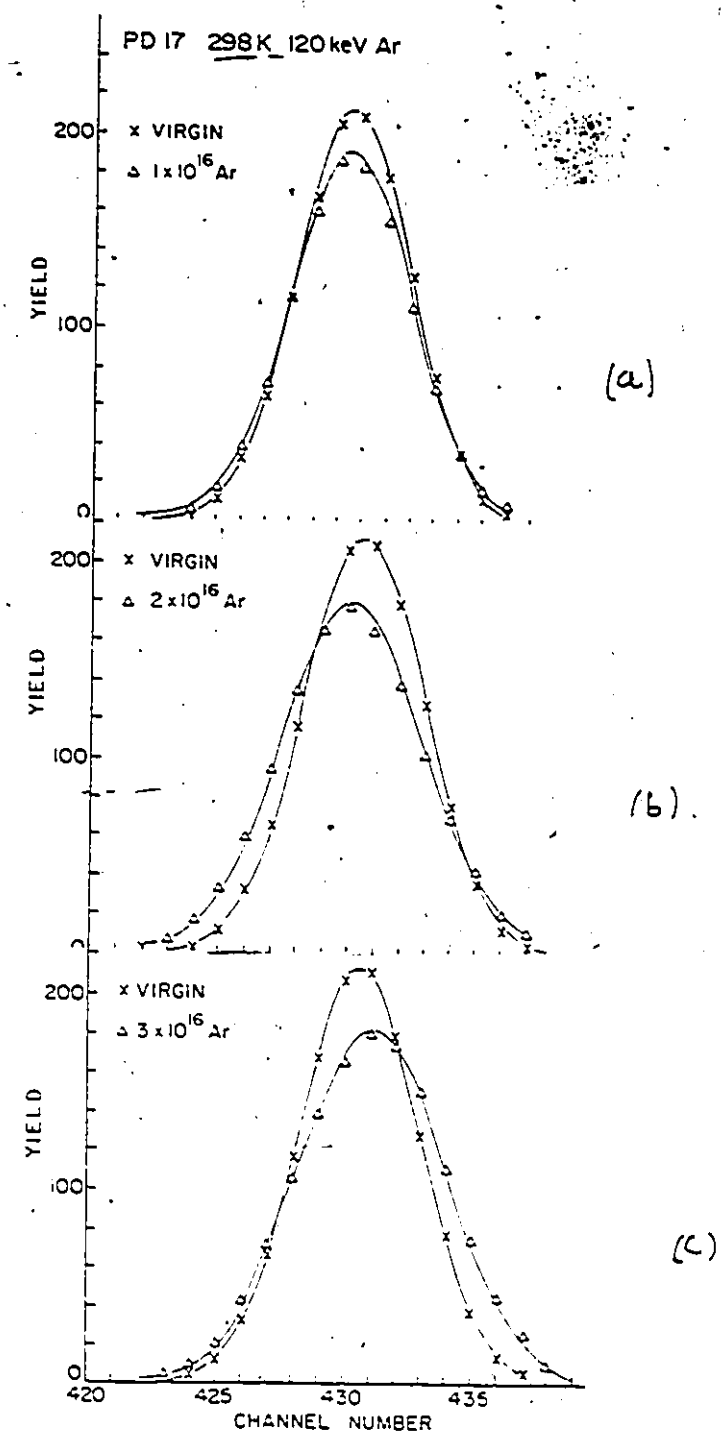

Fig. 6.3: RBS spectrum showing the spreading of Pd in Ni following Ar irradiation
a) $1x10^{16}$ b) $2x10^{16}$ c) $3x10^{16}$ cm^{-2}

and occurs as a consequence of the ion sputtering of Pd that has migrated to the sample surface. Figures 6.5(a)-(c) show similar plots for samples irradiated at 298K to various doses (0-1.1x10^{16} cm^{-2}) of 145 KeV Kr^{+} ions, while Figs. 6.6(a)-(b) show the Pd profiles at 40K and 473K following a dose of $\sim$ 1.1x10^{16} Kr^{+} cm^{-2} respectively. In Table 6.1, the mixing parameter $\Delta\sigma^2$ is tabulated for the two different ions as a function of ion dose and temperature.

6.1.2 Dose Dependence of Mixing

Figure 6.7 shows the measured spreading parameter $\Delta\sigma^2$, following Ar irradiation, plotted as a function of Ar dose at various irradiation temperatures. Figure 6.8 is a similar plot for Kr irradiation. For both types of irradiations, the observed mixing ($\Delta\sigma^2$) exhibits a linear dependence on ion dose, ϕ, over the temperature and dose range examined. This linear dependence on dose suggests a diffusion-like spreading of the Pd marker ($\Delta\sigma \propto \phi^{\frac{1}{2}}$) similar to what is typically observed following thermal treatment.

6.1.3 Ion Dependence of the Mixing Parameter

In Table 6.2 the ratio of the mixing parameter $\Delta\sigma^2_{Kr}/\Delta\sigma^2_{Ar}$ at a constant dose of $\sim$ 1x10^{16} cm^{-2} is tabulated. At 40K, the spreading induced by Kr-irradiation is a factor of 2.2 more than that induced by Ar-irradiation. At higher temperatures, the ratio decreases, probably because of the increased contribution of both thermal and radiation enhanced diffusion effects. In fact at 573K, as will be shown in the next section, pure thermal annealing contribution accounts for more than 50% of the observed mixing. The value of $\Delta\sigma^2_{Kr}/\Delta\sigma^2_{Ar} \sim 2.2$, measured at 40K, is close to the ratio of the deposited damage energies, $F_D(Kr)/F_D(Ar) \sim 2.1$, calculated at the

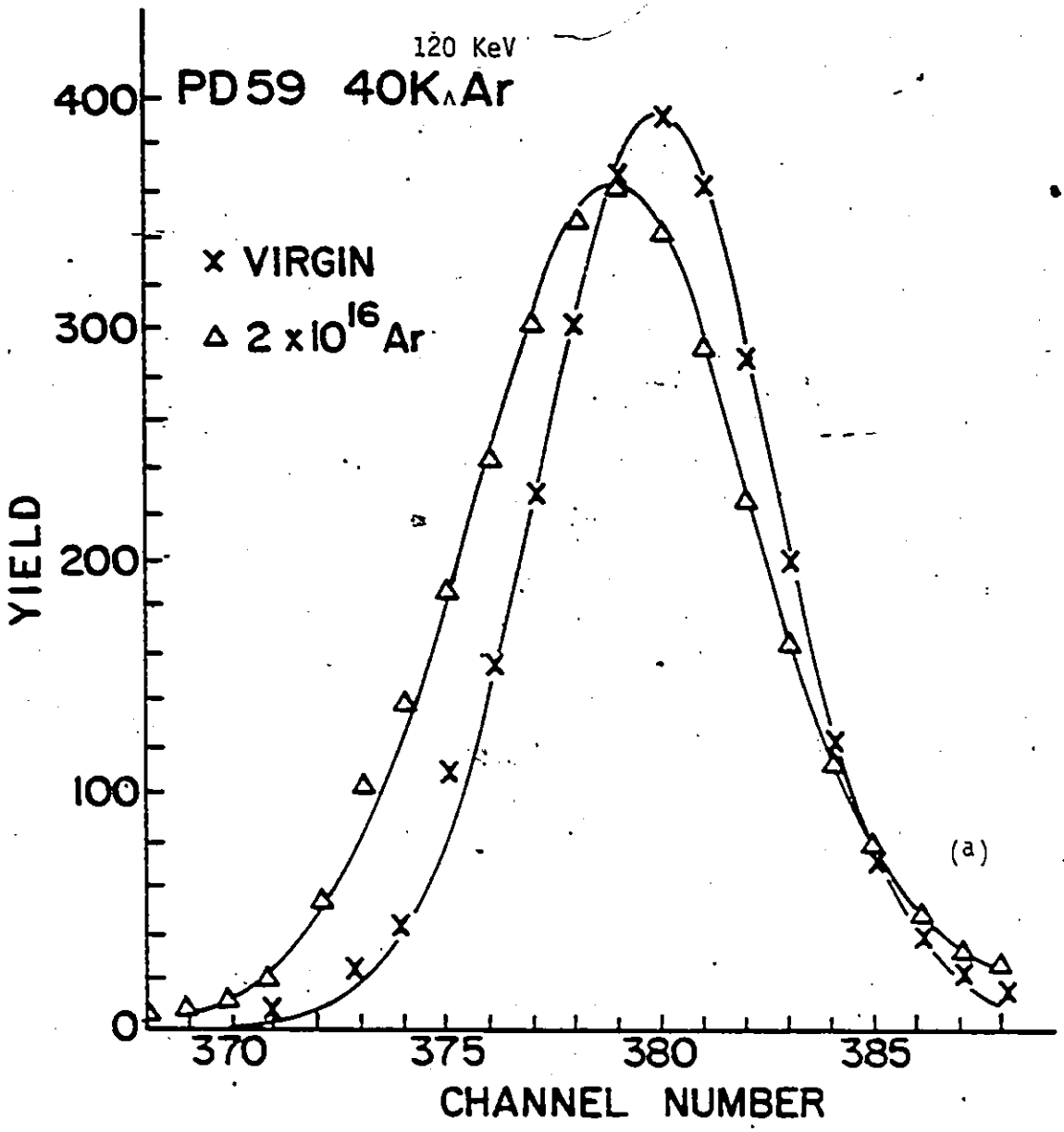

Fig. 6.4: RBS spectra of buried Pd marker before and following 120 KeV Ar^+ irradiation to a dose of 2×10^{16} cm^{-2}.
a) 40K (b) 298K (c) 473K.

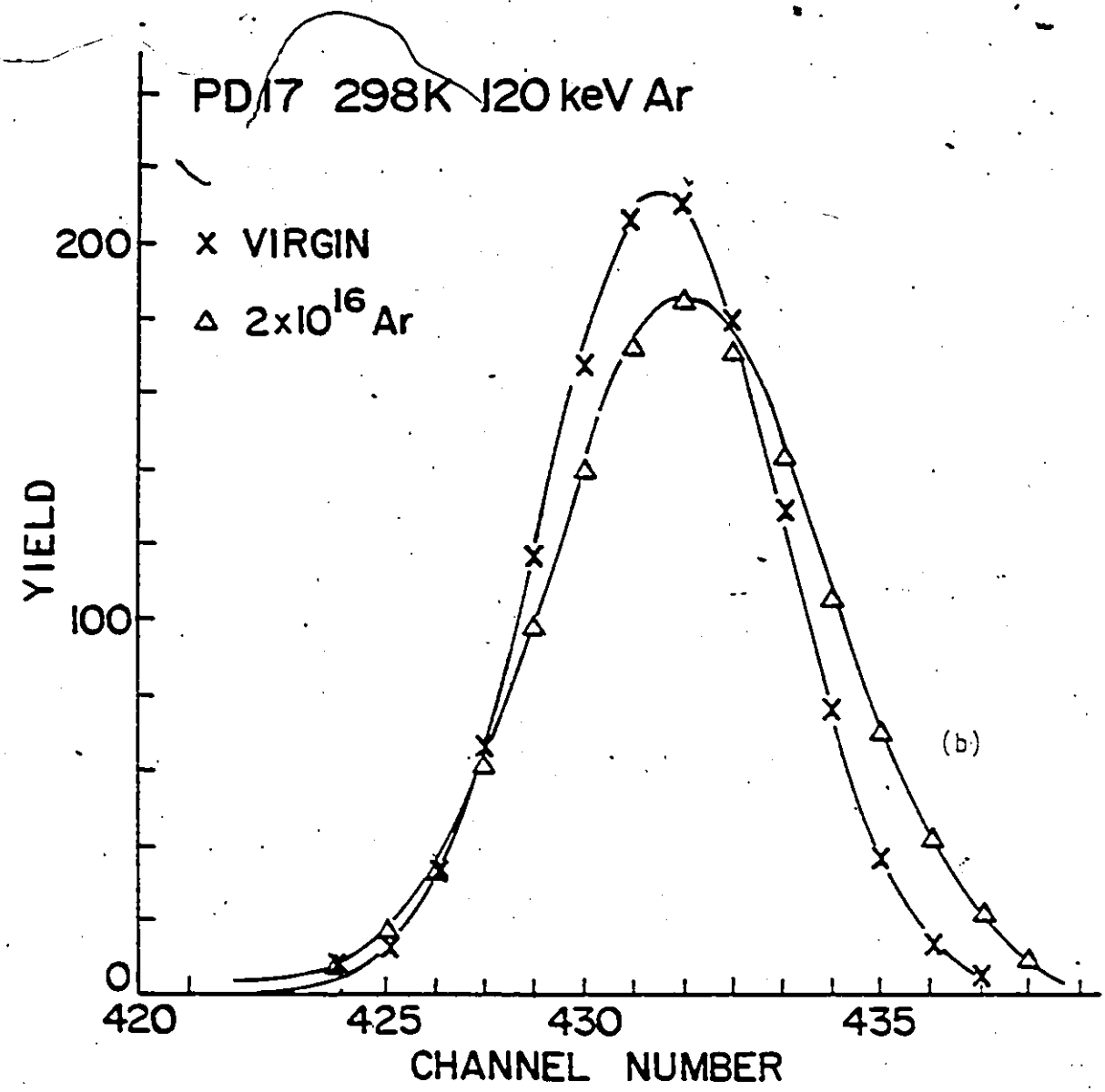
PD17 298K 120 keV Ar
x VIRGIN
Δ 2x10^16 Ar
YIELD
200
100
0
420
425
430
435
CHANNEL NUMBER
(b)

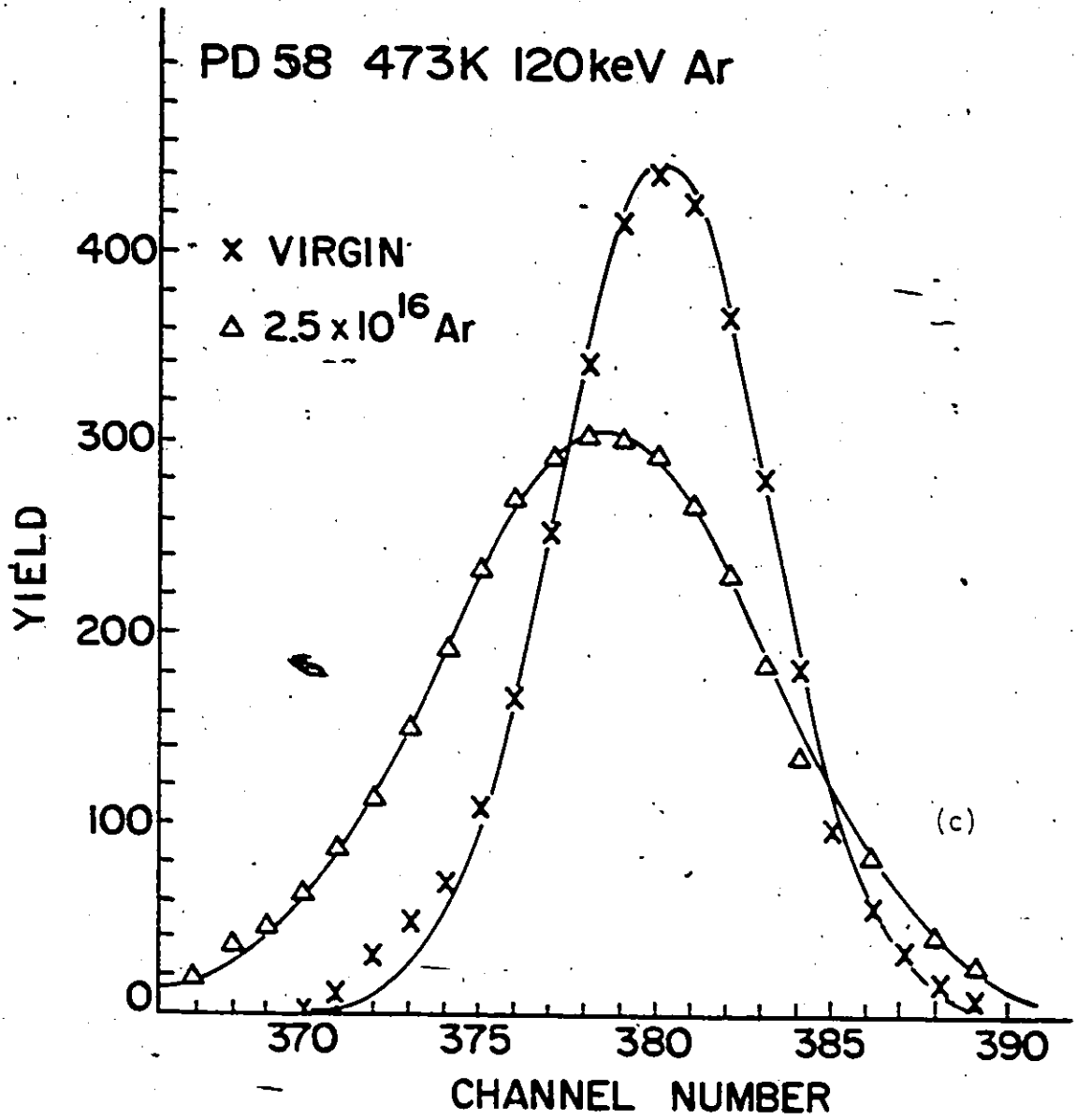
PD 58 473K 120keV Ar
× VIRGIN
△ 2.5 x 10^16 Ar
YIELD
400
300
200
100
0
370
375
380
385
390
CHANNEL NUMBER
(c)

position of the marker. This observation suggests that the greater effectiveness of Kr-irradiation is due mainly to the greater elastic energy deposition (and therefore larger number of displacements) by Kr ions at the marker position.

6.1.4 Comparison with Collision Cascade Models

The various collision cascade mixing models were discussed in chapter 3. These models in general predict a linear dependence of the mixing variance on both the ion dose, ϕ, and the elastic energy, F_D, deposited at the marker position. In particular, Sigmund's (1981) model suggests that the interaction between the low-energy matrix recoils and the marker atoms is the dominant contribution to mixing and predicts a mixing variance given by

$$\Delta\sigma^2 = \frac{\bar{I}}{3}\,\Gamma \cdot \frac{F_D(x)}{N} \cdot \xi_{21}\,\frac{R_c^2}{E_c} \cdot \phi \qquad (6.3)$$

where $\Gamma \sim 0.608$, $F_D(x)$ is the nuclear deposited energy at x, ξ_{21} is the ratio of the stopping cross-section for matrix-impurity and matrix-matrix collisions ($\xi_{21} = \frac{C_{21}}{C_{22}}$, where C_{21} and C_{22} are the coefficients in the power law scattering cross-section), E_c is a minimum energy below which displacements cannot occur and R_c^2 is the mean square displacement associated with E_c. The calculated $\Delta\sigma^2$ values (assuming $E_c \sim E_d \sim 34$ eV, $R_c^2 \sim 1\ nm^2$) predicted by Eq. (6.3) for 120 KeV Ar irradiation and 145 KeV Kr^+ irradiation are shown as dashed lines respectively in Figs. 6.7 and 6.8. The predicted values are at least ~ 10 times smaller than those observed experimentally (at 40K, $\Delta\sigma^2$(measured) $\sim$ 2 5 nm^2, $\Delta\sigma^2$(calculated) $\sim$ 2 nm^2 for 1×10^{16} Ar irradiations). In addition, this model predict

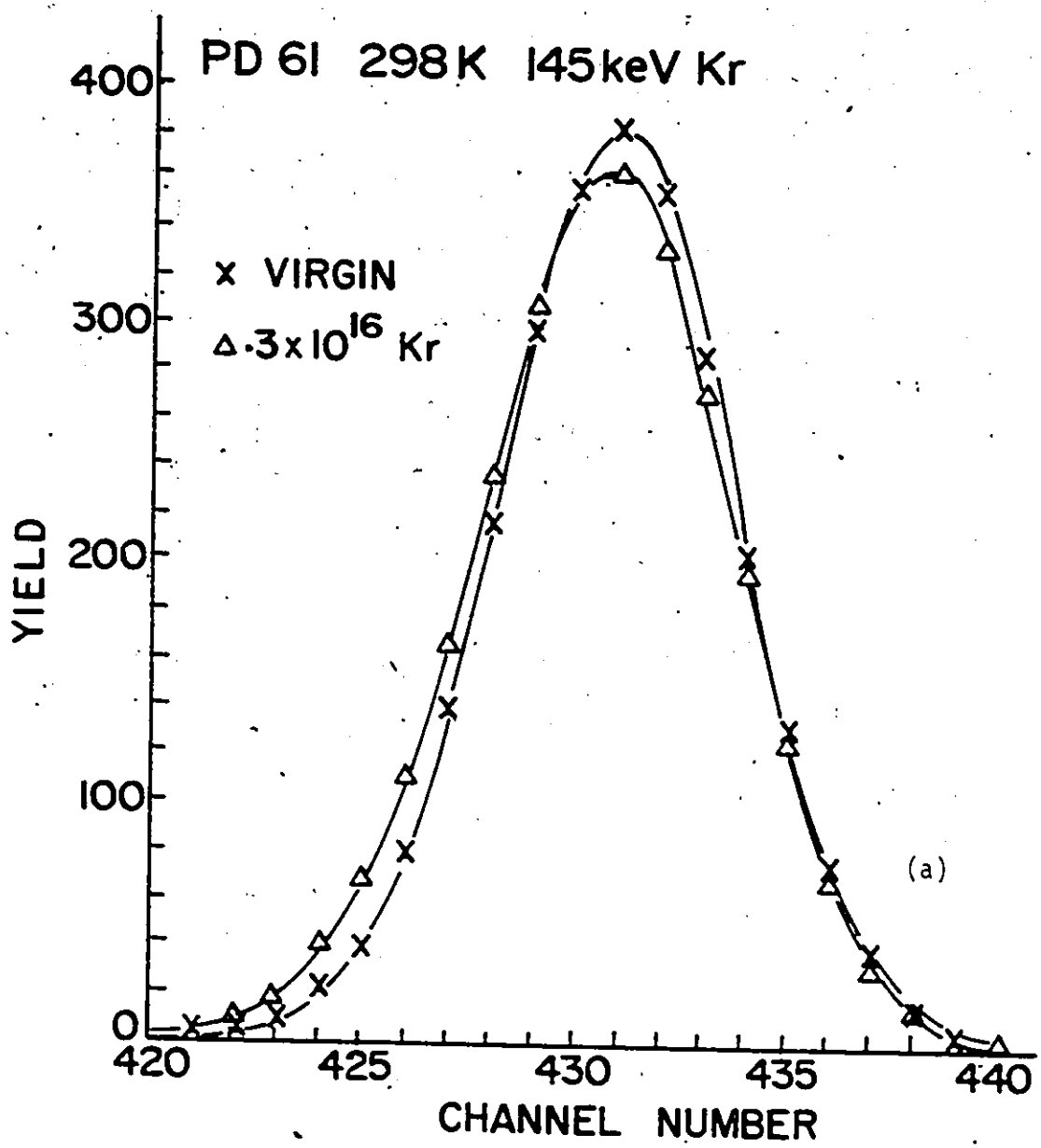

Fig. 6.5: RBS spectra of buried Pd marker before and following Kr^+ irradiation at 298K.
a) 0.3×10^{16} cm^{-2} (b) 0.62×10^{16} cm^{-2} (c) 1.06×10^{16} cm^{-2}.

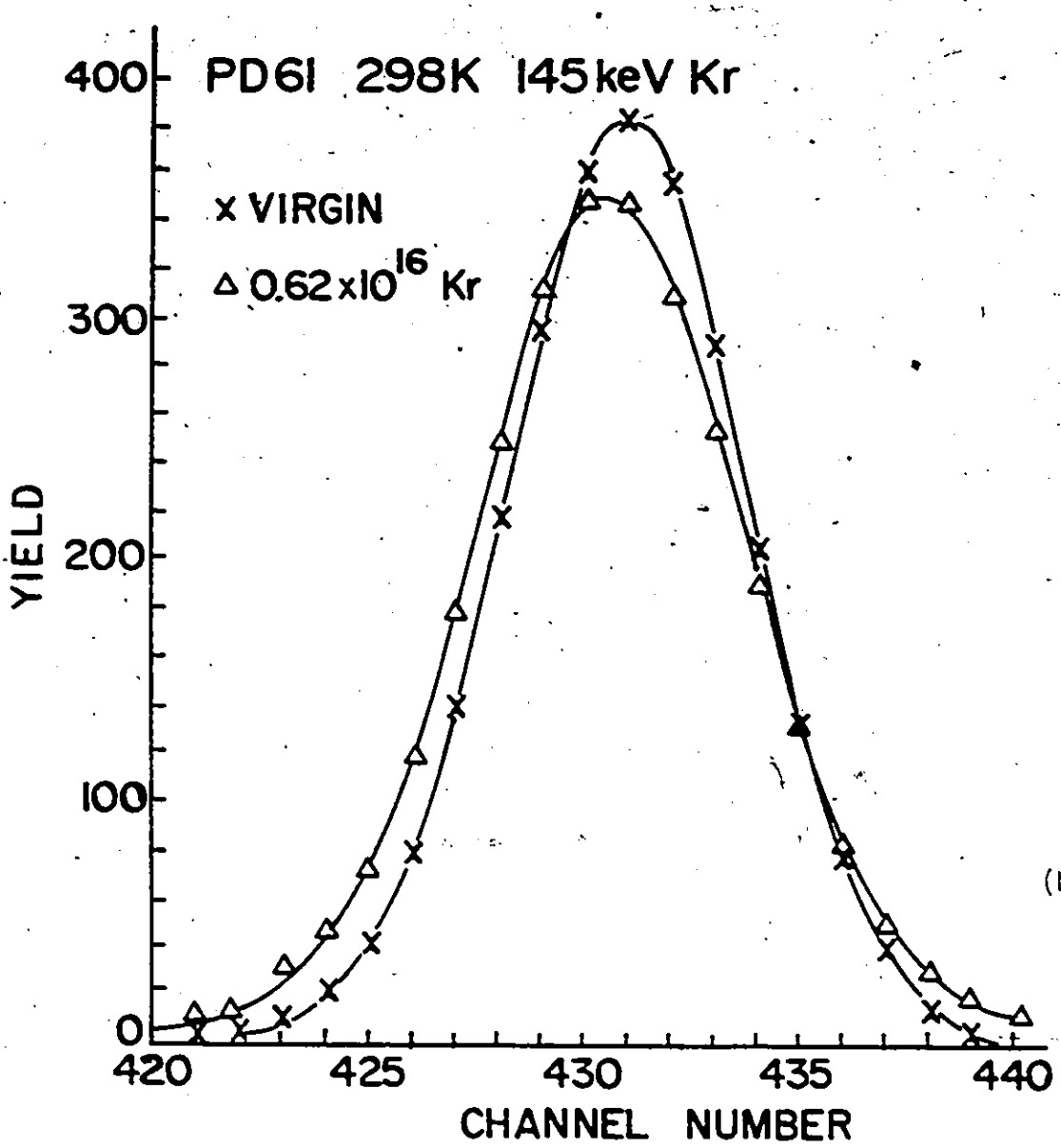
PD61 298K 145keV Kr
× VIRGIN
△ 0.62×10^16 Kr
YIELD
400
300
200
100
0
420
425
430
435
440
CHANNEL NUMBER
(b)

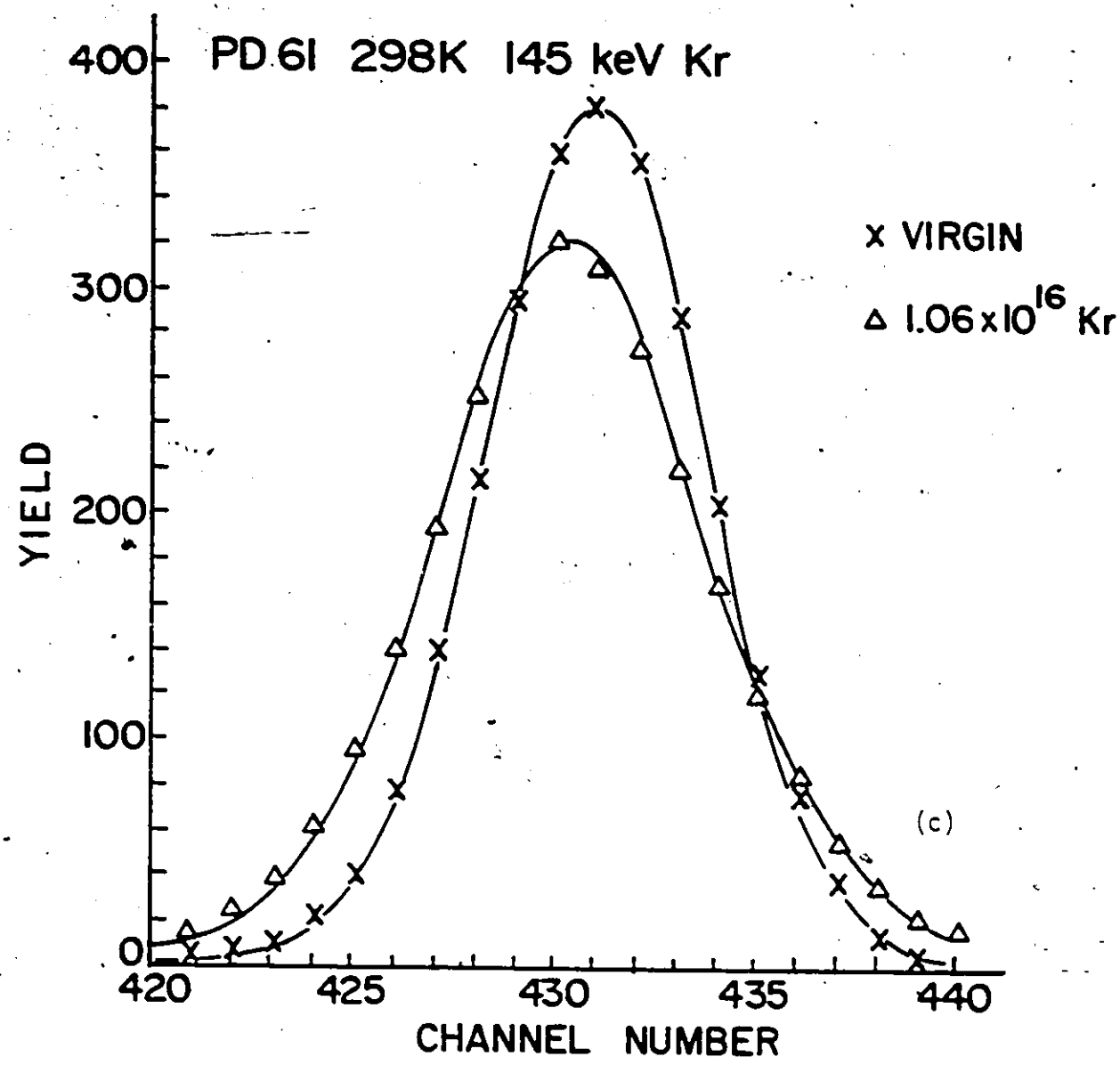
PD 61 298K 145 keV Kr
400
300
200
100
0
YIELD
420
425
430
435
440
CHANNEL NUMBER
x VIRGIN
Δ 1.06x10^16 Kr
(c)

a net shift in the marker peak position with dose due to a relocation of matrix atoms past the marker. As pointed out in section 6.1.1, the observed peak shifts can all be accounted for by small fluctuations in the analyzing He^+ beam energy and ion sputtering. Consequently, the predicted peak shifts are not observed in the present investigations. Matheson's (1981) model which includes contributions from both low- and high-energy recoils was also discussed in section 3.3.2. This model predicts variances of mixing $\Delta\sigma^2$ close to observed variances within a factor of 2 ($\Delta\sigma^2_{calc} \sim 40\ nm^2$ vs $\Delta\sigma(measured) \sim 60\ nm^2$) for $\phi = 1x10^{16} cm^{-2}$ of 145 KeV Kr^+ ions.

Note that the predicted linear dependence of $\Delta\sigma^2$ on ion dose, ϕ, and nuclear deposited energy, F_D, were indeed observed. This observation suggests that the qualitative picture of ion beam mixing at low temperatures, as resulting from cumulative displacements created by each ion, is correct. The higher values of $\Delta\sigma^2$ observed experimentally vis-a-vis predicted values suggest that factors other than purely collisional events also contribute to the mixing of this temperature regime.

6.1.4. Temperature-Dependence of Mixing

For both Ar and Kr irradiations, the spreading of the marker exhibits two types of behaviour when $\Delta\sigma^2$, at constant dose, is plotted versus temperature - an almost temperature-independent region from 40 - 300K and a strongly temperature-dependent region above $\sim$ 400K (Fig. 6.9). The temperature-independent mixing observed between 40K and 300K has been observed also in other systems: e.g. Bøttiger et al.

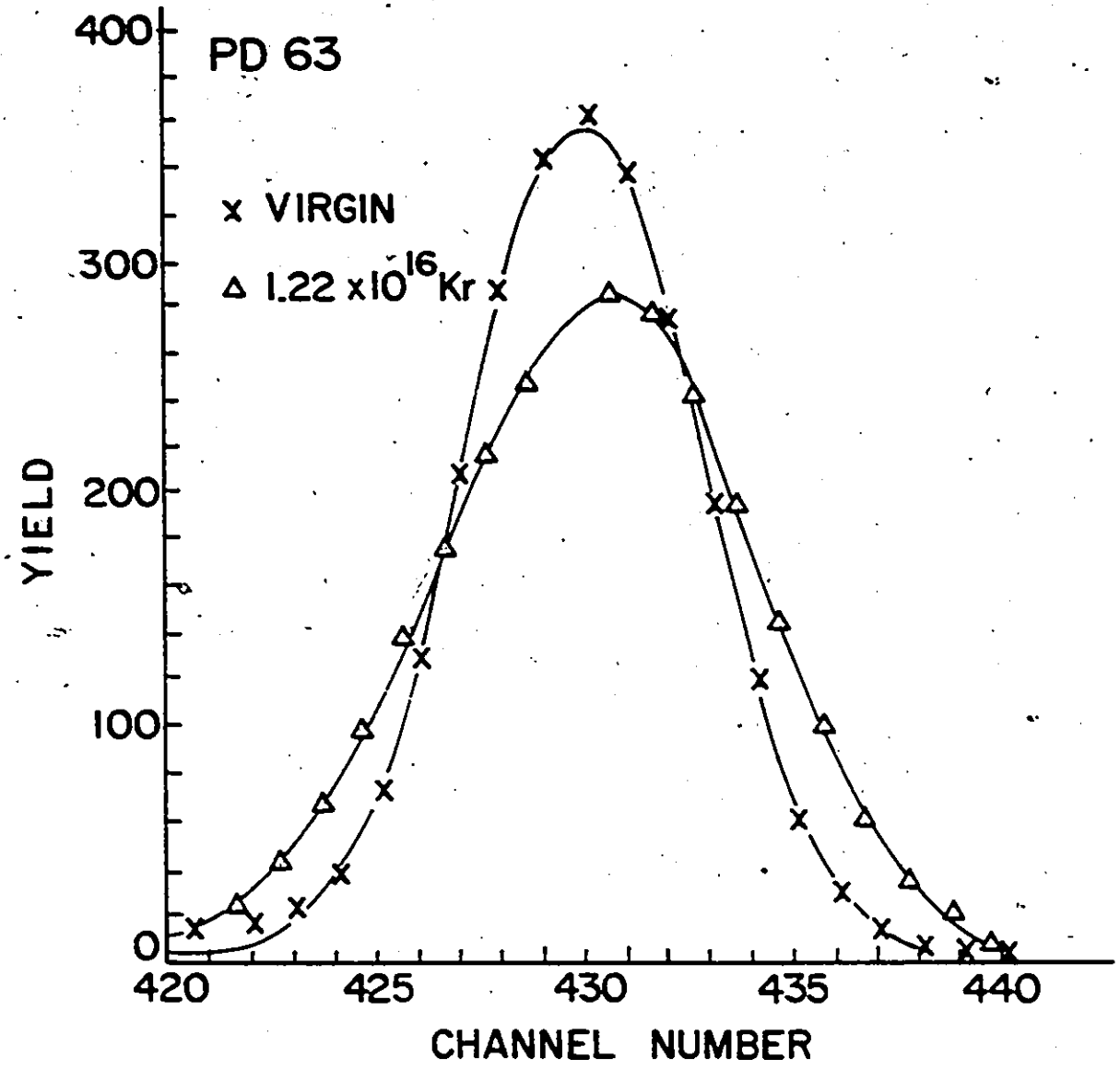

Fig. 6.6: RBS spectra of buried Pd marker before and following Kr irradiation at ~ constant dose at two temperatures.
(a) 40K (b) 473K.

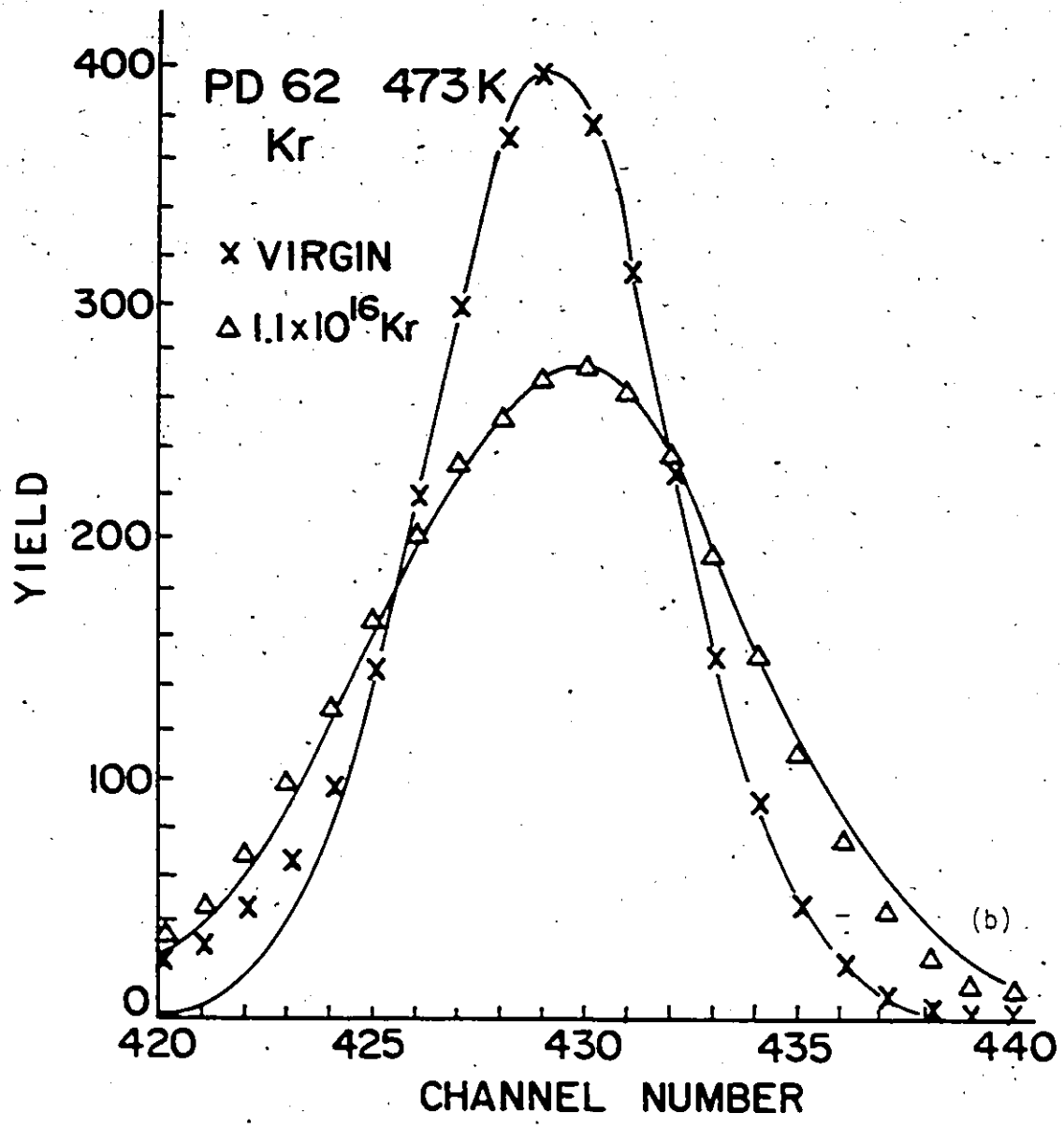
PD 62 473K
Kr
× VIRGIN
△ 1.1×10^16 Kr
YIELD
CHANNEL NUMBER
0
100
200
300
400
420
425
430
435
440
(b)

Table 6.1: Measured Mixing Parameter $\Delta\sigma^2$ as a function of dose and temperature for Ar and Kr irradiations.

T	Ar Irradiation		Kr Irradiation	
	Dose ($\times 10^{16}$ cm^{-2})	$\Delta\sigma^2$ (nm)^2 $\times 10$	Dose ($\times 10^{16}$ cm^{-2})	$\Delta\sigma^2$ (nm)^2 $\times 10$
40K	0.68	1.41±1.2	0.34	1.55
	1.9	4.57	0.68	3.21
	3.2	8.18	1.22	6.92
	4.5	10.15	1.22	6.92
298K	1.0	3.00	0.29	1.55
	2.0	9.16	0.62	3.22
	3.0	10.90	1.06	6.93
	4.0	12.72		
473K	.64	5.25	0.36	5.01
	1.91	16.25		
	2.54	24.20	1.1	13.42
573K	0.5	22.45	553K 0.48	11.13
	1.0	40.14	0.95	26.74

Table 6.2: Ratio of measured mixing parameters for 120 KeV Ar and Kr 145 KeV irradiations at various temperatures for $\phi=1 \times 10^{16}$ cm^{-2}

Temp (°K)	$(\frac{\Delta\sigma^2}{\phi})_{Ar}$ (nm^4/ion)	$(\frac{\Delta\sigma^2}{\phi})_{Kr}$ (nm^4/ion)	$(\Delta\sigma^2/\phi)_{Kr}/(\frac{\Delta\sigma^2}{\phi})_{Ar}$
40	0.25	0.55	2.2
298	0.35	0.66	1.9
473	0.886	1.23	1.4
553	-	2.43	-
573	3.33	-	-

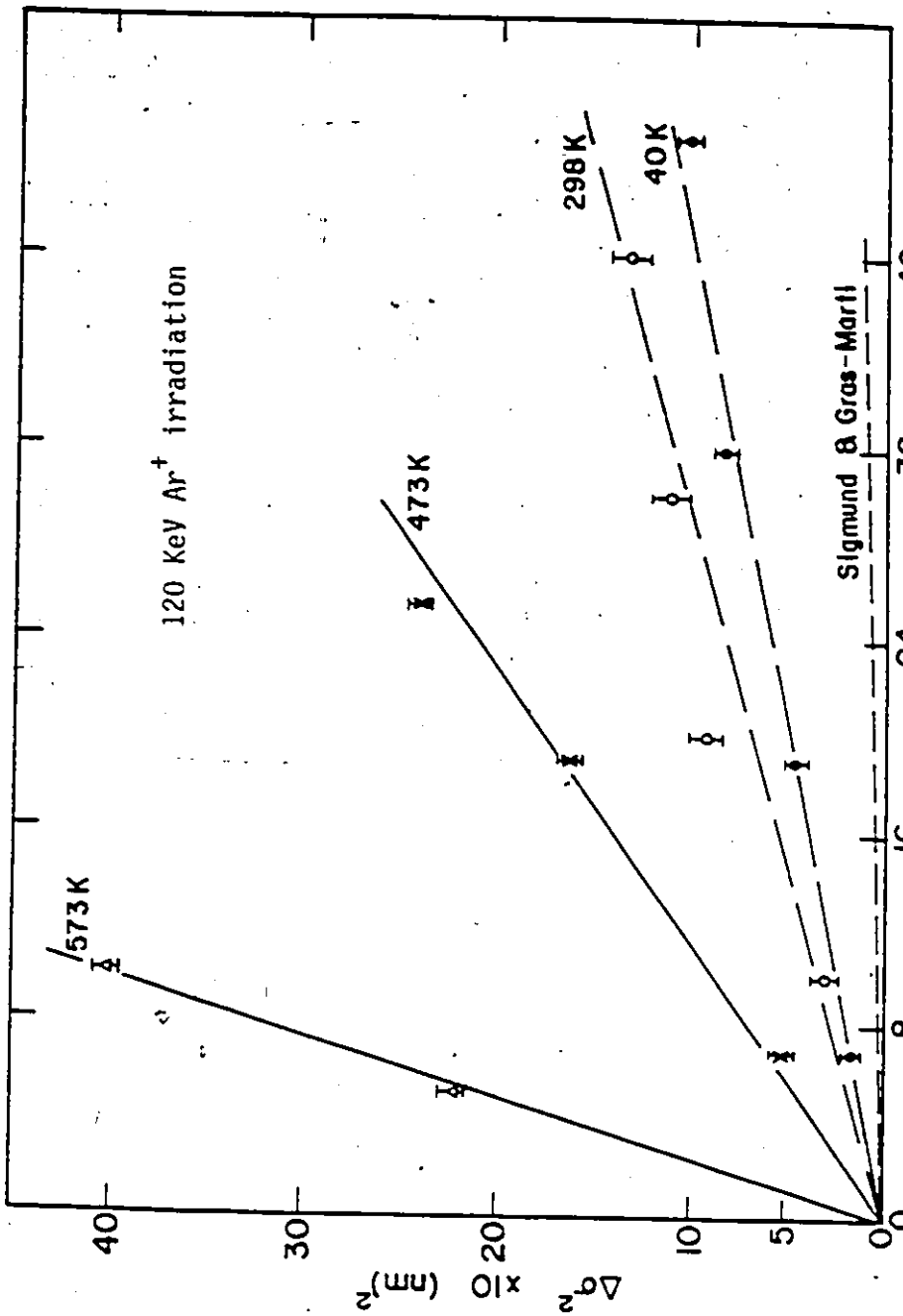

Fig. 6.7: Dose-dependence of the spreading variance at various temperatures.

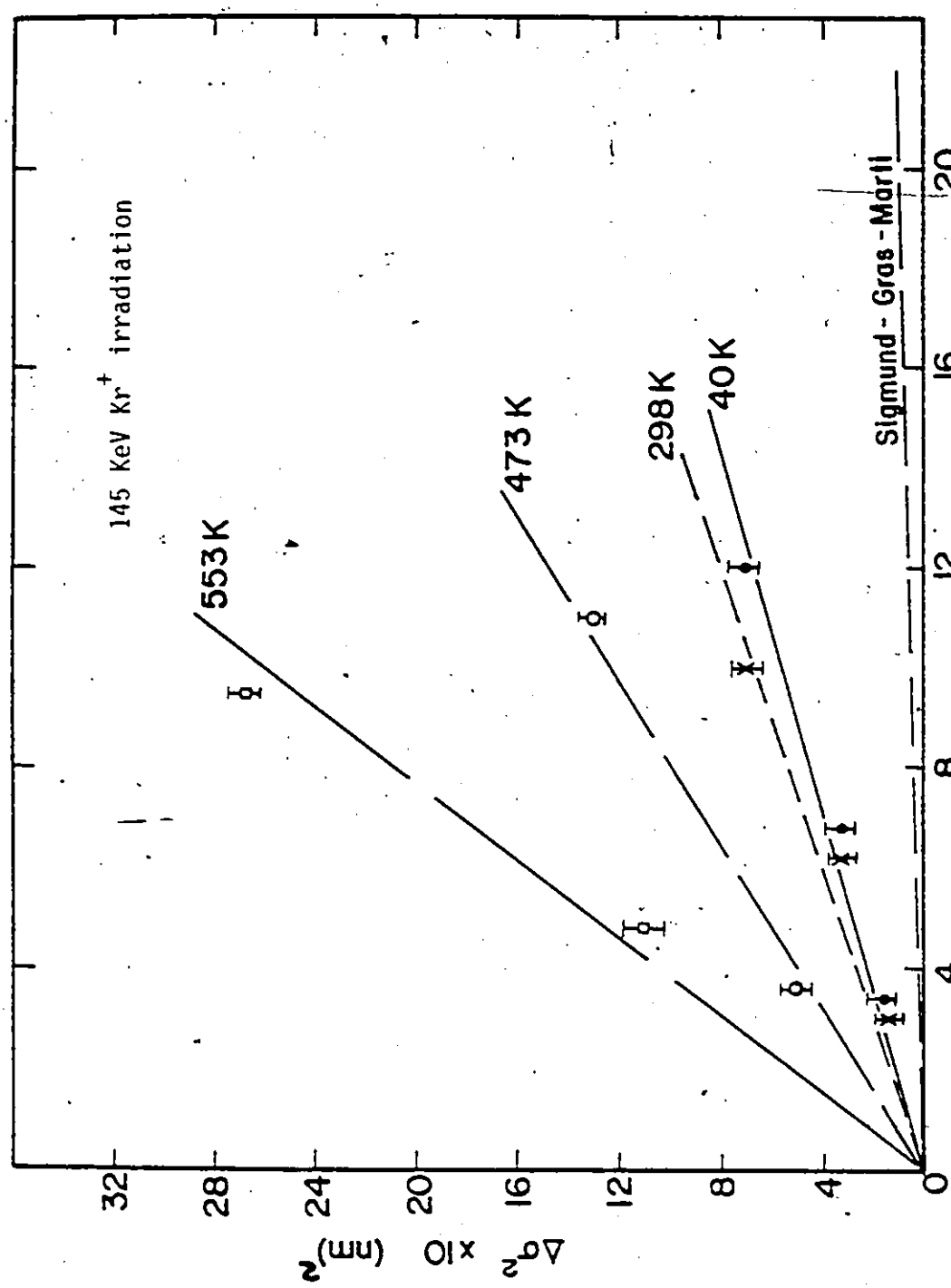

Fig. 6.8: Dose-dependence of the mixing parameter at various temperatures.

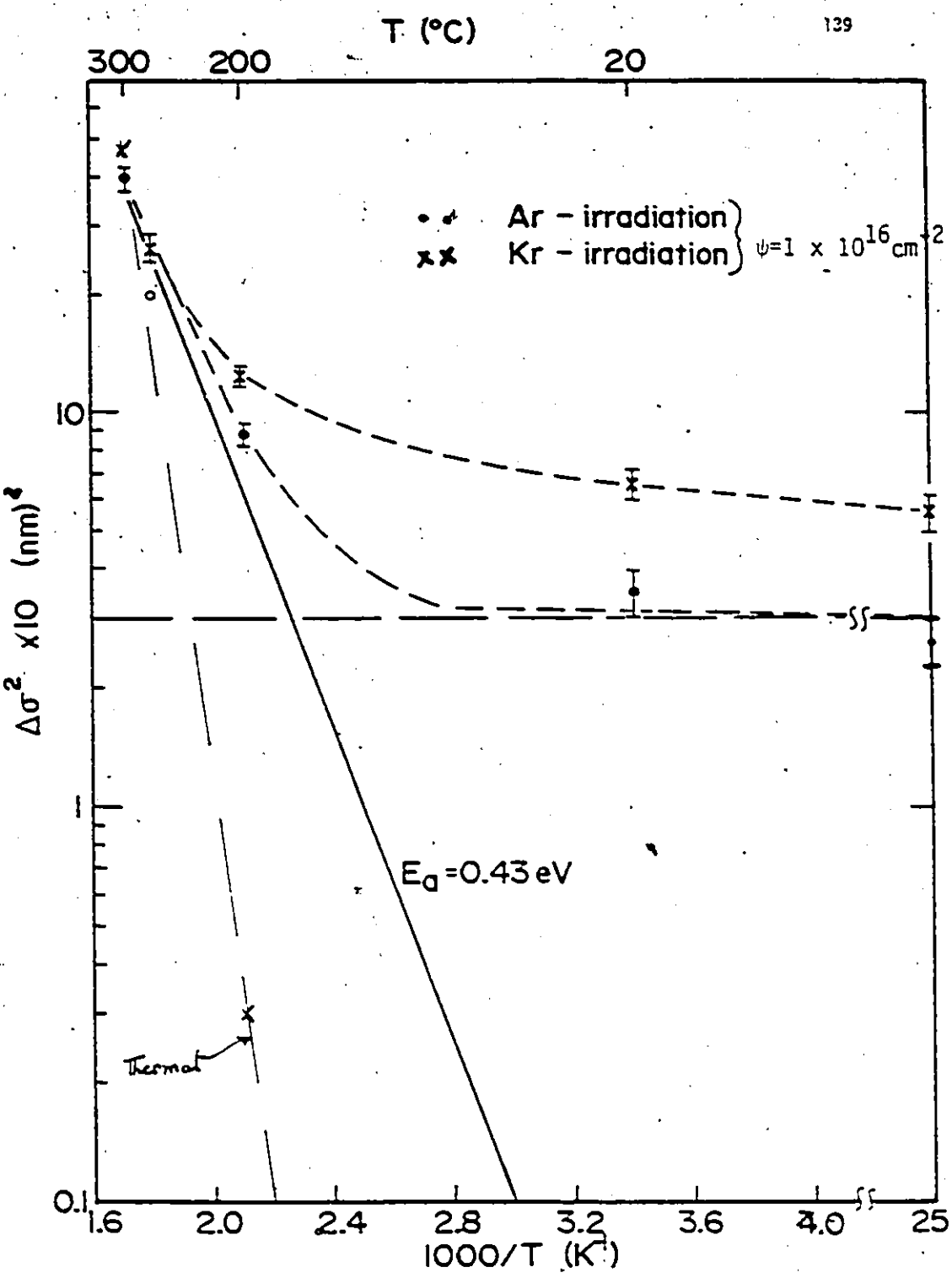

Fig. 6.9: Temperature-dependence of the mixing parameter, $\Delta\sigma^2$

(1985, Au markers in Ni), Averback et al. (1982, Ni in Si) and Match et al. (1985), Ni^{63} in Ni), and appears to be a general feature of ion beam mixing. Also shown in Fig. 6.9 are the pure thermal annealing results. No measurable spreading of the Pd marker was observed for specimens annealed, without irradiation, at $T \lesssim 400K$. The figure shows that above $\sim$ 400K the mixing parameter, $\Delta\sigma^2$, shows a strong temperature dependence. In this temperature regime, collision cascade, thermal and radiation-enhanced diffusion effects contribute to the observed mixing:

$$\Delta\sigma^2 = \Delta\sigma^2_{th} + \Delta\sigma^2_{cascade} + \Delta\sigma^2_{red}$$

In the temperature range where thermal contribution is not significant, the radiation-enhanced contribution can be estimated by subtracting the $\Delta\sigma^2$ values measured at low temperature ($\sim$ 40K) from the high temperature values. This of course assumes that at low temperatures defect diffusion is largely suppressed and therefore that the measured Pd spreading at low temperatures is due mainly to collisional mixing events. The $\sim$ constant low temperature $\Delta\sigma^2$ between 40K and 300K in Fig. 6.9 ($\sim$ 25 nm^2 for Ar and $\sim$ 60 nm^2 for Kr at 40K) are assigned to purely collisional mixing. These values compare well with those found recently ($\sim$ 30 nm^2) by Bøttiger et al. (1985) for the spreading of Au markers in Ni bombarded with 150 KeV Ar^+ ions at 20K. The radiation enhanced contribution is shown as a solid line in Fig. 6.9, and gives an activation energy of $\sim$ 0.43±0.07 eV and a pre-factor $\Delta\sigma^2_0$ of $\sim$ 220 nm^2. Published values of the vacancy migration

energy in Ni (Wollenberger, 1983) range from 0.92 to 1.4 eV, while the activation energy for stage III recovery of resistivity (assigned to vacancy migration) in electron-irradiated Ni is $\sim$ 1.03 eV (Harkness et al., 1975). Thus the measured activation energy $E_a \sim 0.43\pm0.07$ eV is close to $\frac{1}{2}$ the vacancy migration energy in Ni.

A model of radiation enhanced diffusion was presented in chapter 3, and will be discussed further in section 6.2. The salient point here is that, when annihilation of defects occurs primarily by mutual recombination of vacancies and interstitials, a radiation enhanced diffusion coefficient is obtained, which is given by (Chap. 3.3)

$$D_{rad} = 2\left(\frac{\alpha K_0 D_v}{\pi R_{iv} N}\right)^{\frac{1}{2}} \qquad (6.5)$$

where K_0 is the defect production rate, D_v is the diffusion coefficient of vacancies and R_{iv} is the radius of the recombination volume, Ω_{rc}, where Ω_{rc} is $\sim$ 100 times the atomic volume Ω. Thus

$$D_{rad} \propto K_0^{\frac{1}{2}} \exp^{-\frac{E_v^m}{2kT}} \qquad (6.6)$$

i.e. the activation energy associated with D_{rad} is one-half the vacancy migration energy. What is measured here is the spreading variance, $\Delta\sigma^2$, and is not a diffusion coefficient in the classical sense. However if the spreading is also radiation-enhanced, the enhanced spreading will be expected to show a similar dependence on K_0 and temperature. This dependence on temperature is indeed observed and the measured $E_a = 0.43\pm0.07$ eV is taken as a confirmation that radiation-enhanced spreading is the

dominant mixing mechanism in this temperature range. At a particular dose (e.g. 1×10^{16} cm^{-2}), the mixing may be described as

$$\Delta\sigma^2 = \Delta\sigma_0^2 \exp^{-\frac{E_a}{kT}} \tag{6.7}$$

with $\Delta\sigma_0^2$ and E_a as given in the text.

Using this model $\Delta\sigma^2/\phi$ is then given approximately by

$$\frac{\Delta\sigma^2}{\phi} = 2\{\frac{\alpha K_0 D_v}{\pi N R_{iv}})\}^{\frac{1}{2}} \cdot \frac{1}{\dot{\phi}} \tag{6.8}$$

where ϕ is the dose, $\dot{\phi}$ is the dose rate, αK_0 is used since only a fraction of the defects produced are able to escape the displacement cascade. It is this fraction αK_0 that ultimately contributes to diffusion. The measured $\frac{\Delta\sigma^2}{\phi} = 6\times10^{-29}$ cm^4/ion at 473K ($\phi = 1\times10^{16}$ Ar$^+$ cm^{-2}) while the calculated value for the dose rate used (3.1×10^{12} cm^{-2} sec^{-1}) is $\sim 4.5\times10^{-29}$ cm^4/ion ($\alpha = 1$). If α is taken to be 0.1, then the calculated value is about an order of magnitude less than measured. The differences in the calculated and measured values may be due to additional contribution to mixing by long range migration of the defects to internal sinks. Such order of magnitude difference between the measured and calculated values has also been observed for Si-irradiated Ni-Sb (S.M. Myers (1980)).

6.2 ION MIXING OF Ni/Pd BILAYER COUPLES

In this section, results are presented of the mixing of Ni/Pd bilayer couples induced by 120 KeV Ar^+ irradiation and/or thermal annealing. Irradiation temperatures range from 298 to 673 K and ion doses from 0.5 to 4×10^{16} Ar^+ ions cm^{-2}. Two dose rates were used ($\sim 5 \times 10^{12}$ and $\sim 6 \times 10^{11}$ ions cm^{-2} sec^{-1}). In order to assess the thermal contribution to the observed mixing, samples annealed at these temperatures (without ion irradiation) were also studied.

Samples for these studies were prepared as described in section 5.1. To study the ion beam and/or thermal induced mixing of small-grained Ni/Pd bilayer couples, samples were prepared by sequential evaporation, without breaking vacuum, of $\sim$ 100 nm Ni followed by $\sim$ 40 nm Pd film on polycrystalline Ni and sapphire substrates. Fig. 6.10 shows the results of Auger depth-profiling of such samples, and indicates that sequential evaporation of the two layers ensures a clean interface free of either oxygen or carbon contamination. Intermixing between large-grain polycrystalline (or single crystal) Ni and evaporated Pd films were also studied with a view to assess the influence of grain size on the mixing rates. Samples for this type of study were prepared by evaporating a layer of Pd, $\sim$ 40 nm thick, on electropolished single crystal (100 orientation) or polycrystalline Ni substrates.

Analyses of the mixing is principally by RBS with 2 MeV $^4He^+$ ions except for samples annealed at high temperatures ($\sim 700^oC$). For the 700^oC samples, extensive interdiffusion occured and the RBS signal due to Ni could not be resolved from the Pd signal. Such samples were profiled using the Auger sputter profiling technique.

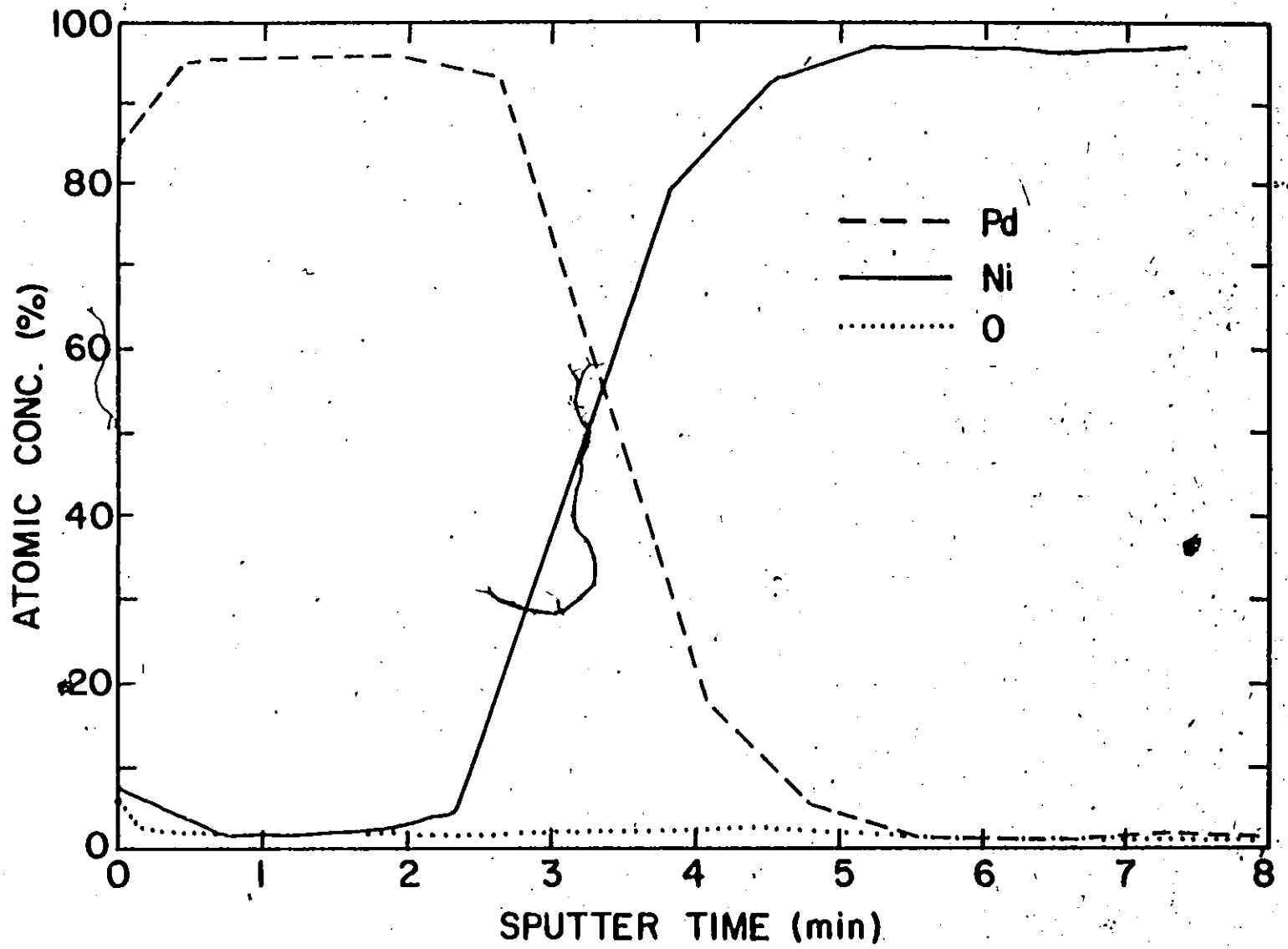

Fig. 6.10: Auger sputter depth-profile of Ni/Pd bilayer couple indicating a clean interface between the two evaporated layers.

The results are divided into five sections. Section 6.2.1-6.2.3 are concerned with mixing in small-grained Ni/Pd films. In section 6.2.1 ion mixing results for samples irradiated at temperatures ranging from 287-473 K are presented and discussed. These results are compared with the results presented in section 6.1 on the spreading of thin Pd markers in Ni. In section 6.2.2 results of the ion-/thermal-induced mixing for samples irradiated at 573-673 K are presented. In this temperature regime, mixing in these small-grained couples is characterized by an initial rapid intermixing of the Ni/Pd layers and appears to be influenced by grain-boundary diffusion. Results on the experiments designed to estimate the grain-boundary diffusion effects are presented in section 6.2.3. In section 6.2.4 results of intermixing between single crystal (or polycrystalline) Ni and small-grain Pd overlayer films are presented and compared with the results discussed in sections 6.2.1-6.2.3. Finally, the development of film microstructure following ion bombardment was studied by TEM. The result and the influence on the mixing rates are presented and discussed in section 6.3.

6.2.1 Ion Mixing of Ni/Pd Couple Between 298-473 K

Results reported in this section are concerned with the intermixing of small-grained Ni and Pd films. Results for single crystal Ni exhibiting small-grained Pd overlayer films will be presented in section 6.2.4.

Fig. 6.11 shows the RBS spectra of a Ni/Pd bilayer sample before and after irradiation at 423 K with 1×10^{16} and 2×10^{16} Ar^{+} ions cm^{-2}. The backscattering signals after irradiation have been shifted to match the original interface in order to clearly reveal the intermixing. The re-

PAGE 146 OMITTED
IN PAGE NUMBERING.

PAGE 146 OMISE
DANS LA PAGINATION.

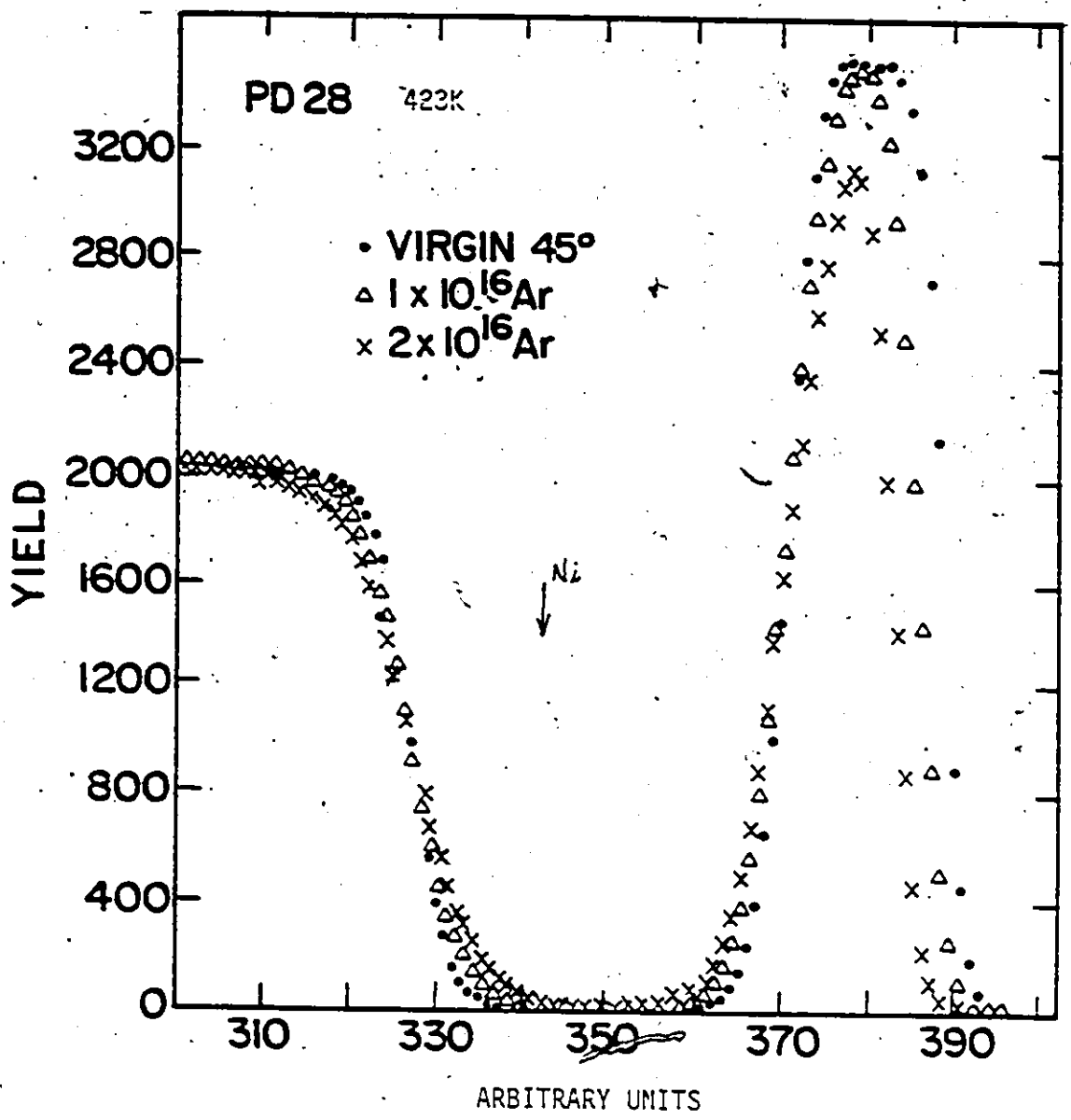

Fig. 6.11: RBS spectra of a Ni/Pd bilayer couple before and after irradiation at various doses at 423K.

duced width of the Pd signals after irradiation is due to the reduced thickness of the Pd overlayer caused by sputtering, while the reduction in the Pd peak height signal after a dose of 2×10^{16} ions cm^{-2} is due to the fact that the thickness of the remaining Pd overlayer ($\sim$ 20 nm) is now comparable to the depth resolution of the detection system. The channel position where the Ni signal would appear if Ni were on the surface is marked by the arrow in Fig. 6.11.

The salient feature of the profiles in Fig. 6.11 is the broadening with ion dose, of the high energy edge of the Ni signal. The low energy edge of the Pd signal also showed broadening. The Ni profiles are shown in an expanded form in Fig 6.12. These profiles are smooth and show no steps that would indicate the presence of a compound formation. This feature is characteristic of all the samples studied for temperatures up to 473K and for all ion doses up to 4×10^{16} cm^{-2}. Figures 6.12 and 6.13 show the Ni profiles before and after irradiation to 3×10^{16} Ar^{+} cm^{-2} while Fig. 6.14 shows the Ni spectra, corresponding to the interface region before and after irradiation for a sample irradiated at 473K.

(i) Characterization of Mixing

The spectra exhibit an error function-type dependence on depth (channel number); the high energy edge of the Ni spectra were least-square fitted to complimentary error functions.

$$Y(n) = \frac{Y_0}{2}\,\mathrm{erfc}\left(\frac{x}{2\sigma}\right) \qquad (6.9)$$

using the spreading standard deviation σ as fitting variable. In this equation, $Y(n)$ is the backscattering yield in channel n, Y_0 is the peak yield and x is the depth measured from the original interface. x is given by

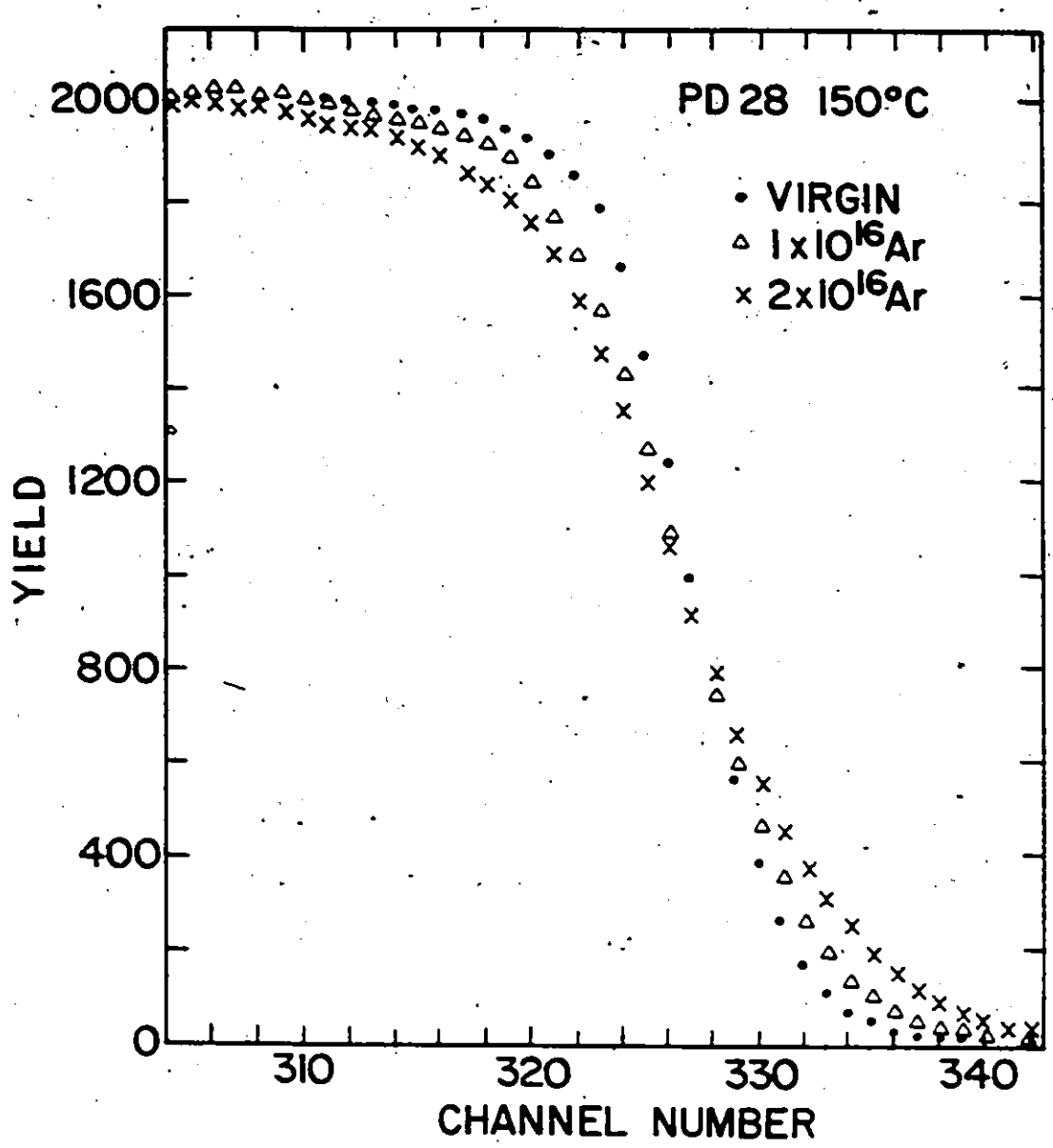

Fig. 6.12: Expanded view of the Ni signal near the interface region revealing the increased broadening of the interface with ion dose.

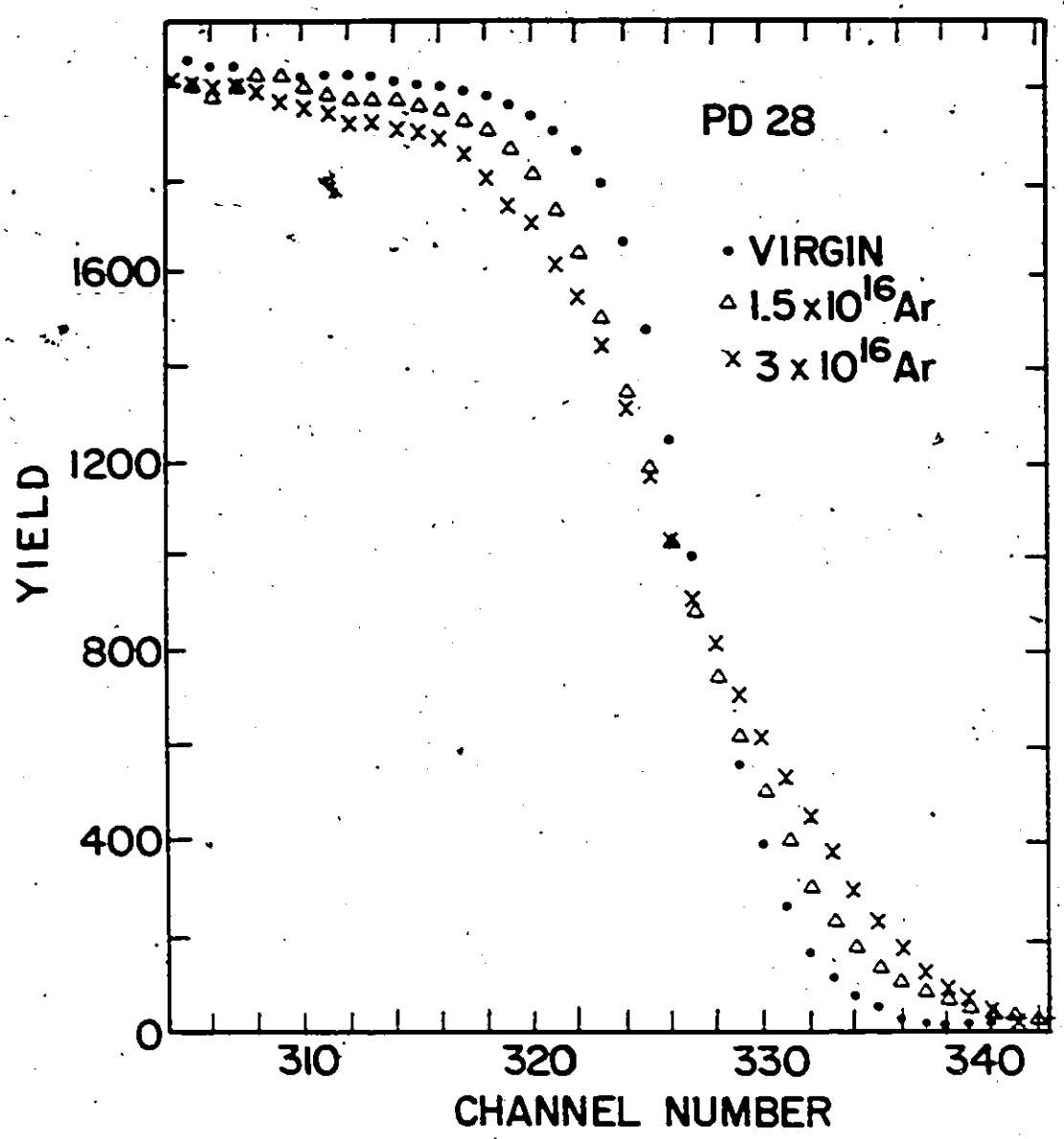

Fig. 6.13: Expanded view of the Ni RBS signal near the interface region before and after irradiation at 423K.

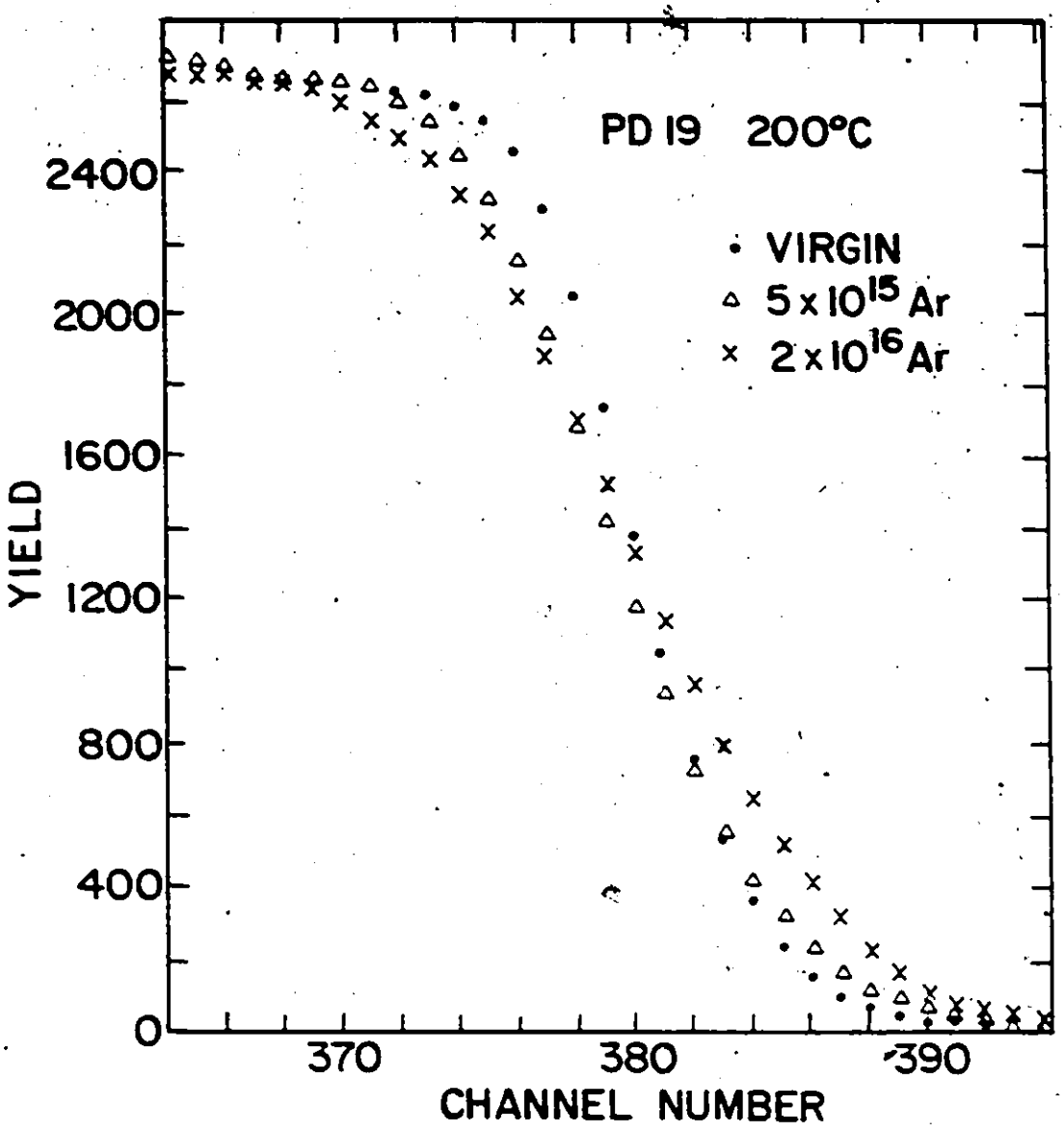

Fig. 6.14: Expanded view of the Ni RBS signals near the interface region showing increased broadening of the interface following irradiation at 473K.

$$x = \frac{(n-n_0)\Delta E}{N[\varepsilon_0]_{Ni}^{Ni-Pd}} \qquad (6.10)$$

where n is channel position, n_0 is channel number of the interface, ΔE is energy equivalence of each channel, $[\varepsilon_0]_{Ni}^{Ni-Pd}$ is the stopping cross-section for He^+ ions backscattering from Ni atoms in Ni-Pd alloy matrix and N is the alloy atomic density. Thus

$$Y(n) = \frac{Y_0}{2}\,\mathrm{erfc}\left[\frac{(n-n_0)\Delta E}{2\sigma[\varepsilon_0]_{Ni}^{Ni-Pd}\cdot N}\right] \qquad (6.11)$$

Deviations from error function distributions were observed at high doses ($\sim 4\times10^{16}$ cm^{-2}) and high temperatures (> 473 K). In some cases, the low energy edge of the Pd distributions was also fitted to an error function distribution, provided that the Pd film still approximated to diffusion conditions of a semi-infinite film (see for example the profile after 1×10^{16} Ar^+ cm^{-2} irradiation in Fig. 6.11).

The net contribution of ion beam mixing and/or temperature to the increased broadening of the interface was deduced by subtracting in quadrature the variance of the unirradiated spectrum (σ_0^2) from the variance, σ_{irr}^2, after irradiation

$$\Delta\sigma^2 = \sigma_{irr}^2 - \sigma_0^2 \qquad (6.12)$$

This is then converted to a depth variance via

$$\Delta\sigma_{mix}^2 = \frac{\Delta\sigma^2(\Delta E)^2}{(N[\varepsilon_0]_{Ni}^{Ni-Pd})^2} \qquad (6.13)$$

The alloy atomic density, N, varies from $\sim$ pure Ni to $\sim$ pure Pd in

the mixed layer; consequently, the average value of $N(7.97 \times 10^{22}\ cm^{-3})$ at the 50% composition was used in the calculations.

(ii) Dose-dependence of the mixing parameter, $\Delta\sigma^2$

In order to study the effect of increasing dose on mixing, samples were irradiated, at constant dose rate, to different doses. Table 6.3 shows the measured mixing parameter $\Delta\sigma^2$ at various doses for a sample irradiated at 298 K. These data include only $\Delta\sigma^2$ values consistent with the assumptions leading to Eq. (6.8), i.e. for doses low enough ($<4 \times 10^{16}$ cm^{-2}) that the observed mixing is confined to regions near the interface. These $\Delta\sigma^2$ values are plotted in Fig. 6.15 as a function of Ar^+ dose. Error bars give the statistical uncertainties in determining the $\Delta\sigma^2$ values by the least squares method. At all temperatures a linear dependence of $\Delta\sigma^2$ on irradiation dose, ϕ, is observed, suggesting a diffusion-like ion-beam induced broadening of the interface. The magnitude of this mixing at 298K is $\Delta\sigma^2 = 34.6 \pm 10.5$ nm^2 after a dose of 1×10^{16} Ar^+ cm^{-2}.

(iii) Temperature dependence of mixing

As illustrated in Fig. 6.15, $\Delta\sigma^2$ shows a weak dependence on temperature increasing from $\sim$ 34.6 nm^2 at 298 K to $\sim$ 60 nm^2 at 423 K after a dose of 1×10^{16} Ar^+ cm^{-2}. Within the uncertainties of the measurements there is virtually no difference between the $\Delta\sigma^2$ values for samples irradiated at 298K and those irradiated at 393K. At 473K, the mixing parameter commences to exhibit a strong dependence on temperature.

In Fig. 6.16, the $\Delta\sigma^2$ values at $\phi = 1 \times 10^{16}$ cm^{-2} are plotted versus reciprocal temperature. The curve exhibits two types of behaviour:

Table 6.3: Measured values of the mixing parameter, $\Delta\sigma^2$ as a function of Ar^+ irradiation dose for a sample irradiated at 298 K with 120 KeV Ar ions at a rate of $\sim 3\times10^{12}$ ions cm^{-2} sec^{-1}.

Dose (1×10^{16} cm^{-2})	$\Delta\sigma^2 \times 10$ $(nm)^2$
1	3.46±1.05
1.5	5.59±1.5
2.5	12.95±1.7
3.0	16.12±1.9

Table 6.3: Mixing Parameter $\Delta\sigma^2$ at different temperatures

Temp. (K)	Dose, ($\times 10^{16}$ cm^{-2})	$\Delta\sigma^2$ ($\times 10^5$ nm^2
298	1	3.46±1.05
	1.5	5.59
	2.5	12.95
	3.0	16.12
393	0.5	3.23
	1.0	6.8
	2.7	15.2
423	1.0	6.62
	1.5	9.31
	2.0	14.89
	3.	21.25
473	0.2	4.73
	0.5	8.1
	1.0	13.6
	2.0	25.44

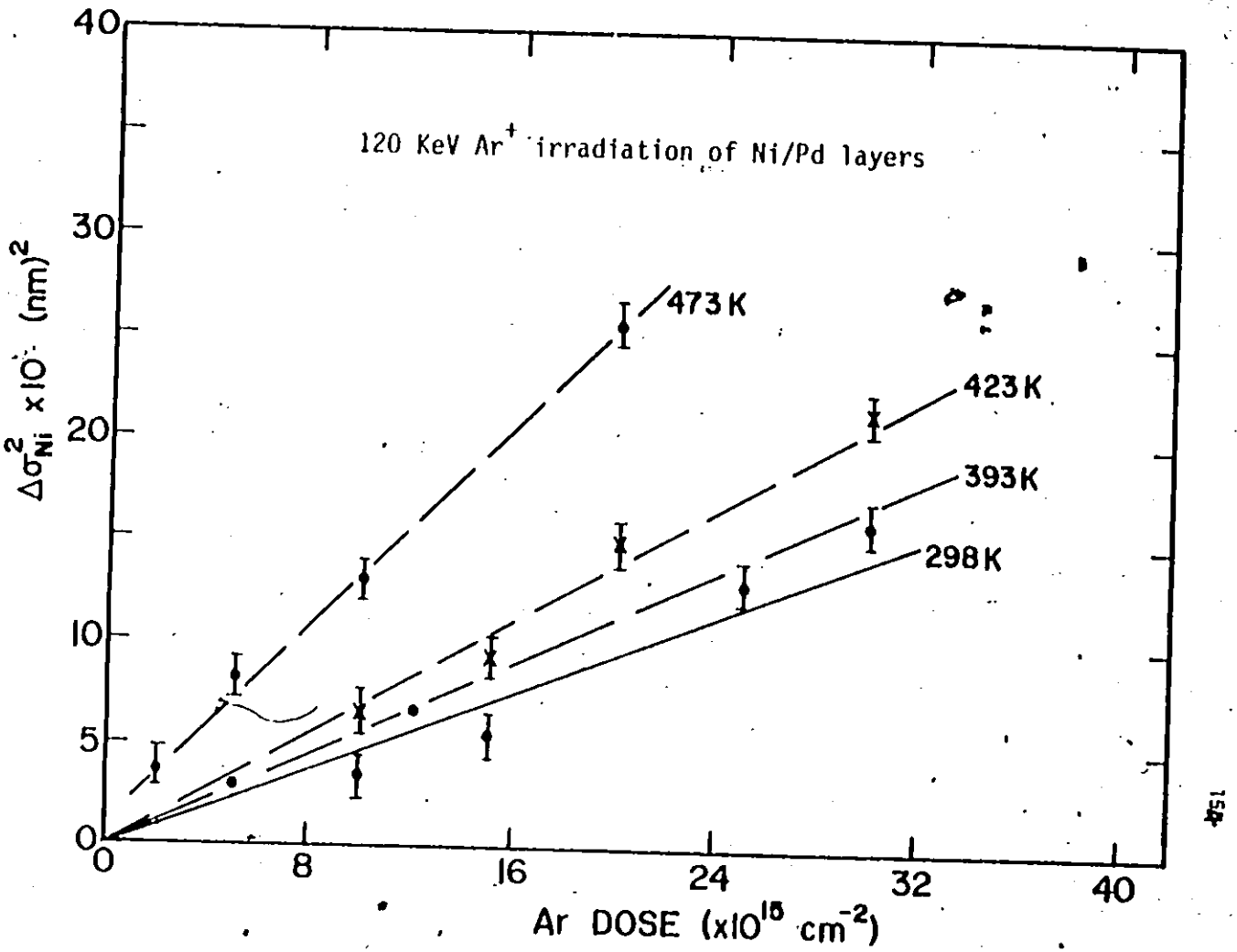

Fig. 6.15: The dependence of the mixing parameter of a bilayer couple on Ar irradiation dose.

1) between 298 and 423K, it is linear and weakly dependent on temperature and 2) above 423K it becomes strongly dependent on temperature. In the first temperature region, the slope of the curve gives an apparent activation energy, $E_a \approx 0.10 \pm 0.06$ eV. This small activation energy is similar to activation energies typically observed for interstitial diffusion ($\sim$ 0.15 eV for Ni), and in the present investigation it is probably due to the enhanced mixing produced by the diffusion of interstitials escaping the collision cascades. It is noted, notwithstanding, that the temperature regime under consideration (298-423K) spans the entire stage III recovery temperature (300-400K) characteristic of freely migrating vacancies observed in electron- and neutron-irradiated Ni and Pd (section 3.2). The results presented in this section suggest that stage III recovery is suppressed until $\sim$ 473K (i.e. beginning of stage IV recovery). A possible explanation of this behaviour is that the damage structure resulting from 120 KeV Ar^+ irradiation does not consist of isolated defects but rather these defects are in the form of vacancy and interstitial clusters. The activation energy E_a = 0.1 eV measured between 298 and 423K then corresponds to the release of trapped interstitials. Release of trapped vacancies does not occur until $\sim$ 473K where their migration begins to contribute appreciably to the mixing parameter, $\Delta\sigma^2$. This picture is consistent with experimental findings (section 3.2) on the nature and stability of defects produced in Ni irradiated with Ni^{++} (Chen 1973) and Sb^+, Sb_2^+ (Al-Tamini et al, 1985) ions. The activation energy in the region where mixing shows a strong temperature-dependence will be discussed in the next section where a comparison is made between observed mixing in bilayer and marker experiments. Here, we simply note that the suppression of stage III recovery is evident in many published results of ion beam mixing in metal systems. Bottiger et al's (1985) work on the

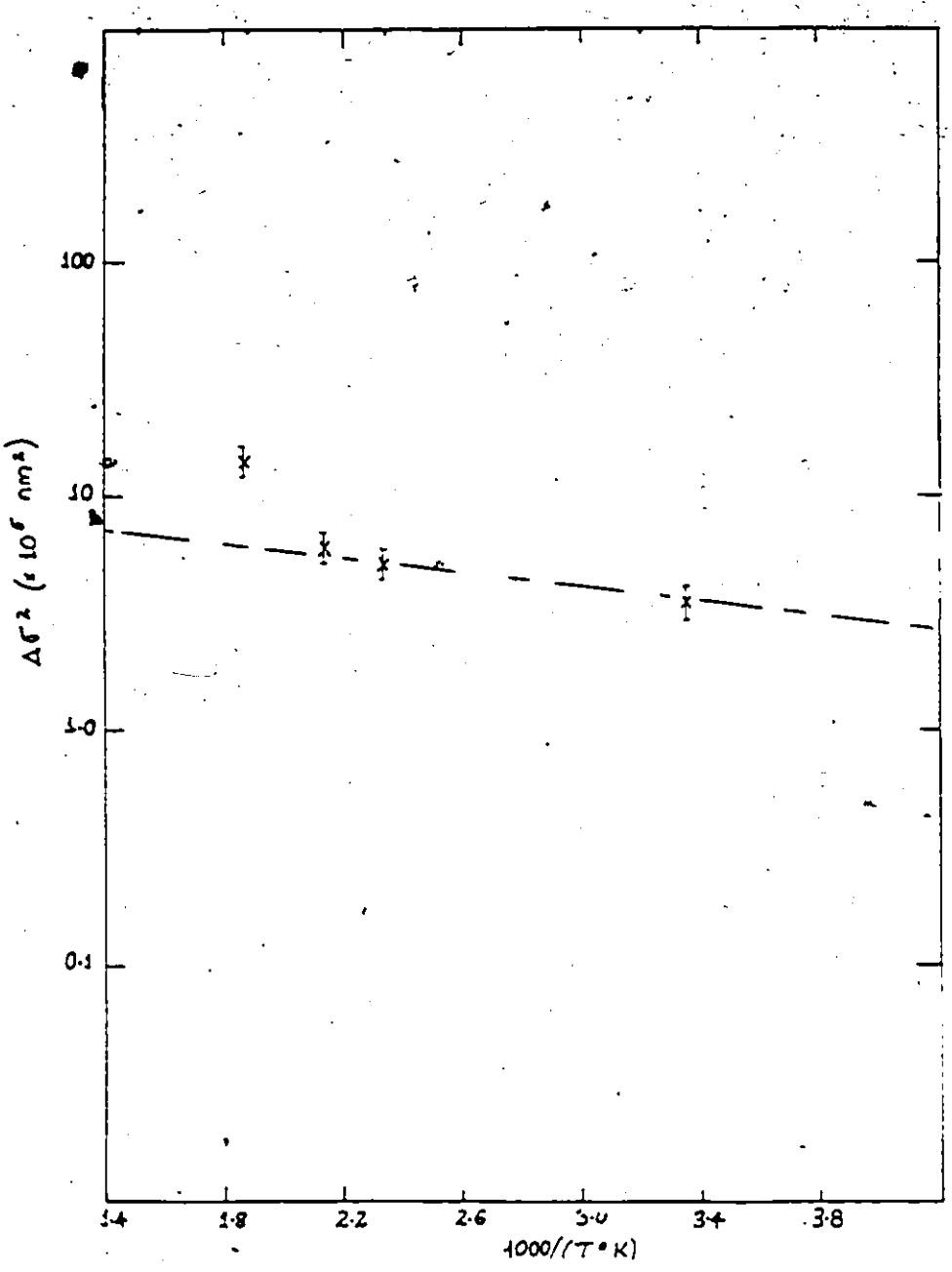

Fig. 6.16: Arrhenius plot of the mixing parameter, $\Delta\sigma^2$.

mixing of Ni/Au induced by 150 keV Ar irradiation is typical. In this system, a strong temperature dependence is not apparent until above ∿ 420 K, the beginning of stage IV recovery in Ni.

iv) Correlation between bilayer and buried marker experiments

A comparison is now presented of the results from the marker spreading experiments discussed in section 6.1 to those for mixing of Ni/Pd bilayer couples. In Fig. 6.17 the measured $\Delta\sigma^2$ values following Ar^+ irradiation to a dose of $1x10^{16}$ $Ar^+ \cdot cm^{-2}$ are plotted versus reciprocal temperature over the temperature range spanned by the two types of measurement. The full circles are the Pd marker spreading data while the open circles are for the bilayer results. At 298 K the mixing parameter $\Delta\sigma^2$ values measured either on the marker or the bilayer samples are identical, while at 473 K the bilayer results are slightly larger than those for markers. The data points for the bilayer experiments at 393 and 423 K, lie, within error, on a smooth curve through the marker data points. It is therefore concluded that mixing properties, at each temperature, induced by 120 keV Ar irradiation of bilayers and buried markers are identical. This conclusion is not unexpected in view of the fact that Ni and Pd are mutually soluble over the entire composition range.

From radiation damage point of view, the energy deposited by a 120 keV Ar ion near the interface of a Ni/Pd couple is similar to that deposited at a Pd marker buried ∿ 40 nm below a Ni overlayer. Consequently, a similar number of atomic displacements and ion beam mixing should result. A denser Ar collision cascade will be expected in Pd and may lead to a spike-enhanced mixing in the bilayer because of the heavier mass of Pd (106) relative to Ni (58). However, the atomic packing in Pd is less

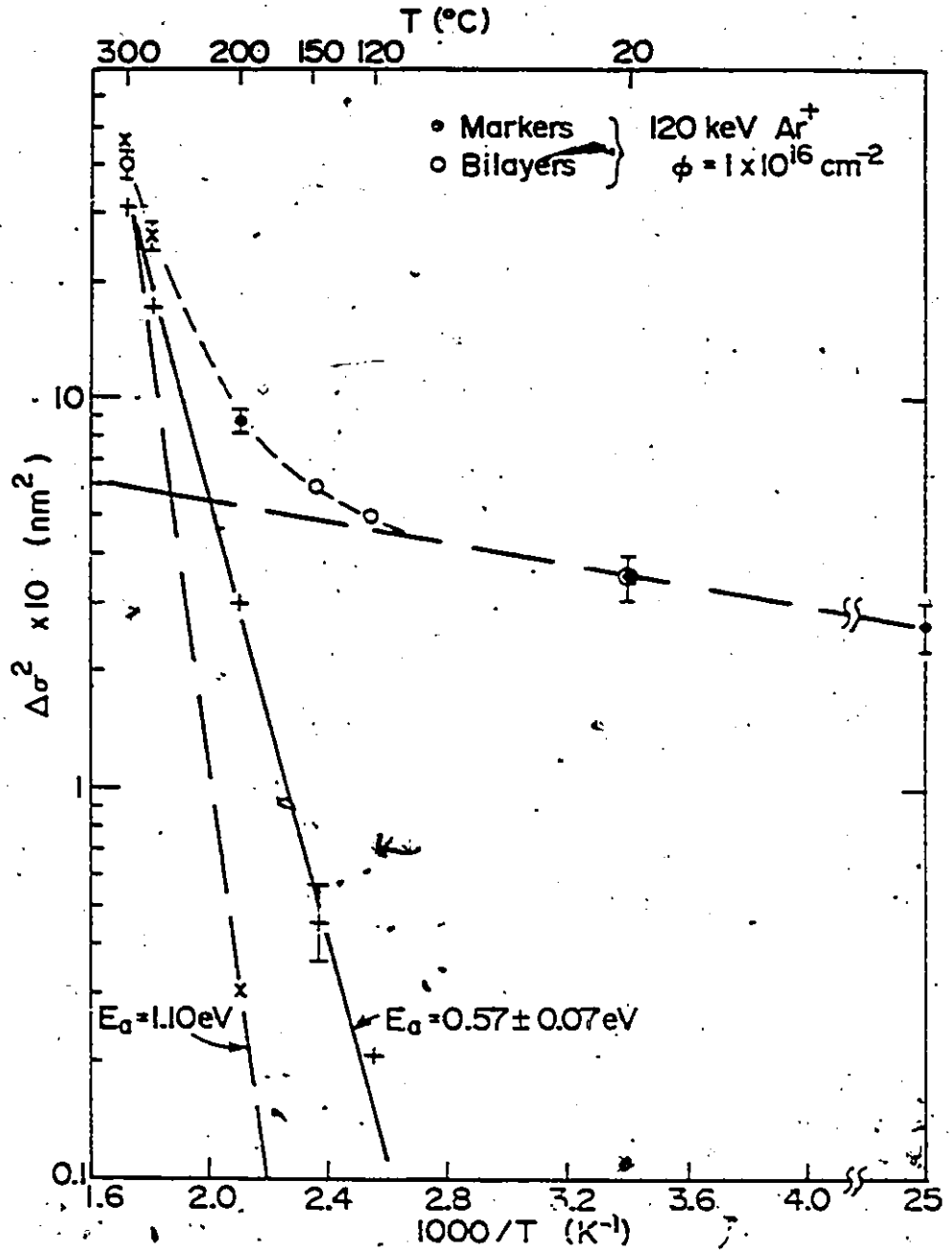

Fig: 6.17 Arrhenius plot of the mixing parameter for marker and bilayer couple.

dense (6.8×10^{22} cm^{-2}) than in Ni which leads to a similar deposited energy density, θ, ($\sim$ 0.3 eV/atom) based on the statistical average cascade dimensions in Ni and Pd. Thus if spikes indeed contribute to the mixing, the effect will be similar in both the bilayers and buried markers.

In Fig. 6.17, the slowly increasing mixing observed between 40 K and 393 K is ascribed to collision-cascade induced mixing though, as discussed earlier, the diffusion of interstitials escaping the collision cascade appears to contribute also. Thus the observed mixing above 393 K is due to both thermal and collision cascade induced contributions. In Fig. 6.17, the collision cascade contribution to $\Delta\sigma^2$ has been subtracted and the resulting radiation enhanced contribution is shown as the solid line. The dashed line represents the results of the measured spreading variance for samples annealed, without irradiation, at these temperatures. Below 473 K no measurable increase was observed in the variance of the thermally annealed markers. An apparent activation energy for radiation enhanced diffusion $E_a = 0.57 \pm 0.07$ eV was calculated from the solid linear curve. Within the errors of the measurements, this is $\sim$ one half of the value ($E_a \approx 1.10 \pm 0.07$ eV) measured for thermally annealed samples which suggests that the enhancement of mixing observed above $\sim$ 423 K is due largely to vacancy-interstitial recombination outside the collision cascades in accordance with the radiation enhanced diffusion model described in section 3.3.3 (Eq. (3.29). These energies are rather low; for example, the value of 1.1 eV determined for the annealed specimens is close to values typically determined for the recovery of resistivity in heavy-ion irradiated (1.04 eV) or cold worked (.9-1.27 eV) Ni and Pd specimens. More will be presented about these properties in section 6.2.3 but the results suggest that the as-prepared

specimens contain large concentrations of defects or grain boundaries. In section 6.2.3 it will be shown that this low activation energy is due largely to grain boundary diffusion.

(v) Estimate of the diffusion coefficients, D

Within the framework of the diffusion equations described in sections 6.1 and 6.2, the time evolution of the concentration profiles for a thin film buried between two semi-infinite layers (Eq. (6.2) and for a bilayer sample (Eq. 6.9) gives the following relationship between the measured mixing variances and diffusion coefficient D.

$$\Delta\sigma^2 = 4Dt \tag{6.14}$$

where t is the irradiation time. The time t is related to the dose ϕ and dose rate $\dot{\phi}$ by

$$t = \frac{\phi}{\dot{\phi}} \tag{6.15}$$

so that

$$D = \frac{1}{4}\Delta\sigma^2 \cdot \frac{\dot{\phi}}{\phi}$$

A constant diffusion coefficient D independent of concentration is assumed in this analysis. Table 6.5 shows the calculated values of D at different temperatures for samples irradiated to a dose of 1×10^{16} Ar^+ cm^{-2}. In the context of irradiation induced mixing, a more meaningful parameter is the extent of diffusion induced, per ion, by the irradiation. This quantity, $\frac{\Delta\sigma^2}{\phi}$, is also shown in Table 6.5. The $\frac{\Delta\sigma^2}{\phi}$ values range from 2.5×10^{-29} cm^4/ion at 40 K to 40×10^{-29} cm^4/ion at 573 K, while the corresponding diffusion coefficients range from $\sim 3.4\times10^{-17}$ to 5.5×10^{-16} cm^2/sec.

Table 6.5: Measured mixing parameter $\Delta\sigma^2$ and corresponding diffusion coefficients following 120 KeV Ar^+ irradiations at various temperatures.

T (K)	$\Delta\sigma^2$ ($\times 10$ (nm^2)	D_{rad} ($\times 10^{-17}$ cm^2-sec^{-1})	$\Delta\sigma^2/\phi$ ($\times 10^{-29}$ cm^4/ion)
40	2.5	3.44	2.5
298	3.5	4.81	3.5
393	5	6.88	5.0
423	6	8.25	6.0
473	14	19.25	14
553	26	35.75	26
573	40	55.00	40

6.2.1.2 Collision Cascade Mixing Model

A model is proposed for the collisionally-induced broadening of the interface between two layers. This model is applicable to (1) non-compound forming systems, (2) systems mixed at moderate doses where the mixing is confined to regions near the interface, and (3) low enough temperatures that radiation-enhanced diffusion effects are suppressed.

As discussed in chapter 3, one consequence of energy deposition into the lattice by an energetic heavy ion is the creation of a cascade of moving atoms. In each collision cascade, the deposited nuclear energy creates a large number of moving atoms. The net effect, for a collision cascade spanning an interface between layers of different elemental composition is an intermixing between the layers; this is called cascade mixing. For doses typical of ion-beam mixing ($\sim 10^{16}$ ions/cm^2), an implanted region receives $\sim 10^3$ successive overlapping cascades resulting in a cumulative effect of ballistic mixing. Figure 6.18 illustrates the individual collision cascades initiated by each ion impact while Fig. 6.19 shows that after a sufficient dose ($\sim 10^{16}$ cm^{-2}) cascade overlap has occured and the resultant atomic mixing is then a result of successive overlapping cascade.

Let the region of the sample covered by each cascade be $\sigma_c << A_s$ where A_s is the sample area. If each ion impact results in an average displacement $\ell = \sqrt{D\tau}$ where τ is a characteristic time constant and D is the diffusion coefficient, then after two overlapping impacts, the net displacement will be $\sqrt{2}\,\ell$, and after g such impacts $\sqrt{g}\,\ell$. Now g, the number of overlapping cascades, is

$$g = \phi\sigma_c \qquad (6.16)$$

where ϕ is the ion dose and σ_c is the area covered by each cascade. Then

LOW DOSE << 10^{13} << HIGH DOSE

ions/cm^2

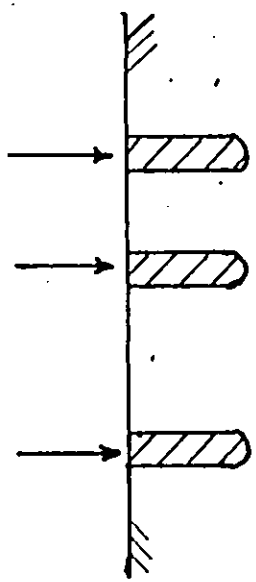

Fig 6.18

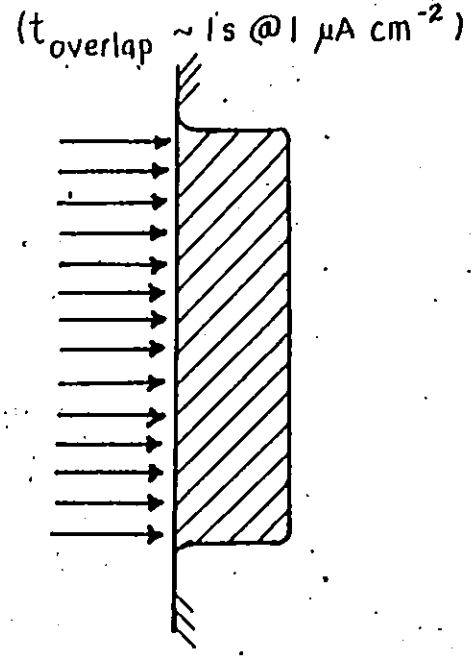

Fig 6.19

Fig.6.18 Schematic illustrating individual collision cascades

Fig.6.19 Cascade overlap resulting from cummulative bombardment

the characteristic thickness of the mixed layer after a dose of ϕ will be

$$\sqrt{\phi\sigma_c}\,\ell \quad . \tag{6.17}$$

Thus the evolution of the concentration profiles near the interface following ion irradiation can be described as

$$C(X,\phi) = \frac{C(0)}{2}\,\mathrm{erfc}\left[\frac{X}{\ell\sqrt{\phi\sigma_c}}\right] \tag{6.18}$$

in the case of a semi-infinite bilayer sample, and as

$$C(X,\phi) = \frac{M(0)}{2\ell\sqrt{\phi\sigma_c}}\exp - \frac{X^2}{4\ell^2\phi\sigma_c} \tag{6.19}$$

in the case of a narrow marker buried between two semi-infinite layers of matrix, where $M(0)$ is the initial amount of material (cm^{-2}) present before bombardment. Equation (6.19) is valid also when ion-induced spreading of an initially narrow and Gaussian distribution of an overlayer film is being studied. In this case M is not constant since erosion occurs by sputtering and $M(\phi)$ must be used. In the case of composition profiling by RBS, Eqs. (6.18) and (6.19) can be converted to RBS yield profiles such that Eq. (6.18) becomes

$$Y(X,\phi) = \frac{Y(0)}{2}\,\mathrm{erfc}\left[\frac{X}{\ell\sqrt{\phi\sigma_c}}\right] \quad .$$

The measured spreading variance is then given by

$$\Delta\sigma^2 = \ell^2\cdot\phi\sigma_c \tag{6.20}$$

i.e. the model predicts a linear dependence of $\Delta\sigma^2$ on the ion dose, ϕ, and

cascade dimension, σ_c.

An estimate of the magnitude of mixing predicted by Eq. (6.20) can be made by using reasonable values of the parameters ℓ^2, and σ_c. As pointed out in chapter 3, (Eq. (3.16), most displacements within the cascades are due to low-energy recoils, these recoils being more numerous ($\sim 10^3$:1) than high-energy recoils. Consequently the net long range displacements resulting from those atoms having high energies are ignored. The net mean displacement distance of low-energy recoils estimated by several authors (e.g. Andersen 1979), is usually small, $\sim$ 0.3-1 nm, and does not change much from one ion and target type to another. The area occupied by each cascade, σ_c, on the other hand depends on the ion type, its energy and the target mass.

At this point it is important to distinguish between the averaged statistical cascade dimensions (resulting from a large number of cascades) and the area occupied by individual cascades, σ_c. The individual cascade dimensions have been obtained by Monte Carlo simulation (Walker 1978) and can be vastly different from average statistical cascade dimensions obtained from WSS theory (Winterbon 1974). When the incident ion is heavy, the deposited energy distribution (and therefore damage distribution) within the individual cascade is distributed fairly uniformly within the statistical cascade envelope. The average statistical cascade dimensions accordingly provide a reasonable approximation of the individual cascade dimensions. However for light ions, the individual cascades occupy only a small fraction of the statistical cascade volume and the statistical cascade dimensions calculated from WSS (1974) must be corrected by this volume fraction in order to obtain σ_c for substitution in Eq. (6.20). The magnitude of this one-

dimensional cascade correction factor, (δ_{corr}), has been evaluated by Walker et al. (1978) as a function of mass ratio, and its implication for deposited energy density, θ, within cascades has been discussed by Davies (1982). For a 120 KeV Ar irradiation of Pd ($\frac{M_2}{M_1} = 2.65$), $m = \frac{1}{3}$ is the appropriate power cross-section approximation and the one-dimensional cascade correction is taken from their curve for Ge. This correction for 120 KeV Ar^+ on Pd is $\sim$0.15.

The average statistical cascade dimensions are estimated from the relative transverse straggling $\frac{\langle y^2 \rangle}{\langle \Delta x \rangle^2} = .5953$ and the mean damage depth $\langle x \rangle = 30.8$ nm giving an individual cascade dimension of

$$\delta_{corr} \cdot \langle y^2 \rangle^{\frac{1}{2}} = 3.57 \text{ nm}$$

and cascade area

$$\sigma_c = \frac{\pi}{4} [\delta_{corr} \cdot \langle y^2 \rangle^{\frac{1}{2}}]^2$$

$$= 10 \text{ nm}^2 .$$

Insertion of this value in Eq. (6.20) and a value of 1 nm^2 for ℓ^2 gives a calculated value of

$$\Delta\sigma^2 = 100 \text{ nm}^2$$

as the expected value after a dose of 1×10^{16} Ar^+ cm^{-2}. This estimate compares with $\Delta\sigma^2 = 35$ nm^2 measured at room temperature. Taking into account the simplicity of the model and the uncertainties in ℓ and σ_c, the agreement (within a factor of $\sim$ 3) is reasonable.

6.2.2 Ion Mixing of Ni/Pd Bilayer Couples above 473K

Samples for the experiments described in this section consist (as discussed previously in section 5.1) of polycrystalline Ni or sapphire substrates with evaporated films of Ni ($\sim$ 100 nm) and Pd ($\sim$ 40 nm). The overall thickness ($\sim$ 140 nm) of the evaporated layers is greater than the range of the bombarding ions ($R_p + 2\Delta R_p \sim 90$ nm). Consequently, what is being studied here is the intermixing between the small-grained evaporated Ni and Pd layers. The as-prepared samples were analysed with 2 MeV He^+ ion, then raised to a prescribed temperature and irradiated with 120 KeV Ar^+ ions. After a specific Ar^+ dose, the heater was shut off, the sample allowed to cool and an RBS spectrum of the bombarded samples taken. The effective time the sample is at temperature is estimated from the temperature-time profiles.

Figure 6.20 shows a typical RBS spectra for a Ni/Pd couple irradiated at 573K to various doses of 120 KeV Ar^+ ions. The dots represent the spectrum of the as-prepared sample, with the peak between channels 360 - 396 corresponding to the Pd signal. Also included in Fig. 6.20 (for reference) is the RBS spectrum, taken under identical experimental conditions, of a pure polycrystalline Ni sample. The times indicated in Fig. 6.20 are the times the sample was within 20K of 573 K.

The RBS spectra of Fig. 6.20 indicate a rapid intermixing of the Ni/Pd layers. Even for the lowest ion dose, Ni is seen to have migrated through the Pd overlayer film to the surface resulting in a drop in the Pd surface peak height. The high energy region of the Ni signals

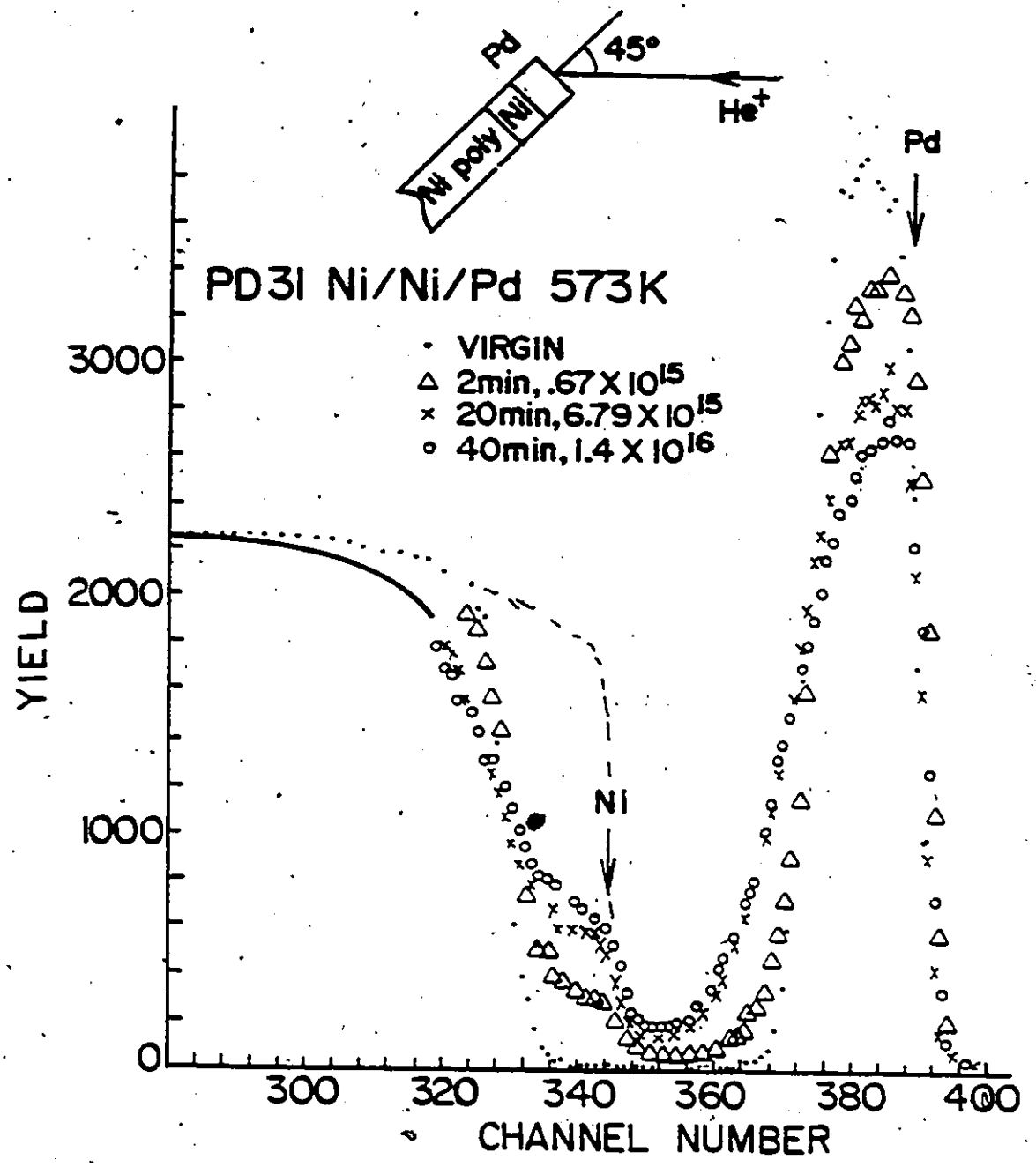

Fig. 6.20: Typical RBS spectra obtained for small-grained Ni/Pd couples irradiated at 573K to various doses of Ar^+ ions.

for the bombarded Ni/Pd couple shows flatish profiles between channels ~ 340 - 348 indicative of an almost uniformly mixed region extending over the thickness of the Pd overlayer film. The height of the plateau increases, initially rapidly with irradiation dose, but slows down at higher doses. The fact that the height of these flat profiles increases with ion dose indicates that stable intermetallic compounds of fixed composition are not being formed. The extent of the mixed region is indicated by the increasing backscattering yield, following irradiation, of the Pd signals in the channel 356 to 376 region, and the reduction in the Ni yields near channel 316 to 336. The total diffusion-affected zone is comparable to $R_p + 2\Delta R_p$ (~ 90 nm) of the bombarding ions and is confined to the small-grained evaporated films.

Figure 6.21 shows typical RBS profiles for a sample annealed, without irradiation, at 573 K. An initial rapid migration of Ni through the Pd film, similar to that observed for the irradiated case, is evident in Fig. 6.21. However, the surface Ni concentration levels are smaller here and, unlike the irradiated case where a surface layer with almost uniform Ni composition was formed, there is a large gradient in the Ni concentration i.e. less uniform layers were formed by thermal annealing. Also the overall extent of thermally-induced intermixing is less than in the irradiated case. The diffusion of Pd through the Ni film (and conceivably Ni through the Pd film) is dominated by a deeply penetrating tail (channels 350-380) whose overall level increases initially with annealing time and then saturates after ~ 20 minutes of anneal. Similar saturation of the Ni distribution can be seen in

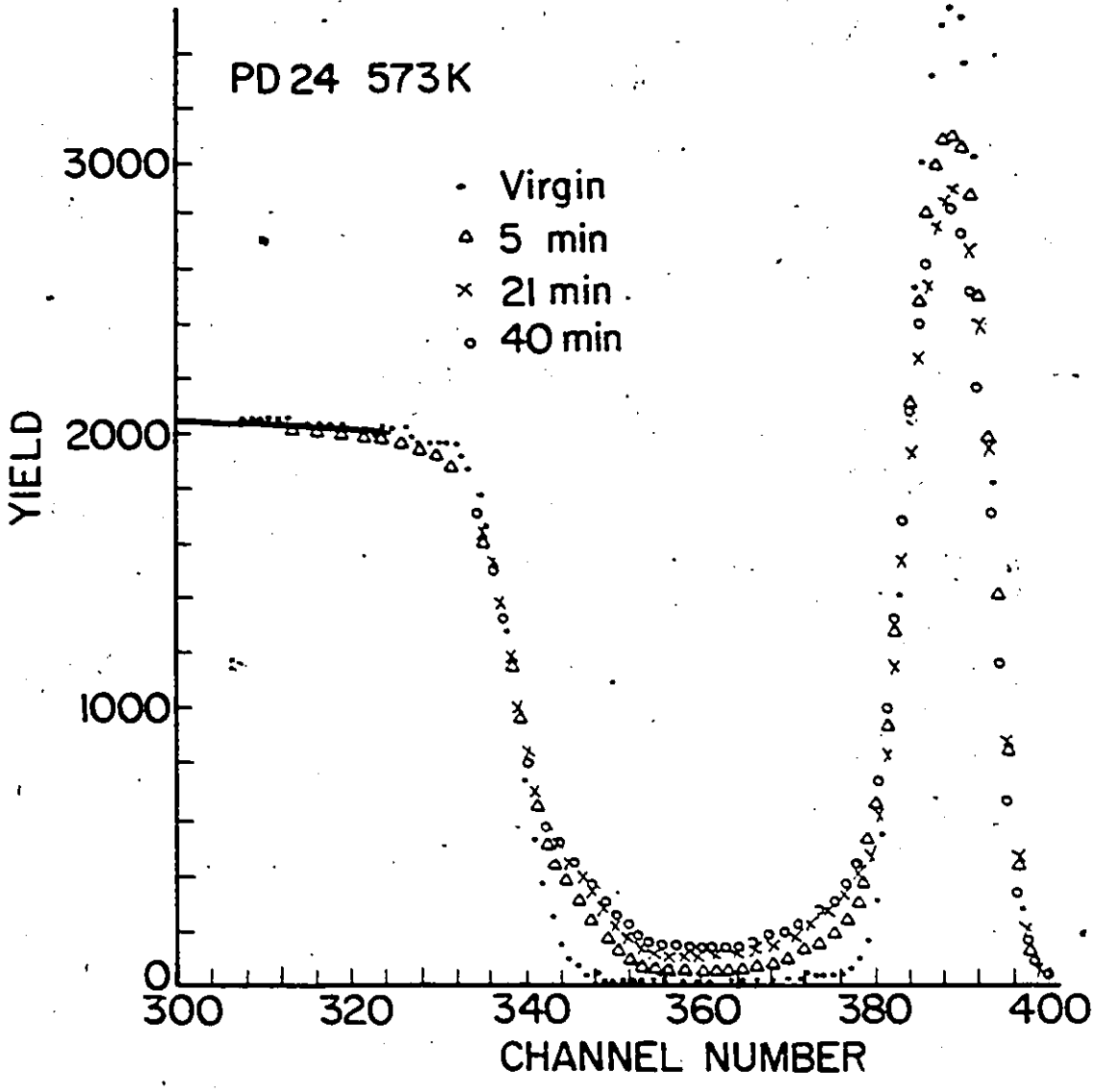

Fig. 6.21: Typical RBS spectra of small-grained Ni/Pd couples for various annealing times at 573K.

the high energy region of the Ni signal. Figure 6.20 shows that there is increased broadening of the interface between the films (near channel 332 for Ni and 376 for Pd) with increasing ion dose. Such broadenings are not evident in Fig. 6.21 and indicate that, at 573 K, bulk diffusion effects do not contribute much to the intermixing observed in the purely thermal anneal case.

The RBS profiles shown in Figs. 6.20 and 6.21 were converted to atomic concentration profiles using the procedure outlined in section 4.3 (Eq. 4.23). The Pd distribution in the alloy was obtained by comparing its RBS yield in the alloy to that of a pure Pd specimen taken under identical experimental conditions (e.g. He^+ beam energy and current). The Ni concentration profiles were obtained in a similar manner, i.e. by comparing the Ni yields in the alloy to the yield of a pure polycrystalline Ni sample. As discussed in section 4.3 the stopping cross-sections of Eq. (4.23) depend on compositions therefore the only way to obtain the concentration distributions is by an iterative procedure and consequently a computer program was written to evaluate these distributions.

Figures 6.22a and 6.22b show the Pd and Ni concentration distributions respectively for the alloy of Fig. 6.20, while Fig. 6.23 shows the distributions for the annealed sample of Fig. 6.21. The error in the concentration levels is due mainly to the statistical errors in the RBS yields and is $\sim$ 5%, while the errors in the depth scale ($\sim$ 10%) arise mainly from the accuracy with which the stopping cross-section [ε_0] for the He^+ ions is known. Figure 6.23 for the annealed specimen shows that the Pd redistribution following annealing is dominated by a

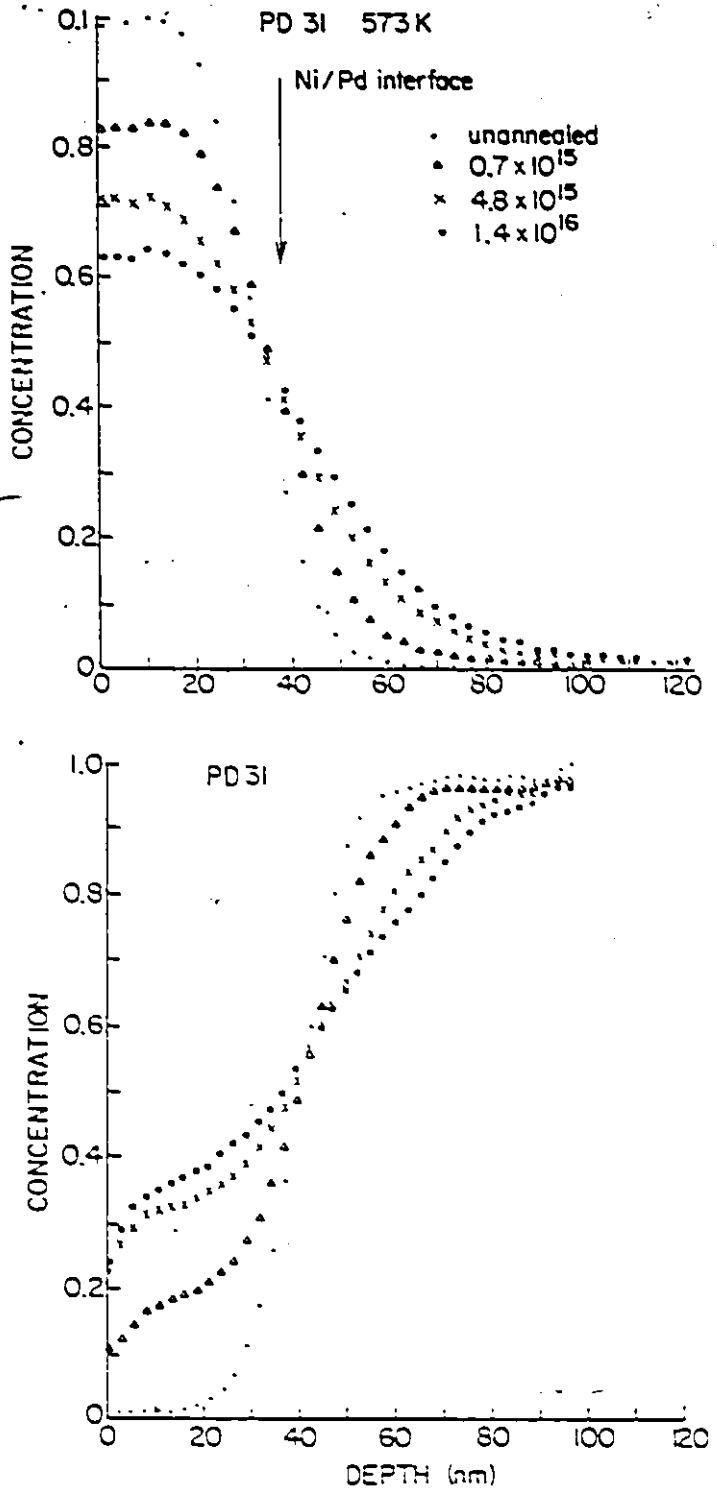

Fig. 6.22: Concentration-depth profile for Ni/Pd bilayer couple irradiated at 573K.
(a) Pd profile (b) Ni profile.

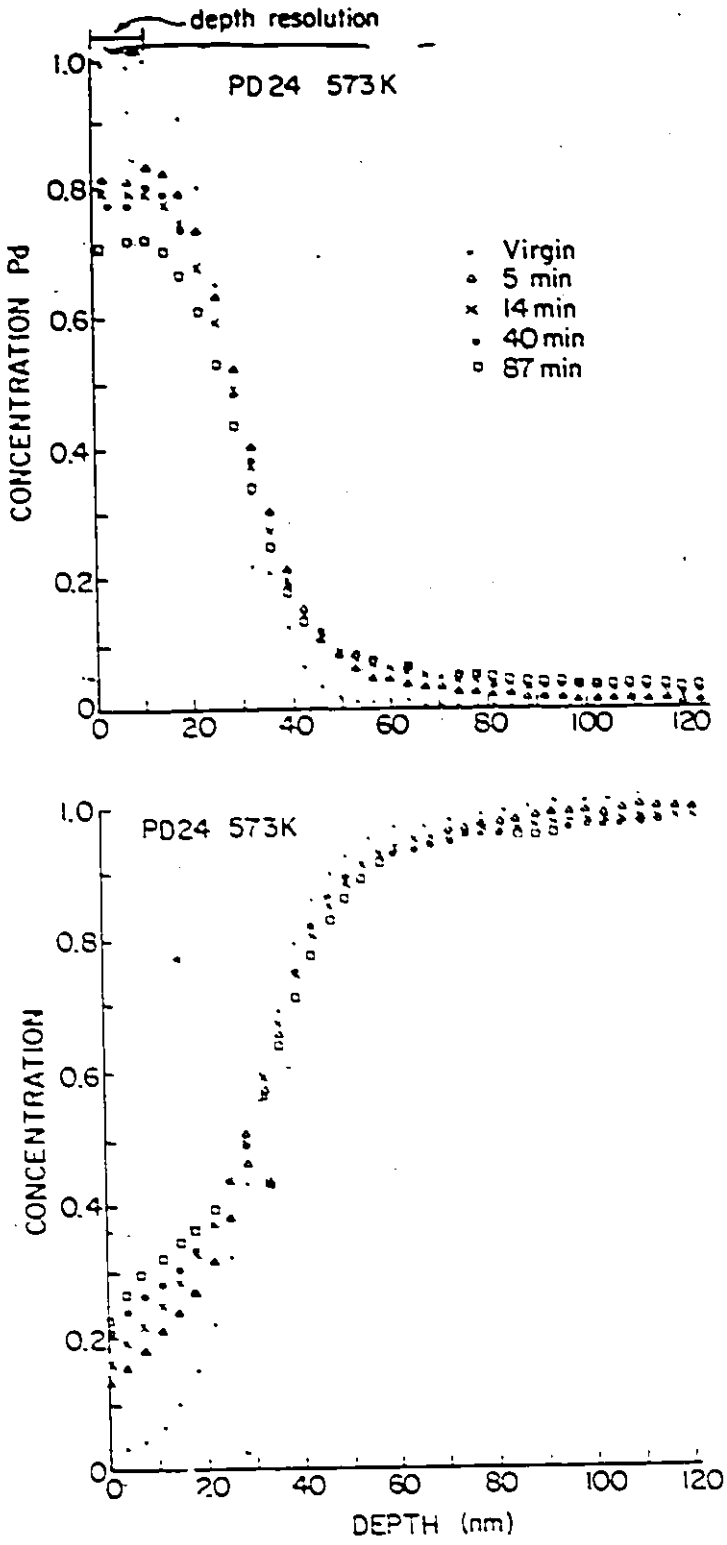

Fig. 6.23: Concentration depth profiles of a Ni/Pd couple annealed at 573K.

(a) Pd profile (b) Ni profile.

penetrating tail extending to a depth of $\sim$ 140 nm, with only a very small broadening of the interface. One possible explanation for this feature is that the redistributed Pd atoms diffused through the Ni grain boundaries with little contribution from bulk diffusions. This state of affairs will continue until the grain goundaries become saturated with solute, then further diffusion will occur with normal bulk-diffusion diffusivities. In Fig. 6.23, the saturation level of Pd in Ni is $\sim$ 3%, which is comparable to the fraction of the grain volume occupied by grain boundaries, $2\delta/\bar{L}$ = 5% where δ is the grain boundary width ($\sim$ .25 nm) and $\bar{L}$ the mean grain diameter of the as-deposited films, was determined by TEM to be $\sim$ 10 nm (see section 6.3). The separate contributions of grain boundary diffusion effects and diffusivities will be elaborated on in section 6.2.3. Here we note that the Pd concentration profile of Fig. 6.22a for the irradiated case does not exhibit a deep penetrating tail of constant composition similar to that observed for the unirradiated, annealed specimens. One possible explanation for this behaviour is as follows: grain boundary diffusion effects similar to that observed in the annealed specimens indeed occurred. However under irradiation, the region of the sample affected by each collision cascade encompasses many grains and grain boundaries (the linear dimensions of 120 KeV Ar cascade $\sim$ 20 nm). The net result is dumping of solute, initially at grain boundaries, directly into the grain interior by the collision cascades. In addition, solute diffusion from the grain boundaries to the grain interior occurs, not by thermal diffusivities but by a larger radiation-enhanced diffusivity

resulting from the increased defect concentrations generated by the collision cascades. As the process continues, the boundaries are fed with solute and then diffuse into grain interior. However the concentration of grain boundaries will decrease over time because of irradiation- (and thermal-) induced grain growth. Consequently radiation-enhanced diffusion within the grains becomes dominant. One then observes a less rapid build-up in the concentration levels as is indeed observed in Fig. 6.22. The mixing process in ion irradiated thin films, at these temperatures, is greatly influenced both by grain boundary diffusion effects and film re-growth.

The features discussed in this section for the thermally- and ion-induced mixing of Ni/Pd films at 573 K are characteristic of all samples bombarded above 423 K. Figures 6.24 and 6.25, for example, are typical of irradiated and unirradiated samples respectively at 523K. Figures 6.26 and 6.27 show typical profiles for samples irradiated and unirradiated at 623K while Fig. 6.28 shows the spectra for a sample irradiated at 673K. At 673, the enhancement of mixing by irradiation is overwhelmed by the thermal contributions.

6.2.2.1 Characterization of Mixing

In this section attempts are made to obtain quantitative information on the degree of mixing at each temperature due either to thermal effects only or to thermal plus ion irradiation. Because of the generally extensive level of intermixing observed and the limited thickness of the overlayer films, analysis based on the solution of simple diffusion equations is not possible. Nonetheless meaningful information regarding the mixing rates can be obtained either by considering the number of

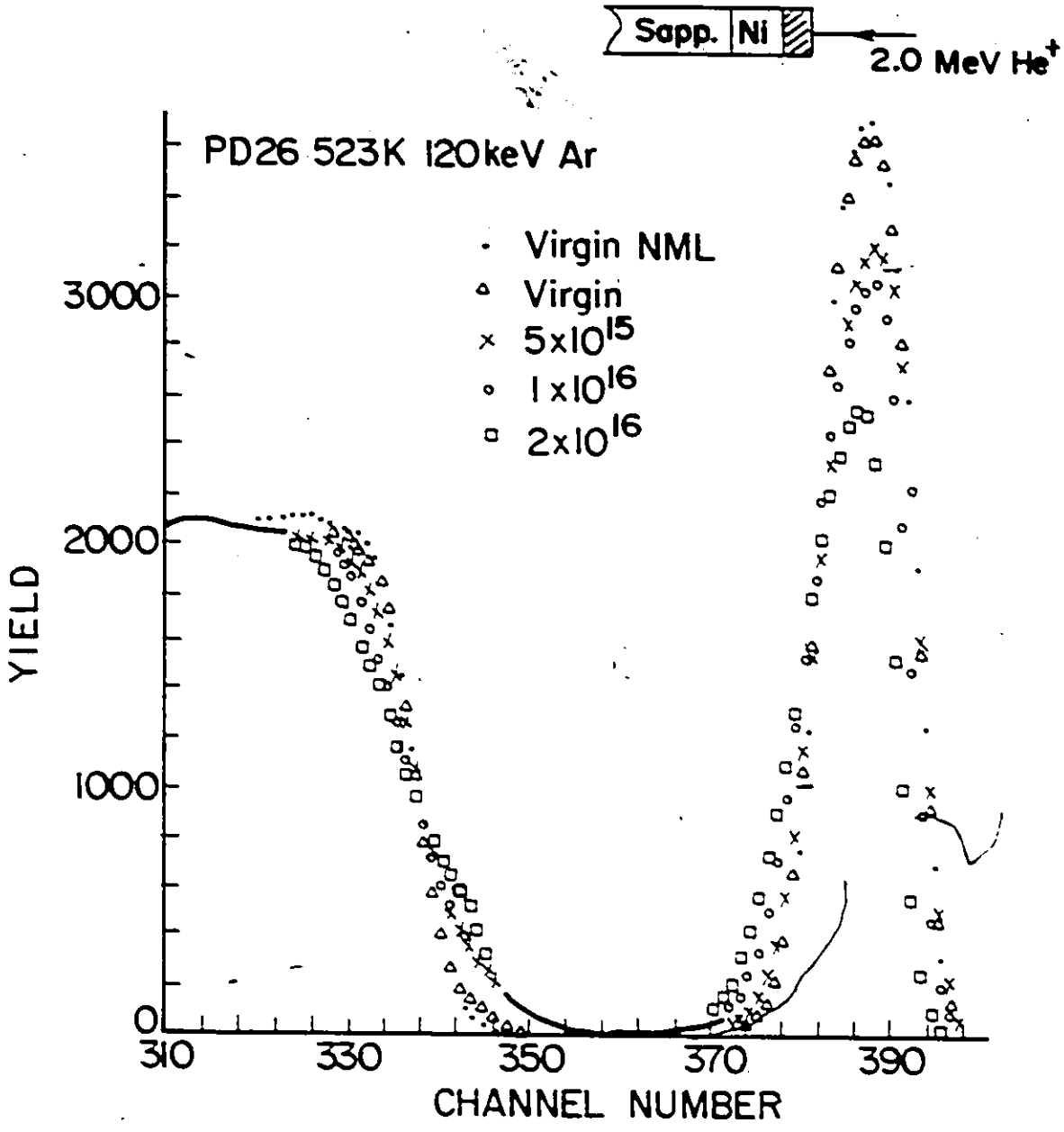

Fig. 6.24: Typical RBS spectra before and after irradiation to various doses of Ar for bilayer couples irradiated at 523K.

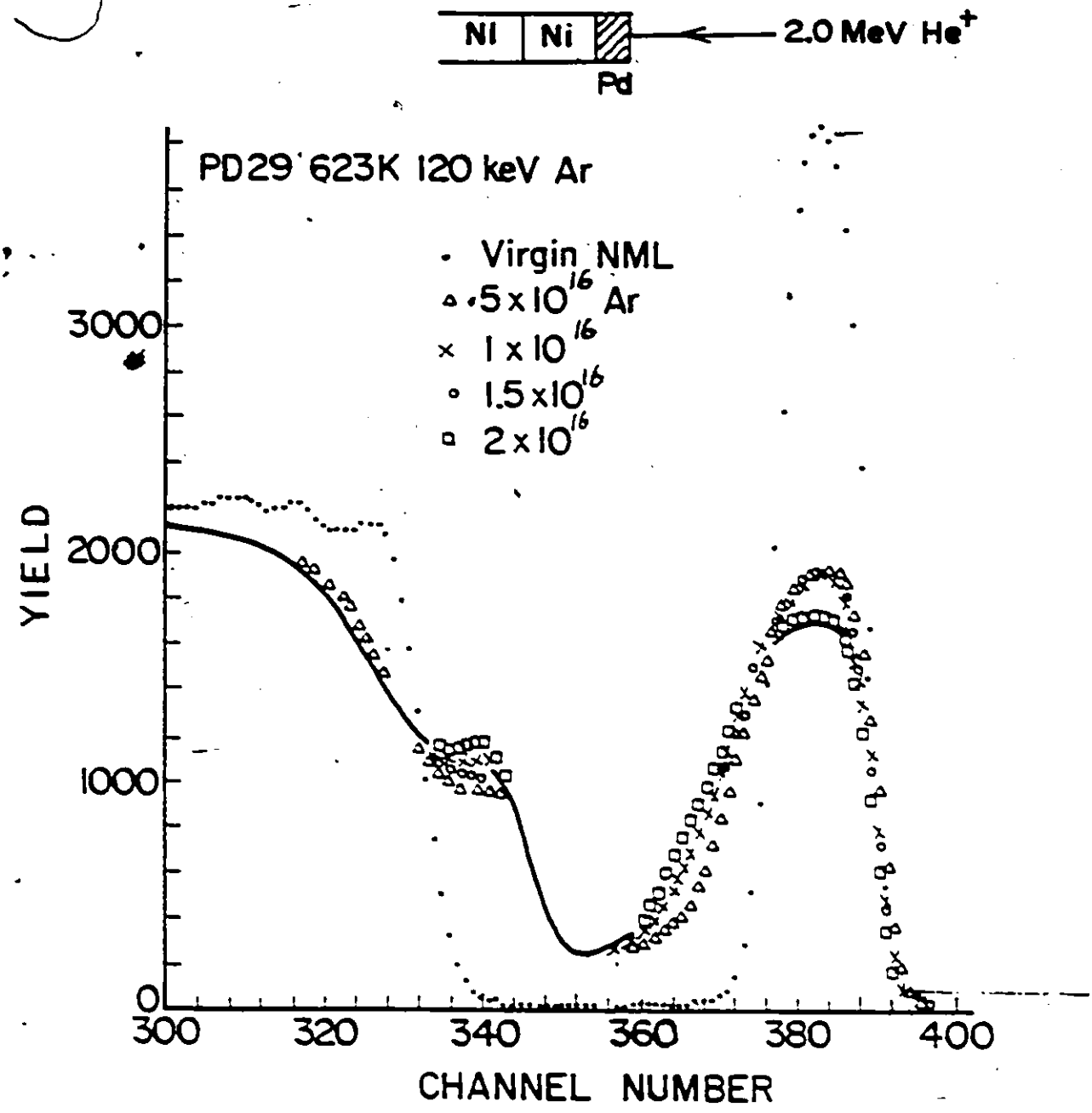

Fig. 6.26: Typical RBS spectra before and after irradiation at 623K to various doses of Ar^+ ions.

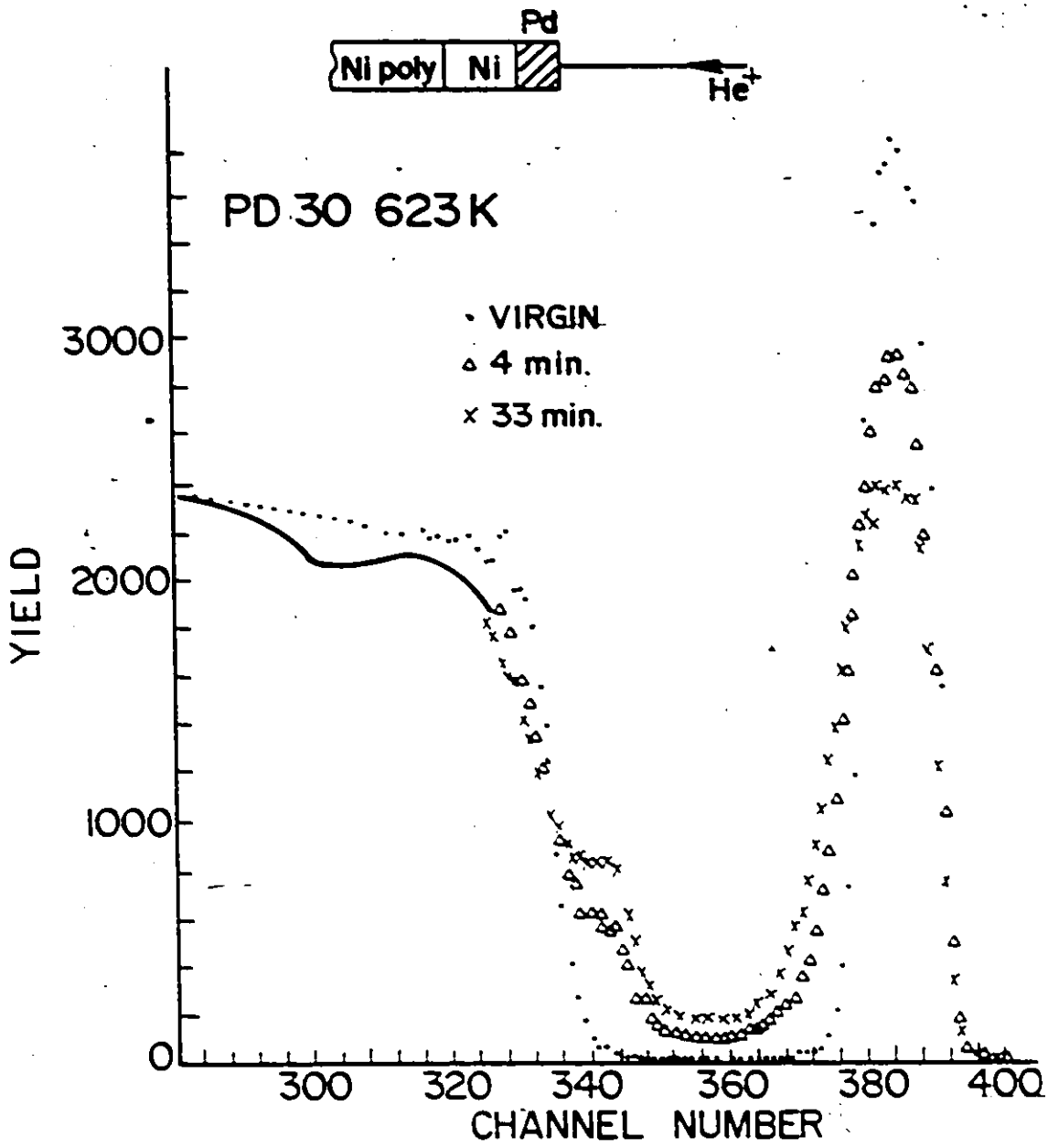

Fig. 6.27: Typical RBS spectra for annealed unirradiated Ni/Pd couple annealed at 623K.

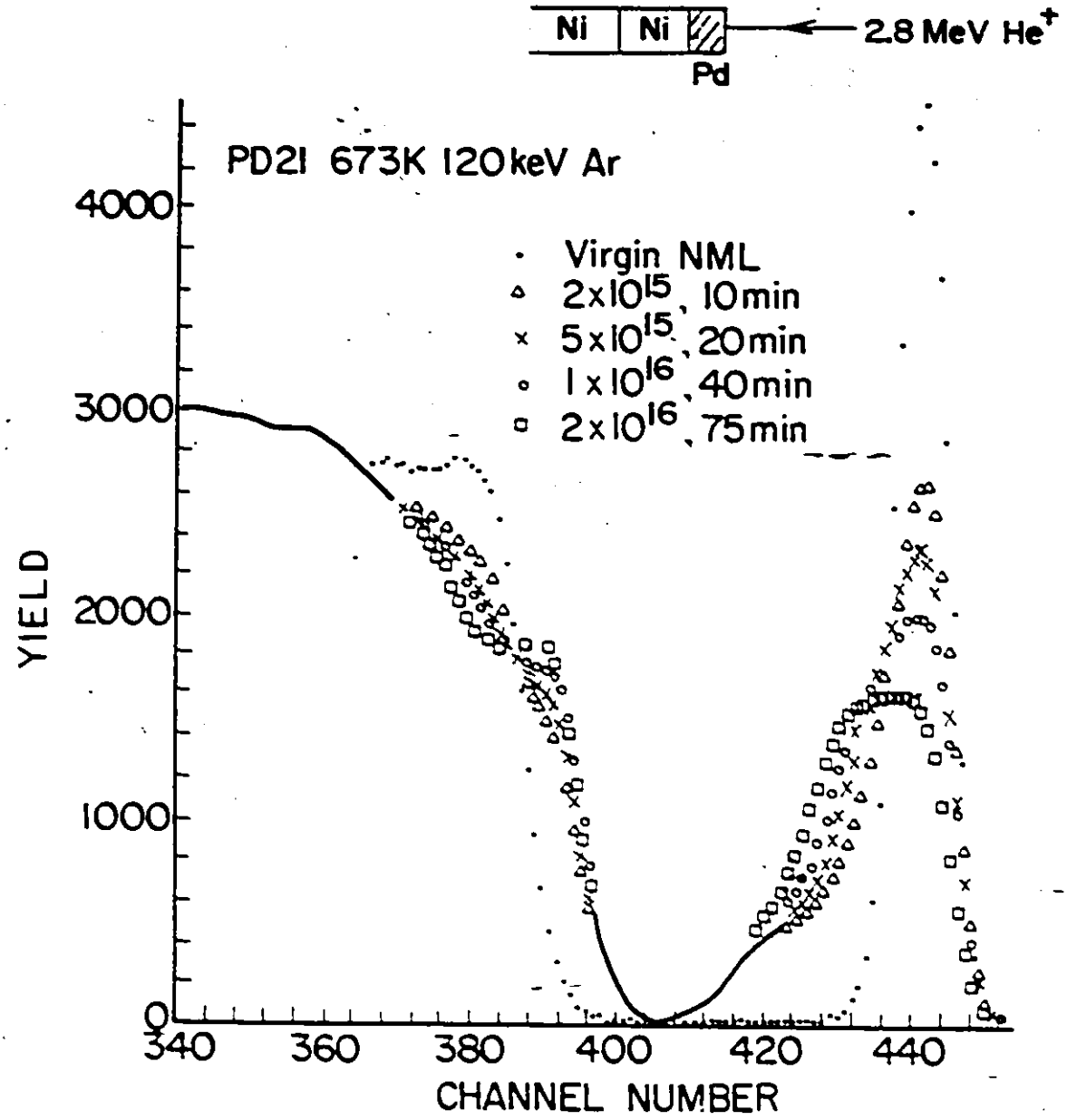

Fig. 6.28: RBS spectra typical of small-grained Ni/Pd couples annealed and irradiated at 673K.

atoms mixed beyond the original interface or the solution of diffusion equations where both lattice and grain boundary diffusion contribute significantly to atomic transport.

6.2.2.2 Number of Mixed Atoms

In this analysis, the numbers of Ni, or Pd atoms cm^{-2} which have been mixed into the other layer, i.e. beyond the initial interface between the two films, are estimated as a function of irradiation dose and temperature. In this analysis, it is assumed that no substantial migration of the initial interface occurred, an assumption which is probably justified because of the relatively invariant depth of the 50% compositon levels in Figs. 6.22 and 6.23. Once corrections for the overlayer film thickness removed by sputtering are made, all the profiles pass through the initial 50% composition point.

In order to obtain the number of mixed atoms, the backscattering yields beyond the 50% level are summed channel by channel. The net backscattering yield due to the mixed atoms is obtained by subtracting the yields due to the unirradiated or unannealed spectrum. In Fig. 6.29 the hatched area then gives the net backscattering yield due to Pd atoms mixed beyond the original interface while the cross-hatched area gives the net yield for mixed Ni atoms. The number of mixed Pd were also estimated from the Ni RBS yields by considering the reduction in the Ni yields due to the presence of Pd atoms. The hatched area W1 of Fig. 6.29b is due to 'missing' Ni atoms and is related to the number of mixed Pd atoms. The equivalent RBS yield due to the mixed Pd atoms, W2, can then be obtained from W1:

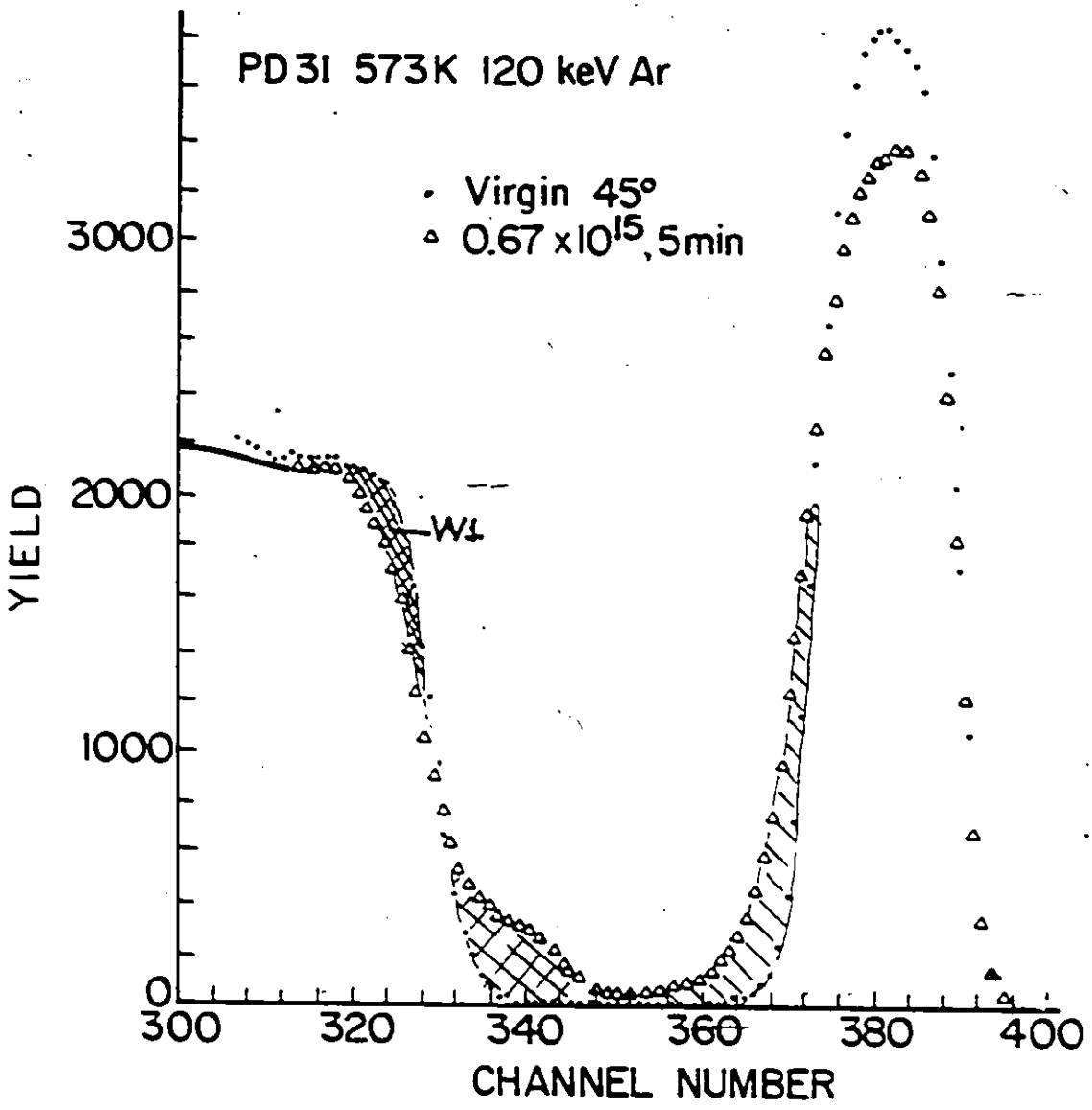

Fig. 6.29: Schematic illustrating how the number of mixed atoms were estimated.

$$W2 = W1 \cdot \frac{\left(\frac{d\sigma}{d\Omega}\right)_{Pd}}{\left(\frac{d\sigma}{d\Omega}\right)_{Ni}} \cdot \frac{[\varepsilon_0]_{Ni}}{[\varepsilon_0]_{Pd}}$$

These yields, W, were converted to the number of mixed atoms via Eq. (4.5)

$$W = (N\Delta X) \cdot Q \cdot \frac{d\sigma}{d\Omega} \cdot \Delta\Omega$$

so that

$$(N\Delta X) = \frac{W}{Q \cdot \frac{d\sigma}{d\Omega} \cdot \Delta\Omega} \quad \text{at. cm}^{-2} \qquad (6.21)$$

where Q is the total incident He^+ ions, $\frac{d\sigma}{d\Omega}$ is the differential scattering cross-section for He^+ ions which is given in Table 4.1 for Ni and Pd, and $\Delta\Omega$ is solid angle subtended at the target by the detector (section 5.2.4).

Figure 6.30 shows the calculated mixed Pd atoms cm^{-2}, plotted as a function of Ar irradiation dose for the various irradiation temperatures. Data for lower temperatures (298 - 423 K) are, within error, similar to that shown for 383 K and are not included for clarity. The error bars are due to the statistical errors in the backscattering yield W in equation (6.21) plus $\sim$ 5% error in $\Delta\Omega Q$. The reproducibility of the measurements is better than the statistical errors and an example is shown in Table 6.6.

Fig. 6.30 shows that below $\sim$ 523 K, the number of mixed atoms cm^{-2} exhibits, approximately, a linear dependence on irradiation dose, and mixing efficiencies (mixed atom/ion) of $\sim$ 0.6 at 383 K and $\sim$ 1.2 at 523 K. At 523 K and above, the curves show two distinct regions: a

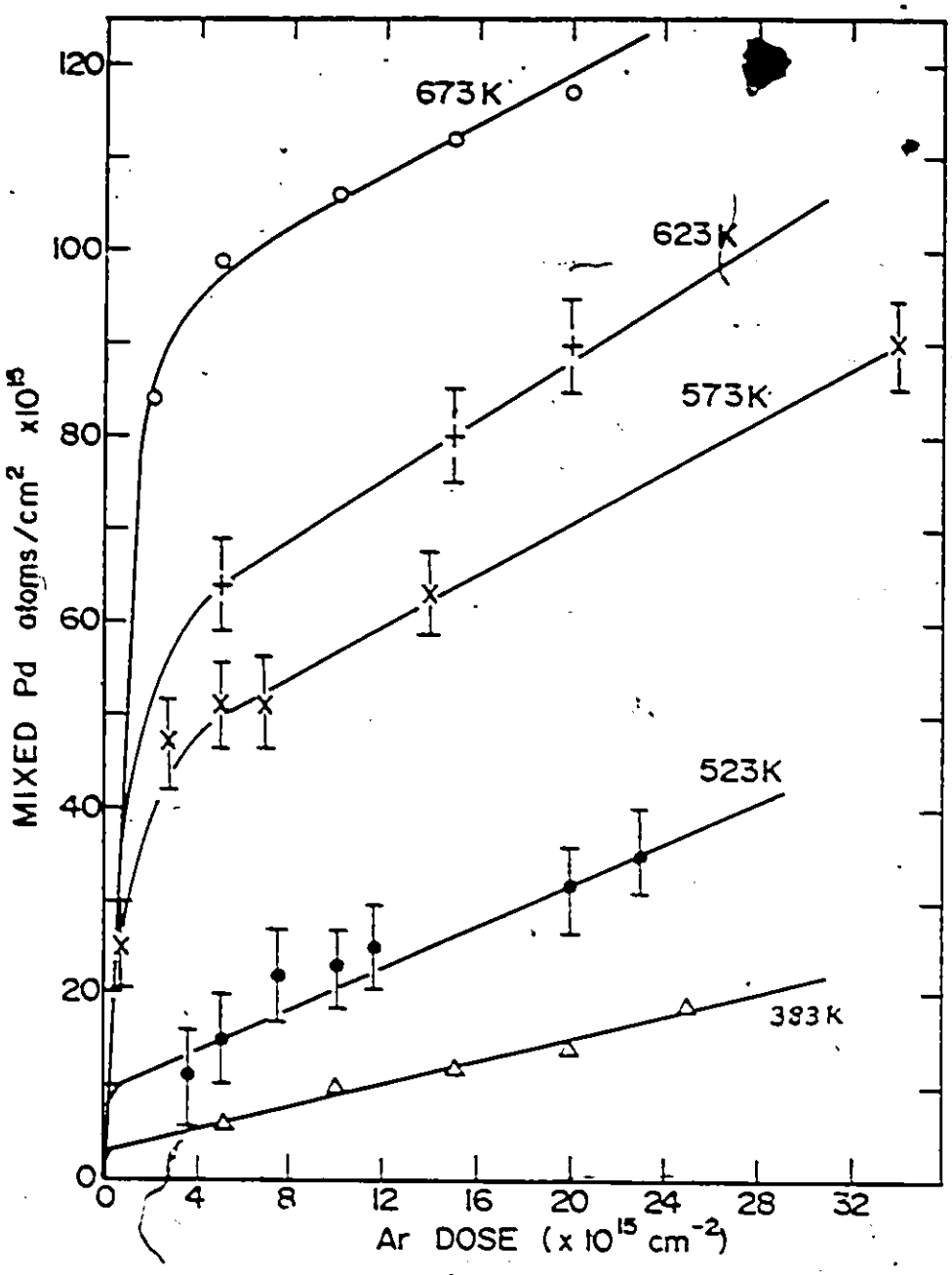

Fig. 6.30: Plot of number of mixed Pd atoms vs irradiation dose at various temperatures.

low dose region where the mixing increases fairly rapidly with irradiation dose, and a second region where the mixing rate slows to a less rapid rate. In the first region the mixing rate increases with irradiation temperature from $\sim$ 6 atoms/ion at 573K to $\sim$ 35 atoms/ion at 673K. We believe that this initial rapid mixing rate is due to atomic migration via the grain boundaries enhanced by solute diffusion from the boundaries to the grain interior. This idea is supported by the experimental observation on thermally annealed specimens shown in Fig. 6.31. This figure shows that, at each temperature, the initial rapid mixing levels and their duration in the annealed cases are similar to those for the irradiated specimens (e.g. at 673K mixed Pd $\sim 65 \times 10^{15}$ cm^{-2} after 4 minutes for the annealed case and 85×10^{15} cm^{2} after $\sim 2 \times 10^{15}$ Ar/cm^{-2} - 6 minutes of irradiation - for the irradiated case). For temperatures $<$ 673K the initial rapid mixing levels for the irradiated cases are higher than for the annealed cases probably because of additional contributions to mixing by collisionally induced mixing and radiation-enhanced mobility into the lattice. In Figs. 6.30 and 6.31, the mixing levels where the initial rapid rate slows to a less rapid rate increases with temperature (e.g. $\sim 45 \times 10^{15}$ cm^{2} at 573K and $\sim 90 \times 10^{15}$ cm^{2} at 673K for irradiated cases). If the mixed atoms in this region were contained entirely within the grain boundaries, one would expect a similar 'saturation level' at each temperature since similar concentrations of grain boundaries exist in these films. The increased saturation levels with increasing temperature is a consequence of the increased diffusion from the grain boundary regions to the grain interior.

Fig. 6.6 Number of Mixed Pd atoms vs Ar dose for two samples irradiated at 623K.

Ar Dose $x10^{15}$ cm^{-2}	Number of Mixed Pd Atoms $x10^{15}$ cm^{-2}	
	PD 26	Pd 32
3.64	-	11.2
5.0	18.1	-
7.4	-	22.3
10	22.6	-
11.6	-	24.5
20	32.0	-
22.9	-	30

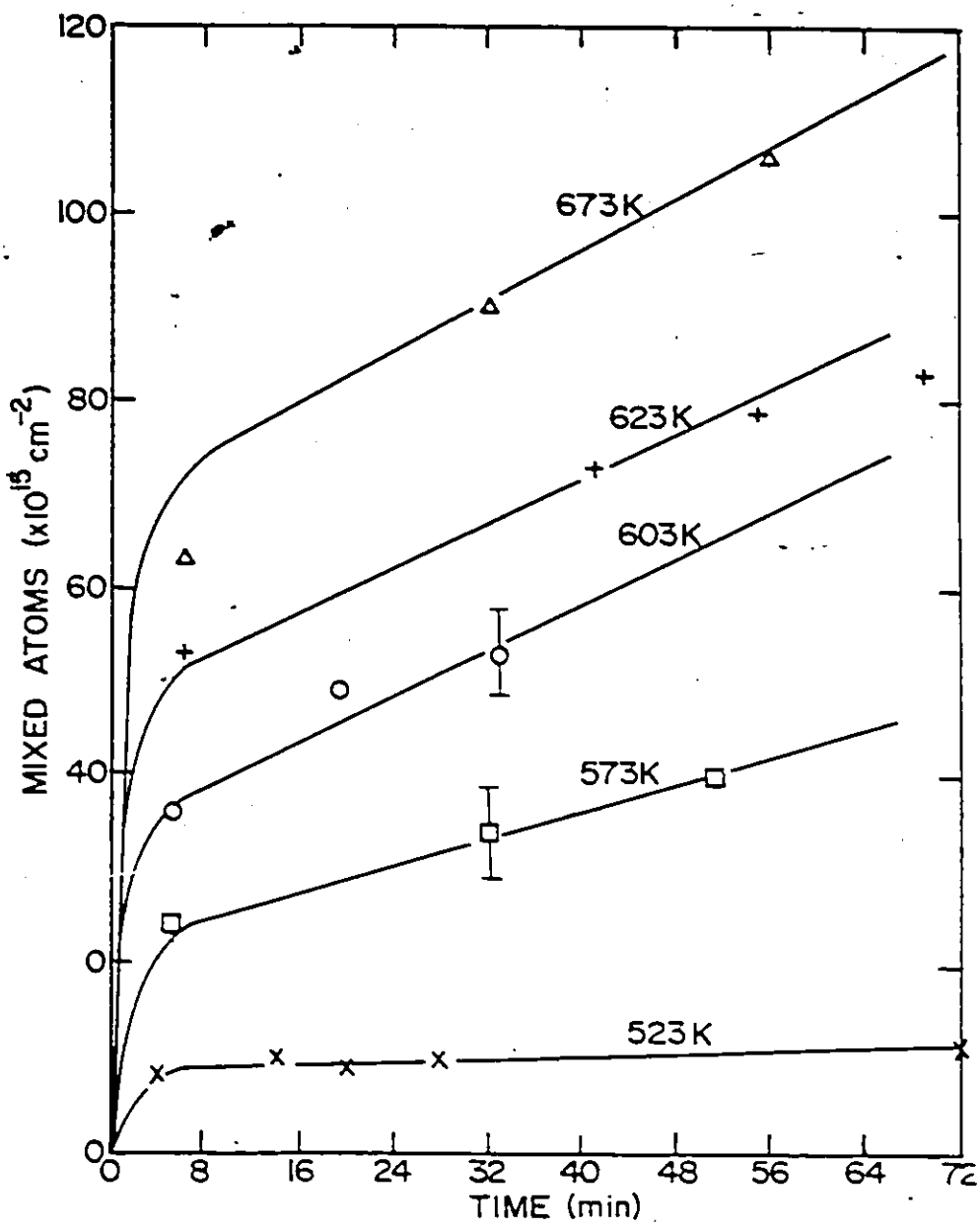

Fig. 6.31: Plot of mixed Pd atoms at various temperatures vs. annealing time.

In the second region, the mixing rate shows a less rapid rate, with mixing efficiencies close to $\sim$ 1.5 at/ion. This slower rate is believed to be due to two major effects. First, at the end of region one, all grain boundaries are saturated with solute and further mixing will occur by normal bulk diffusion (with bulk diffusivities for annealed cases and radiation-enhanced diffusivities for irradiated cases), with the grain boundaries serving mainly as a source of solute and possibly as defect annihilation sinks. Secondly, the concentration of grain boundaries decreases with time either as a consequence of thermally-induced or radiation-induced grain growth or both. The consequence of these effects is a slowing down of the mixing rates, as observed. In section 6.3 the experimental evidence for radiation/thermal-induced film growth will be presented. Here we simply note that other authors, Wang et al (1985) and Liu et al. (1986), have observed grain growth in irradiated Ni and Pd thin films as well. Liu et al's results show that for Pd films irradiated with 185 KeV Ar^+ ions, a saturated grain size is obtained after a dose of $\sim 4 \times 10^{15}$ Ar cm^{-2}. This dose is comparable to the onset of the slower mixing rate region observed in Fig. 6.30 and lends support to the arguments advanced above.

6.2.2.3 Estimate of Diffusion Coefficients

(I) Annealed specimens

Diffusion in small-grained polycrystalline metal films such as those under discussion here is complicated by the fact that diffusion may occur preferentially along grain boundaries and other defects. However, since grain boundaries comprise only a small fraction of the total volume (given roughly by $2\delta/L$ where δ and L are grain boundary width and grain diameter respectively), from a geometric argument alone, only a few at.% of solute could be lodged in the grain boundaries. In the present case, where the mean grain diameter $\tilde{L} \gtrsim 10$ nm and assuming $2\delta \sim .5$ nm, the maximum Pd concentration in the Ni grain boundaries will be $\sim 5\%$. Consequently one would expect a Pd concentration of $\sim$ 2-5% saturating the grain boundaries. On the other hand, in the temperature range under consideration (298-673K), simple lattice diffusion is not expected to contribute much to atomic transport. Borovskii et al. (1970), for example, have measured the inter-diffusion coefficients of a series of Ni/Pd bulk alloys at high temperatures. An extrapolation of their values for a 20% Pd alloy to low temperatures gives a $\tilde{D}_{\ell}(Pd)$ of $\sim 2\times10^{-22}$ cm^2 sec^{-1} at 673K, resulting in a diffusion length $\sqrt{Dt} \ll 0.1$ nm after a 20 hour anneal at 673K.

Figures 6.32(a,b), 6.33(a,b) and 6.34(a,b) show the concentration profiles for samples annealed, without irradiation at 573, 623 and 673K respectively, with the (a) series showing the Pd distribution and the (b) series the distribution for Ni. In these figures, the surface Ni concentration level is seen to increase with annealing time at a specific temperature, and with temperature for constant annealing time. The Pd distributions in Ni are characterized by a deeply penetrating tail extending > 100 nm into Ni; at each temperature, the concentration level (at a

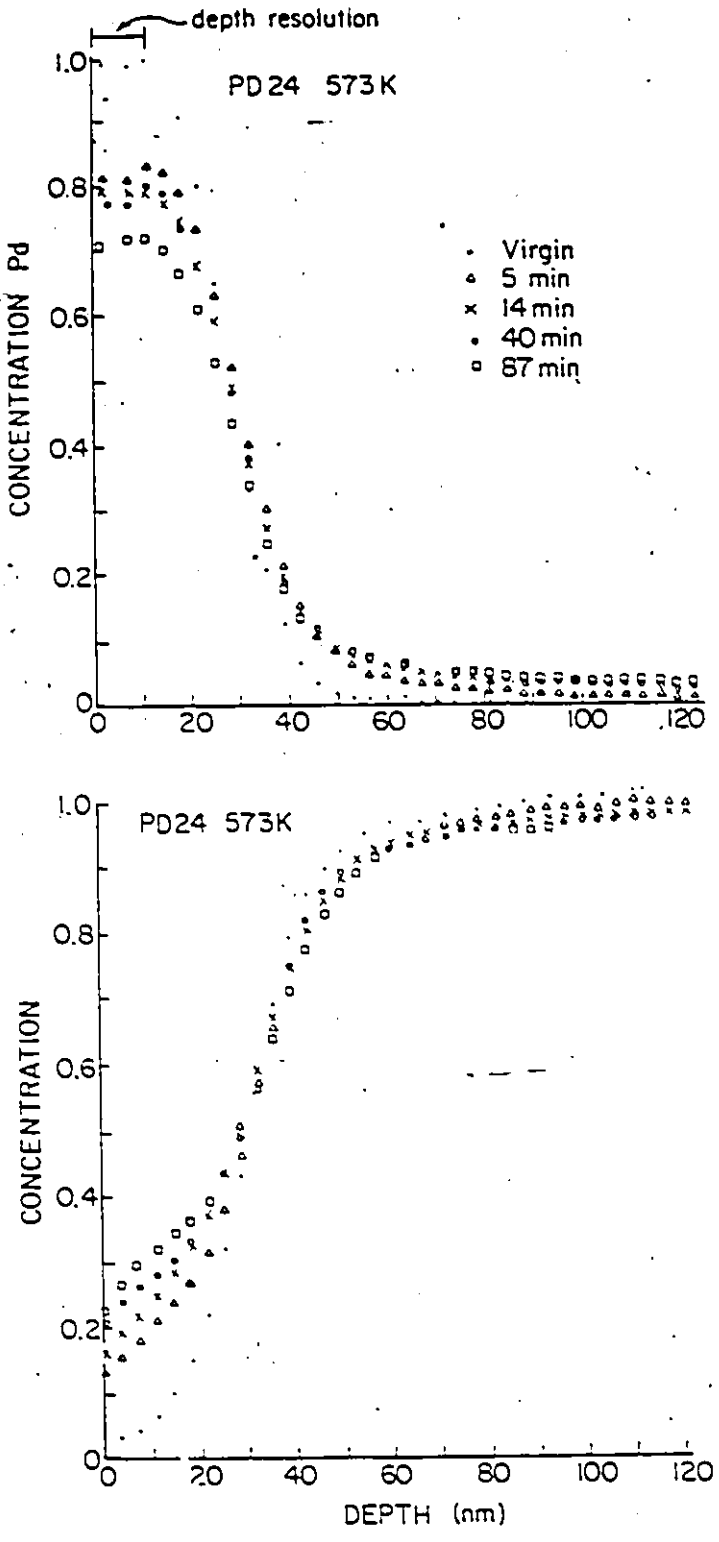

Fig. 6.32: Concentration-depth profile obtained from the RBS spectra of Fig. 6.21 for Ni/Pd couple annealed at 573K.

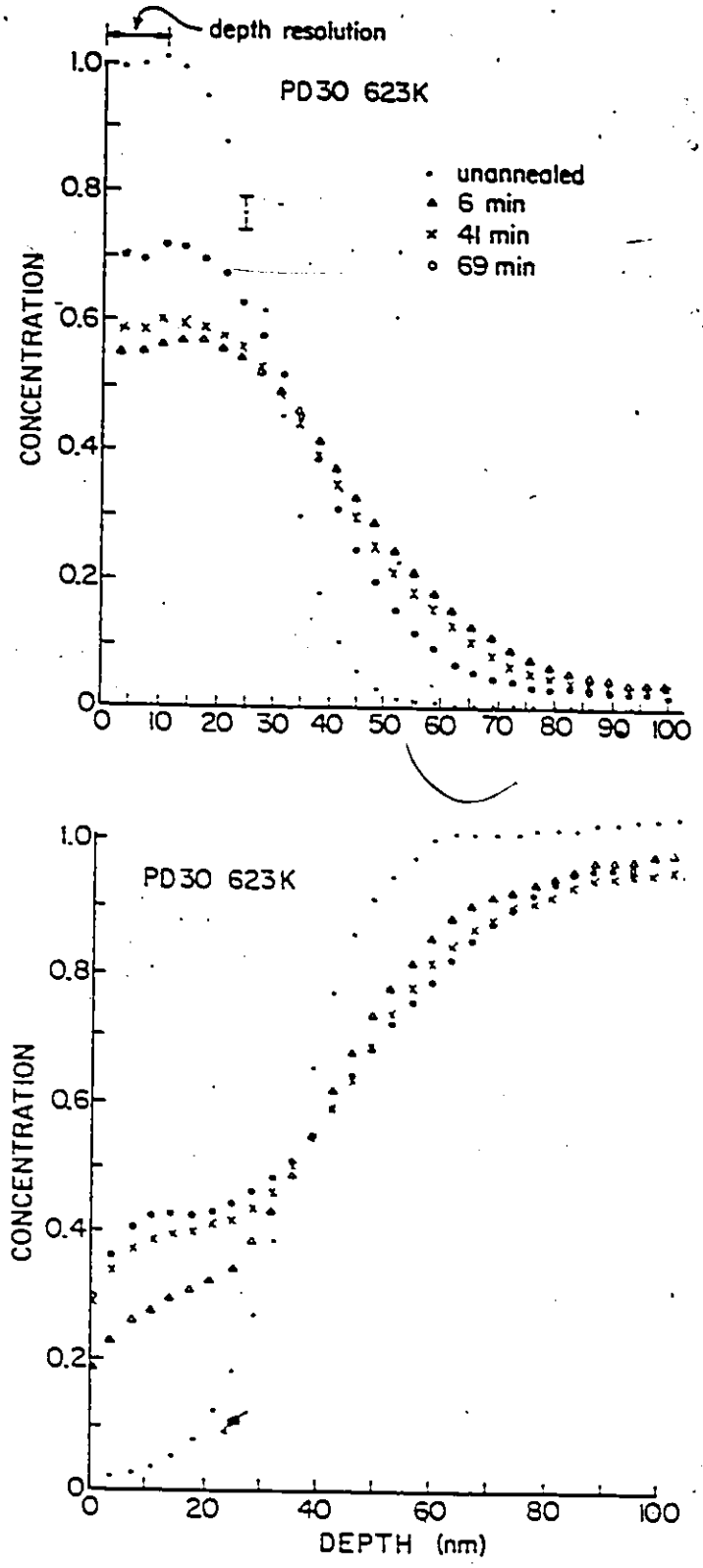

Fig. 6.33: Concentration-depth profile obtained from the RBS spectra of Fig. 6.26 for annealed Ni/Pd couple
(a) Pd profile (b) Ni profile.

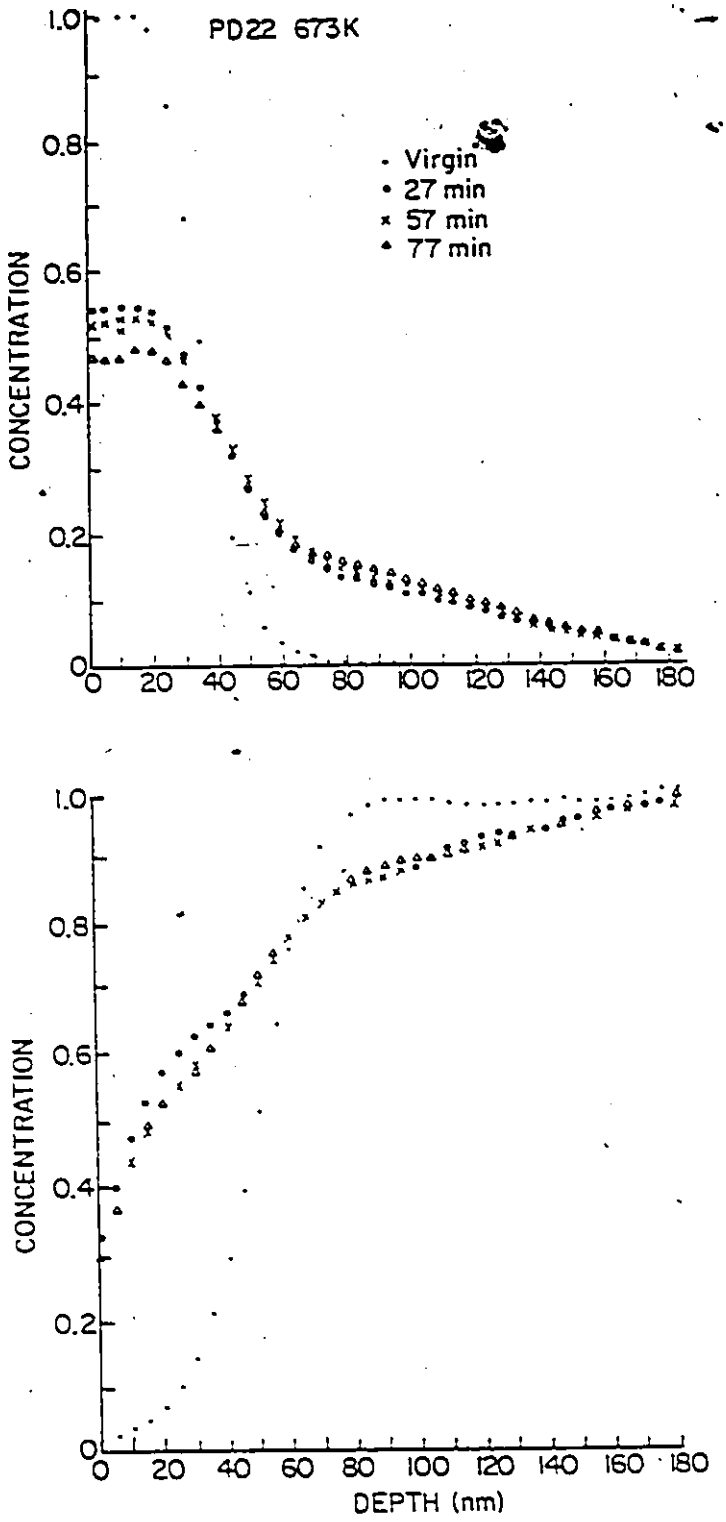

Fig. 6.34: Concentration-depth profile of a small-grained Ni/Pd couple annealed at 673K.
(a) Pd profile (b) Ni profile.

PAGE 190 OMITTED
IN PAGE NUMBERING.

PAGE 190 OMISE
DANS LA PAGINATION.

depth of ∿ 100 nm) saturates after ∿ 40 minutes anneal (at ∿ 2.5%, 5% and ∿ 10% at 573, 623 and 673K respectively). These extensive interdiffusions therefore cannot be explained solely on the basis of grain boundary diffusion, but rather the diffusion model must include contributions from both grain boundary effects and enhanced lattice diffusion. Enhanced lattice diffusion may result from a high, nonequilibrium concentration of vacancies or dislocations (Baluffi et al. (1978)) in the as deposited films and may be orders of magnitude greater than normal lattice diffusivities (Poate et al. 1978).

A theoretical model to describe the interdiffusion in systems such as this, where both grain boundary and lattice diffusion effects contribute to atomic transport, has been presented by Whipple (1955) and discussed extensively by several authors (e.g. Fisher 1951, Levine et al. 1959, Benoit et al. 1975, LeClaire 1963, Gilmer et al. 1976, Holloway et al. 1976 and Gupta et al. 1978). Its application for the finite source and thickness condition of the present work has been described by Suzuoka (1961,1964) and Gilmer et al. (1976). In Whipple's model an idealized single grain boundary, with dimensions 2δ perpendicular to the plane of the film (Fig. 6.35a), is assumed. The concentration profile of the diffusing species at any plane parallel to the film surface therefore consists of two contributions: (1) a concentration C_1 due to lattice diffusion from the initial interface in a direction normal to the film and (2) concentration C_2 due to sideways diffusion from the grain boundaries into the film, so that $C = C_1 + C_2$ where

$$C_1 = C_0 \operatorname{erfc}\left[\frac{y}{2(D'_\ell t)^{\frac{1}{2}}}\right] \qquad (6.24)$$

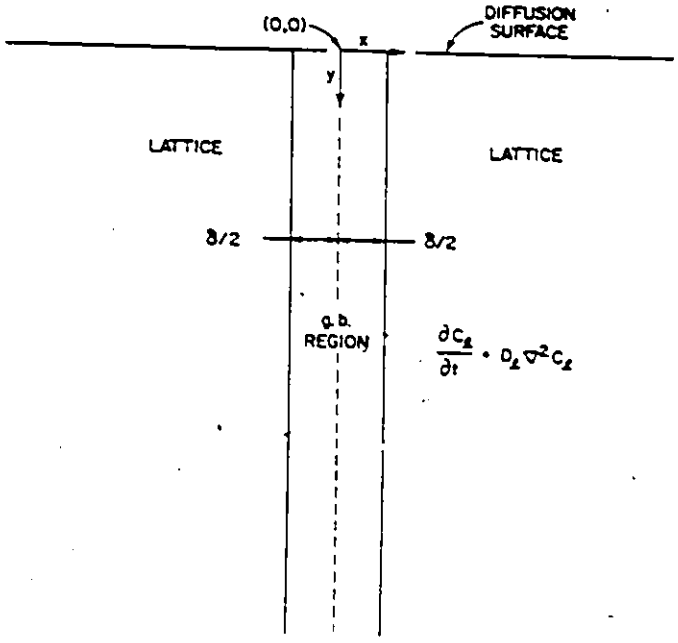

Geometric model for grain boundary diffusion

Fig. 6.35a: Geometric model for grain boundary diffusion.

for a semi-infinite source condition, and

$$C_1 = \frac{M}{2(\pi D t)^{\frac{1}{2}}} \exp \frac{-y^2}{4D_\ell' t} \qquad (6.25)$$

for a finite source. The contribution C_2 of the sideways diffusion is given by

$$C_2 = C_0 \operatorname{erfc}\left(\frac{x-\delta}{2(D_\ell' t)^{\frac{1}{2}}}\right) \operatorname{erf}\left(\frac{y}{2(D_\ell' t)^{\frac{1}{2}}}\right) \qquad (6.26)$$

or

$$C_2 = \frac{M}{\sqrt{\pi D_\ell' t}} \exp \frac{-y}{4D_\ell' t} \operatorname{erfc}\left(\frac{x-\delta}{2\sqrt{D_\ell' t}}\right)$$

for finite source where C_0 is the composition at $y = 0$ (initial interface), y and x are distances measured normal and perpendicular to the film respectively, D_ℓ' is some enhanced lattice diffusion coefficient and t is annealing time. The average concentration in the film measured by profiling techniques such as RBS is an average concentration in the film plane and is obtained by averaging C over the plane:

$$\bar{C} = \frac{1}{L/2} \int_0^{L/2} C_1 dx + 2 \cdot \frac{1}{L/2} \int_0^{L/2} C_2 dx \qquad (6.27)$$

where L is the grain size. Baglin et al. (1978) have shown that for the infinite source condition, provided $L >> 2(D_\ell' t)^{\frac{1}{2}}$, $\bar{C}$ is given by

$$\frac{\bar{C}}{C_0} = \frac{8(D_\ell' t)^{\frac{1}{2}}}{L\pi^{\frac{1}{2}}} + \operatorname{erfc}\left(\frac{y}{2(D_\ell' t)^{\frac{1}{2}}}\right)\left\{1 - \frac{8(D_\ell' t)^{\frac{1}{2}}}{L\pi^{\frac{1}{2}}}\right\} . \qquad (6.28)$$

Gilmer et al. (1976) have considered the problem of grain boundary

assisted diffusion in thin films of finite thickness, and containing multiple grain boundaries. Their analysis shows that, for temperature and diffusion times low enough such that the diffusion length $\sqrt{Dt} << L$, the concentration profile between the grain boundary and the centre of the grain is not appreciably different from the profile that would be obtained from the idealized single grain boundary model. Consequently, the formalisms developed for an isolated grain boundary in a thin film may, in most cases, be applied directly to polycrystalline thin film systems as well.

a) Ni Diffusion in Pd

Equations (6.24)-(6-28) show that, near the interface (small y), the concentration distribution is dominated by lattice diffusion (error function type for infinite source and gaussian for finite source). However at larger distances, the concentrations are dominated by C_2 since C_1 decreases very rapidly with depth. Consequently the grain boundary diffusion coefficients can be determined by considering the concentration levels at these large depths. Before estimating the grain boundary diffusion coefficients, however, we note that Eq. (6.28), describing the average measured concentration, consists of two parts: the first term, which is independent of depth y, describes the rate of the rise of the concentration level, in the film, with annealing time t

$$\frac{\bar{C}}{C_0} = \frac{8(D_\ell' t)^{\frac{1}{2}}}{L\pi^{\frac{1}{2}}}$$

and follows a $t^{\frac{1}{2}}$ dependence. Thus by plotting log $(\frac{\bar{C}}{C_0})$ vs log t, a straight line with slope = 0.5 should be obtained, from which the enhanced lattice

diffusivity D_ℓ' can be obtained. Fig. 6.35b shows a plot of the Ni concentration at the plateau versus time for samples annealed at various temperatures. The plateau concentrations plotted in Fig. 6.35b were obtained by averaging the Ni surface concentrations within $\sim$ 30 nm of the surface. The straight line through the points are drawn with slope = 0.5. D_ℓ' can be obtained from the plateau concentration provided the mean grain diameter, $\bar{L}$, is known. In this analysis an average diameter between the grain dimensions of the as-deposited films and the grain dimensions after anneal is used. Table 6.8 shows the diffusion coefficients (Ni in Pd) calculated using this method. D_ℓ' (Ni and Pd) can also be determined from the second term of Eq. (6.28) which is significant only in the region near the interface. This is obtained by taking the slopes of the concentration profiles. In this case, however, because of the limited thickness of the Pd overlayer, only the short time annealing data can be used. For longer anneal times, the Ni distribution in the film introduces a considerable uncertainty to the error function profile near the interface. The diffusion coefficients are given by

$$D' = \frac{C_0^2}{\pi(t_1 - t_2)} \left\{ \frac{1}{\left(\frac{dc}{dy}\right)_1^2} - \frac{1}{\left(\frac{dc}{dy}\right)_2^2} \right\} \qquad (6.29)$$

where $\left(\frac{dc}{dy}\right)_1$ and $\left(\frac{dc}{dy}\right)_2$ are the gradients, taken near the interface, of the concentration profiles after annealing for times t_1 and t_2 respectively.

Table 6.8 and Fig. 6.35c show the diffusion coefficient for Ni diffusing through Pd obtained by the two methods described above. Except at 523K, the values determined from the plateau concentrations are consist-

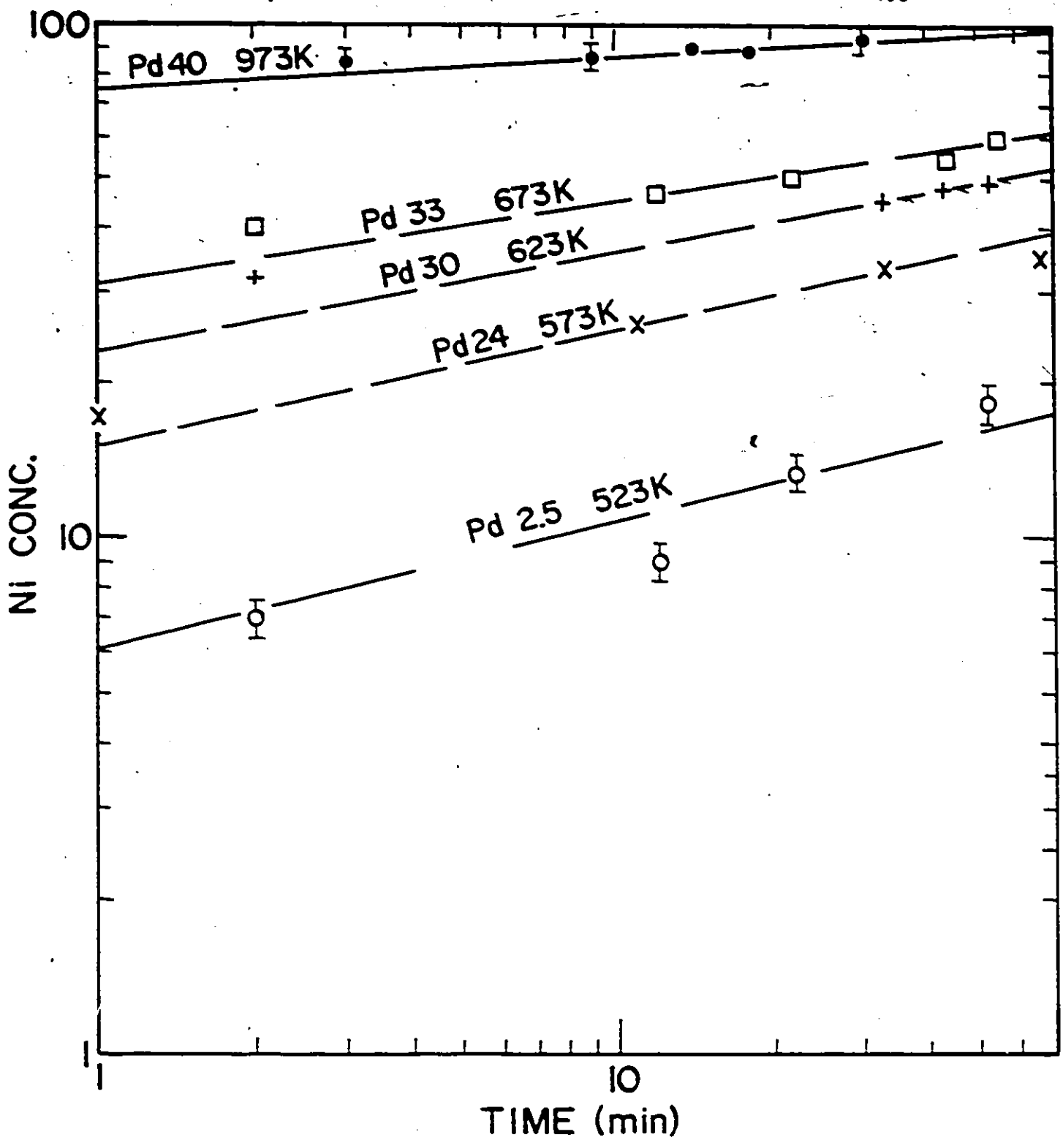

Fig. 6.35b: Plot of the Ni concentration at the plateau vs annealing time at each temperature.

Table 6.8: Measured diffusion coefficients for Ni in Pd for samples annealed at various temperatures.

T(K)	D (Ni in Pd) cm^2/sec $\times 10^{-16}$ from plateau rise	from centre gradient, $\frac{dc}{dy}$
523	0.28±0.07	0.22± 0.05
573	1.02±0.25	3.59± 0.7
603	2.3 ±0.5	11.40± 2.6
623	5.03±1.1	52.0 ±10.4
673	24 ±6.0	
973	110.0	

Table 6.9: Measured Pd (Pd in Ni) diffusion coefficients following annealing at various temperatures

T(K)	D(Pd in Ni) $\times 10^{-16}$ cm^2/sec
523	0.33± 0.08
573	3.04± 0.7
603	7.13± 1.8
623	18.0 ± 4.5
673	56.6 ±14.1

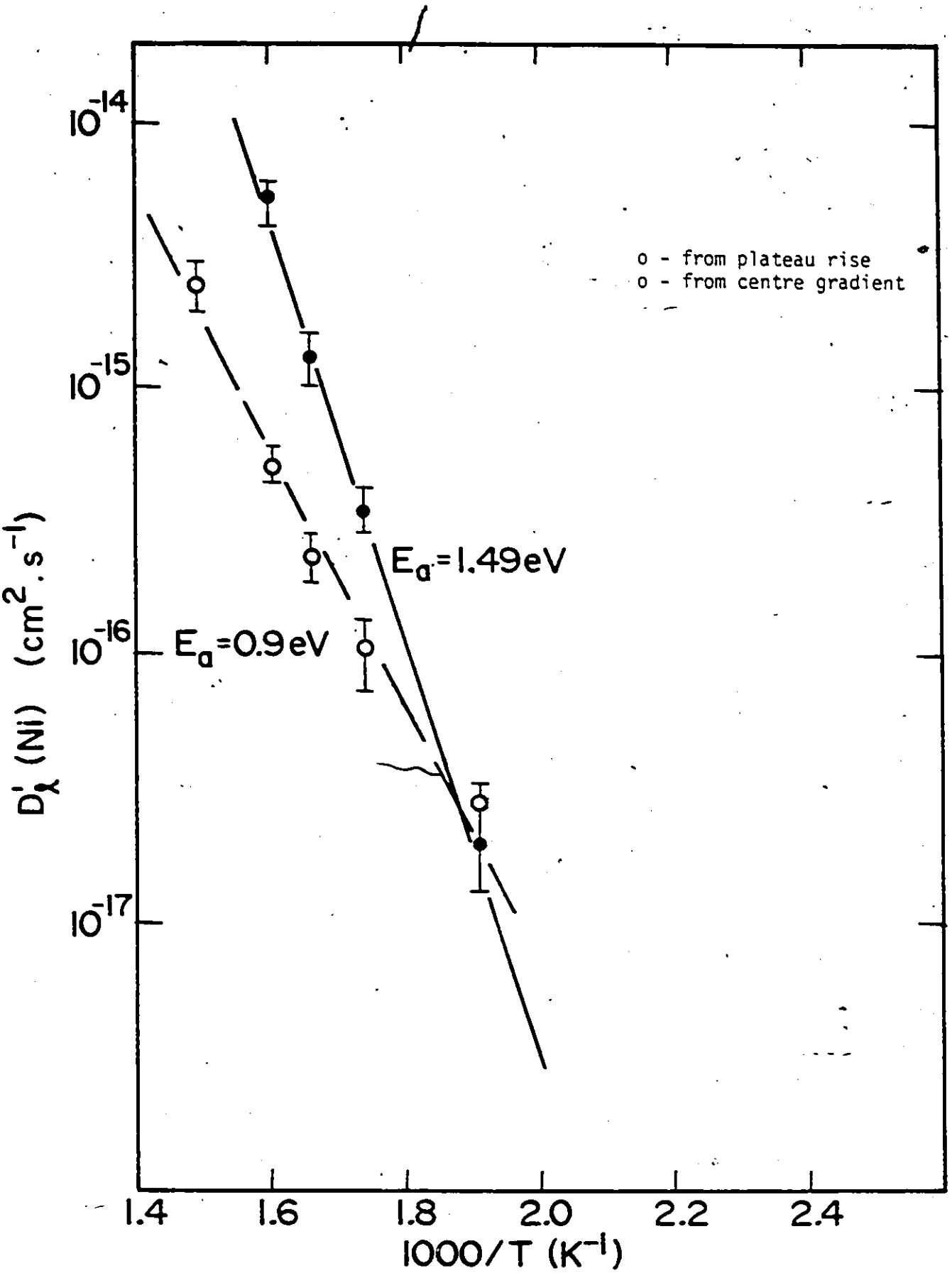

Fig. 6.35c: Arrhenius plot of the enhanced lattice diffusivity of Ni obtained by two methods described in the text.

tently lower by a factor of 3-10 between 573 and 623K. This discrepancy is probably due to the fact that a single average grain diameter ($\sim$ 50 nm) was assumed over the entire temperature range in the calculations.

(b) Pd Diffusion in Ni

The diffusivities for Pd diffusing through Ni were also evaluated from the Pd concentration profile. The observed profiles indicate that at the temperatures and annealing times of the experiments, the Pd overlayer film can be considered a finite source with a concentration profile (in the absence of grain boundary diffusion) of the form

$$C(y,t) = \frac{M}{2\sqrt{\pi D_\ell' t}} \exp \frac{-y^2}{4D_\ell' t}$$

where the symbols have been defined previously. Figures (6.36)-(6.38) show plots of the log of Pd concentration versus the square of penetration distance for samples annealed at 573, 623 and 673K. In the region near the original interface, the curves show a linear dependence of log C_{Pd} on the square of the penetration distance. At deeper depths, however, there is considerable deviation from this Gaussian distribution due to grain boundary assisted diffusion.

From the slopes of the linear portion of the curves near the interface, the lattice diffusivities, D_ℓ', can be obtained. Because of the finite slope of the un-annealed profile the diffusion coefficients were evaluated by subtracting, in quadrature, the slopes of the annealed and un-annealed profiles

$$\frac{1}{S_1^2} - \frac{1}{S_2^2} = (2.3)^2 (4D_\ell')^2 \{t_1^2 - t_2^2\} \qquad (6.30)$$

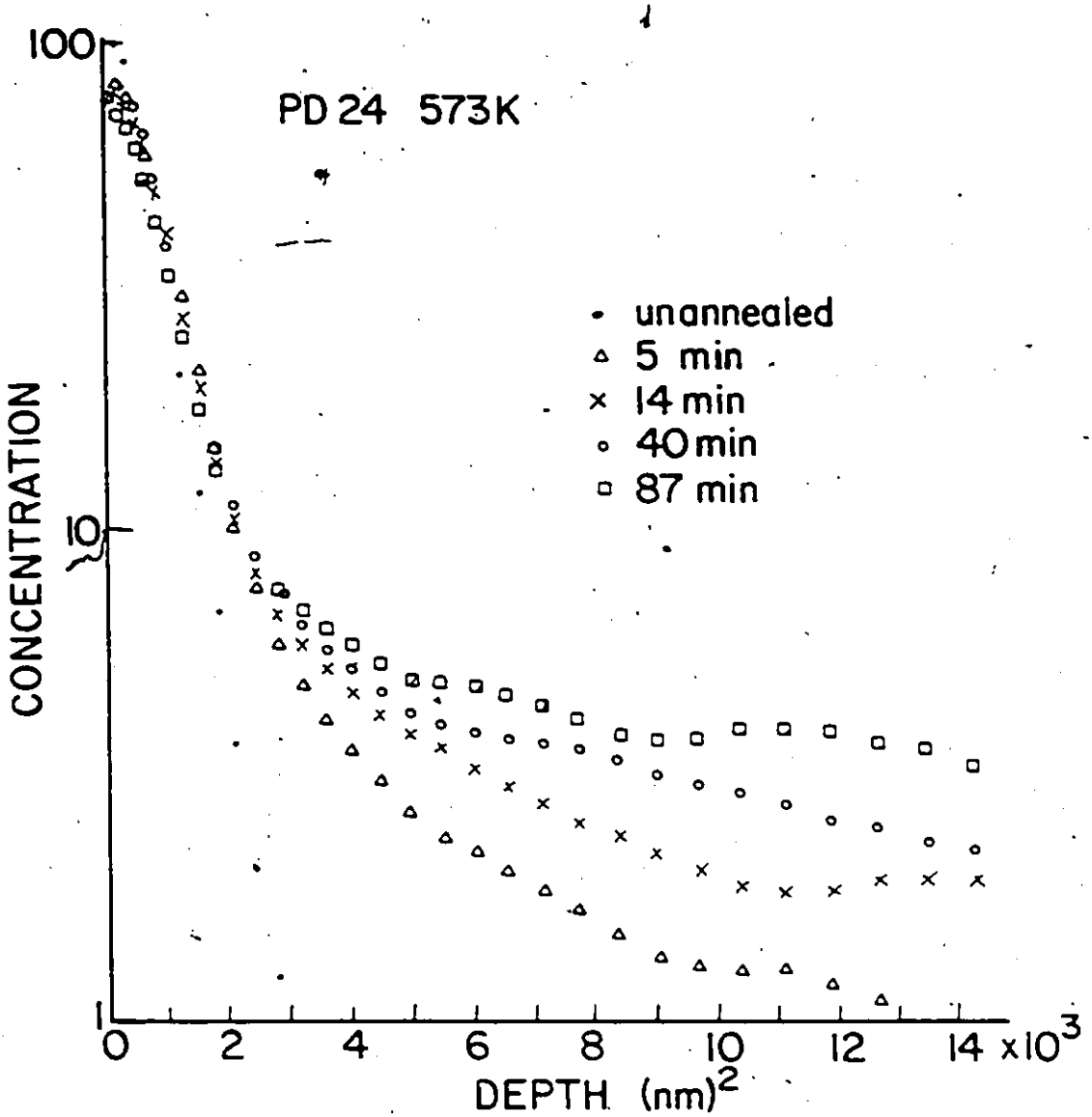

Fig. 6.36: Plot of log Pd concentration vs the square of the penetration depth into Ni for a Ni/Pd couple annealed at 573K.

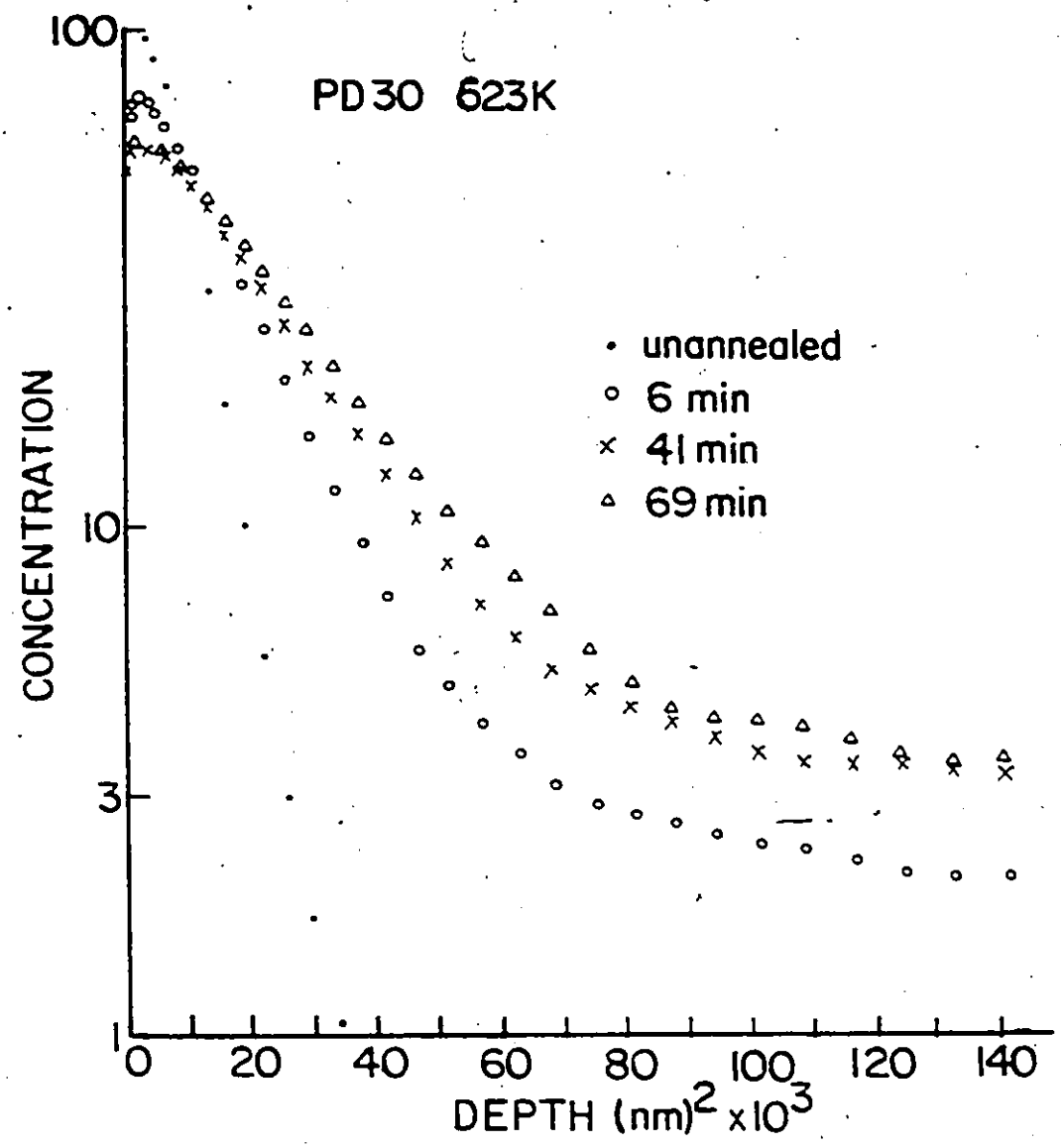

Fig. 6.37: Log of Pd concentration versus the square of the penetration distance for a Ni/Pd couple annealed at 623K.

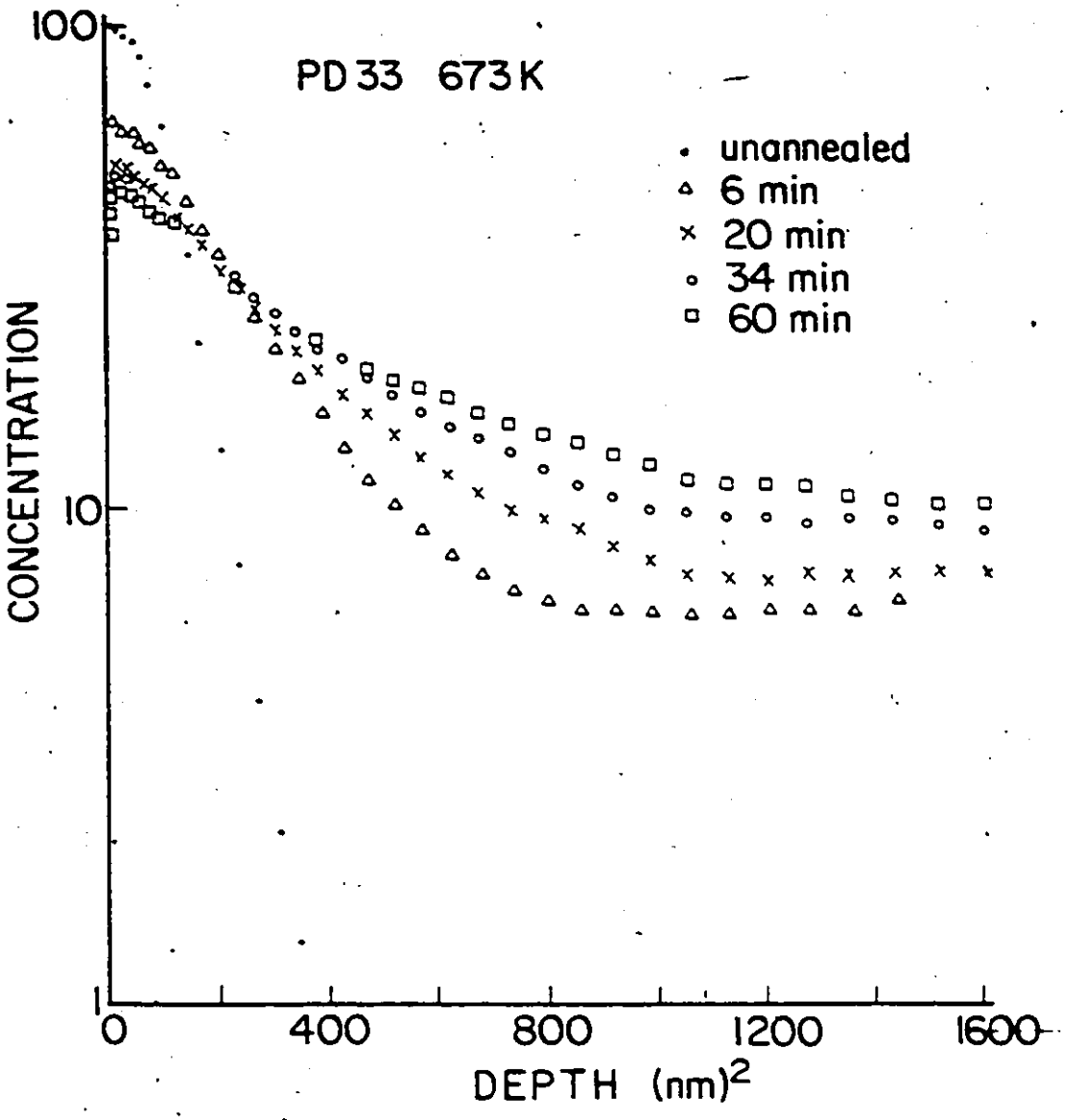

Fig. 6.38: Plot of log Pd concentration vs the square of the penetration distance for a Ni/Pd couple annealed at 673K.

where S_1 and S_2 are the gradients of the log C vs y^2 curves after annealing for times t_1 and t_2 respectively. Table 6.9 lists the diffusion coefficients for Pd in Ni calculated in this manner for various annealing temperatures (523-673). The uncertainties in these values are due mainly to the errors in the concentration levels ($\sim$ 10%), annealing time ($\sim$ 10%) and the gradients ($\sim$ 20%). At high temperatures (623-673K) where considerable Ni surface concentration occurs and hence where short time annealing data had to be used for the analysis, the errors in the D_ℓ' values could easily surpass 50%.

The D_ℓ' values (for Ni in Pd, and Pd in Ni) shown in Tables 6.8 and 6.9 are, within error, of similar magnitude indicating that what is being measured here are the interdiffusion coefficients.

In Fig. 6.39 the Pd diffusivities are plotted versus reciprocal temperature assuming an Arrhenius behaviour. Also shown in the figure are the interdiffusion coefficients $\tilde{D}_L$(Pd) of a 20% Pd-Ni bulk alloy (Borovskij 1967). The present values are orders of magnitude higher than the bulk values. As discussed earlier, these high D_ℓ' values are probably due to enhancement of lattice diffusion in thin films, probably by a high concentration of non-equilibrium (e.g. dislocations) and equilibrium defects present in the evaporated films. The observed activation energy of $\sim$ 1.1±0.07 eV is similar to that observed for the recovery of resistivity (0.9-1.27 eV) in cold-worked Ni and Pd specimens, and lends support to this view of a defect-enhanced lattice diffusivity. Also included in Fig. 6.39 is the D_ℓ' value measured on a sample annealed at 973K (and analysed by the Auger depth profiling technique). This shows that, at high temperatures, the diffusion constants

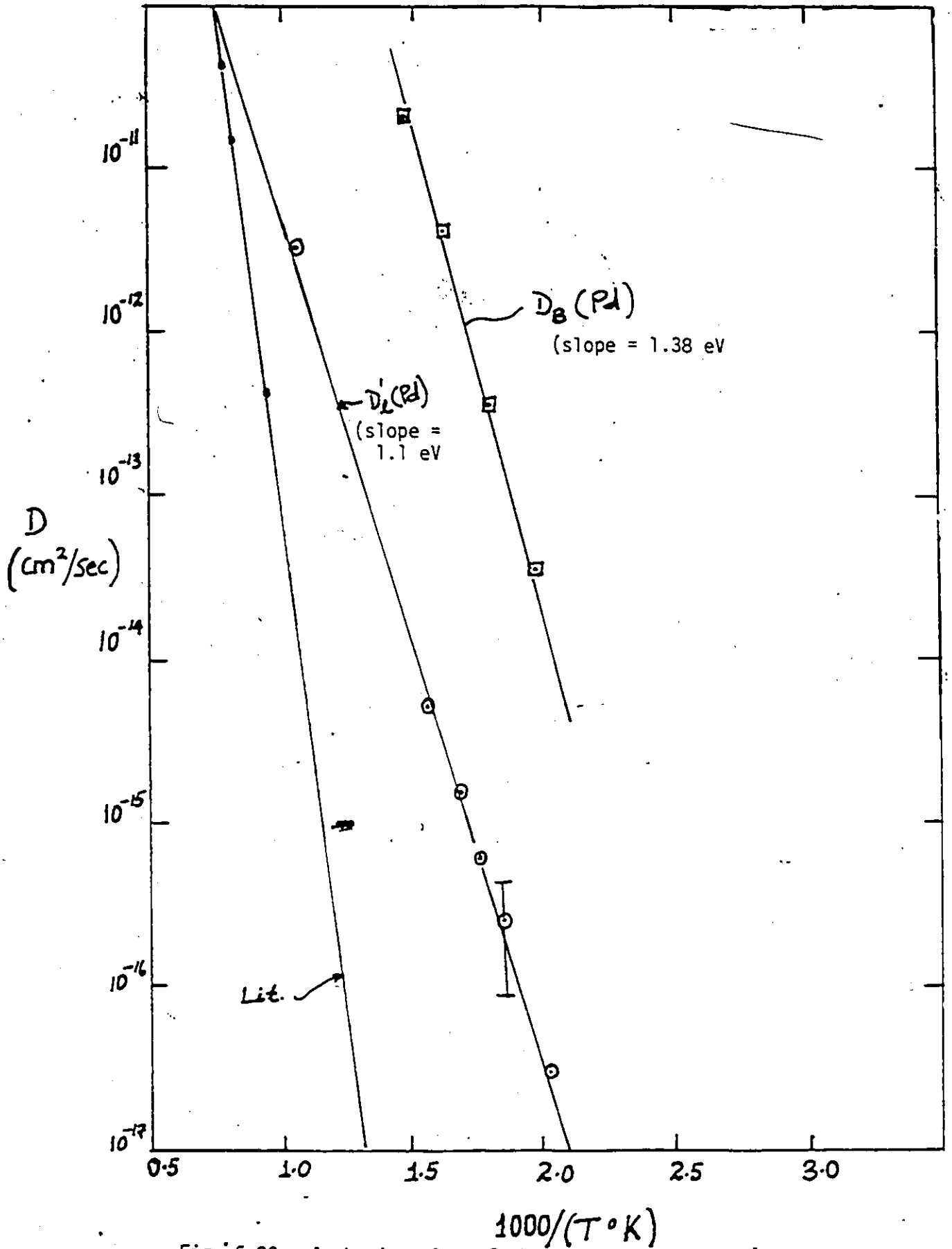

Fig. 6.39: Arrhenius plot of the Pd diffusivities D'_Σ(Pd)

measured in thin films approach bulk values as the role of equilibrium defects becomes dominant.

6.2.3 Pd Diffusion in Ni Grain Boundaries

As mentioned earlier the deeply penetrating tail in the Pd concentration profile is due largely to grain boundary diffusion; hence from its gradient the grain boundary diffusivity, D_B, can be determined. Levine et al. (1960) and LeClaire (1963) have shown that D_B is best evaluated as a lumped parameter δD_B from the equation

$$\delta D_B = \left(\frac{\partial \ell n \bar{C}}{\partial y^{6/5}}\right)^{-5/3} \cdot \left(\frac{4D_\ell'}{t}\right)^{1/2} \cdot (0.66) \qquad (6.30)$$

where δ is the grain boundary width, $\bar{C}$ is the concentration at depth y, where the contribution of lattice diffusion to $\bar{C}$ is small, t is the annealing time and D_ℓ' is the lattice diffusivity.

Figure 6.40 shows the 'whipple' plot of log $\bar{C}$ versus $y^{6/5}$ for the interdiffusion profile of Pd in Ni at 573K. The curve exhibits two regions: near the interface lattice diffusion dominates, while at deeper depths the grain boundary condition dominates. From the gradient of the log $\bar{C}$ versus $y^{6/5}$ curve, a value of $\delta D_B = 2.5 \times 10^{-20}$ cm^3-sec^{-1} was determined. Assuming a grain boundary width $\delta \sim 0.5$ nm, this gives $D_B \sim 10^{-13}$ cm^2-sec^{-1} as the value of the grain boundary diffusion coefficient at 573K. This procedure was used to evaluate D_B at 523K ($D_B \sim 5 \times 10^{-13}$ cm^2-sec^{-1}) and at 623K as well. Assuming a similar grain size and structure in both the Ni and Pd films, and using a simple $y = \sqrt{D_B t}$ for the diffusion length, we estimate that, at 523 Ni would have diffused through the Pd overlayer film

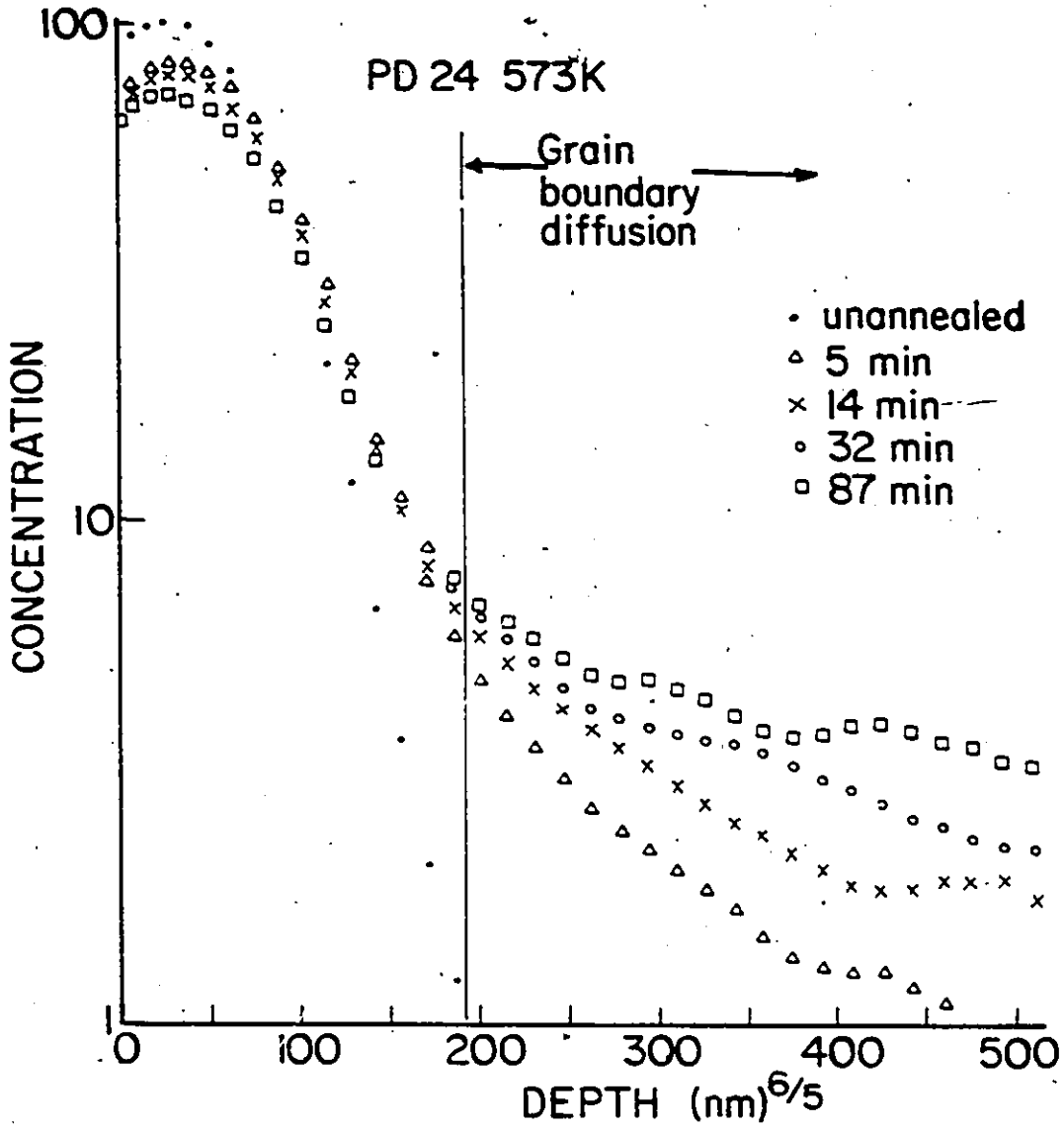

Fig. 6.40: 'Whipple' plot of the Pd concentration for a small-grained Ni/Pd couple annealed at 573K.

($\sim$ 40 nm) after t = 4 minutes, as was indeed observed.

In Fig. 6.39 the D_B values are also shown plotted versus 1/T. The slope gives an apparent activation energy E_B = 1.38 eV for grain boundary diffusion of Pd, and a prefactor $D_B^0 \sim 0.75\ cm^2\ sec^{-1}$. This activation energy is $\sim \frac{1}{2}$ the reported activation energies (2.7-2.8 eV) for self diffusion in Ni and is consistent with expected activation energy for grain boundary diffusion (Atkinson 1985) (0.5-0.7 of activation energy for lattice diffusion). The E_B value is however higher than that determined for the enhanced lattice diffusivity D_ℓ' and supports the argument that the lattice diffusivities in thin films are enhanced by defects.

Grain boundary diffusivities for Ni were not estimated from the Ni profiles. Because of the limited thickness of the Pd overlayer film, reflections at the Pd surface lead to rather flat Ni concentration profiles in the film. Consequently, any slope, $\frac{\partial \ell n \bar{C}}{\partial y^{6/5}}$, taken from such profiles is likely to lead to large errors in δD_B.

(II). Irradiated Specimens

Figure 6.22 shows the Ni and Pd concentration profiles following Ar^+ irradiation at 573K to various ion doses ($0.7 - 14 \times 10^{15}$ ions cm^{-2}). First, one observes that the penetration depth of the Pd distribution in Ni correlates with the range ($R_p + 2\Delta R_p \sim 100$ nm) of the bombarding ions. Secondly, the concentration level of the deep tail (ascribed to grain boundary diffusion) is much less here compared to the levels observed for annealed (without irradiation) specimens (Fig. 6.23). This is revealed more clearly in Figs. 6.41 and 6.42 which show the 'Whipple' plots for irradiated and unirradiated samples respectively. Fig. 6.41 shows that, except for the lowest doses, log C has an approximately linear dependence on $y^{6/5}$ over most of the concentration range and, after a dose of 7×10^{15} cm^{-2}, the distribution can be approximated by a single diffusion coefficient. Also Fig. 6.41 shows increasing build up of Pd concentration near the interface with increasing dose. On the other hand, the profile of the annealed specimens (Fig. 6.42) show two distinct regions, even for long annealing times: Lattice diffusion behaviour near the interface, and grain boundary diffusion dominated behaviour at deeper depths. The Pd concentration at the deepest depth is $\sim$ 4% (after 40 minutes anneal) while it is little more than 1% in the irradiated case. It is as if, in the irradiated case, there is competition between grain boundary diffusion to deeper depths and radiation-enhanced lattice diffusion near the original interface.

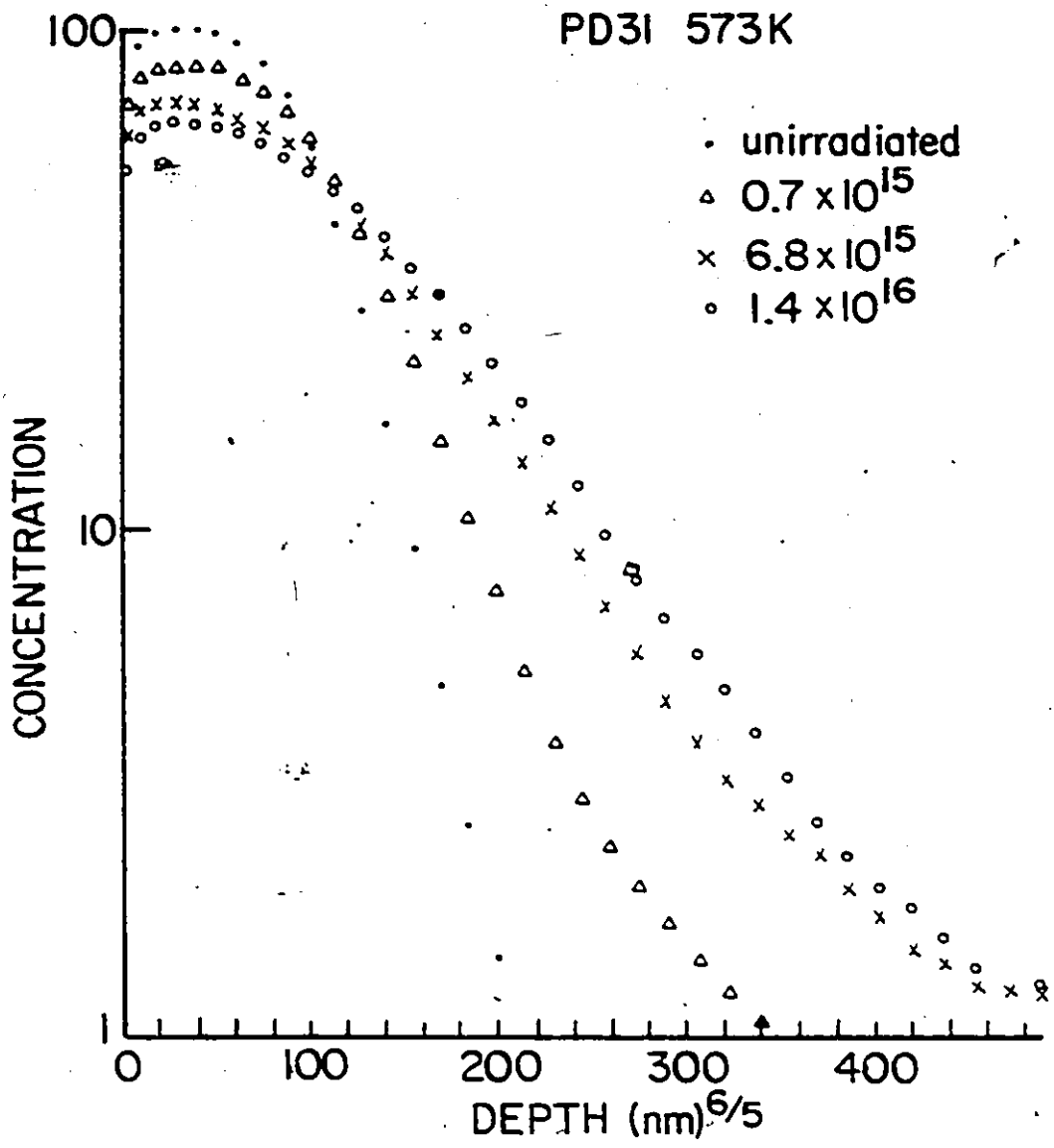

Fig. 6.41: Log of Pd concentration vs $y^{6/5}$ for small-grained Ni/Pd couple irradiated at 573K.

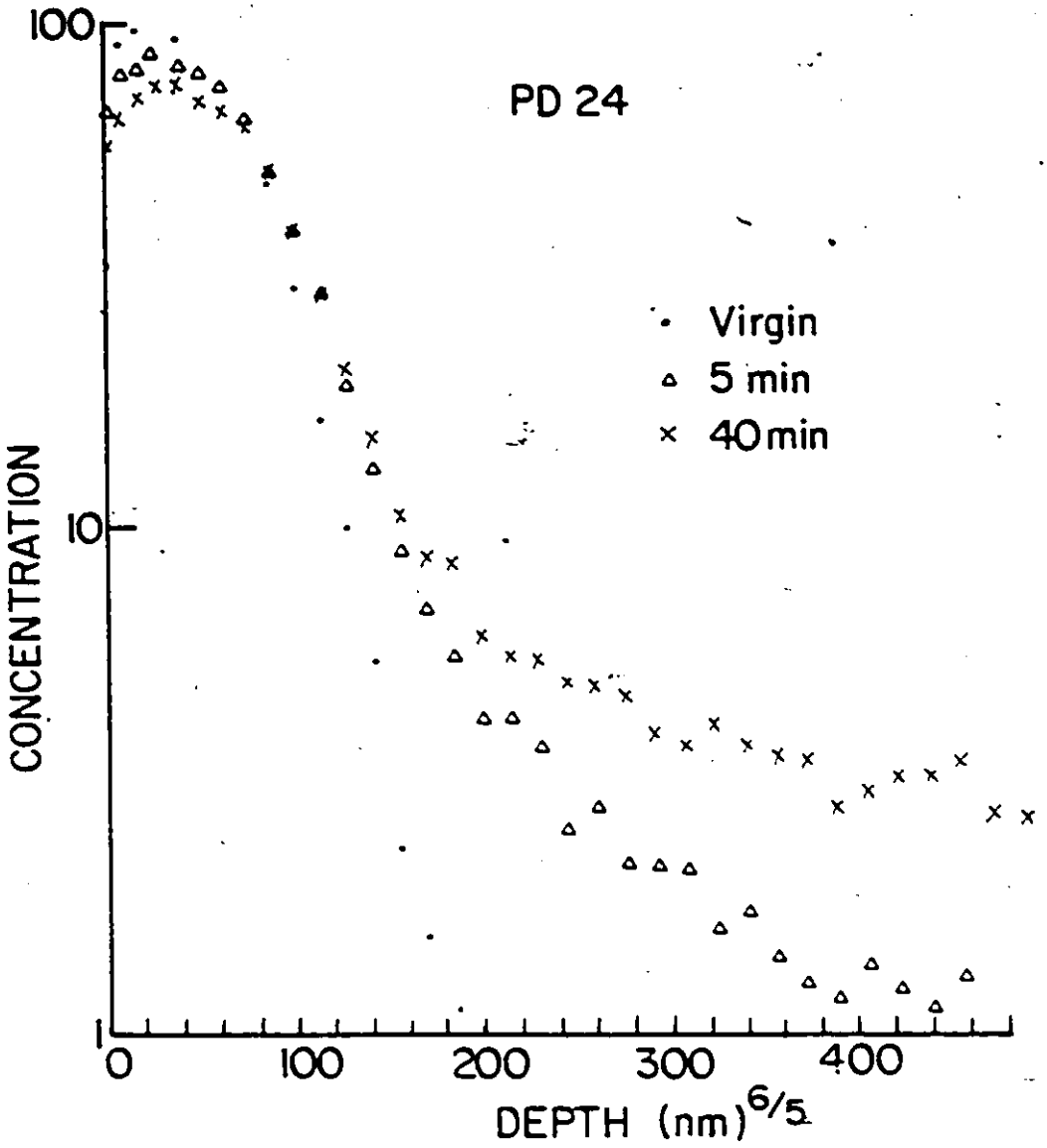

Fig. 6.42: Log of Pd concentration vs $y^{6/5}$ for small-grained Ni/Pd couple annealed, without irradiation, at 573K.

Though the details of the processes responsible for the above behaviour may be difficult to unravel, a qualitative picture that explains the observations can be sketched. Firstly it is well known that apparent activation energies, E_{red}, for radiation-enhanced diffusion processes in metals, in the temperature regime under consideration, are typically of the order of 1/2 the vacancy migration energies (section 3.3.3) while E_B, the activation energy for grain boundary diffusion, are typically $\sim$ 1/2 the activation energy for self diffusion (Gupta et al. 1980). Though D_B^0 ($\sim$ .75 cm^{-2} sec^{-1}), the prefactor for grain boundary diffusion coefficient, is quite large (see last section) compared to D_{red}^0($\sim 10^{-8}$ cm^{-2} sec^{-1} assuming $D_\ell^0 \approx D_{red}^0$), the exponential dependence on the activation energies dominates the diffusivities. Consequently, at 573K, D_B is probably no more than a factor of 10^2 greater than D_{red} compared to $D_B/D_\ell \sim 10^6$. Secondly, as mentioned earlier, the collision cascade affected zone encompasses many grains and grain boundaries. Hence, it may lead to dumping of solute, initially in the grain boundaries, directly into the grain interior and therefore a reduction in the concentration gradient along the boundary. The net result is that, though grain boundary diffusion indeed occurred, the concentration profiles, except at low dose and possibly low dose rates, are no longer distinct lattice and grain boundary portions. The process is also probably helped by irradiation-induced grain growth which may lead to a faster rate of disappearance of grain boundaries compared to purely thermal-induced grain growth.

• Effective Diffusion Coefficients Under Irradiation

In section 5.2.1.2, a collision cascade-induced mixing model was proposed. This model however cannot be used to estimate the diffusivities in the temperature range under present consideration because of thermally-induced diffusion of irradiation-produced defects. In these circumstances, the diffusivities are estimated from thermal diffusion models discussed in the last sections. In this case, however diffusivities at ∿ constant irradiation dose (ϕ) and dose rate ($\dot{\phi}$) were considered and $\phi/\dot{\phi}$ was used in place of the annealing time t.

Figures 6.43 and 6.44 show typical Pd concentration profiles for samples irradiated to various Ar doses at 523 and 573K respectively. In Figs. 6.45 and 6.46 the log of Pd concentration is plotted versus the square of the penetration distance. From the slopes of such curves near the interface, effective diffusion coefficients under irradiation were obtained. From the low dose curve of Fig. 6.46, the contribution of grain boundary diffusion can also be assessed, assuming purely thermal diffusion along the boundary.

The results of the effective diffusion coefficients, D_{eff}, estimated in this manner are shown in Fig. 6.47, where D_{eff} (Pd) is plotted versus 1/T. Also included in the figure are the bilayer results (section 6.2.1) for lower temperatures (298-423K). The thermal annealing result of the last section is also included for completeness. The figure exhibits both a weakly temperature-dependent region below 423K and a strong temperature-dependence above ∿ 423K. Least squares fitting to the region with strong temperature dependence yields an apparent activation energy

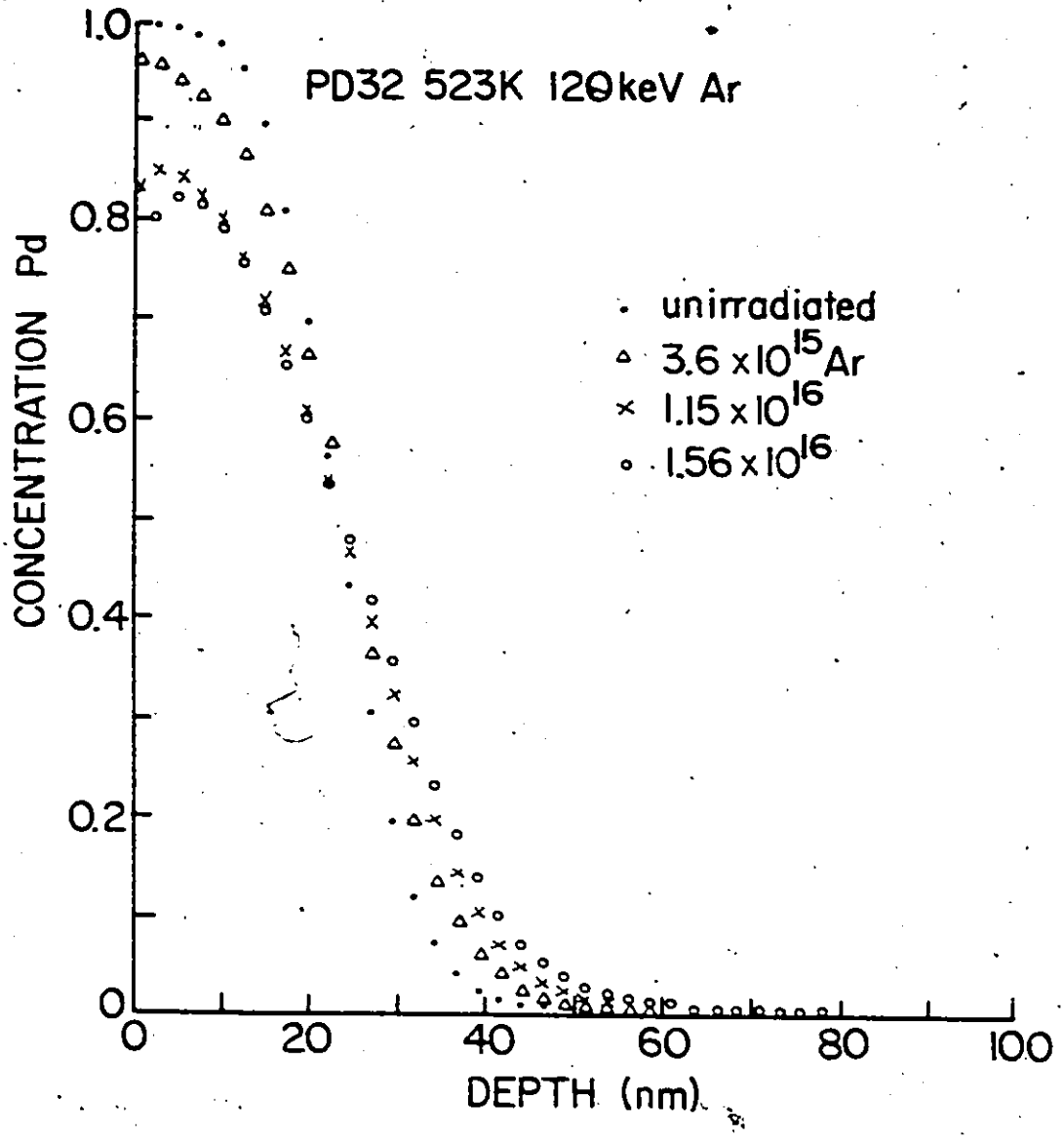

Fig. 6.43: Pd concentration-depth profile for a small-grained Ni/Pd couple before and after irradiation at 523K.

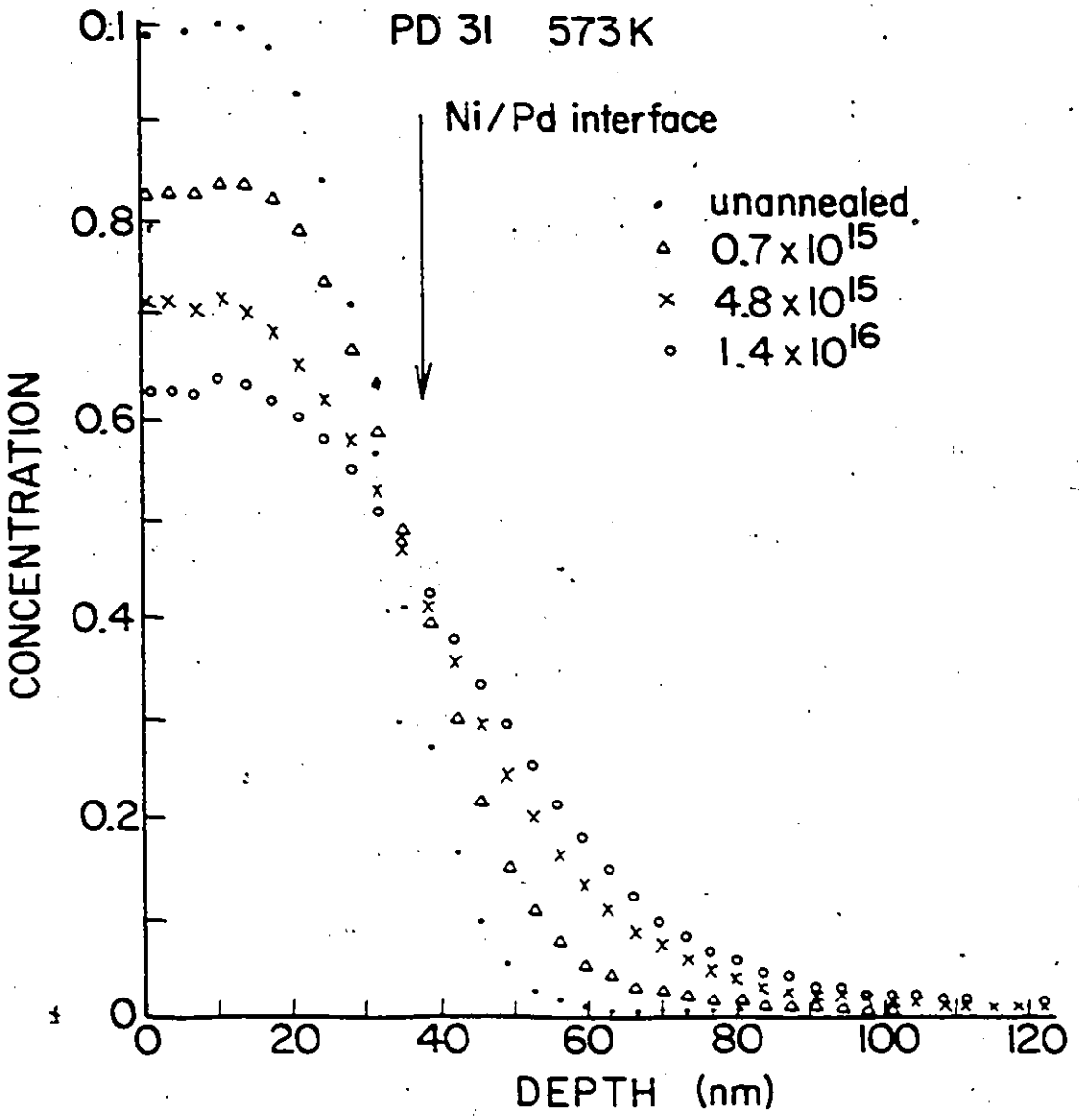

Fig. 6.44: Pd concentration-depth profile for a Ni/Pd couple before and after irradiation at 573K.

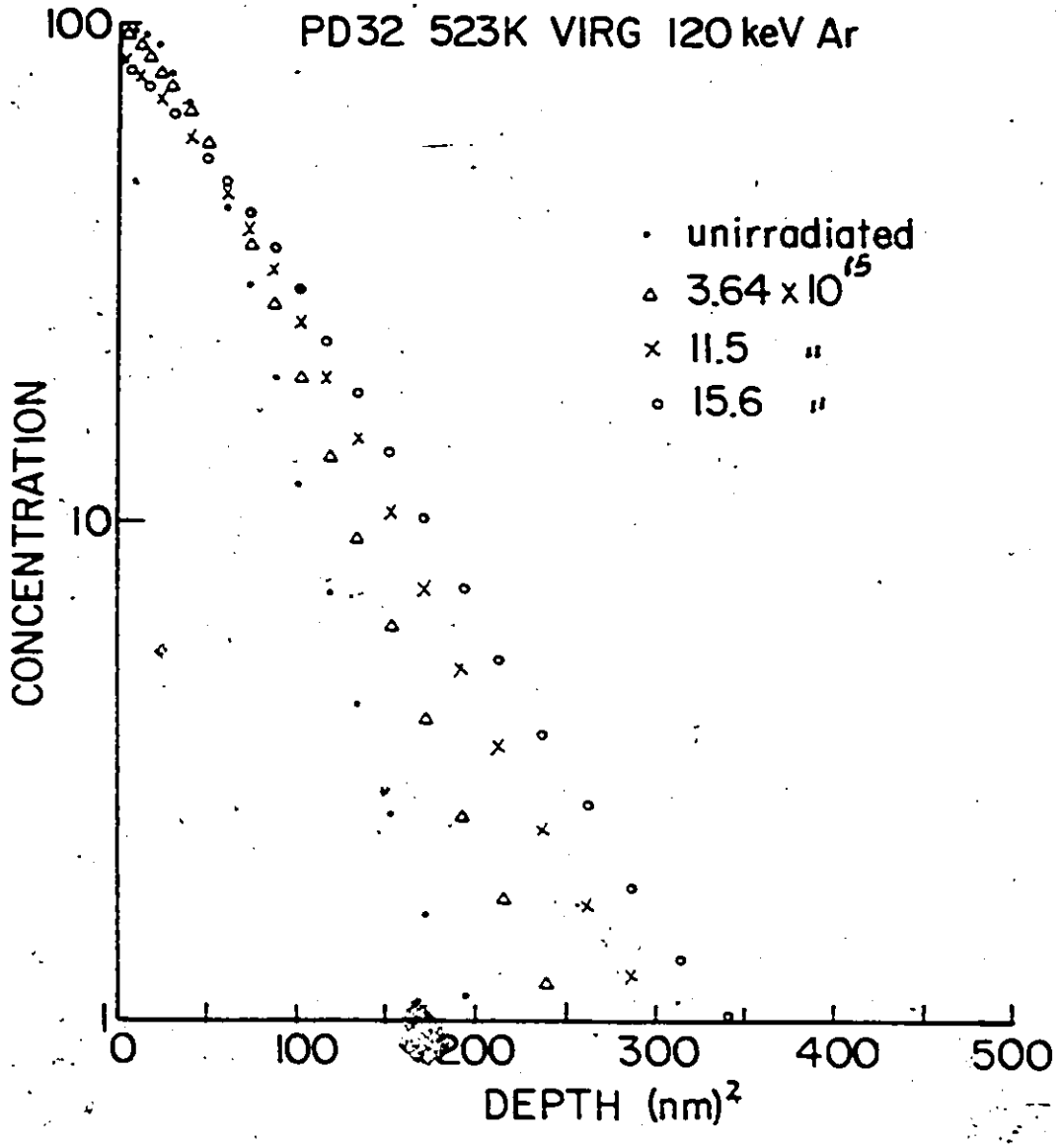

Fig. 6.45: Log of Pd concentration vs the square of the penetration distance into Ni for a sample irradiated at 523K.

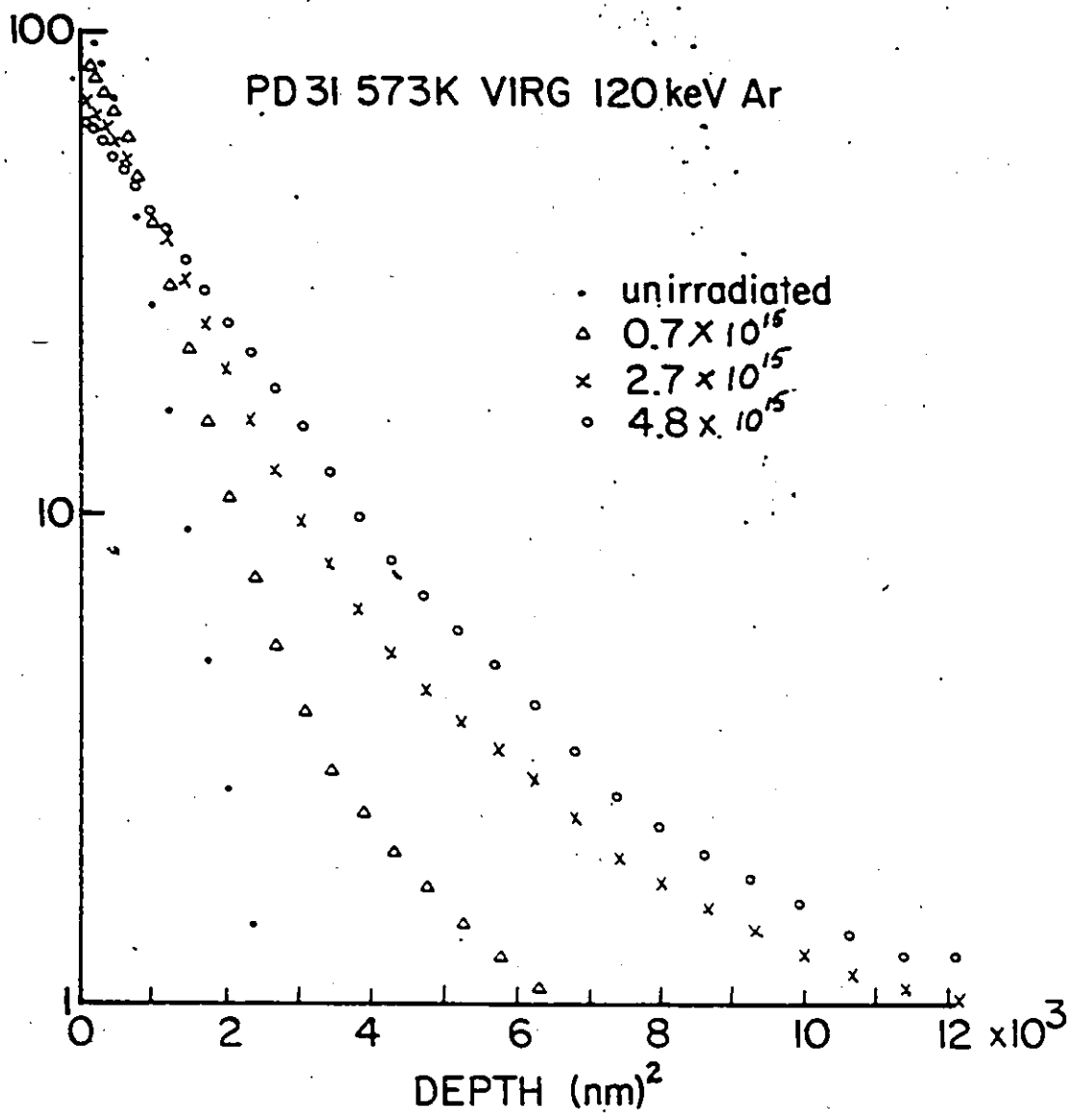

Fig. 6.46: Log of Pd concentration vs the square of the penetration distance into Ni for a sample irradiated at 573K.

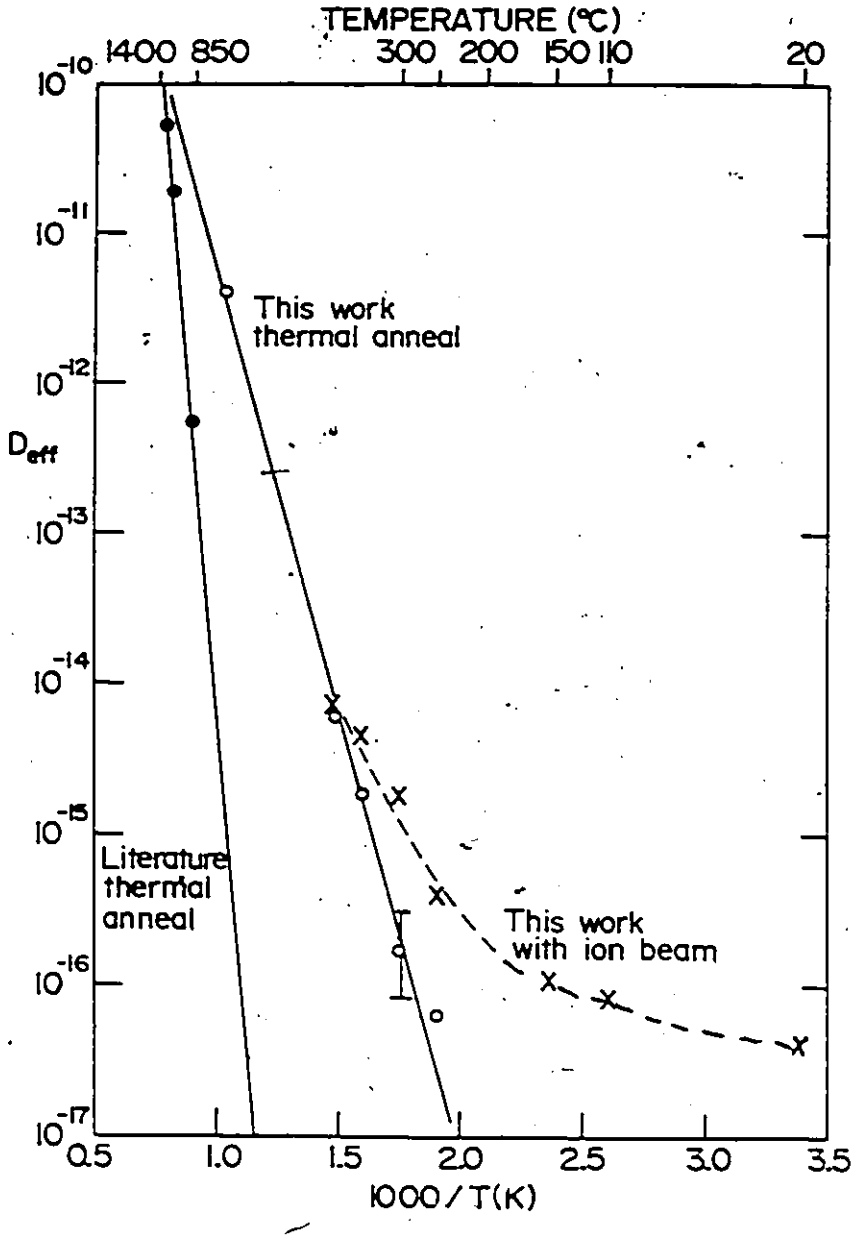

Fig. 6.47: Arrhenius plot of the Pd diffusivities.

$E_a \sim 0.57 \pm 0.07$ eV, similar to that obtained in section 6.1 for the spreading of buried markers; this is $\sim 1/2$ the activation energy for the thermal anneal case. This low activation energy is typical of what is obtained for radiation-enhanced diffusion effects (section 3.3.3) and is due to the enhancement of diffusion by irradiation produced defects.

Because of the very extensive mixing observed for samples irradiated at 673K, the D_{eff} at this temperature, is probably in error by > a factor of two. Figure 6.48, for example, shows the concentration profile for a sample annealed at 673K for 3 hours and then irradiated to various Ar^+ doses ($5\text{-}25 \times 10^{15}$ cm^{-2}). At this temperature both grain boundary and defect-enhanced lattice diffusion is very rapid. The figure shows that after 3 hour anneal Pd distribution extends through the small-grained evaporated Ni film to the polycrystalline Ni substrate. At this temperature, the polycrystalline Ni (grain size $\sim$ 1 mm) is effectively a barrier to diffusion (at 673K $D_\ell \sim 5 \times 10^{-22}$ cm^2 sec^{-1}). Consequently Pd accumulates at the evaporated Ni/polycrystalline Ni interface and is subsequently reflected into the film. This process is evident in the concentration profiles for the 3 hour anneal of Fig. 6.48. Subsequent ion bombardment led to homogenization of the concentration profile, especially in the region of maximum elastic energy deposition and therefore maximum defect production. Ion-induced mixing between thin film Pd and large-grain (single crystal and polycrystal) Ni will be discussed in the next section. Here we simply note that the Pd profile after a dose of 2.5×10^{16} cm^{-2} shown in Fig. 6.48 indicates that the effective diffusion coefficient is very high, though its value cannot be obtained from the profile.

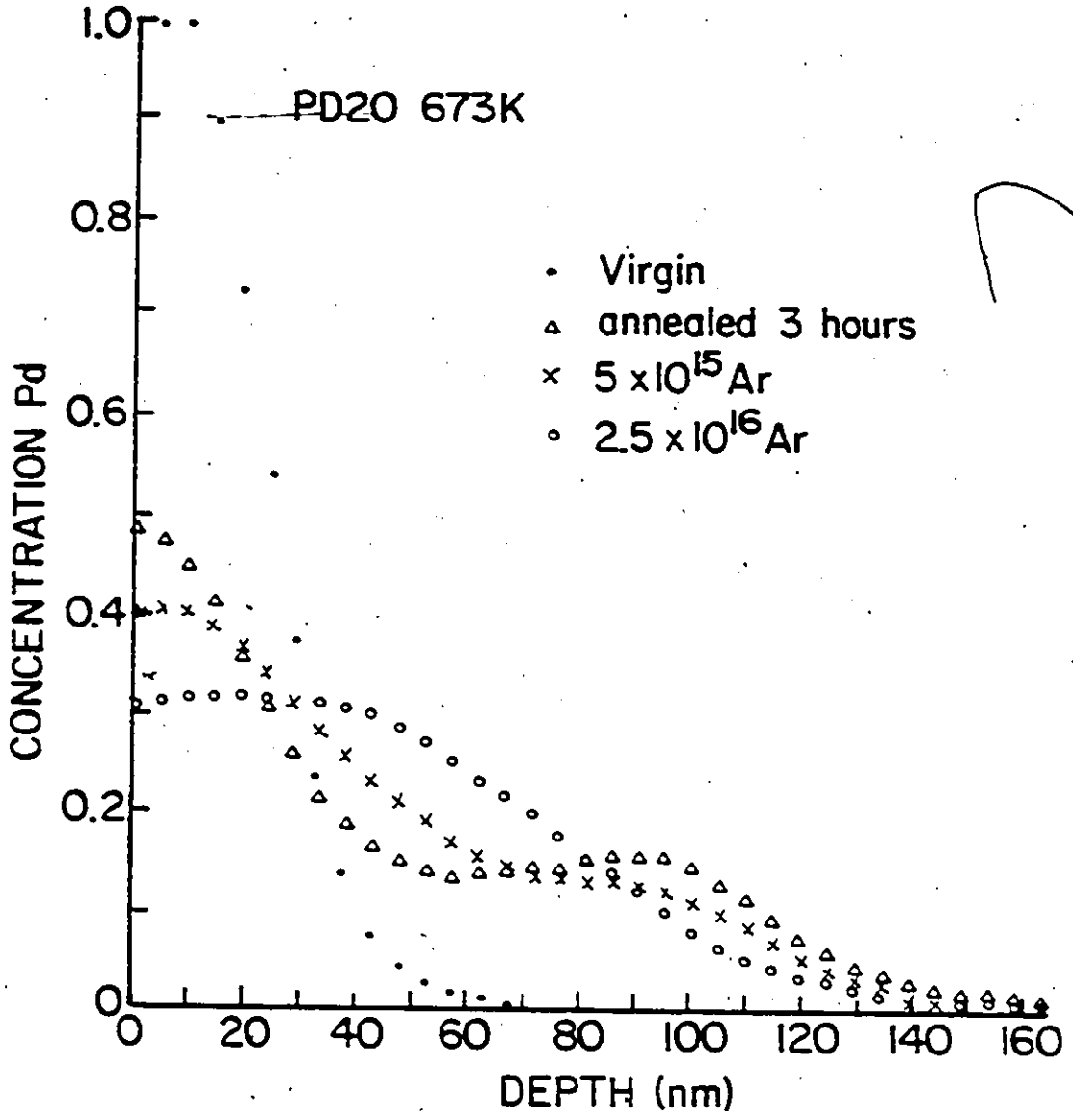

Fig. 6.48: Pd concentration-depth profile for a small-grained Ni/Pd couple annealed for 3 hrs. at 673K and then irradiated with various doses of Ar ions at 673K.

6.2.4 Ion Mixing of Thin Film Pd and Large-Grain Ni

In this section the experimental results of the mixing of evaporated Pd film with large-grain polycrystalline Ni (grain size ∿ 1 mm) and single crystal Ni (100 orientation) are presented and discussed.

6.2.4.1 Annealed Specimens

Figure 6.49 shows the RBS spectra, before and after annealing, typical of polycrystalline Ni/Pd couples annealed, without irradiation, at 573K. Similar spectra for single crystal Ni/Pd couple annealed at 648K are shown in Fig. 6.50. The figures show a rapid migration of Ni through the Pd film to the surface. The low energy edge of the Pd signal and the high energy edge of the Ni signal show only very small broadenings of the initial interface, indicating that interdiffusion through the lattice is very small, and that much of the interdiffusion is due to Ni migrating through the Pd grain boundaries. Also the penetrating tail observed in the high energy edge of the Ni signal is not observed in the low energy portion of the Pd signal, signifying that grain boundary diffusion of Pd into these large grain Ni specimens is not significant at this temperature.

The RBS spectra of Figs. 6.49 and 6.50 were converted into concentration-depth profiles and are shown in Figs. 6.51 and 6.52. Figure 6.51 contrasts sharply with Fig. 6.32 (for small-grained Ni/Pd couple) where a deeply penetrating Pd tail extending to > 100 nm into Ni, and a Ni surface concentration of ∿ 30% were observed. In Fig. 6.51 (and Fig. 6.52) no such extensive diffusion of Pd is observed, justifying the previous explanation of grain boundary diffusion. The Ni concentration

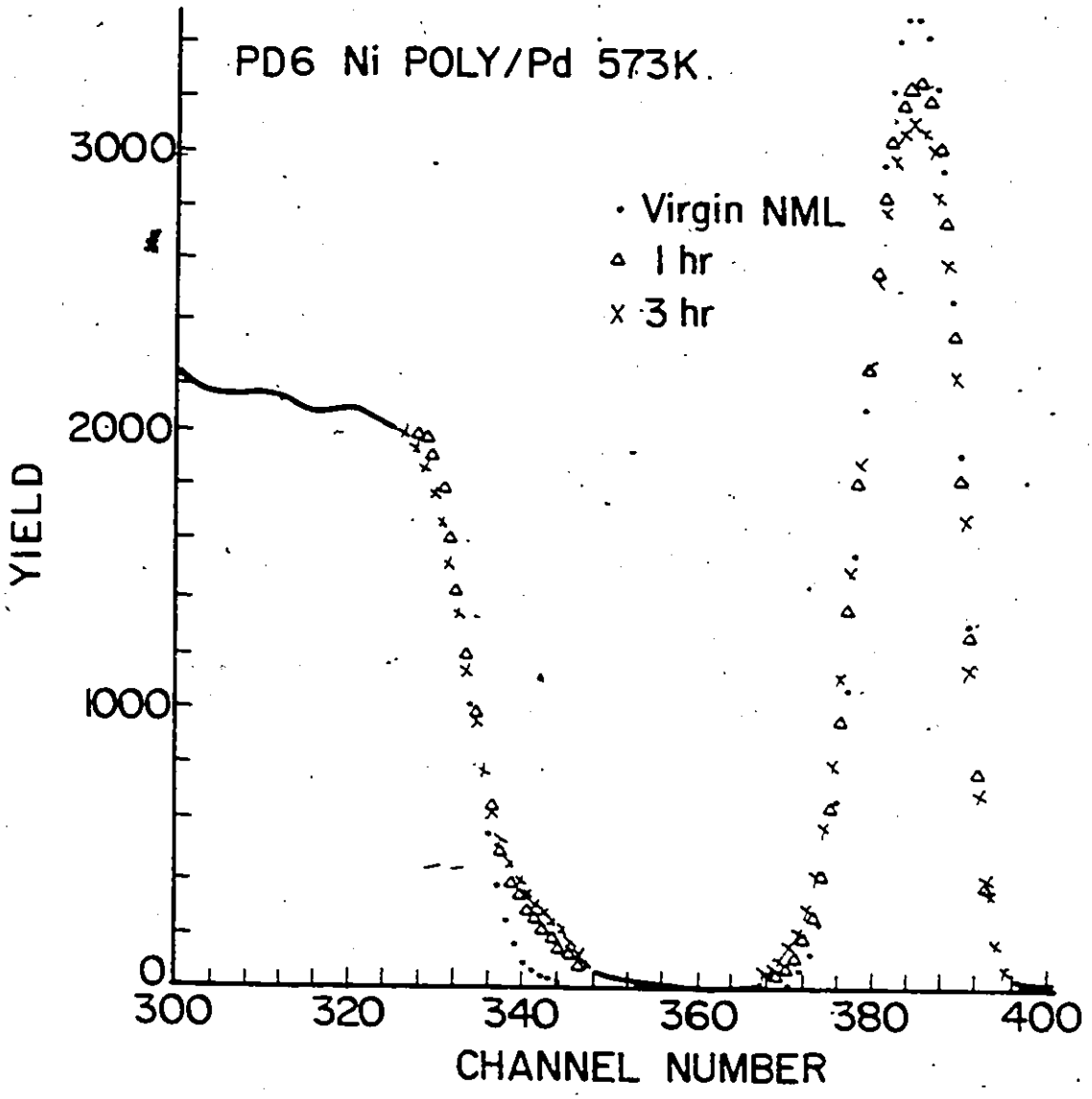

Fig. 6.49: RBS spectra typical of large-grain Ni/Pd couples before and after annealing at 573K.

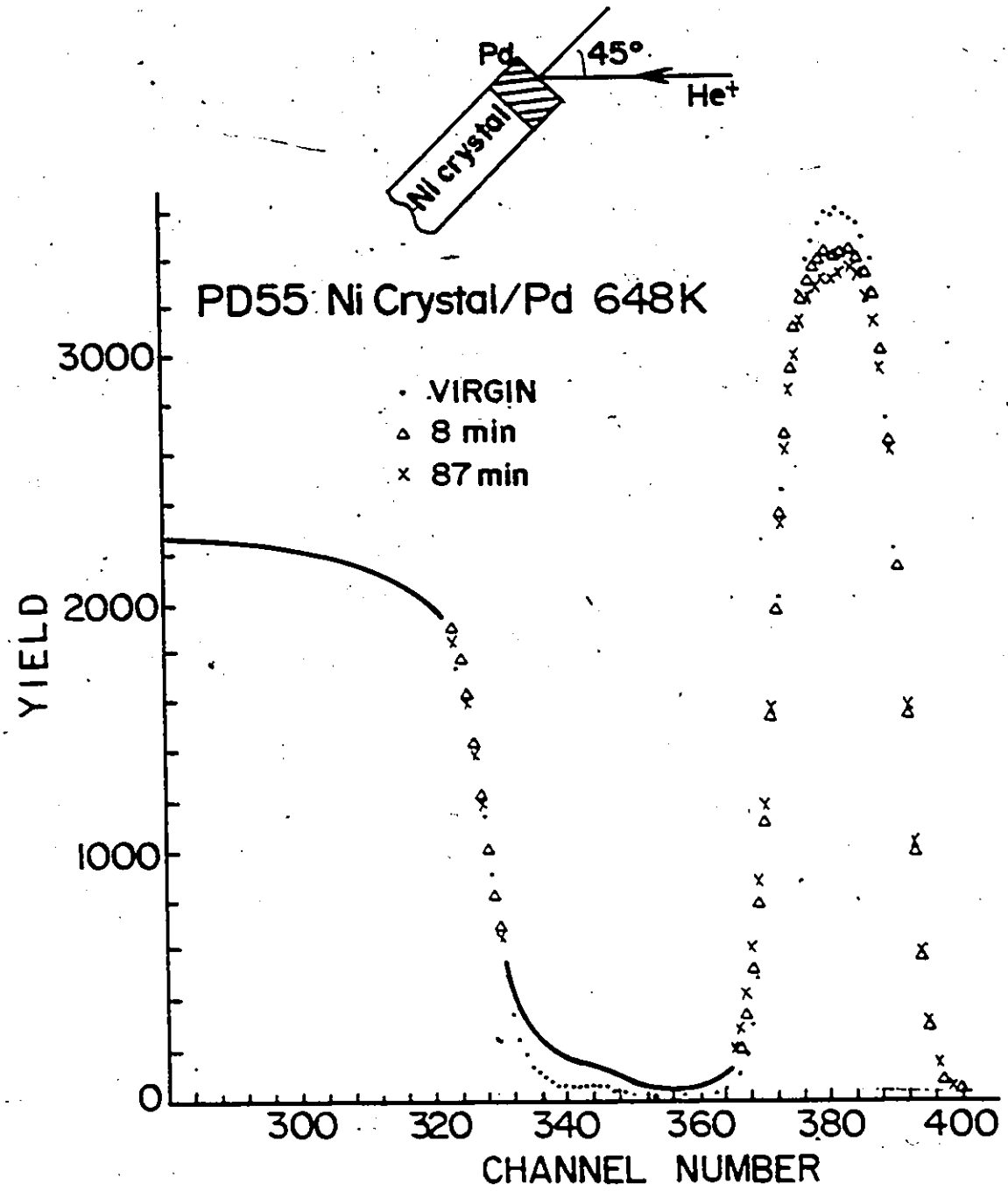

Fig. 6.50: RBS spectra typical of single crystal Ni/Pd couples annealed at 648K.

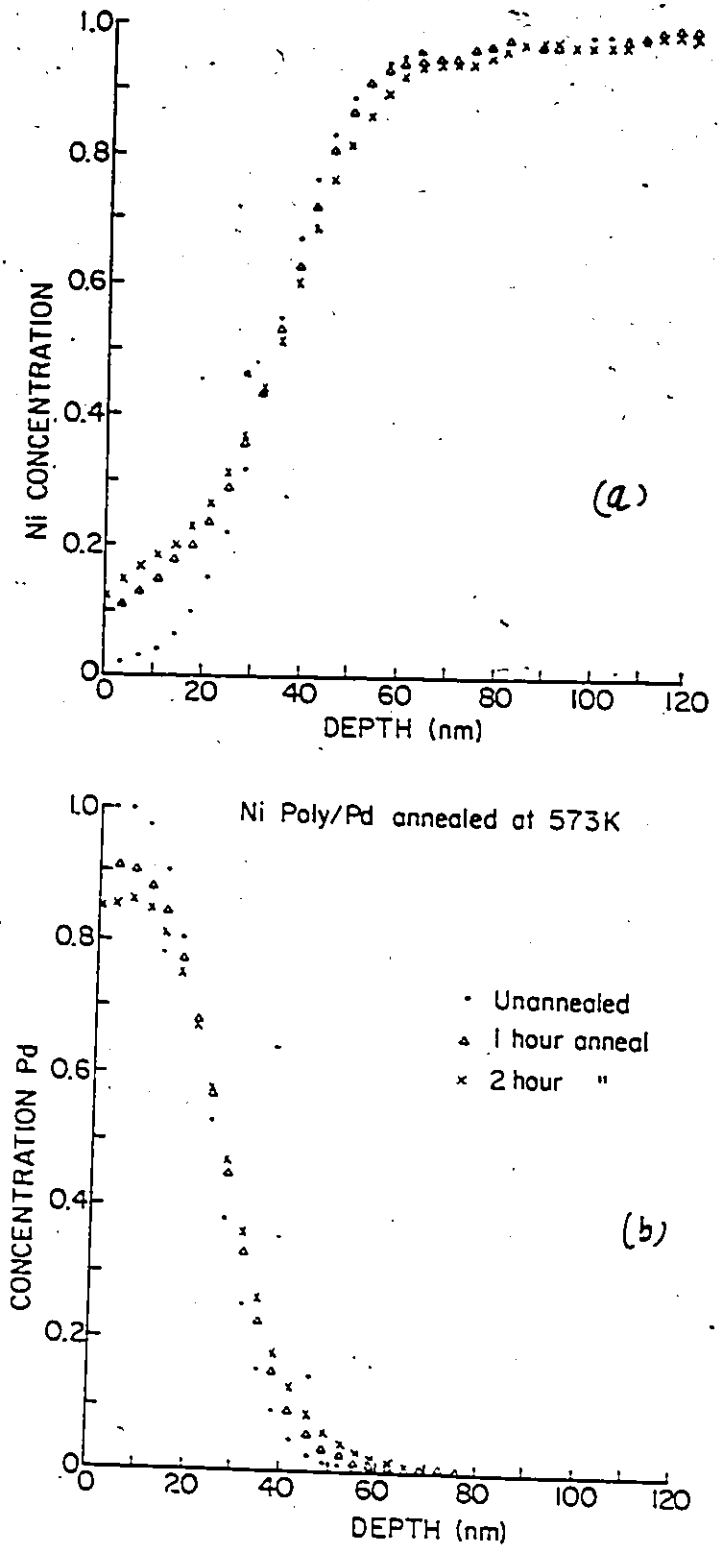

Fig. 6.51: Concentration-depth profile for the large-grain Ni/Pd couple of Fig. 6.49
(b) Pd profile a) Ni profile.

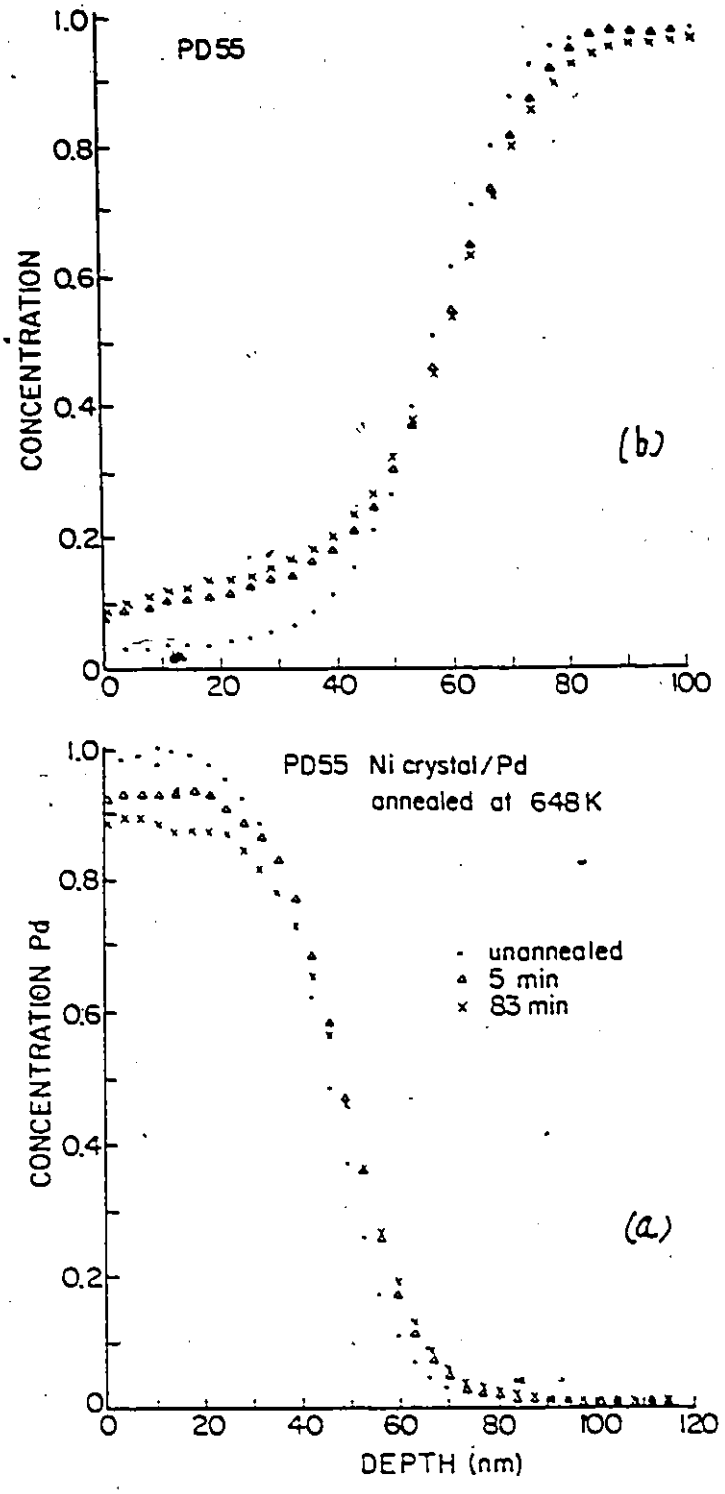

Fig. 6.52: Concentration-depth profile for single crystal Ni/Pd couple annealed at 648K.
(a) Pd profile (b) Ni profile.

near the surface amounts to only $\sim$ 10% after $\sim$ 60 minutes anneal at 573K. The Ni concentrations are somewhat larger than necessary to saturate the Pd grain boundaries ($\sim$ 5%) assuming the same grain size and structure in this case as described previously for Pd on evaporated Ni film. One possible explanation for this is that diffusion through the Pd film was enhanced by defects present in the as-prepared film. Secondly, once the Ni atoms have diffused to the Pd surface, they may then diffuse back into the film.

Effective diffusion coefficients for these annealed samples were obtained by taking the gradients of the concentration profiles near the original interface. In this analysis the gradients of the profiles after two different annealing times (1 and 3 hours for samples annealed at 573K) were considered since the change in the gradient between the as-prepared profile and the first annealing cycle is greatly influenced by grain boundary diffusion of Ni through the Pd film. The results of this analysis (Table 6.10) gives $\tilde{D}(Ni) \sim 2.2\pm0.8\times10^{-17}$ cm^2 sec^{-1} and $\tilde{D}(Pd) \sim 1.57\pm0.6\times10^{-17}$ cm^2 sec^{-1} at 573K, and $\tilde{D}(Pd) \sim 0.51\pm2\times10^{-17}$ cm^2 sec^{-1}, $\tilde{D}(Ni) \sim 1.55\pm0.6\ 10^{-17}$ cm^2 sec^{-1} for Ni crystal/Pd film couples annealed at 648K . The errors in these values are large because as Figs. 6.51 and 6.52 show, the slope near the interface did not change much with annealing cycles. Because of the inverse square-dependence of D on the gradients, a 50% error in the gradients can easily lead to a factor of 4 error in D. Also the reduction in the gradients at the interface following the initial rapid diffusion of Ni through the Pd film necessarily introduces some error to the subsequent gradients and may lead to high values for $\tilde{D}$; consequently the values reported here are probably upper limit values.

Nonetheless, the measured $\tilde{D}$ values are considerably lower than those determined for small-grained Ni/Pd couples (sections 6.2.1-6.2.3). At 573K the present values are about a factor of 30 less than that reported in section 6.2.2. At 648K, $\tilde{D}$(Pd), for Pd diffusing into single crystal Ni, is $\sim$ 3 orders of magnitude less than is measured on small-grained Ni/Pd couple and is in qualitative agreement with extrapolated values (Borovskii et al. 1967) for a 10% Ni/Pd bulk alloy.

At first sight it is surprising that similar values of $\tilde{D}$ were obtained for polycrystalline Ni/Pd couples annealed at 573K, and single crystal Ni/Pd couples annealed at 648K. One possible explanation for this is that the Pd layer after annealing at 648K forms some epitaxial relationship with the underlying single crystal Ni. Consequently the Pd grain size in this case is probably larger than in the polycrystalline Ni case resulting in a reduced influence of grain boundary diffusion on the profile. Indeed RBS/channeling analysis in the aligned and non-aligned directions after 83 minutes anneal shows $\sim$ 10% reduction in the Pd peak yield for the aligned direction, thus confirming the epitaxial nature of the film.

6.2.4.2 Irradiated Specimens

Figure 6.53 shows the RBS spectra for a Ni crystal/Pd couple irradiated at 298K to various doses (0-35x10^{15} cm^{-2}) of 120 KeV Ar^{+} ions. The spectra have been shifted to compensate for the Pd layers removed by sputtering and to reveal more clearly the ion-induced broadening of the initial interface, similar to that observed for small-grained Ni/Pd couples at this temperature in section 6.2.1. Irradiated

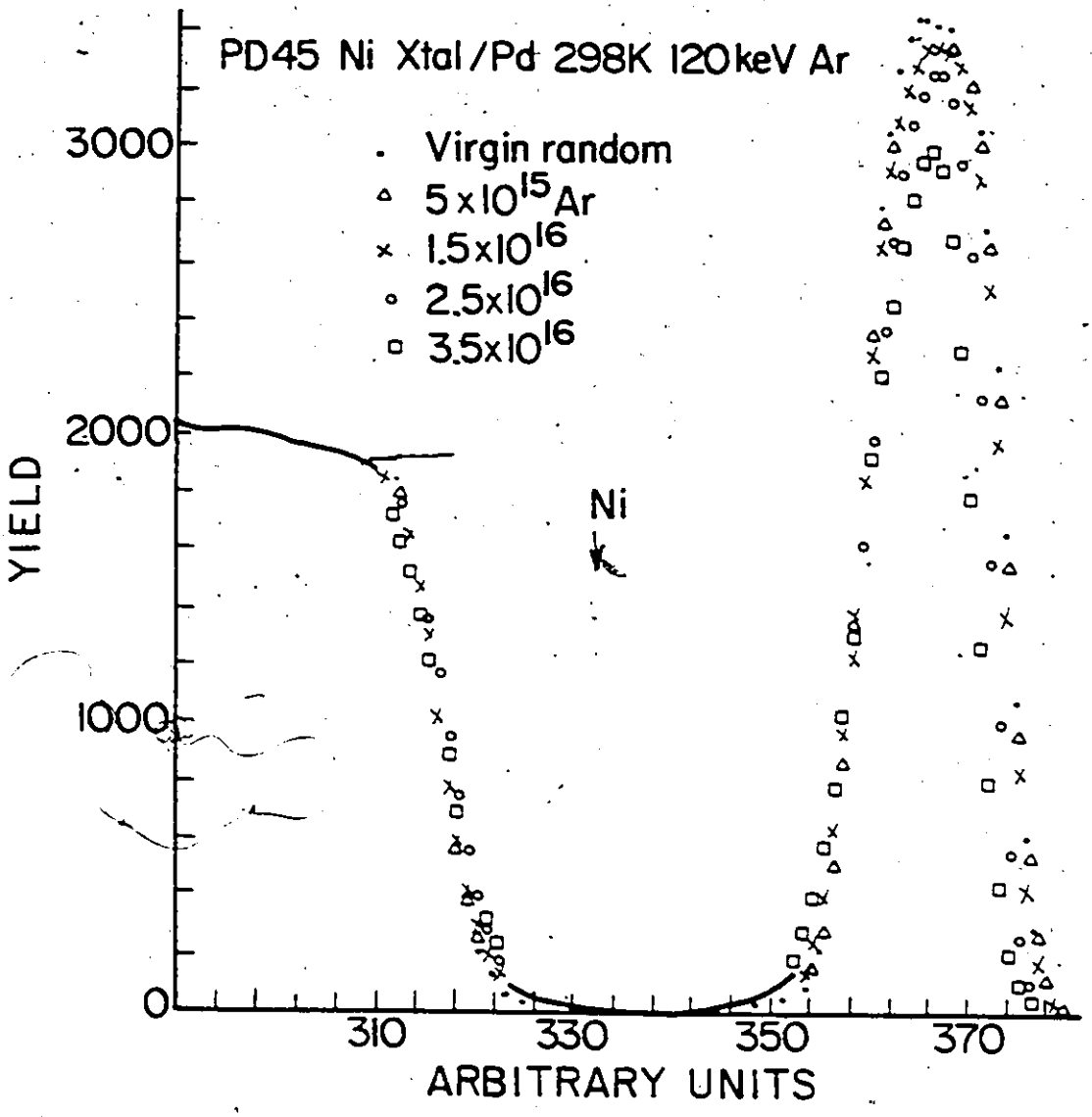

Fig. 6.53: RBS spectra of Ni crystal/Pd couple before and after irradiation to various doses of Ar.

polycrystalline Ni/Pd couples also show similar behaviour. The high energy edge of the Ni signal, and the low energy edge of the Pd signal (for doses $\leq 2.5\times10^{16}$ cm^{-2}) can be fitted to error function profiles from which a mixing parameter $\Delta\sigma^2$ can be extracted (as described previously in section 6.2.1). The present results give $\Delta\sigma^2 = 102.5\pm11$ $(nm)^2$ ($\phi = 2.5\times10^{16}$ cm^{-2}) for the mixing parameter and $\Delta\sigma^2/\phi = 4.1\times10^{-29}$ cm^4/ion as the diffusion coefficient per ion in qualitative agreement with the results reported in section 6.2.1 for small-grained specimens. This result indicates that at 298K grain boundary diffusion either in the small-grained Ni or single crystal Ni/Pd couples is not important and the observed mixing is entirely attributable to collisionally induced mixing.

Figures 6.54 and 6.55 show the RBS spectra for polycrystalline Ni/Pd couples irradiated at 573K and 673K respectively to various Ar doses (0-30×10^{15} Ar^+ cm^{-2}). Figures 6.54 and 6.55 compare with Figs. 6.49 and 6.50 for samples annealed, without ion bombardment, at similar temperatures. In Figs. 6.54 and 6.55 a dose of 5×10^{15} Ar^+ cm^{-2} took $\sim$ 15 minutes, so that the spectra for the highest doses compare with that for the first annealing cycle in Fig. 6.49 and the last annealing cycle in Fig. 6.50. The two sets of figures show similar initial rapid diffusion of Ni through the Pd film by grain boundary diffusion effects discussed in the previous sections. In addition, however, the spectra of the irradiated specimens show larger broadening of the initial interface due in part to both collisionally-induced mixing and radiation-enhanced diffusion. Also the low energy edge of the Pd signal in Fig. 6.55 shows penetrating tails (between channels 336-352), indicating possible diffusion

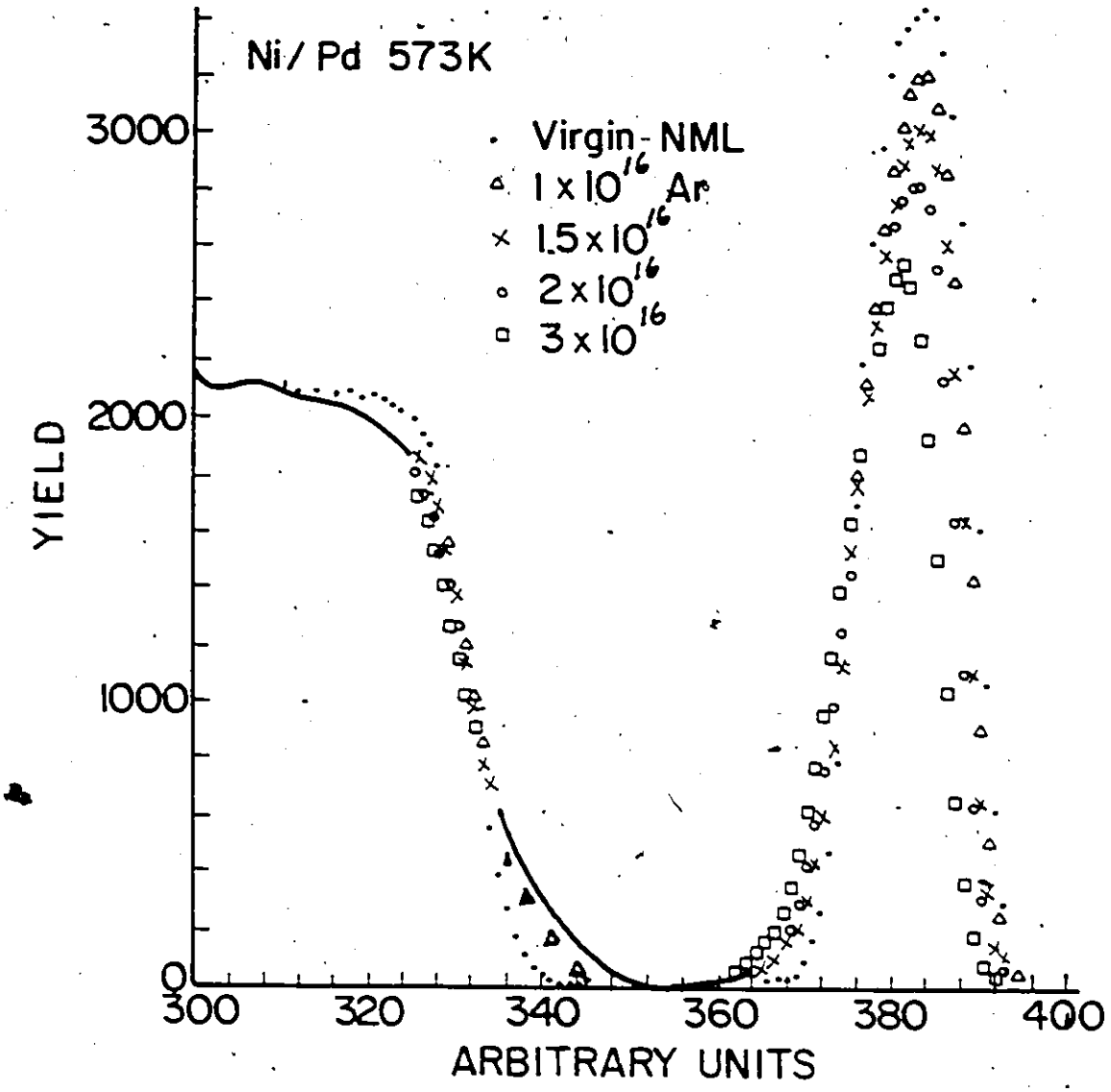

Fig. 6.54: RBS spectra of large-grain Ni/Pd couple before and after irradiation at 573K.

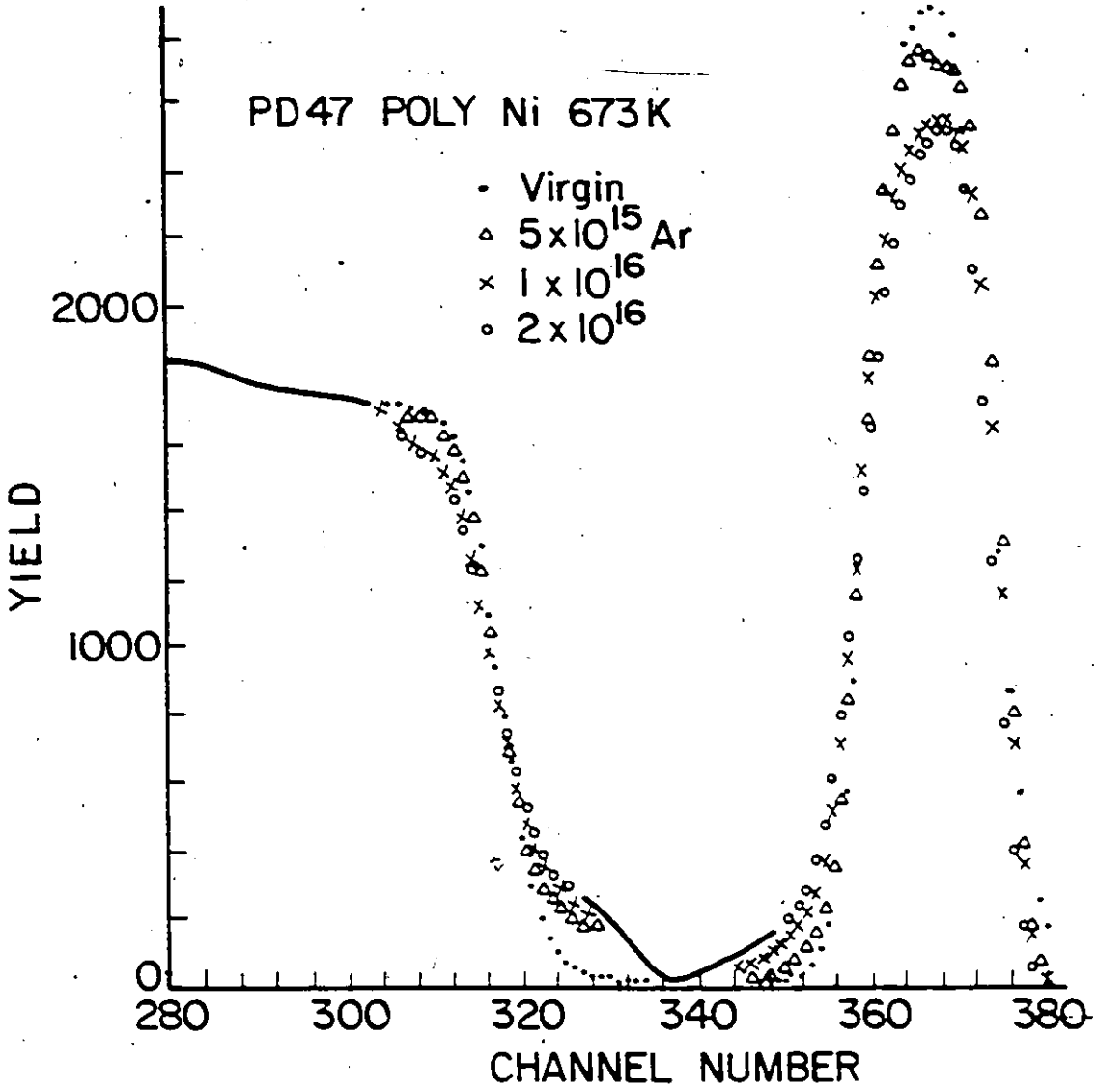

Fig. 6.55: RBS spectra of large-grain Ni/Pd couple before and after irradiation at 673K.

of Pd along grain boundaries or dislocations in the large-grain Ni substrate. However, this feature was hardly observable for the unirradiated, annealed specimens and must therefore be irradiation-induced. This fact, in addition to the large grain size of the Ni ($\sim$ 1 mm), suggests that the penetrating tail is probably not due to grain boundary diffusion. On the other hand, radiation damage in metals following heavy ion irradiation is typically observed as dislocations (Pronko 1974, Chen 1973, Al-Tamimi et al. 1985) rather than isolated wholly-displaced atoms. Conceivably, such dislocations can give rise to rapid diffusion paths, resulting in penetrating tails. Figure 6.55 shows that the depth of the penetrating tail compares with the ion range ($R_p + 2\Delta R_p \sim 100$ nm) thus indicating that Pd migration is limited to the ion range, and strongly suggests that diffusion along dislocations resulting from ion bombardment is responsible for the observed penetrating tail.

Figures 6.56 and 6.57 show the concentration-depth profiles derived from the RBS spectra of Figs. 6.54 and 6.55. Compared to the profiles shown in Figs. 6.40 and 6.48 for small-grained Ni/Pd specimens irradiated at similar temperatures, one observes a dramatic reduction in the interdiffusion for the large-grain Ni/Pd couples especially at 673K. In Fig. 6.56a, the surface Pd concentration at high doses (15 and 20×10^{15} cm^{-2}) is somewhat in doubt because, as Fig. 6.54 shows, the reduction in the peak Pd yield is partly due to sputtering effects. For example after a dose of 30×10^{15} Ar^+ cm^{-2}, almost half of the original film ($\sim$ 40 nm) was removed by sputtering, and the thickness of the remaining film is now comparable to the detector resolution. The true Pd surface concentrations can be extracted, however, from the Ni profiles (Fig. 6.56b)

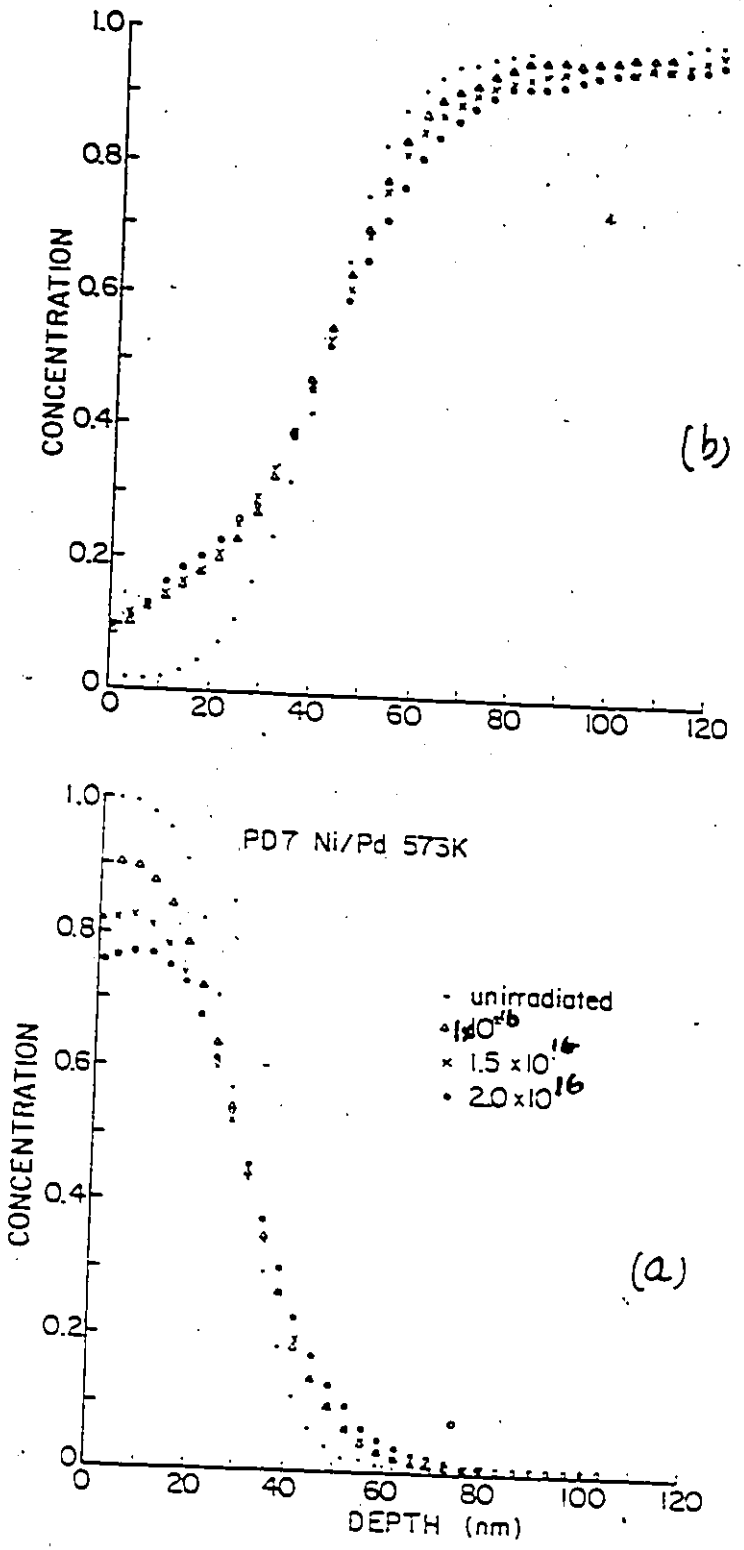

Fig. 6.56: Concentration-depth profile for the large-grain Ni/Pd irradiated at 573K

(a) Pd profile (b) Ni profile.

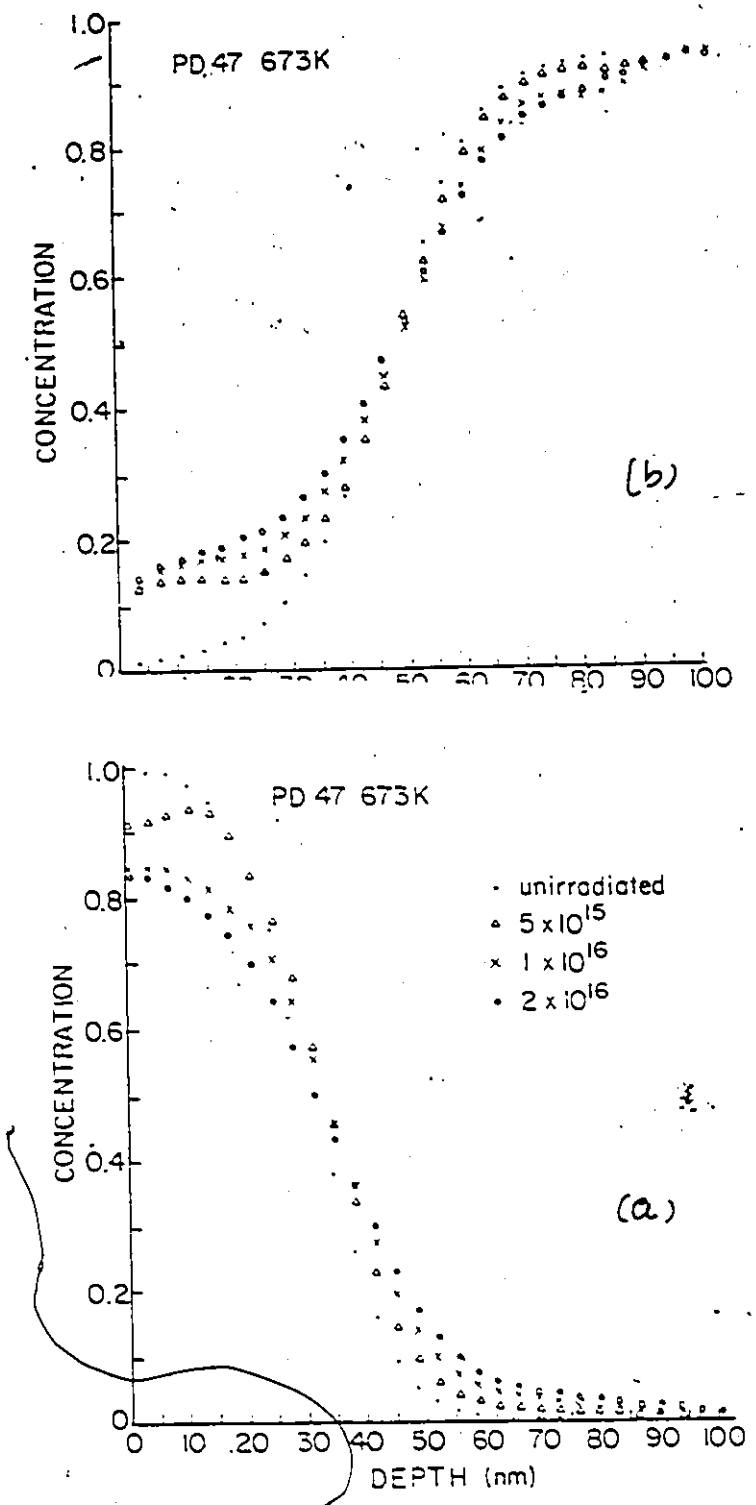

Fig. 6.57: Concentration-depth profile for large-grain Ni/Pd couple irradiated at 673K.
(a) Pd profile (b) Ni profile.

which were calculated independently of the Pd profile. The figures show that even for doses that are ∿ a factor of 5 higher than those used for the small-grained couples, the interdiffusion in the large-grain Ni/Pd couples are still some factor of 3-4 lower. Obviously the absence of a high density of grain boundaries in the latter is mostly responsible for this behaviour. As pointed out in section 6.2.3, at 673K extensive lattice diffusion under irradiation results in the overlap of diffusion fields from adjoining grains and consequently results in concentration profiles from which the separate lattice and grain boundary portions are no longer distinguishable. Such overlapping fields are not observed in Fig. 6.58 which is a 'Whipple plot' of the concentration profiles for the large-grain Ni/Pd couple irradiated at 673K. Both the lattice and dislocation-assisted portions are clearly distinguishable, simply because the Ni grain sizes are large enough to prevent overlap of diffusion fields from adjoining grains.

Effective diffusion coefficients under irradiation for these large-grain Ni/Pd couples, calculated as outlined in section 6.2.3, are listed in Table 6.10 together with those for the annealed specimens. Also included in the table are some typical small-grain D values, and D_d, the coefficient for diffusion along the rapid diffusion path in large grain Ni at 673K. The table shows that for irradiated specimens, their diffusion is enhanced by more than one order of magnitude compared to unirradiated annealed specimens, and in contrast with irradiated small-grained Ni/Pd couples where an enhancement of ∿ a factor of 2 was observed at 648K and almost none at all at 673K where grain boundary

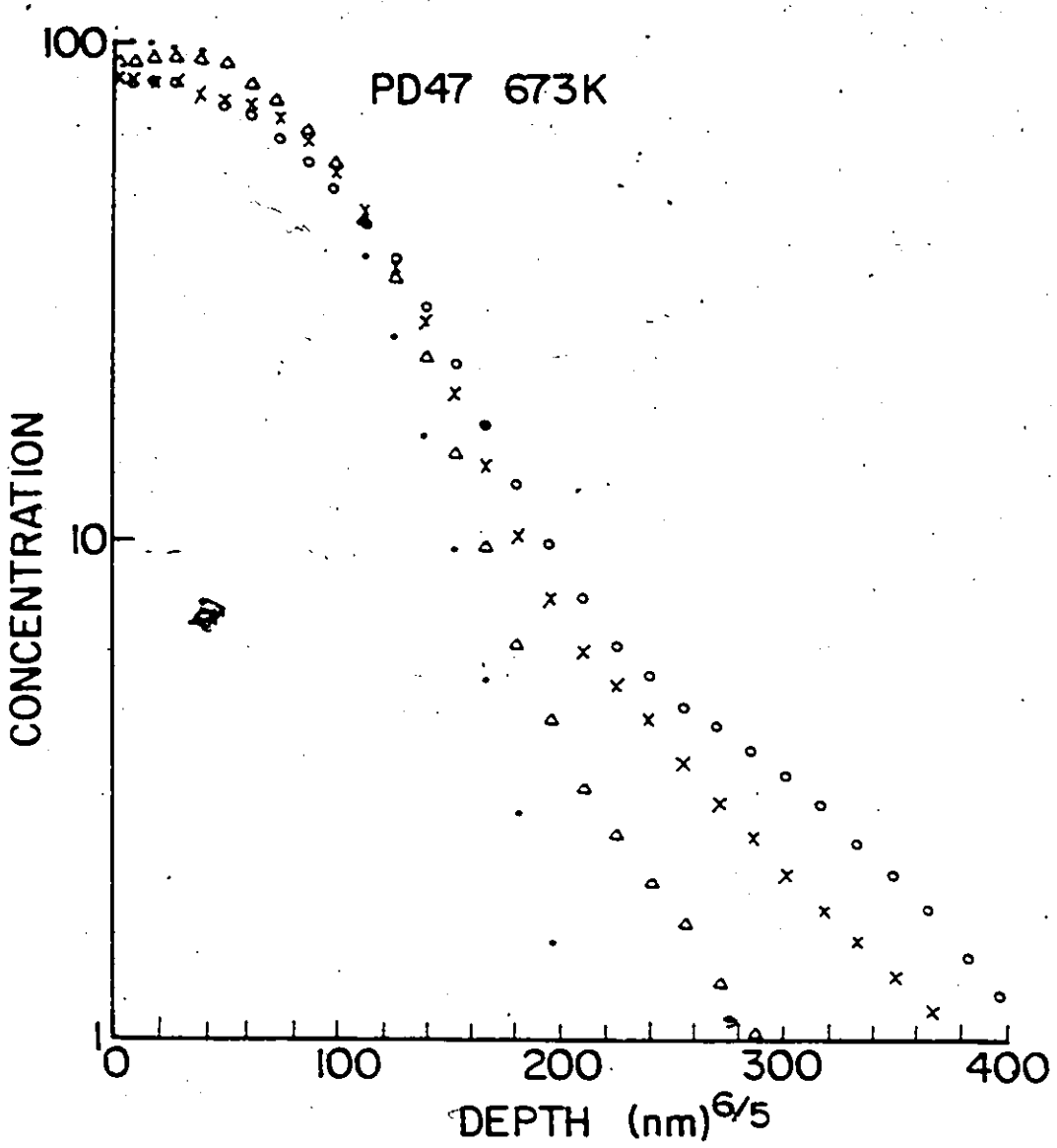

Fig. 6.58: Whipple plot of the Pd concentration for the large-grain Ni/Pd couple irradiated at 673K.

effects overwhelmed the interdiffusion. Also, compared to small-grained specimens, both the thermal and radiation-enhanced coefficients are lower in this case. In fact at 673K, D_{rad} (large grain) $< D_{\ell}$(small grain) suggesting that in the analysis and interpretation of ion beam-induced mixing of thin metal films at elevated temperatures ($\gtrsim$ 400K in this case) grain boundary diffusion effects may be as important as irradiation effects. Also D_d(Pd) for large grain specimens (1.32×10^{-14} cm^2 sec^{-1} at 673K) is more than 2 orders of magnitude less than in the small-grain couples.

Table 6.10 Measured effective diffusion coefficients for large-grain-Ni/Pd couples annealed/irradiated at various temperatures.

1. Annealed

T(K)	Sample	D_ℓ(Ni) x 10^{-17} cm^2-sec^{-1} Large Grain	D_ℓ(Ni) x 10^{-17} cm^2-sec^{-1} Small Grain	D_ℓ(Pd) x 10^{-17} cm^2-sec^{-1} Large grain	D_ℓ(Pd) x 10^{-17} cm^2-sec^{-1} Small grain
573	Poly Ni/Pd	2.2 ±0.8	35.9±0.7	1.57± .6	30.4±0.7
648	Ni crystal/Pd	1.55±0.6	-	0.51± 0.2	-

2. Irradiated

298	Ni crystal/Pd	5.1± 1.0	-	-	6.8
573	Poly Ni/Pd	30.5± 5.1	-	50.3± 10.0	300
673	Poly Ni/Pd	34.0± 6.7	-	61.5± 12.0	700

6.3 IRRADIATION INDUCED GRAIN GROWTH OF Ni/Pd THIN FILMS

In this section results are presented of the experiments performed to assess the evolution of film microstructure resulting from ion bombardment of Ni/Pd films. Samples for these experiments were prepared, as described in section 5.1, on freshly cleaved NaCl crystals and consist of ∿ 30 nm Ni and 30 nm Pd evaporated layers. The NaCl/film composites were irradiated to various doses (0-20x10^{15} cm^{-2}) of 120 KeV Ar^{+} ions at 298K and 573K. The resulting microstructures of the films were studied with transmission electron microscopy (TEM), and the results are correlated in the mixing results reported in section 6.2.

Figure 6.59 shows the TEM micrographs and respective diffraction patterns for unirradiated films and for films irradiated to 5 and 20x10^{15} Ar cm^{-2} at 298K. The micrograph and diffraction pattern of the unirradiated specimen show that the as-prepared film consists of small-grained randomly oriented grains with mean grain diameter $\bar{L}$ ∿ 10 nm. Figure 6.59(b) shows that considerable recrystallization and grain growth results from 120 KeV Ar^{+} irradiation. The micrographs indicate increased average grain size with increasing Ar dose. Also the diffraction rings become increasingly sharper and spotty; after a dose of 2x10^{16} cm^{-2}, the patterns show largely discontinuous spotty pattern. These spotty patterns reflect the increased grain size in the film. The mean grain diameter, $\bar{L}$, after a dose of 2x10^{16} cm^{-2} is ∿ 50 nm; ie. it is comparable to the film thickness.

Figures 6.60 and 6.61 show the TEM micrographs and diffraction patterns for specimens irradiated at 573K with 2x10^{16} Ar^{+} cm^{-2} and 5x10^{15} Kr^{+} cm^{-2} respectively. The micrograph of the Ar-irradiated film

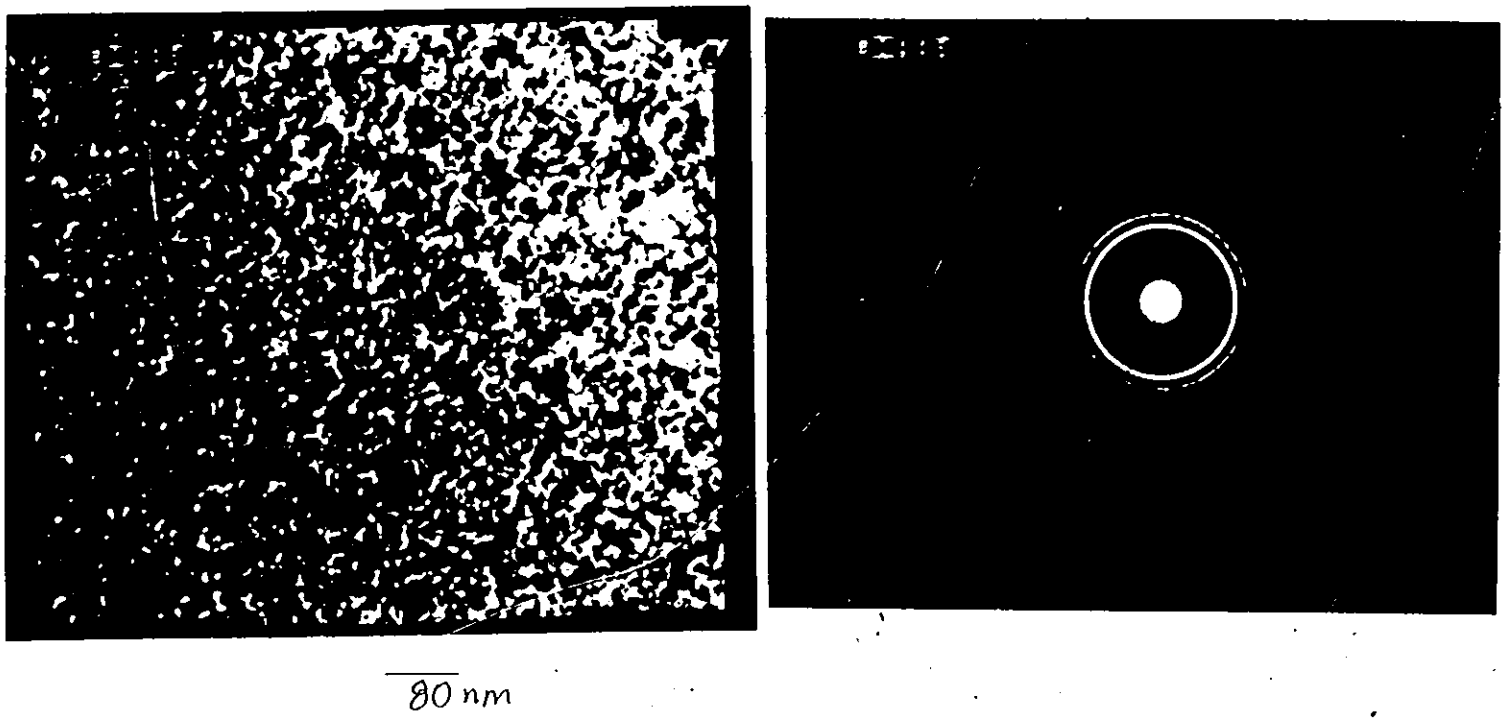

Fig. 6.59: TEM micrographs and diffraction patterns of the evaporated, unirradiated Pd/Ni films.

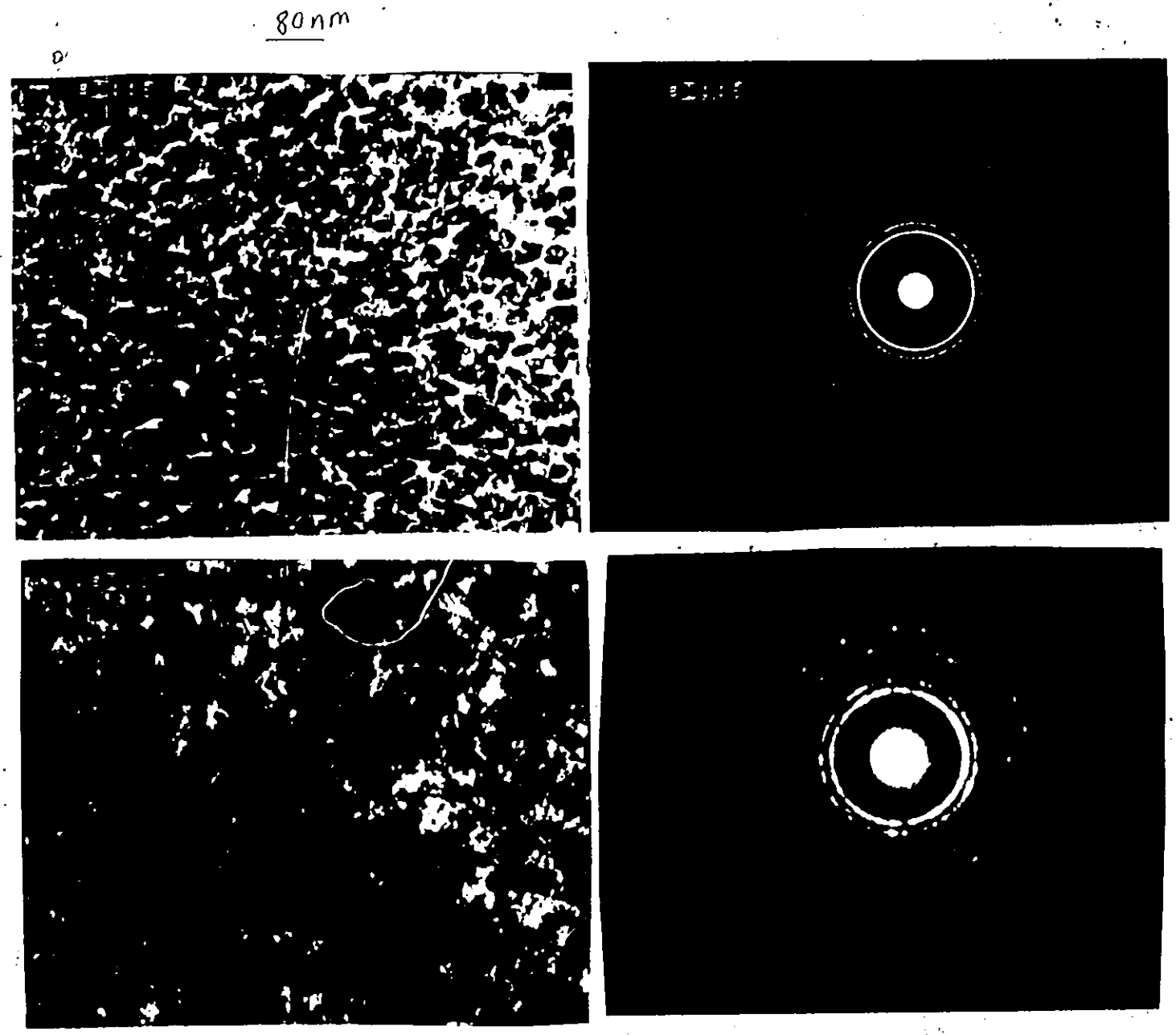

Fig. 6.59(b) TEM micrograph and diffraction pattern for films irradiated at 298K to 5 and 2×10^{15} Ar^{+} cm^{-2}

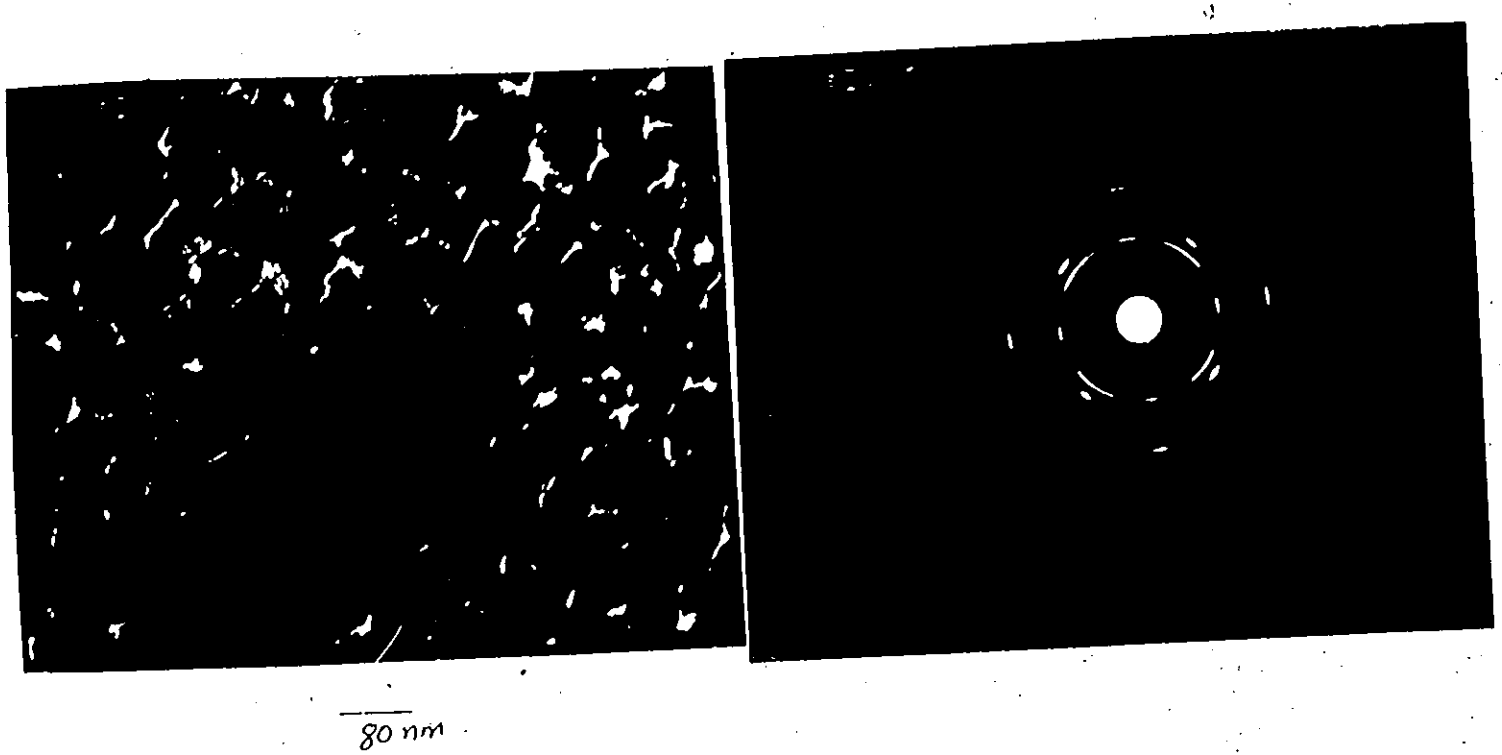

Fig. 6.60: TEM micrograph following Ar irradiation at 573K to 2×10^{16} Ar^{+} cm^{-2}.

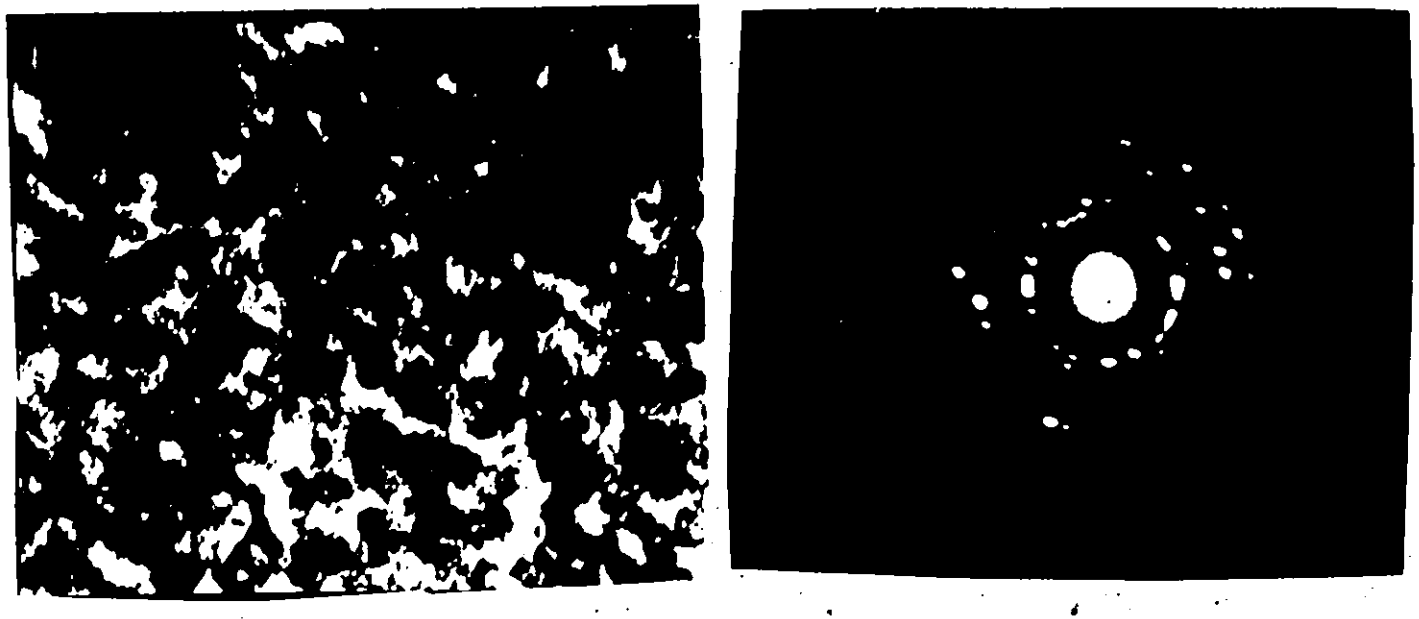

Fig. 6.61: TEM micrograph following Kr^+ irradiation at 573K to $5x10^{15}$ Kr^+ cm^{-2}.

shows a uniform microstructure with average dimensions ∿ 60 nm. The diffraction pattern shows strong diffraction spots indicating preferred orientation of some of the grains. The Kr-irradiated specimens have larger average grain size ∿ 80 nm (note the different scales on the micrographs) and the diffraction pattern shows only discontinuous spotty patterns. Such patterns reflect the increased grain size in the film. It also indicates that the grains are essentially randomly oriented. The larger grain size and the lower dose needed to achieve it in the case of Kr-irradiation are probably due respectively to the cascade size and damage energy of Kr^+ ions compared to Ar^+ ions. The epitaxial nature of the Ar-irradiated film is probably due to the influence of thermal effect.

The observed thermal- and irradiation-induced grain growth are in qualitative agreement with the arguments presented in section 6.2.3 that the rapid initial mixing levels observed ultimately slow to a less rapid rate partly because of increased average grain size and reduction in the density of grain boundaries.

6.4 ELECTROCATALYSIS OF THE HYDROGEN EVOLUTION REACTION ON ION MIXED Ni/Pd

In this section results are presented of the experiments performed to study the H_2-evolution reaction on ion beam mixed Ni/Pd alloys. The electrolyte was a concentrated caustic solution made from ~ 30 ω/O KOH and doubly distilled water. The solution and electrode preparations for these measurements, as well as the potentiostatic polarization techniques have been described in section 5.3. In section 6.4.1 results of these measurements on polished Ni specimens are presented and compared with similar measurements by other workers on polished Ni. The qualitative features of the potential-current density measurements are also discussed. In section 6.4.2 results are given for Ni covered with a layer of evaporated Pd and finally in 6.4.3 results are given for the ion beam mixed Ni/Pd alloys.

6.4.1 Current-Potential Measurements on Polished Ni

Fig. 6.62 shows typical plots of electrode potential, E,(volts) versus log current density, i (mA cm^{-2}) for polished Ni specimens. The electrode potentials reported in the figure were measured vs a Dynamic Hydrogen Electrode (DHE) as described in section 5.2, and the potential of this reference electrode is also indicated in the figure (E_{Ref}). The currents are the total cell currents, ie. corrections for ohmic losses were not made. The dots represent the results of the first polarization sweeps (-1.3 to 0 V) of the present investigation, while the upper dashed line is due to measurements by Miles et al. (1976) on polished Ni in 50 w/o KOH at the same temperature as this investigation, 80°C. The lower dashed curve, due to Appleby et al. (1978), shows the potential-

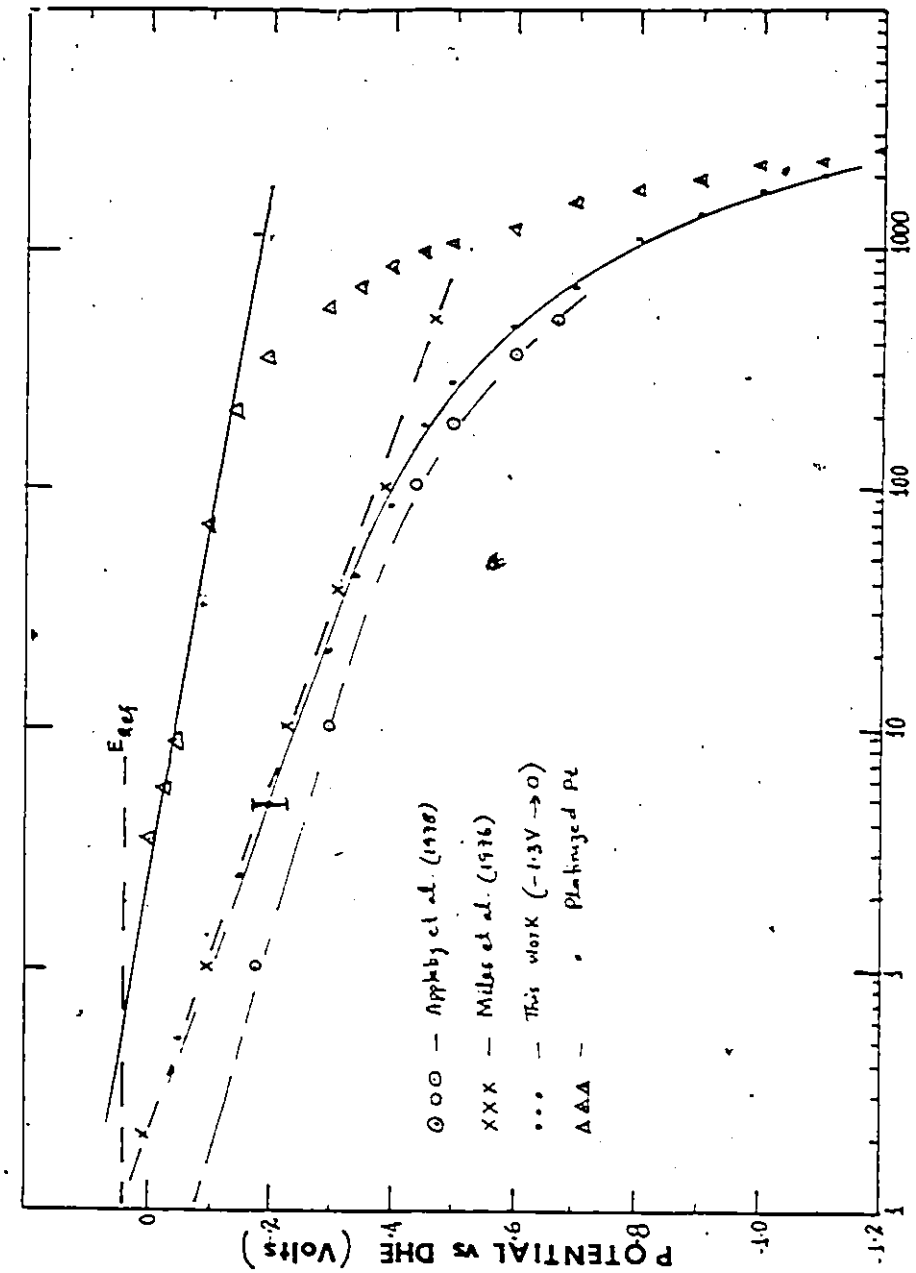

Fig. 6.62: Overpotential of Ni electrodes for hydrogen evolution in

current curve measured on Ni in 34 w/o KOH at 90°. Appleby's potentials were measured versus a reversible hydrogen electrode and are necessarily ∿ 40 mV lower than the value of the present investigation.

Figure 6.62 shows, within error (± 20 mV), that these measurements are the same. The curve of potential vs log i exhibits two types of behaviour: a) in the low current density range, the potential increases (negatively) linearly with log i, (b) at high current densities, the potential increases markedly with increasing current density. This latter increase is due mostly to the increased ohmic drop in the electrolyte as well as at the electrode-electrolyte interface. The result of the present investigation (and Appleby's) shows that the linear dependence of potential on log i extends to ∿ 150 mA/cm^2. Miles' results which have been corrected for ohmic losses, show a linear behaviour up to i ∿ 500 mA/cm^2. The Tafel slope $\partial\eta/\partial\log i$ of the linear portion is ∿ -140 mV/decade. As discussed in section 4.4, by extrapolating the linear portion to the reference potential (E_{Ref}), the exchange current density, i_0, for hydrogen evolution on the electrode can be determined. Figure 6.62 shows that i_0 for H_2-evolution on smooth Ni is ∿ 1×10^{-4} A/cm^2.

6.4.2 Current-Potential Measurements on Ni Covered with Evaporated Pd

Figure 6.63 shows the plot of potential vs log i obtained for Ni specimens covered with ∿ 40 nm of evaporated Pd. The dots show the first positive sweep (-1.3 to 0 V) while the crosses show the negative sweep (0 to -1.3 V). The curve shows that at low overpotentials ≤ -1V, the increase in potential with increasing current is larger than the 140 mV/decade measured on polished Ni though the precise relation is not

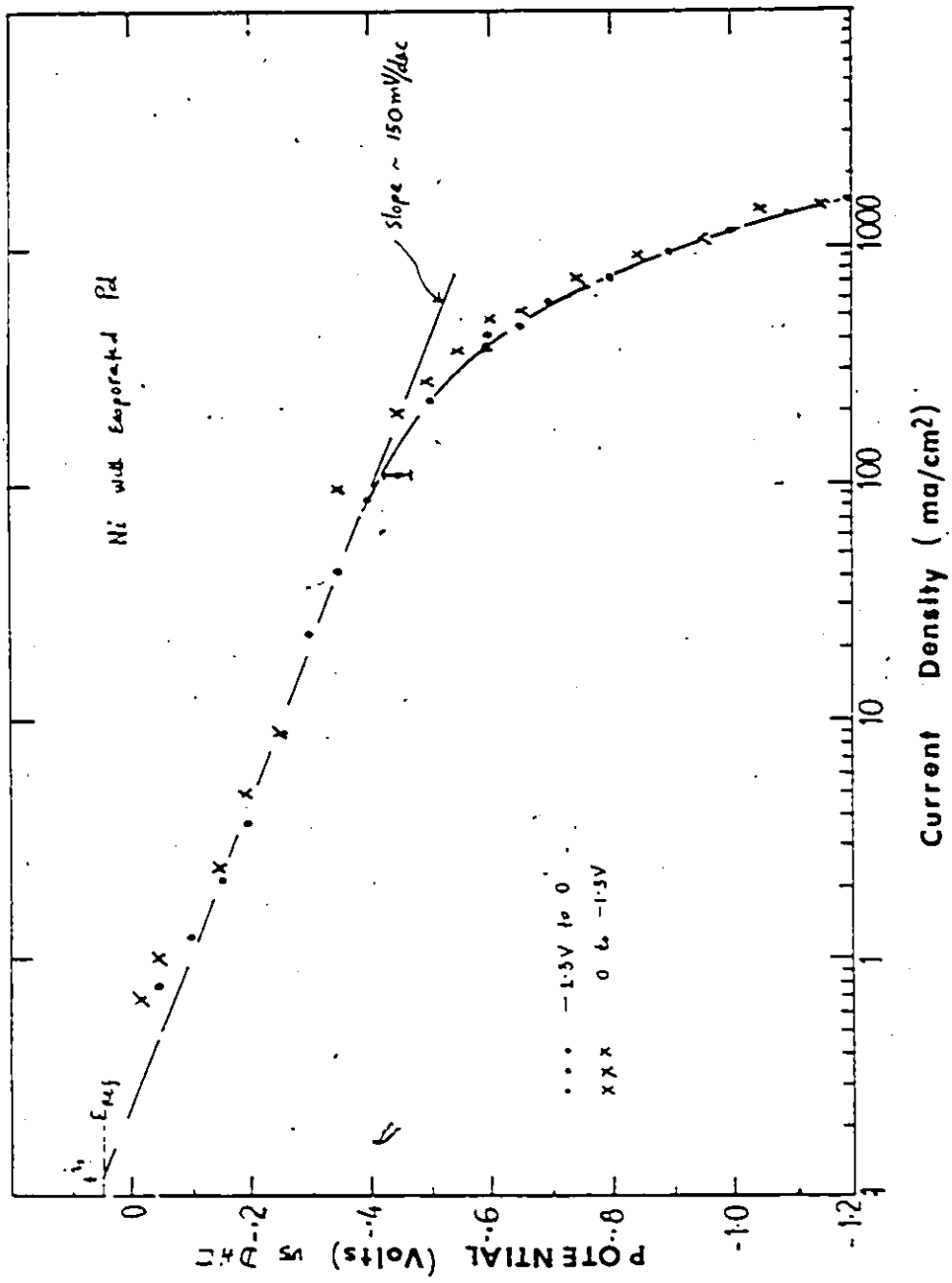

Fig. 6.63: Overpotential for the hydrogen evolution on the Ni electrode covered with evaporated Pd layer vs. log current density

obvious from the figure. For example at a potential of 50 mV, the respective currents are $\sim$ 0.75 mA/cm^2 on Ni/evaporated Pd, and 0.5 mA/cm^2 on polished Ni. For overpotentials > .1V the behaviour of the Ni/evaporated Pd electrode is virtually identical to that of smooth Ni. The curve shows a Tafel slope b $\sim$ 150 mV/decade in the mid-current range and exchange current $i_0 \sim 1.3 \times 10^{-4}$ A/cm^2. These are similar to b $\sim$ 140 mV/decade and $i_0 \sim 1.1 \times 10^{-4}$ A/cm^2 measured on smooth Ni. In contrast to smooth Ni however, the Ni/evaporated Pd electrodes exhibit greater hysteresis ($\sim$ 60 mV at high current densities) between the positive and negative-going sweeps. In fact, at higher current densities, the potential increases more rapidly on the Ni/evaporated Pd electrode than on smooth Ni. For example at -0.8V, the measured current densities are $\sim$ 750 mA/cm^2 on Ni/evaporated Pd electrode, and $\sim$ 1100 mA/cm^2 on smooth Ni.

Figure 6.64 shows the scanning electron microscope (SEM) photograph of the Ni/evaporated Pd cathode following cathodic polarization. The figure shows that in some regions of the sample (Fig. 6.64a) the evaporated film had peeled off due to poor adhesion to the substrate. Figure 6.64(b), which is an expanded view of the region where the film remains intact, shows the existence of holes, cracks and blistered regions. EDAX analysis of the two regions of Fig. 6.64(b) showed that the light region consisted mainly of Ni. The morphology of this specimen probably explains why the observed current-potential curve of this cathode is similar to that of a polished Ni cathode: relatively poor adhesion between the evaporated Pd film and the Ni substrate, or pin holes in the Pd film leads to penetration of electrolyte through the film. Consequently the electrode-electrolyte interface being studied is not simply the

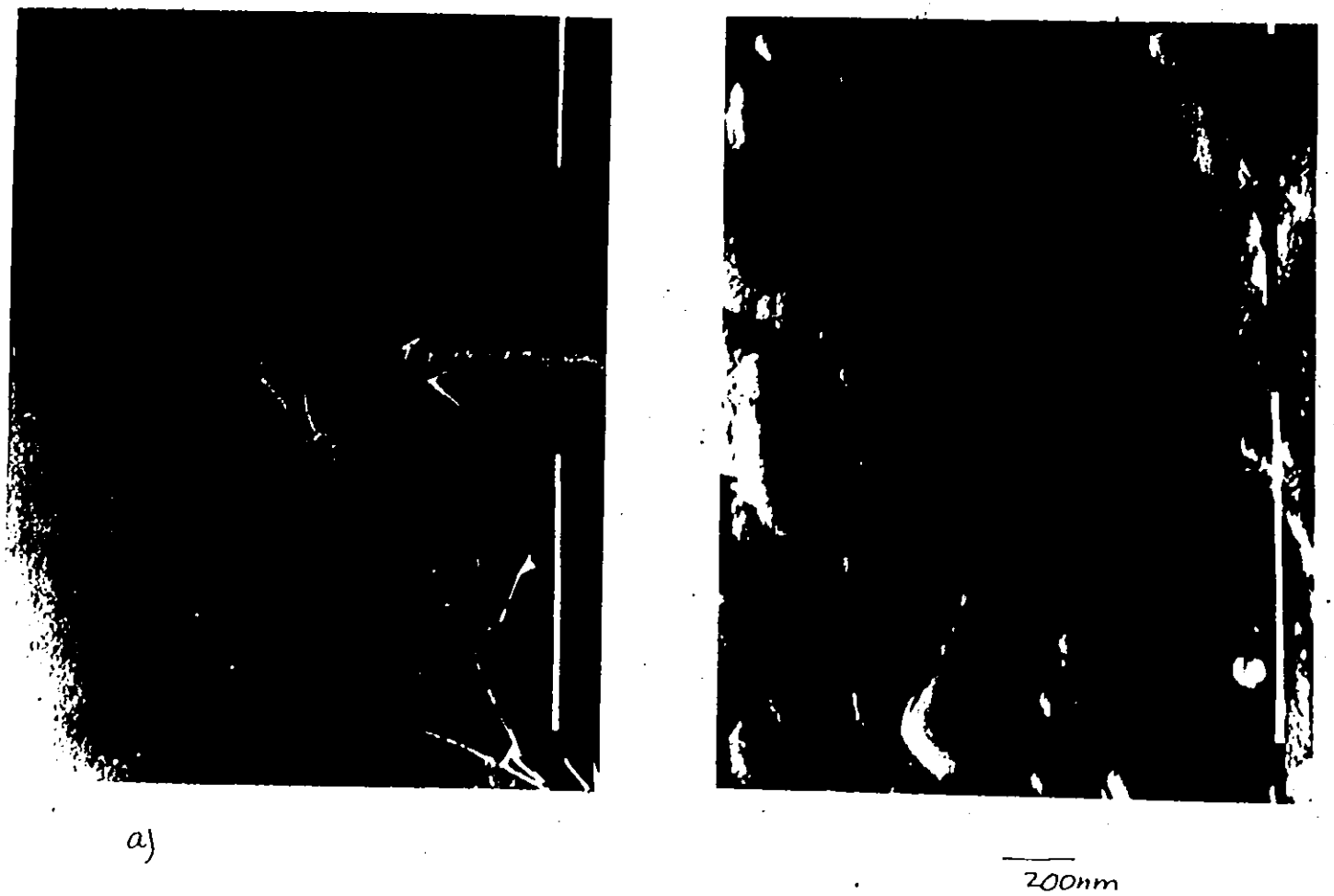

Fig. 6.64: SEM micrograph of a Ni/evaporated Pd cathode following cathodic polarization showing regions where the film had peeled off (a).

Pd film/electrolyte interface but a combination involving the film interface and the Ni/electrolyte interface. At high current densities, gas evolution is vigorous, but some of these are trapped between the Ni electrode and the overlaying Pd film resulting in increased ohmic losses due to the entrapped gas at the interface causing a rapidly increasing potential with increased currents. At the intermediate current densities where gas evolution is not so vigorous, the contribution of trapped gas bubbles to ohmic losses is expected to be less leading to a current-potential behaviour that is similar to that for smooth Ni.

6.4.3 Current-Potential Relation for Ion Mixed Ni/Pd Alloys

Figures 6.65-6.67 show the plot of overpotential versus log i for ion mixed Ni/Pd alloy cathodes having Pd surface concentrations of ∿ 55%, 70% and 90% Pd respectively. The figures show several regions: a) at low overpotentials, the potentials increase relatively slowly, ∿ 50 mV/decade with increasing current, b) at larger potentials (≥ .1V, the potential increases more markedly with current with a slope that depends somewhat on the Pd concentration, c) at still larger potentials, ohmic contributions to the overpotential become large and the overpotential increases most markedly with current. Tafel slopes were obtained by drawing straight lines through the positive-going sweeps. The extent of the ∿ 50 mV/decade region also appears to depend on the Pd surface concentration; for example, the change from 50 mV/decade to a higher Tafel slope occurs at ∿ 30, 5 and 3 mA/cm^2 for alloys with 55, 70 and 90% Pd respectively. A similar change of Tafel slope, b, from b ∿ 40 mV/decade to ∿ 120 mV/decade has been observed by Hoare et al. (1958) on a series of Ni/Pd bulk alloys (0 to 100% Pd) in 2N H_2SO_4. For pure Pd, a Tafel

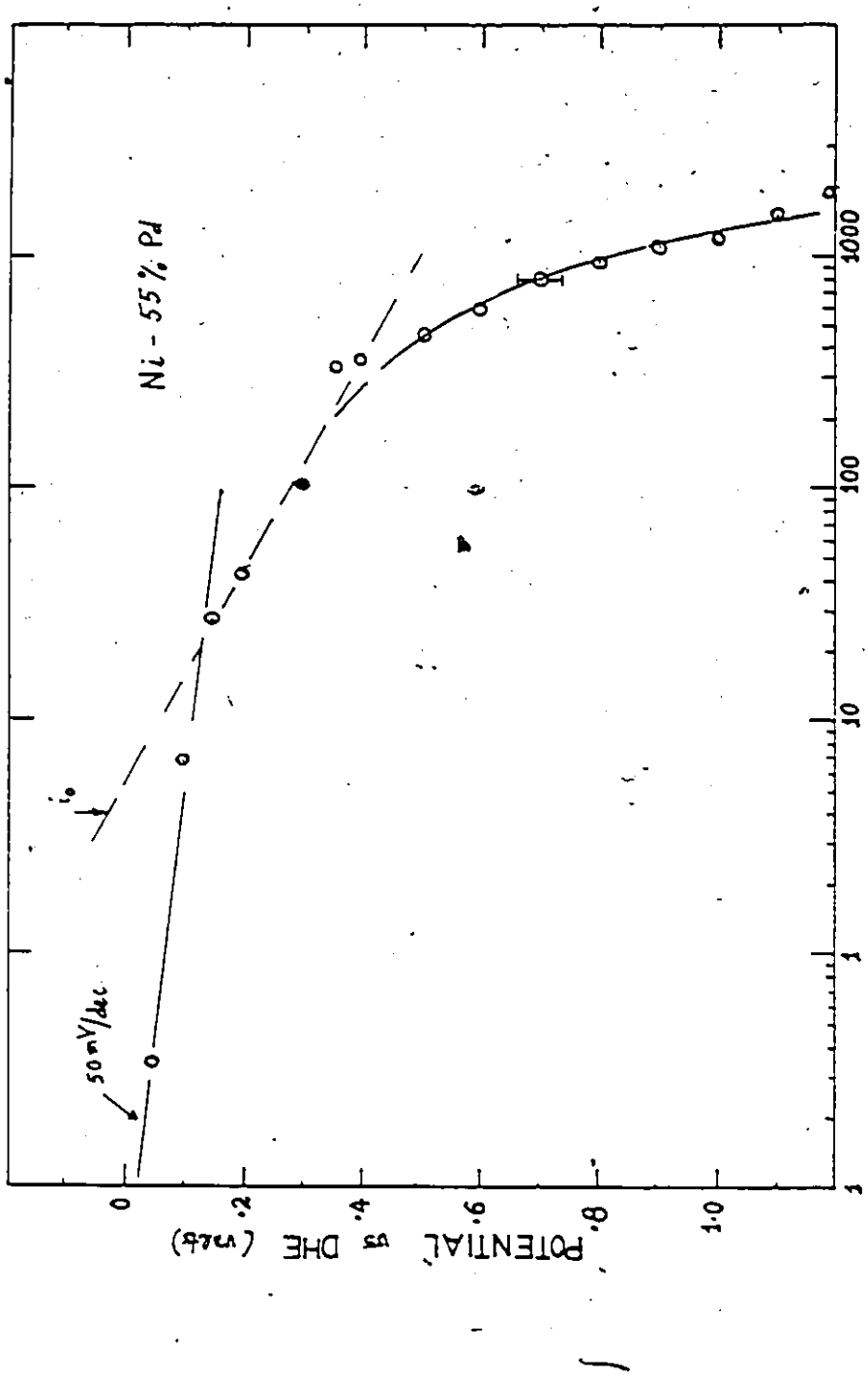

Fig. 6.65: Overpotential-current density relation for the hydrogen evolution reaction on a Ni-55% Pd alloy.

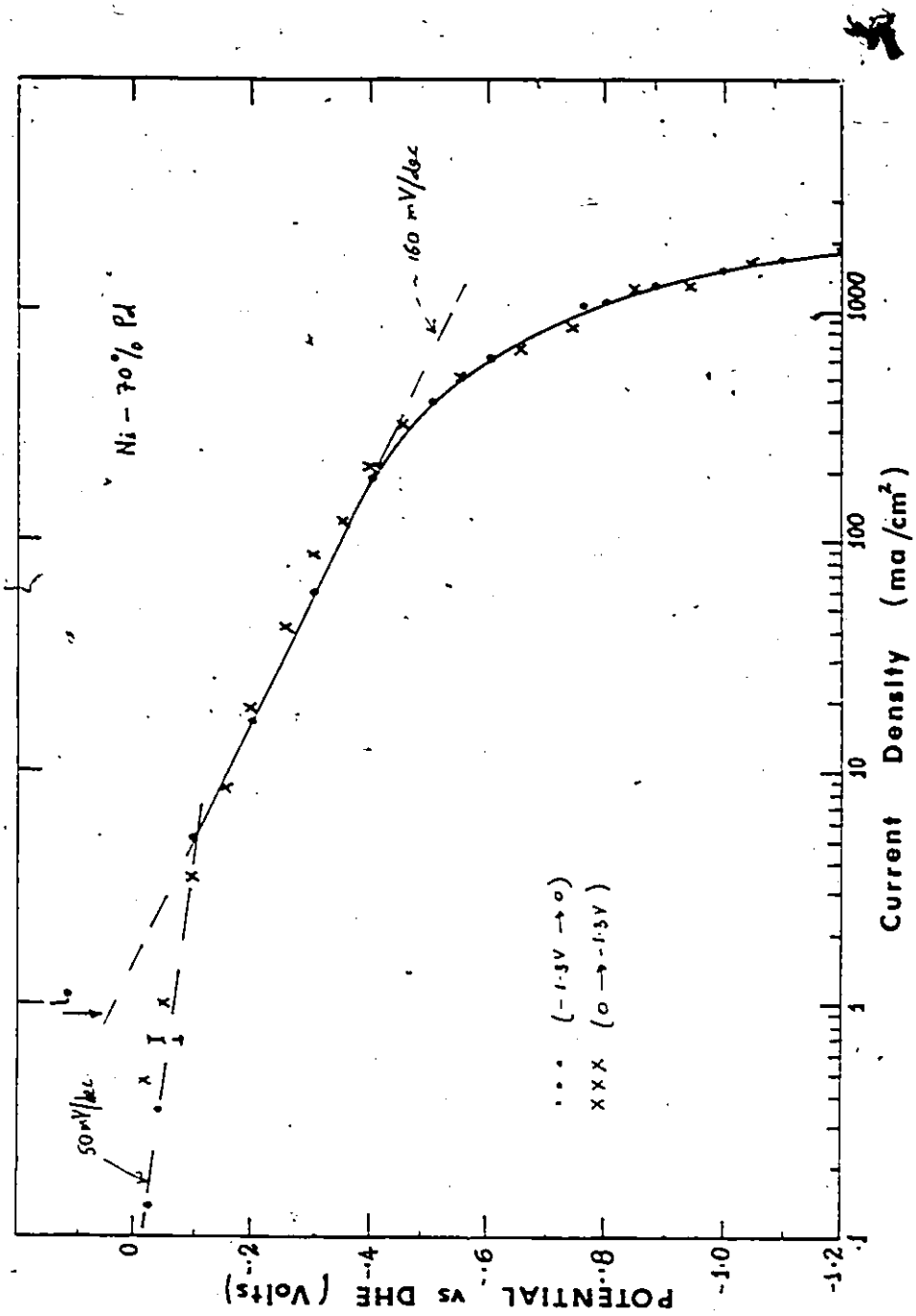

Fig. 6.66: Overpotential-current density curve for hydrogen evolution on Ar ion beam mixed Ni-70% Pd alloy.

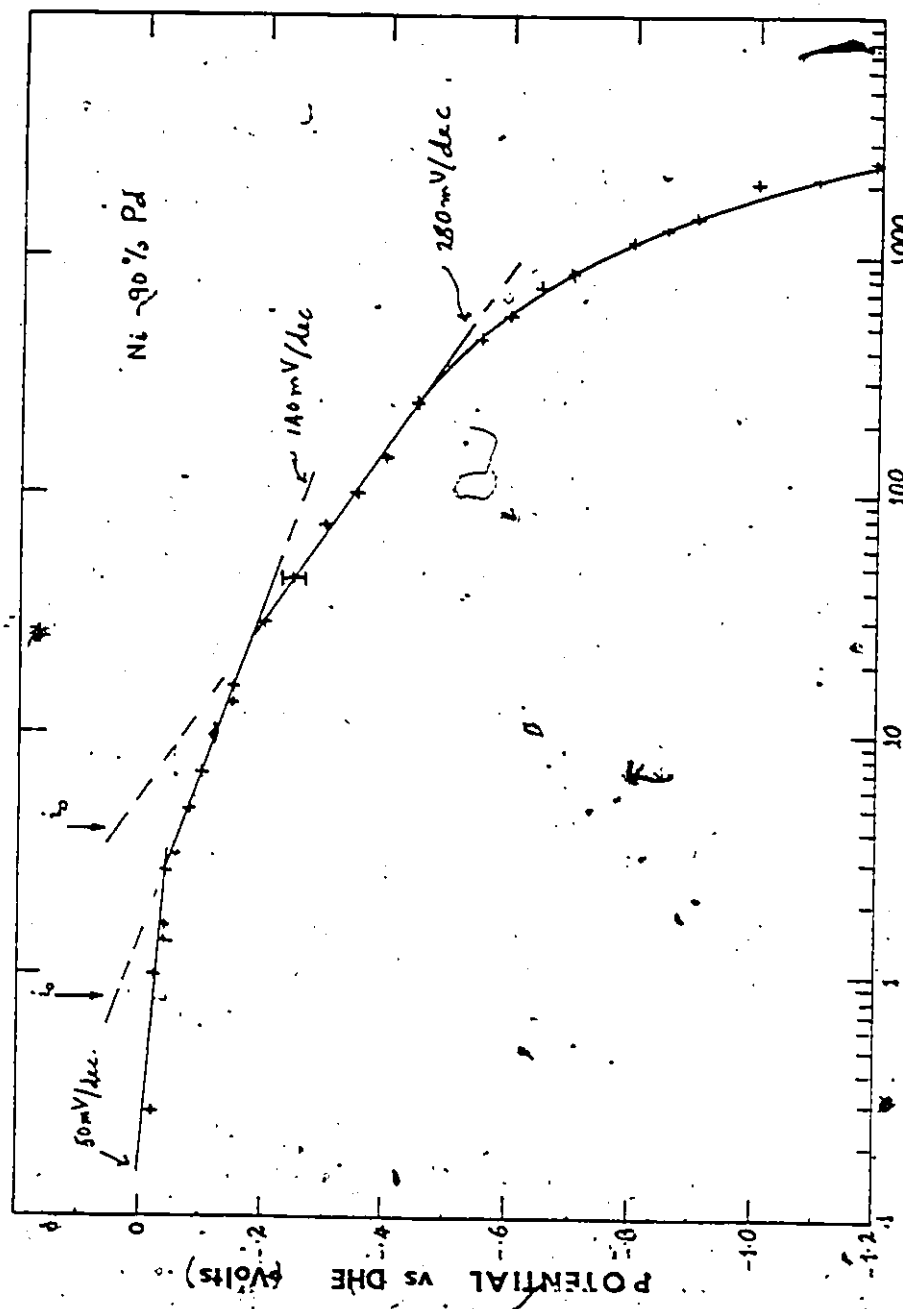

Fig. 6.67: Overpotential-current density curve for hydrogen evolution on ion beam mixed Ni-90% Pd alloy.

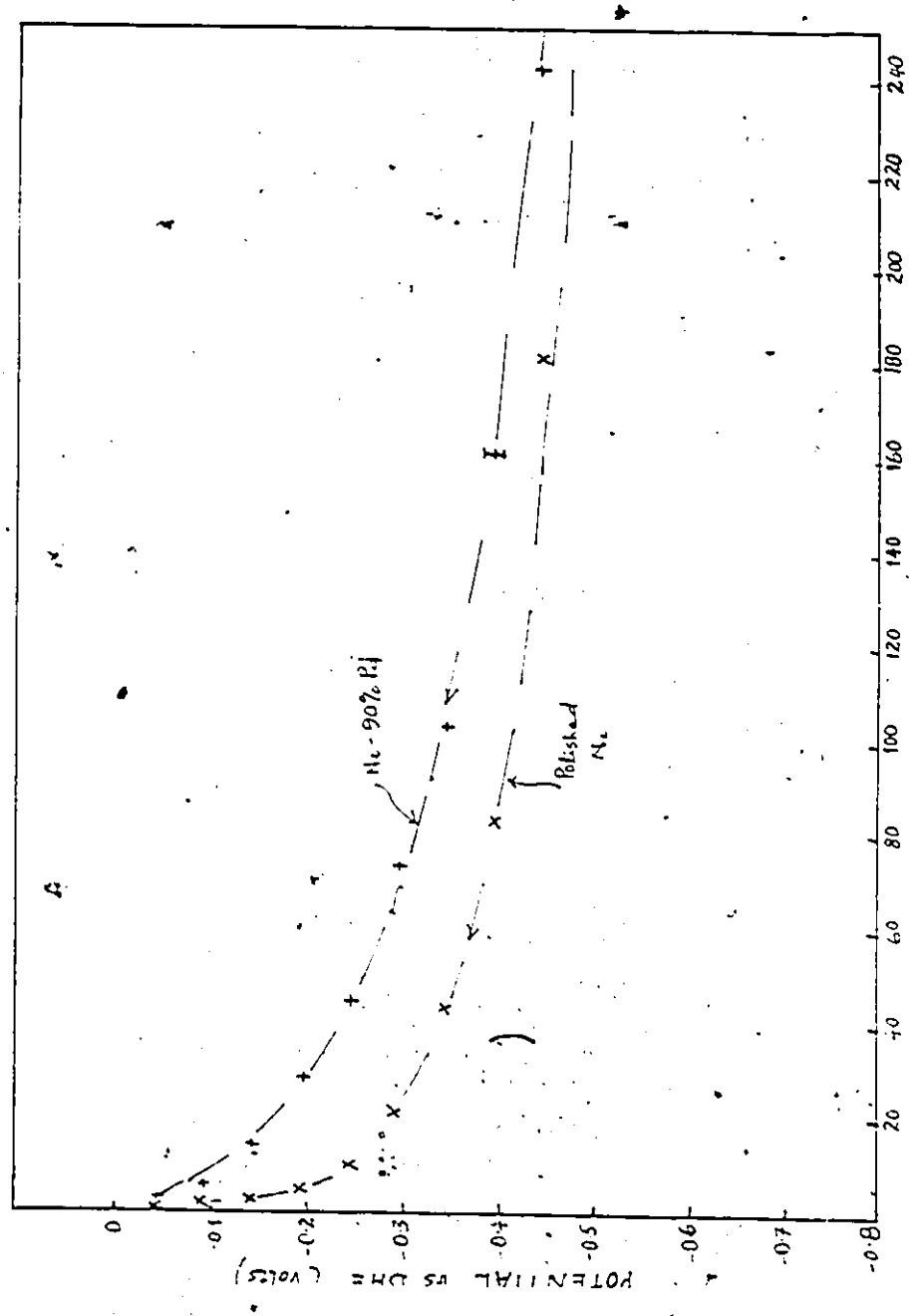

Fig. 6.68: Linear plot of cathode potential vs. current density.

slope of only ∿ 40 mV/decade was obtained.

As discussed previously in section 3.3, the performance of an electrode as a catalyst is often assessed on the basis of its exchange current density, i_0, for the reaction, and the current through the cell at specified constant potentials. In Table 6.13, the Tafel slope b, exchange current density i_0, and current density i at specified cathode potentials, measured on the various alloy cathodes studied are listed. Data for a platinized Pt electrode is also included for reference though the area of such an electrode is really not known. Figure 6.68 shows a linear plot of cathode potential versus current density i for smooth Ni and a Ni/Pd alloy containing ∿ 90 atomic % surface Pd. Table 6.13 shows that all the alloys studied showed improved performance over smooth Ni with i_0 increasing from ∿ $1x10^{-4}$ A/cm^2 for pure Ni to ∿ $8x10^{-4}$ A/cm^2 at low overpotentials for the 90% at % Pd alloy. Also, the current through the cell at specified potentials $\leq$ -0.6V is higher with alloy cathodes than with smooth Ni. For example at an electrode potential of -0.1V the cell current is almost a factor of 5 higher with alloy electrodes than with smooth Ni and at -0.2V the 55 at % alloy is ∿ a factor of 8 more active than Ni. Similar improved catalytic activity of Ni/Pd bulk alloys for H_2 evolution has been observed by Hoare et al. (1958) and Green et al. (1964) and the effect has been attributed (Conway et al. 1957 and Hoare et al. 1958) to greater ease of hydrogen desorption from Pd surfaces, resulting apparently from the lower heat of adsorption of hydrogen on Pd compared to Ni. The Tafel slopes of b ∿ 50 mV/decade measured on the 55 and 70 atomic % Pd alloys at low overpotentials is consistent with this view of electrochemical desorption being the rate-determining step on these alloys.

Table 6.13: Tafel slope, b, exchange current i_0 and current density i at specified cathode potentials.

% Pd	Tafel slope b (mV/dec)		i_0 (A/cm^2)		Current density (mA/cm^2) at various overpotentials			
	Low*	High*	Low†	High†	50 mV	100 mV	200 mV	400 mV
0	150		1.1×10^{-4}		0.5	1.1	5	82
55	50	220	$\sim10^{-4}$	4×10^{-4}	0.4	5	43	350
70	50	160	$<10^{-4}$	8×10^{-4}	0.7	5.2	17	190
90	140	280	8×10^{-4}	4×10^{-3}	1.3	7	29	160
Evaporated Pd	150		1.3×10^{-4}		0.5	1.2	4.9	90
Platinized Pt	50		8×10^{-4}		8.5	70	350	850

* Low ≡ Low overpotential region.
High ≡ Large overpotential region.

The relationship between the improved activity (over smooth Ni) of the alloyed cathodes and their surface Pd concentration is not clear, especially at large overpotentials ($\geq$ -0.2V). For overpotentials $\leq$ -0.1V, the current through the cell appears to increase with increasing surface concentration of Pd in the alloy. For larger overpotentials, the Ni-55% Pd alloy shows the most improved activity over smooth Ni. For example, at -0.4V the cell current with Ni-55% Pd cathode is more than a factor of 4 higher than for smooth Ni, while the 90% Pd alloy is only a factor of 2 higher than smooth Ni. Perhaps this apparent decrease of activity for the alloys with high Pd content is fortuitous. Visual observations on these electrodes during the experiments indicate considerably more uniform and vigorous H_2-evolution than on the high Ni alloys, with the onset of observable gas evolution occurring at lower current densities on the high Pd alloys than on the high Ni alloys. Thus at each potential in the high overpotential region ($\geq$ -0.1V), the hydrogen coverage on the high Pd alloys is considerably more than on the high Ni alloys. Such a high coverage may lead to a higher ohmic drop at the electrode/solution interface, and also to a slow discharge step and consequently to less current through the cell. It is suggested that the change of Tafel slope (from a Tafel slope b = 40 mV/decade to a higher slope) occurs at decreasing current densities with increasing Pd surface concentration because the rate of increase in hydrogen gas coverage on the alloys is different. Increased gas evolution and surface coverage apparently occurred with increasing surface Pd concentration. In the absence of corrections for IR drops, the true activation overpotential is not known. It should be pointed out here that apparent reduced electrode activity

with Pd content has also been observed for Ni/Pd alloys (Hoare et al. 1958) at low overpotentials (near-50 mV). They found that alloy cathodes with high Ni content ($80\% \leq Ni \leq 99\%$) have higher activity than Ni or alloys with nickel content between 30 and 80 atomic %; this was attributed to preferential segregation of Pd to the alloy surface. Hoare et al. did not analyze their results for catalytic activity at large overpotentials but their data show that at an overpotential of $\sim$ -0.15V, the activity of the 56% Pd alloys is more than a factor of 2 larger than that of a 75% Pd alloy, although the activities of the alloyed electrodes are much less than that observed on hydrogen-charged Pd. Indeed for alloys with > 25% Ni, there is a gradual increase in apparent activity. It is believed that these observations are also consistent with the explanation given above.

Figures 6.69 and 6.70 show, respectively, SEM photographs, following cathodic polarization, of the 55% and 70% Pd alloy cathodes. Figure 6.69(a) shows a rather featureless morphology of the as-prepared sample while 6.69(b), which shows the morphology after five days of cathodic polarization sweeps, also indicates a rather uniform surface feature. Figure 6.70(a) shows the SEM photograph spanning the region exposed (light) and unexposed (dark) to the electrolyte, while Fig. 6.70(b) is an expanded SEM view of the region exposed to the electrolyte. The uniform features observed on these electrodes contrast with those observed for Ni/evaporated Pd cathodes and suggest that ion mixing produces alloys with better film/substrate adhesion and uniform surface features.

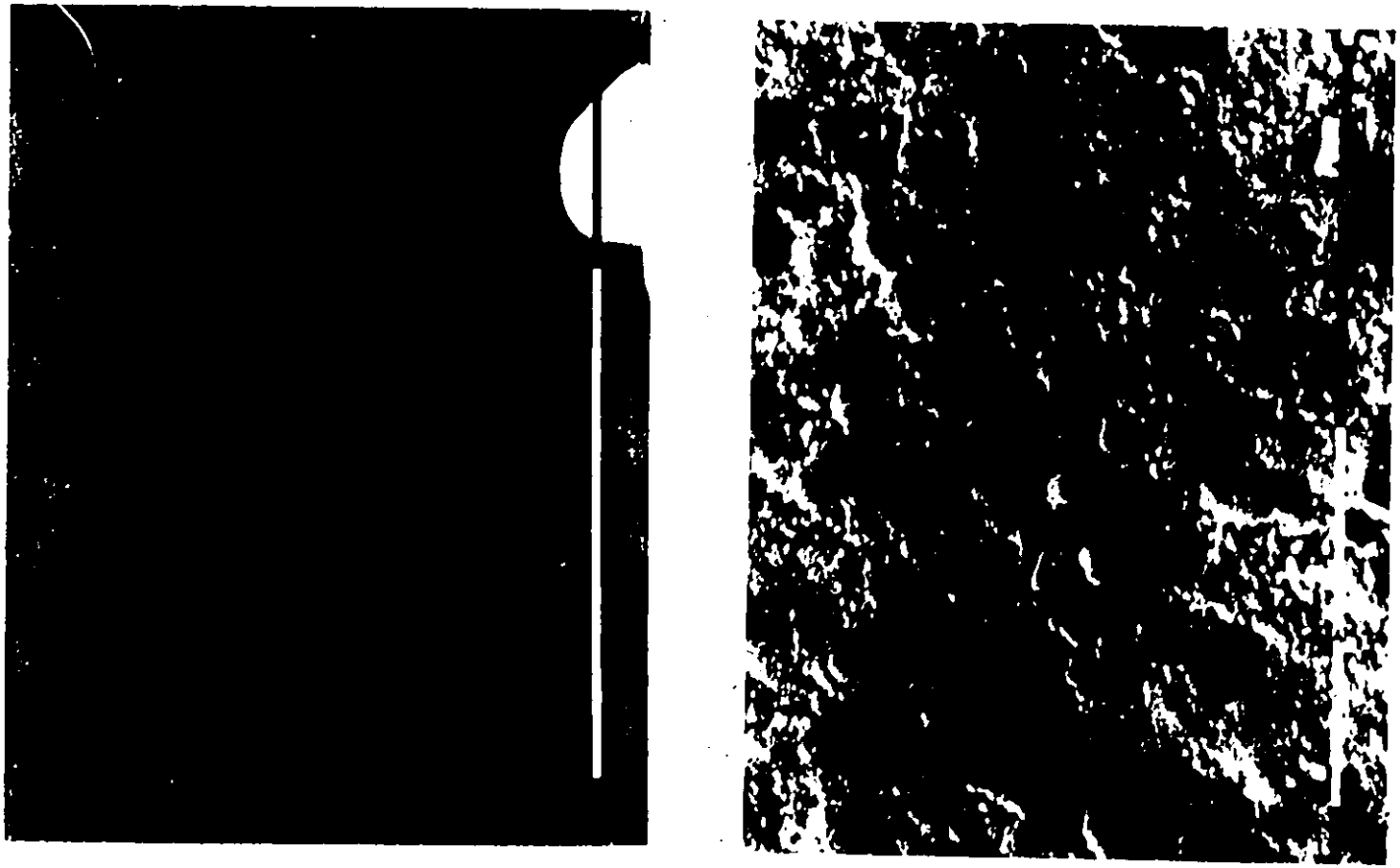

a) b)

Fig. 6.69: SEM micrograph of the Ni-55% Pd cathode following cathodic polarization a) as prepared b) after 5 days in the cell.

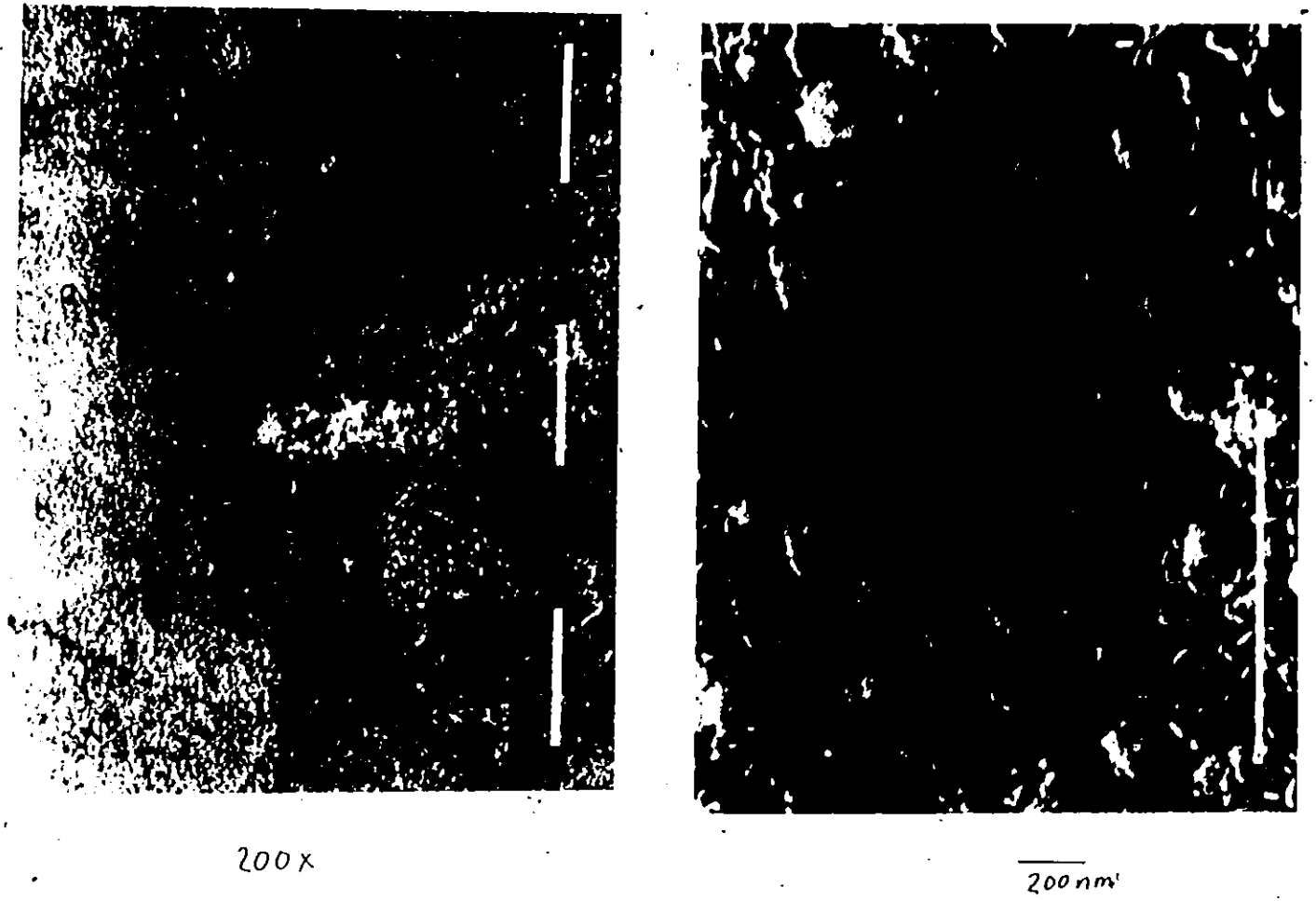

Fig. 6.70: SEM micrograph of the Ni-70% Pd cathode following cathodic polarization. (b) expanded view of the region exposed to the electrolyte.

6.5.4 Time-Dependence of η-log i

Time-dependence behaviour of the electrodes was also studied by subjecting the cathodes to several polarization sweeps. No significant changes were observed for electrodes subjected to 4 polarization sweeps. The 55% Pd alloy was studied over several days. Each day it was subjected to four polarization sweeps, at the end of which it was removed from the cell and stored overnight in a pre-electrolysed KOH solution. Figure 6.71 shows the current-potential curve obtained for this electrode after the 4th and 5th days of polarization. After the 4th day measurements, the electrode was left overnight in the cell and maintained at 100 mA/cm^2. The 5th day curve then represents the polarization curve obtained after the electrode had been in the solution at 100 mA/cm^2 for ∿ 12 hours. Up to ∿ -0.1V the curves are virtually identical, and also similar to the first polarization sweep measurements (Fig. 6.65). At more negative potentials, the 4th day measurements remain similar to the first day measurements but the 5th day results show reduced activity; this is due, perhaps, to electrode poisoning by electrolysis products in solution.

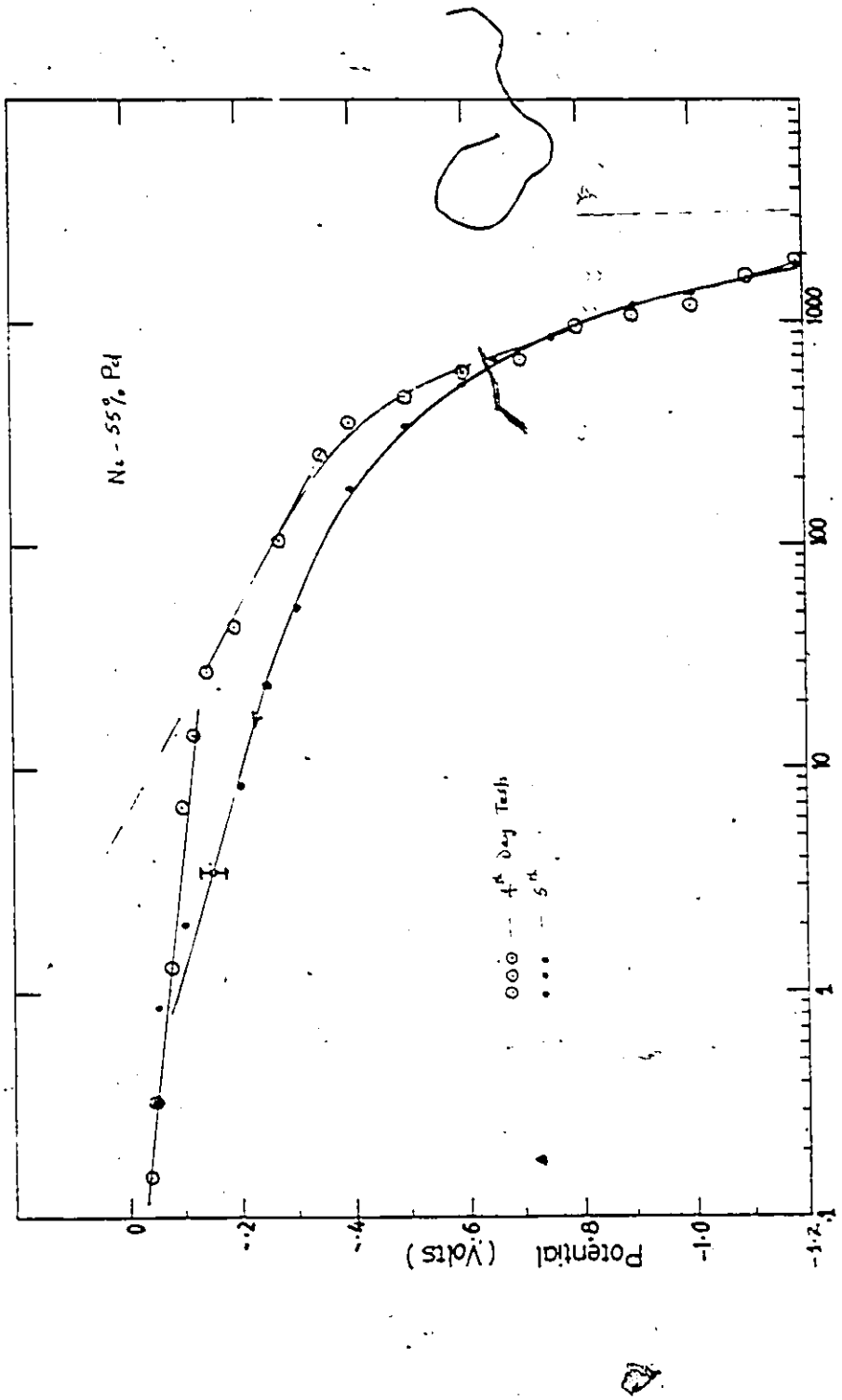

Fig. 6.71: Potential current density curve following 5 days of polarization for the 55% Pd alloy.

CHAPTER 7

CONCLUSIONS

In this chapter, results of the present investigations are summarized and the conclusions drawn from them are highlighted.

1. Ion induced mixing of Pd Markers in Ni, and of Ni/Pd Bilayers

The spreading of Pd markers in Ni can be adequately described by a Gaussian distribution within a limited dose range. The increase in the variances depends on both the ion type and irradiation temperature. At high temperatures ($\gtrsim$ 473K) and high doses ($\gtrsim 1\times10^{16}$ cm^{-2} for Kr irradiation and $\gtrsim 2\times10^{16}$ cm^{-2} for Ar), the profiles deviate considerably from Gaussian distribution. The observed shifts in the Pd peak position following ion bombardment could all be accounted for by small fluctuations in the analyzing He^+ beam energy and ion sputtering of the Ni overlayer. Thus the mean marker peak shift predicted by Sigmund et al. (1981) was not observed in this work.

i) Dose Dependence:

For both markers and bilayers, the measured mixing parameter, $\Delta\sigma^2$, shows a linear dependence on ion dose, ϕ, at all temperatures $\lesssim$ 573K, and for both Ar and Kr irradiation.

ii) Ion Dependence:

At 40K, the spreading of Pd marker induced by Kr^+ irradiation is $\sim$ a factor of 2.2 times larger than that due to Ar^+ irradiation in qualitative agreement with the ratio of the damage energies, $F_D(Kr)/F_D(Ar)$), deposited at the marker position.

iii) A collision cascade mixing model which takes into account the cumulative effect of ion bombardment and the deposited energy density, θ, within the cascade generated by each ion was proposed to explain the ion-induced broadening of the interface between two layers. The mixing parameter $\Delta\sigma^2$ estimated from this model ($\sim$ 100 nm^2) compares well with the measured values ($\sim$ 35 nm^2 after a dose of 1×10^{16} cm^{-2} at 298K).

iv) The mixing results, $\Delta\sigma^2$ values, measured on bilayers correlated well with the marker spreading results. At temperatures where the two types of measurements overlap, the $\Delta\sigma^2$ values are identical.

v) For samples annealed without irradiation, no measurable spreading of the Pd marker, or broadening of the bilayer interface, was observed for annealing temperatures $\leq$ 400K. Above $\sim$ 400K, thermally induced mixing shows Arrhenius-type behaviour with an activation energy of $\sim$ 1.1±0.07 eV.

vi) Between 40 and $\sim$ 400K for the marker spreading experiments and between 298 and $\sim$ 400K for the bilayers, ion induced mixing ($\Delta\sigma^2$) shows a weak dependence on temperature with activation energy $\sim$ 0.1 eV.

vii) Above $\sim$ 473K, the mixing in bilayers is characterized by an initial rapid grain boundary diffusion of both Ni and Pd with high initial mixing efficiency (atoms/ion) that depends on temperature ($\sim$ 6 atoms/ion at 573K and $\sim$ 35 atoms/ion at 673K).

viii) Defect-enhanced lattice diffusion coefficients $D'_{\ell}(Ni)$, were evaluated under thermal annealing conditions for Ni diffusing in Pd. The values range from $\sim 0.22 \times 10^{-16}$ cm^2-sec^{-1} at 523K to 52×10^{-16} cm^2-sec^{-1} at 673K. The corresponding values for Pd diffusion in Ni, $D'_{\ell}(Pd)$, range from ~ 0.33 to 56.6×10^{-16} cm^2-sec^{-1} in the same temperature range.

ix) The grain boundary diffusion coefficient, D_B, for Pd diffusing in Ni grain boundaries was evaluated. The D_B values range from $\sim 5.4 \times 10^{-14}$ cm^2-sec^{-1} at 523K to $\sim 3 \times 10^{-11}$ cm^2 sec^{-1} at 623K, with an apparent activation energy $E_B \sim 1.38$ eV and a pre-exponential $D_B^o \sim 0.75$ cm^2 sec^{-1}.

x) For irradiated thin film bilayer specimens, grain boundary diffusion to deeper depths (> 100 nm) was apparently suppressed.

xi) The diffusion coefficient values under irradiation, D_{rad}, range from ~ 4 to 70×10^{-16} cm^2-sec^{-1} at 523K and 673K respectively with an apparent activation energy ~ 0.57 eV.

xii) Near $\sim$ 673K, mixing resulting from thermal interdiffusion overwhelms the irradiation induced effects.

xiii) The present investigations suggest that ion beam mixing of evaporated metal films at elevated temperatures is greatly influenced by grain boundary diffusion effects.

xiv) The dose rate dependence of mixing observed in the present investigation was inconclusive vis-a-vis the dose rate dependence predicted by the RED model.

2. Mixing of Large-Grain Ni and Evaporated Pd Layers

i) For annealed specimens, lattice diffusion coefficients (for Pd diffusing in Ni) are some factor of 80 to 100 less compared to values determined for the evaporated Ni/Pd films.

ii) Grain boundary diffusion of Ni through the evaporated Pd film occurred, but not of Pd into Ni.

iii) Under irradiation conditions, diffusion of Pd into Ni was enhanced by more than an order of magnitude but the values are still less than in the small-grain case.

iv) A deep penetrating tail of Pd distribution extending approximately to the ion range, was observed for the irradiated specimens but not for annealed unirradiated specimens. It is believed that this rapid diffusion path results from dislocations generated by collision cascades. The coefficient of diffusion along these paths was determined to be $\sim 1.3 \times 10^{-14}$ cm^2-sec^{-1} at 673K.

3. Irradiation Induced Grain Growth

i) TEM observations reveal irradiation induced recrystallization and grain growth of films evaporated on NaCl substrates.

ii) The average grain size increased from $\sim$ 10 nm to $\sim$ 50 nm after a dose of $\sim 2 \times 10^{16}$ Ar^+ cm^{-2} for specimens irradiated at 298K.

iii) Ar irradiation at 573K led to a more uniform grain structure with average diameter $\sim$ 60 nm after a dose of 1×10^{16} cm^{-2}. The film also exhibits texture.

iv) Kr irradiation results in a greater grain growth rate with average grain diameter ~ 80 nm for specimens irradiated at 573K to a dose of 5×10^{15} cm^{-2}. The larger grain size and the low Kr dose needed to achieve it is believed to be due to the larger energy density deposited by Kr^+ ions vis-a-vis Ar^+ ions.

4. Electrocatalysis of the H_2-Evolution Reaction

i) Smooth Ni specimens gave results that are in excellent agreement with those reported in the literature under similar experimental conditions.

ii) Ni cathodes with evaporated Pd give results that are virtually identical to smooth Ni. SEM observations of the electrode surface show that this is due to spalling of the film resulting from poor adhesion between the film and Ni substrate.

iii) All the ion-mixed cathodes show superior performance (based on cell current at specified potentials) over smooth Ni for overpotentials $\gtrsim$ -0.4V. At low overpotentials ($\gtrsim$ -0.1V), a Tafel slope b ~ 50 mV/decade typical of pure Pd was observed on the alloys.

iv) The 55% Pd cathode shows the best performance over Ni. It is suggested that the apparent decrease of activity with increasing Pd content is due to increased gas coverage and therefore increased ohmic-loss contribution to the potential.

v) In the important region of potential technological application (400-1000 mA/cm^2), no improved performance was observed as the potential becomes dominated by IR losses due to gas bubble formation.

REFERENCES

Akano U., Davies J A., Smeltzer W.W., Tashlykov I.S. and Thompson D.A. Nucl. Instr. Meth. 81/82.

Al-Saffar A.H., Ashworth V., Grant W.A. and Procter R.P.M., Corr. Sci. 18 (1978) 687.

Al-Saffer A.H., Ashworth V., Bairamov A.K.O., Chivers D J., Grant W.A and Procter R.P.M., Corr. Sci. 20 (1980) 127.

Al-Tamini Z.Y., Grant W.A., Carter G., Stevanovic D.V., and Thompson D.A., Nucl. Instr. Meth. B7/8 (1985) 124.

Andersen H.H., Appl. Phys., 18 (1979) 131.

Angus H.C., Phys. Technol. 12 (1981) 245.

Appleby A.J., Grepy G. and Jacqueline J., Int. J. of H_2 Energy 3 (1978) 21.

Appleby A.J. and Crepy, Proc. Symp. on Industrial Water Electrolysis (1978).

Ashworth V., Baxter D., Grant W.A. and Procter R.P.M., Corros. Sci. 17 (1977) 947.

Ashworth V., Procter R.P.M. and Grant W.A., Thin Solid Films, 73 (1980) 179.

Ashworth V., Grant W.A., Procter R.P.M. and Wright E.J., Corros. Sci. 18 (1978) 681.

Ashworth V., Grant W.A., Procter R.P.M. and Wright E.J., Corr. Sci. 18 (1978) 681.

Atkinson A., AERE Harwell, AERE-R10588.

Averback R.S., Thompson L.J. Jr., Moyle J. and Schalit M., J. Appl. Phys. 53 (1982) 1342.

Averback R.S., Nucl. Instr. Meth. B15 (1986) 675.

Averback R.S. in Ion Implantation and Ion Beam Processing of Materials, Eds. Hubler G.K., Holland O.W., Clayton C.R. and White C.W., (Elsevier Sci. Publ. N.Y. 1984) p. 25.

Balej J., Int. J. Hydrogen Energy 10, 2 (1985) 89,

Baglin, J.E.E. and Poate J.M., Thin Films - Interdiffusion and Reactions. Eds. Poate J.M., Tu K.N. and Mayer J.W. (Wiley Intersci. Pub. 1978) p. 305.

Barbabai U., Cavaline M., Bombers G., Dearnaley G. and Wilkins M.A., Corr. Sci. 20 1 (1980) 19.

Barz A.J. and Nicolet M.-A., Appl. Phys. A 33 (1984) 167.

Benjamin J.D. and Dearnaley G. (1976), Inst. Phys. Conf. Series #28 (Institute of Physics, London) p. 141.

Benoit P. and Martin G., Thin Solid Films 25 (1975) 181.

Bennett M.J., Houlton M.R. and Dearnaley G., Corr. Sci. 20 1 (1980) 69.

Besenbacher F., Böttiger J., Nielsen S.K. and Whitlow H.J., Appl. Phys. A29 (1982) 141.

Bhattacharya R.S., Pronko P.P., Rai A.K., McCormick A.W. and Raffoul C., Nucl. Instr. Meth. B7 18 (1985) 694.

Bidwell L.R., Acta Crysta 17 (1964) 1473.

Bockris J. O'M. and Srinivasan S. in 'Fuel Cells: Their Electrochemistry' McGraw-Hill N.Y. (1969).

Bockris J.O'M., Conway B.E., Yeager E. and white R.E., Eds. Comprehensive Treatise on Electrochemistry Vol. 2 (1981) p. 16.

Bockris, J.O'M., Conway B.E., Yager E. and Sarangapani, Eds. Comprehensive Treatise on Electrochemistry Vol. 9 (1983) 17.

Bockris J.O'M. and Reddy A.K.N., in Modern Electrochemistry Vol. 2, Plenum N.Y., 1970.

Bockris J.O'M., Damjanovic A. and Mannan R.J., J. Electroanal. Chem. and Interf. Electrochem. 18 (1968) 349.

Bohr N., Phil. Mag. 30 (1915) 581.

Born M. and Mayer J.E. (1932), Z. Physik 75 1 (1932) 96.

Borovskii I.B. in Diffusion Data 1, 1 (1967) p. 31.

Bøttiger J., Nielsen S.K. and Thorsen P.T., Nucl. Instr. Meth. B7l8 (1985) 707.

Bottiger J.,Nielsen S.K. and Thorsen P.T. Proc. IBMM 1984

Brooman E.W. and Kuhn A.T. J. Electroanal. Chem. and Interf. Electrochem., 49 (1975) 325.

Chen C.W., Mastenbrook A. and Elen J.D., Rad. Eff. 16 (1972) 127.

Chen C.W., Phys. Stat. Sol., 16 (1973) 197.

Chu W.K., Mayer J.W. and Nicolet M.-A., Backscattering Spectrometry, Academic Press, N.Y., 1978.

Clark G.J., Marwick A.D. and Poker D.B., Nucl. Instr. Meth. 209/210 (1983) 107.

Clayton C.R., Nucl. Instr. Meth., 182/183 (1981) 865.

Covino Jr. B.S., Needham Jr. P.B. and Conner G.R., J. Electrochem. Soc. 125 (1978) 370.

Conway B.E. and Bockris J. O'M., J. Chem. Phys. 26, 3 (1952) 532.

Covino Jr. B.S., Sartwell B.D. and Needham Jr. P.B., J. Electrochem. Soc. 125 (1978) 366.

Damjanovic A, Dey A. and Bockris J. O'M, Electrochimica Act., 11 (1966) 791

Davies J.A. Proc. NATO Adv. STudy Institute, Trevi, Italy, Aug. 1981.

Dearnaley G., Goode P.D., Miller W.S. and Turner J.F. Proc. Int. Conf. Conf. on Applic. of Ion Beams to Metals, Albuquerque, New Mexico, 1973.

Dearnaley G., Nucl. Instr. Meth. B7/8 (1985) 158.

Dearnaley G., J. Met. 34, 9 (Sept. 1982) 18.

Dearnaley G. and Goode P.D., Nucl. Instr. Meth. 189 (1981) 117.

Dearnaley G., Thin Solid Films, 197 (1983) 315.

Dienes G.J. and Damask A.C., J. Appl. Phys., 29, 12 (1958) 1713.

Green J.A.S. and Lewis F.A., Trans. Far. Soc., 60 (1964) 2234.

Fedrozo L., Guzman L., Molinari A., Girardi S. and Bohora P.L., Nucl. Instr. Meth. B7/8 (1985) 711.

Ferber H., Kasten H., Wolf G.K., Lorenz J.W., Schweickert H. and Folger, H., Corr. Sci. 20 (1980) 117.

Fisher J.C., J. Appl. Phys. 22, 1'(1951) 74.

Fontana M.G. and Green N.D., Corrosion Engineering (McGraw-Hill,N.Y. 1978).

Fontana M.G. and Green N.D., Corrosion Engineering (McGraw-Hill, N.Y. 1978) 325.

Galerie A., in Ion Implantation into Metals. Eds. Ashworth V., Grant W.A. and Procter R.P.M. (Pergamon, Oxford 1982) 190.

Gilmer G.H. and Farrel H.H., J. Appl. Phys. 47, 9 (1976) 3792.

Gilmer G.H. and Farrel H.H., J. Appl. Phys. 47, 10 (1976) 4373.

Giner J., J. Electrochem. Soc. 111, 3 (1964) 376.

Goode P.D., Inst. Phys. Conf. Ser. #28 (Institute of Physics, Bristol, 1976) 154.

Grant W.A. (1975) Inst. Phys. Cohf. Ser. 28 (1975) 127.

Grenness M., Thompson M.W. and Chan R., J. Appl. Electrochem. 4 (1974) 211.

Guinan M.W. and Kinney J.H., J. Nucl. Mat. 103/104 (1981) 1319.

Bonzales E.R. in Hydrogen Energy Progress, Proc. 3rd World Hydrogen Energy Conf. Tokyo (1980) 127. Eds. Veziroglu T.N., Fueki K. and Ohta T.

Gupta D. and Ho P.S., Thin Solid Films 72 (1980) 399.

Gupta D., Campbell D.R. and Ho P.S. in Thin Film-Interdiffusion and Reactions, Eds. Poate J.M., Tu K.N. and Mayer J.W. (Wiley-Interscf. Pub. 1978) 161.

Haff P.K. and Switkowski Z.E., J. Appl. Phys. 48 #8 (1977) 3383.

Ham F.S., J. Phys. Chem. Solids 6 (1958) 335.

Harkness S.D. and Peterson, N.L. Eds. Radiation Damage in Metals, Proc. Seminar of the Americ. Soc. Metals, Metals Park, Ohio Nov. 1975.

Hartley N.E.W., Wear, 34 (1975) 427.

Hartley N.E.W., in Ion Implantation, Ed. Hirvonen J.K., Acad. Press N.Y. (1980) 321.

Hoare J.P. and Schuldiner S., J. Phys. Chem. 62 (1958) 229.

Hoare J.P. and Schuldiner S., J. Electrochem. Soc. 107, 10 (1960) 820.

Holloway P.H., Amos D.E. and Nelson G.C., J. Appl. Phys. 47, 9 (1976) 3769.

Horak J.A. and Blewitt T.H., Nucl. Techn. 27 (1975) 416.

Hubler G.K. and McCafferty E., Corr. Sci., 20 (1980) 103.

Hultgren R. and Zapffe C.A., Trans. Amer. Inst. Mining Met. Eng. 133 (1939) 58.

Johnson W.L., Cheng Y.T., Van Rossum M. and Nicolet M.-A., Nucl. Instr. Meth., B7/8 (1985) 657.

Kasten H. and Wolf G.K., Electrochim. Acta,25 (1980) 1581.

Kelly R. and Sanders J.B., Surf. Sci., 57 (1976) 143.

Khanna S.K. and Sonnenberg K., Rad. Eff., 59 (1981) 91.

King W.E. and Benedek R., J. Nucl. Mat., 117 (1983) 26.

Kinchin G.H. and Pearse R.S., Rept. Prog. Phys. 18, 1 (1958)

Kita H., J. Electrochem. Soc., 113 (1966) 1095.

Kornilov I.I., Nickel and Its Alloys (Oldsbourne Press, N.Y. 1963) 105.

LeClaire A.D., J. Appl. Phys., 14 (1963) 351.

L'Ecuyer J., Davies J.A. and Matsunami N., Rad. Eff. 47 (1980) 229.

Leroy et al. Proc. Symp. on Water Electrolysis vol. 74-4, Electrochem. Soc. Meeting, Princeton (1978) 63.

Levine H.S. and McCallum C.J., J. Appl. Phys. 31, 3 (1960) 595.

Liau Z.L., Tsaur B.Y. and Mayer J.W., J. Vac. Sci. Techn. 16 (1979) 2.

Lichter B.D., Thompson N.G., Appleton B.R. and Kelly E.J., in Ion Implantation Into Metals, Eds. Ashworth V. et al. (Pergamon, Oxford 1982) 97.

Lindhard J., Nielsen V. and Scharff M., Kgl. Dan. Vid. Selsk. Mat. Fys. Medd. 36, 10 (1968).

Lindhard J., Scharff M. and Schiott H.E., Kgl. Dan. Vid. Selsk. Mat. Fys. Med. 33, 14 (1963).

Lindhard J. and Scharff M., Phys. Rev. 124 (1961) 128.

Littmark U. and Hoffer W.O., Nucl. Inst. Meth., 168 (1980) 329.

Liu J., Presentation at the Commemorative Symp. on Atomic Collisions in Solids, CRNL (July 1986) Chalk River, Ont.

Macht M.P., Müller A., Naundorf V. and Wollenberger H., Proc. The Metal. Soc. Fall Meeting (1985), Toronto, Canada.

Matteson S., Roth J. and Nicolet M.-A., Rad. Eff. 42 (1979) 217.

Matteson S., Paine B.M. and Nicolet M.-A., Nucl. Inst. Meth. 182/183 (1981) 53.

Matteson S. and Nicolet M.-A., Ann. Rev. Mater. Sci. 13 (1983) 339.

Matteson S., Appl. Phys. Lett. 39, 3 (1981) 288.

Matteson S., Nucl. Instr. Meth. B7/8 (1985) 716.

Mayer J.W., Tsaur B.Y., Lau S.S. and Hung L.S., Nucl. Inst. Meth. 182/183 (1981) 1.

Mehrer H., Kronmüller H. and Seager A., Phys. Stat. Sol. 10 (1965) 725.

Miles M.H., Kissel G., Lu P.W.T. and Srinivasan S., J. Electrochem. Soc. 123 (1976) 332.

Miles M.H., J. Anal. Chem. and Interf. Electrochem. 60 (1975) 89.

Munn P. and Wolf G.K., Nucl. Inst. Meth. B7/8 (1985) 205.

Murray J.N., Proc. World Hydrogen Energy Conf. Tokyo (1980) 15.

Myers S.M., Amos D.E. and Brice D.K., J. Appl. Phys. 47, 5 (1976) 1812.

Myers S.M., Nucl. Inst. Meth. 168 (1980) 265.

Nagakawa M., Böning K., Rosner P. and Vogl G., Phys. Rev. B, 16 (1977) 5285.

Naguib H.M., Kriegler R.J., Davies J.A. and Mitchel J.B., J. Vac. Sci. Technol., 13 (1976) 396.

Nicolet M.-A. and Picraux S.T. Eds. 1984: Ion Mixing and Surface Layer Alloying - Recent Advances. Noyes Publications, Park Ridge, New Jersey (1984).

Norris D.I.R. (1969a), Phil. Mag. 19 (1969) 527.

Norris D.I.R. (1969b), Phil. Mag. 19 (1969) 653.

O'Grady W.E. and Wolf G.K., 159th Meeting Electrochem. Soc., Minneapolis 1981. J. Electrochem. Soc. 122, 1 (1981) 128C.

Paine B.M. (1982), J. Appl. Phys. 53, 410 (1982) 6828.

Paine B.M. and Averback R.S. (1985), Nucl. Inst. Meth. B7/8 (1985) 666.

Parikh N.L., Ph.D. Thesis, McMaster Univ. (1985).

Picraux S.T., Follstaedt D.M. and Delafond J. (1981): in Proc. Mat. Res. Soc. Meeting Boston, MA, Nov. 1981.

Poat J.M., Tu K.N. and Mayer J.W., Eds. Thin Films - Interdiffusion and Reactions, (Wiley Intersci. N.Y. 1978).

Poker D.B., Holland W.O. and Appleton B.R. in: Ion Implantation and Ion Beam Processing of Materials, Eds. G.K. Hubler, P.W. Holland, C.R. Clayton and C.W. White (Elsevier Sci. Pub., N.Y. 1984, pg. 73.

Prigent M., Proc. Symp. on Industrial Water Electrolysis (1978) 234.

Rabette P., Deane A.M., Tench A.J. and Che M., Chem. Phys. Lett. 60 (1979) 348.

Schuldiner S. and Hoare J.P., J. Phys. Chem. 61, 6 (1957) 705.

Sanders J.B., Can. J. Phys. 46 (1968) 455.

Shafer S., M. Eng. Thesis, McMaster University (1977).

Sigmund P., 1968. Bull. Amer. Phys. Soc. 13 (1968) 464.

Sigmund P. (1969a), Phys. Rev. A 184 (1969) 383.

Sigmund P. (1969b), App. Phys. Lett. 14 (1966) 114.

Sigmund P., Rad. Eff. 1 (1966) 15.

Sigmund P., Gramerti A. (1981) Nucl. Inst. Meth. 182/183 (1981) 25.

Sigmund P. , Appl. Phys. A30 (1983) 43.

Simons E.N., Guide to Uncommon Metals, Elsevier Pub. Co., N.Y. (1967) 133.

Smeltzer W.W., Haering R.R. and Kirkaldy J.S., Act. Met., 9 (1961) 886.

Sprague J.A., Westmoreland J.E., Smidt F.A. Jr. and P.R. Malberg 1974. J. Nucl. Mat. 54 (1974) 286.

Mulberg P.R., J. Nucl. Mat. 54 (1974) 286.

Srinivasan S. and Salzano F.J., Int. J. H_2 Energy 2 (1977) 53.

Stern M. and Wissenberg H., J. Electrochem. Soc. 106 (1960) 759.

Suzuoka T., Trans. Jap. Inst. Metals 2 (1961) 25.

Suzuoka T., J. Phys. Soc. Japan 19 (1964) 839.

Thompson D.A., Akano U., Davies J.A. and Smeltzer W.W., in Ion Implantation into Metals, Eds. Ashworth V., Grant W.A. and Procter R.P.M. (Pergamon Press, Oxford 1982) p. 46.

Thompson D.A., Rad. Eff. 56 (1981) 105.

Tomashov N.D., Chernova G.P. and Fedoseeva T.A., Corrosion 36, 4 (1980) 201.

Tsaur B.Y. and Mayer J.W., Appl. Phys. Lett., 37, 4 (1980) 389.

Voinov M., Bühler D. and Tannenberger H., J. Electrochem. Soc. 121, 3 (1974) 119C.

Walker R.S., Ph.D. Thesis, McMaster University, Hamilton, Ont. Canada (1978).

Wang P., Thompson D.A., Smeltzer W.W., Nucl. Instr. Meth. B7/8 (1984) 97.

Wang Z.L., Nucl. Instr. Meth. B2 (1984) 784.

Westendorp H., Wang Z.L. and Saris F.W., Nucl. Instr. Meth. 194 (1982) 453.

Westmoreland J.E., Sprague J.A., Smidt F.A. and Malberg P.R., Rad. Eff. 26 (1975) 1.

Whipple R.T.P., Phil. Mag., 45 (1954) 1225.

Winterbon, K.B., Sigmund P. and Sanders J.B., Kig. Dan. Vid. Selsk. Fys. Medd. 37, 14 (1970).

Winterbon K.B., Ion Implantation Range and Energy Deposition Distribution, (Plenum, N.Y., 1979).

Wolf G.K., Topics in Current Chem. 85 (1979) 74.

Wolf G.K., Nucl. Inst. Meth. 182/183 (1981) 875.

Wolf G.K., Rad. Eff. 65 (1982) 107.

Wollenberger H., in Physical Metallurgy, eds. Cahn R.W. and Haasen P. (Elsevier SCi. Pub. N.Y. 1983) 1160.